The Pennsylvania State University
The Graduate School

QUASI-STATIC ROTOR MORPHING CONCEPTS FOR ROTORCRAFT PERFORMANCE IMPROVEMENTS

A Dissertation in
Aerospace Engineering
by
Mihir Mistry

Submitted in Partial Fulfillment
of the Requirements
for the Degree of

Doctor of Philosophy

December 2012

The thesis of Mihir Mistry was reviewed and approved* by the following:

Farhan Gandhi
Professor of Aerospace Engineering
Dissertation Advisor, Chair of Committee

Edward Smith
Professor of Aerospace Engineering

Joseph Horn
Professor of Aerospace Engineering

Timothy Miller
Senior Research Associate - Applied Research Laboratory

George A. Lesieutre
Professor of Aerospace Engineering
Head of the Department of Aerospace Engineering

*Signatures are on file in the Graduate School.

Abstract

The current research is focused on two separate quasi-static rotor morphing concepts: Variable span and variable camber. Both concepts were analyzed from the perspective of the performance improvements they allow for, as well as their design requirements. The goal of this body of work is to develop a comprehensive understanding of the benefits and implementation challenges of both systems.

For the case of the variable span rotor concept, the effects on aircraft performance were evaluated for a UH-60A type aircraft. The parametric analysis included the performance effects of the rotor span and rotor speed variation, both individually as well as in combination. The design space considered the effect of three different gross weights (16000 lbs, 18300 lbs and 24000 lbs), for a window of $\pm 11\%$ variation of the rotor speed and a range between $+17\%$ to -16% of radius variation (about the baseline) for a range of altitudes. The results of the analysis showed that variable span rotors by themselves are capable of reducing the power requirement of the helicopter by up to 20% for high altitude and gross weight conditions. However, when combined with rotor speed variation, it was possible to reduce the overall power required by the aircraft by up to 30%.

Complimentary to the performance analysis, an analytical study of actuation concepts for a variable span rotor was also conducted. This study considered the design of two active actuation systems: Hydraulic pistons and threaded rods (jackscrews), and two passive systems which employed the use of an internal spring type restraining device. For all the configurations considered, it was determined

that the design requirements could not be satisfied when considering the constraints defined.

The performance improvements due to a variable camber system were evaluated for a BO-105 type rotor in hover. The design space considered included three different thrust levels (4800 lbs, 5500 lbs and 6400 lbs) for a range of altitudes and seven different camber distribution schemes (with up to 10 degrees of camber). Based on the analysis it was shown that variable camber was capable of reducing power up 18% for high thrust levels at high altitudes. Furthermore, it was found that a linearly distributed camber configuration, wherein the maximum camber was at the root, showed the best power reduction. For an untwisted blade (which would be advantageous in high speed flight), introducing spanwise camber variation would result in hover performance levels comparable to a twisted blade. Furthermore, the power reductions calculated were shown to be the result of a reduction of induced power due to the shift of the blade lift inboard due to the direct lift increase as a result of camber variation.

The variable camber design presented in the current study exploits the warp-twist relationship of open-section beams. To that effect, a unique actuation structure was developed and implemented in a proof-of-concept variable camber prototype which was built using an existing CH-46E blade section. This prototype was shown to be capable of producing up to 18 degrees of distributed camber with a relatively low input warping of up to 0.18 inches. The results from the specifically developed finite element model of the prototype correlated very well with experimental data. The finite element results indicated the requirement of a shear-deformable core for proper camber deformation in the presence of centrifugal and aerodynamic loads.

Table of Contents

List of Figures

List of Tables

Acknowledgments

I would like to express my deep gratitude toward my advisor Dr. Farhan Gandhi for giving me the opportunity to focus on and pursue my academic goals at the Penn State Vertical Lift Research Center of Excellence (VLRCOE). I would like to especially thank him for his time, patience and above all his perseverance he showed towards me during my doctoral research. His advice and guidance has helped me mature as a capable research engineer.

I would also like to thank my committee members; Dr. Edward Smith, Dr. Joseph Horn and Dr. Timothy Miller, for their guidance as I conducted my research. Their critiques helped me hone in on the pertinent issues relating to my research. I especially would like to thank Dr. Smith for all the help and guidance he has offered me over the years.

For the duration of my doctoral research I was funded as a National Defense, Science and Engineering Graduate (NDSEG) Fellow. For that I want to thank the Department of Defense (DoD) and the American Society for Engineering Education (ASEE) for providing for such an excellent program without which I would not be able to complete my work.

I would like to thank Mr. Sam Evans for his immense help in procuring the CH-46 blade section used as part of my doctoral research. Furthermore, I would also like to thank the US Navy Naval Air Systems (NAVAIR) Command's Vertical Lift Center Of Excellence (VLCOE) for donating the blade section which was vital to my research.

The assistance of Mr. Rick Auhl, Mr. Mark Catalano and Mr. Kirk Hiller is also greatly appreciated. Their constant support of any project that I have undertaken at the department is irreplaceable. The entire administrative staff at

the Aerospace Engineering department have alway been there to lend a helping hand and I am very appreciative of their support. I would also like to thank Mr. Jerry Anderson and Mr. Joshua Cleaver from the Engineering Shop Services (ESS) department for their extensive support in building the variable camber prototype. Furthermore, the guidance of Mr. Bill Genet at the Learning Factory with regards to machining techniques is also greatly appreciated.

Lastly, I would like to thank everyone who made this journey an unforgettable one. My parents for constantly providing me with the support and encouragement that gave me the motivation to move forward towards the finish line, I would not be able to get this far without their unwavering support. My fiancée Greeshma for her support and patience in dealing with my odd and sometimes long working hours. My friends at the Vertical Lift Research Center of Excellence (VLRCOE) without whom this journey would have been incomplete; Eric Hayden, Eui Sung Bae, Conor Marr, Maryam Khoshlahjeh, Julien Austruy, Silvestro Barbarino, Sreenivas Nampy and Taha Ozdemir for their constant support as my goto people whenever I needed any advice or help. I especially would like to thank my roommate, colleague and good friend Gabriel Murray who in addition to being another one of my goto people for technical advice was also a constant personal support.

Dedication

Dedicated to my loving and very supportive parents.

CHAPTER 1

Introduction

1.1 Background and Motivation

The role helicopters play in aviation has increased exponentially since the availability of the worlds first mass produced helicopter in 1942, the Sikorsky R-4. The advantages it lends to both the civilian and military sectors is irreplaceable, especially for search and rescue operations, where its capability to hover for periods of time is unmatched by other types of aircraft. Furthermore the capability to take off and land without the need of a runway allows for the transportation of goods, people and services to remote and inaccessible places.

However, for all its benefits, they are also plagued with problems associated with their relatively complex operating aerodynamic and dynamic environments as compared to fixed wing aircraft. In particular most of these problems emanate from the main rotor which produces the primary lifting capability. For example, even in the simplest flight condition of hover, due to the rotation of the main rotor blades they experience radially varying velocities 1.1(a). On the other hand, figure 1.1(b) (Ref. [28]) shows some of the problems associated with the complex

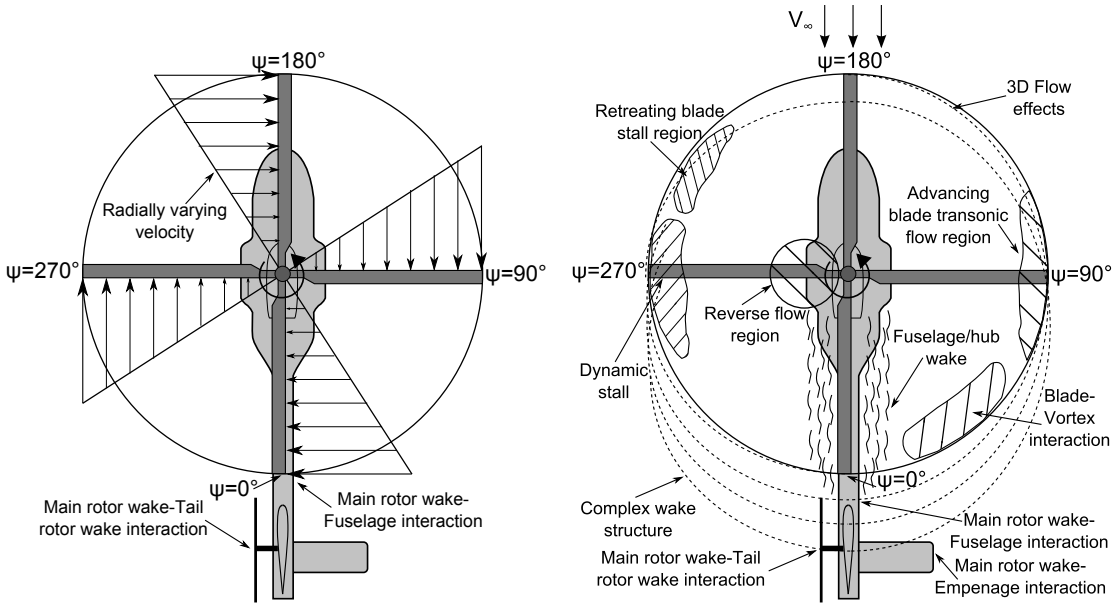

(a) Hover case (b) Forward flight case

Figure 1.1. Complex helicopter aerodynamic environments

aerodynamic environment that the rotor operates in when in forward flight.

As can be seen, the variation of the aerodynamic environment experienced by the helicopter rotor is diverse not only with flight condition but also with azimuth. Historically, engineers generally design the rotor blades to have a specific blade planform and introduce azimuthal changes in blade pitch via a swashplate for primary control in forward flight. This approach, although well proven, has two major drawbacks. The first being the design selection of the fixed blade planform represents a compromise as the optimal configuration also varies with flight condition. The second problem stems for the widely azimuthally varying aerodynamic environment of the rotor blade in forward flight. This variation contributes to a significant amount of noise and vibration introduced into the aircraft cabin, and noise emanated to the surrounding environment. The reduction of this noise and vibration, while not paramount for aircraft efficiency, is important for the "jet smooth" ride of helicopters among other considerations. A classical swashplate configuration is only capable of introducing once-per-revolution changes in blade pitch which are insufficient to abate this noise and vibration, for this an inputs of at least N-1, N and/or N+1 per revolution are needed (N is the number of blades).

Two possible methods to resolve the issues relating to the complex aerodynamic environment are the quasi-static (as a function of flight condition) and dynamic (as a function of azimuth) rotor control inputs. The first method related to the direct change of the blade planform to better suit the flight condition, examples of this are variations of the twist, chord, camber and span of the blades. Whereas the second method allows for the introduction of the N-1, N, N+1/rev inputs into the rotor system which falls under the category of Higher Harmonic Control (HHC). A method of HHC is to control the motion of the swashplate in the fixed frame at more than once per revolution (Fig. 1.2). Another approach to introducing HHC is the use of Individual Blade Control (IBC) where, as the name implies, each blade is controlled individually in the rotating frame. This can be done by either varying the blade pitch input via a variable length pitch link (Fig. 1.2) or directly via dynamic blade morphing. The research work presented is in the area of rotor blade morphing and as such the focus of the literature review presented in the following sections will relate to it as well.

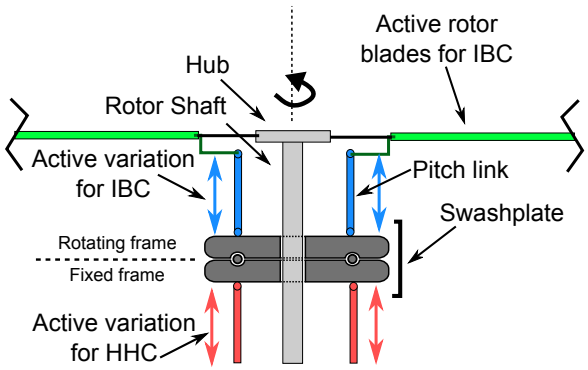

Figure 1.2. Schematic representation

1.2 Rotor morphing technologies

Active rotor blade morphing is not a new concept, however, it was not until the 1960's when this area of research garnered significant interest from government labs, private industry and academia alike. The different concepts of achieving individual blade control using rotor morphing are listed in table 1.1. In the proceedings sections, details of the evolution of the designs for these various concepts

are discussed.

Table 1.1. Rotor morphing concepts

Name	Dynamic Actuation	Quasi-Static Actuation
Trailing Edge/Gurney Flap	X	X
Variable Twist/Active Tip	X	X
Variable Span		X
Variable Chord	X	X
Variable Camber	X	X
Variable Nose Droop	X	

Although not a direct rotor morphing concept, rotor speed variation is also a powerful way of improving aircraft performance. In particular, use of variable rotor speed technologies with various rotor morphing concepts can amplify the performance benefits. Therefore, following the discussion of rotor morphing concepts, selected research bodies analyzing the effects of variable speed rotors will also be discussed.

1.2.1 Active trailing edge/Gurney flaps systems

Flaps have been used production helicopters since 1947 when Charles Kaman, founder of Kaman Helicopters, used them for primary control of the K-125. However, this design called for the use of servo flaps (Fig. 1.3) which comprised of flap system to be attached to the trailing edge of the main rotor blade. The focus of these research is within the scope of rotor blade morphing and as such, the review is on on-blade plain flaps. These type of flap systems have been shown to not only reduce the noise and vibration [29, 30, 31] emanating from the rotor system but also to improve the performance of the aircraft as well [32]. The major problem in designing active trailing edge devices is to be able to produce the required forces to overcome the aerodynamic moments of the flap while being able to operate at high frequencies (N-1,N,N+1/rev) within the confines of the blade.

Figure 1.4 shows the timeline of active flap research on the horizontal axis with the maturation of the technologies represented by the vertical axis. In the proceeding sections the evolution of various piezo and non-piezo based active flap actuation technologies will be discussed.

Figure 1.3. Kaman K-Max Servo Flap

1.2.1.1 Piezo ceramic based trailing edge flap actuation technologies

A review of literature shows two majors types of piezo ceramic based actuators, among others, used to actuate trailing edge flap: Piezo-bender devices and Piezo-stack devices, all of which used the reverse piezo effect of materials for actuation. An overview of the piezo-effect is presented in Ref.[33]. As can be seen in Fig. 1.4 the earliest research work done in this area was in the late 1980's at the Massachusetts Institute of Technology (MIT) by Spangler and Hall [34]. As part of this research work the authors developed and tested benchtop and wind tunnel models. The design called for the use of a piezo-bender actuator which was clamped at one end (leading edge spar) and the free tip was connected via a set of nylon hinges to a 10% chord flap (1.5(a)). Piezo-benders actuate when a voltage is applied to the piezo-ceramic causing in-plane strain which if is differntially applied leads to a vertical tip deflection. The actuation of the flap in this arrangement was caused due to the bending of the piezo-bender which is translated to a pitching of the flap via the hinges. It was observed, as expected, that the flap deflection degraded with an increase in airspeed, note that the wind tunnel test were for subsonic velocities of up to 78 ft/sec (23.8 m/s).

Further development of the piezo-bender active flap concept at MIT was undertaken by Prechtl and Hall in 1994 [35, 36] wherein the hinges of the original design were replaced with flexures and a tapered piezo-bender was used (Fig. 1.5(b)). These design modifications allowed the authors to reduce parasitic friction forces

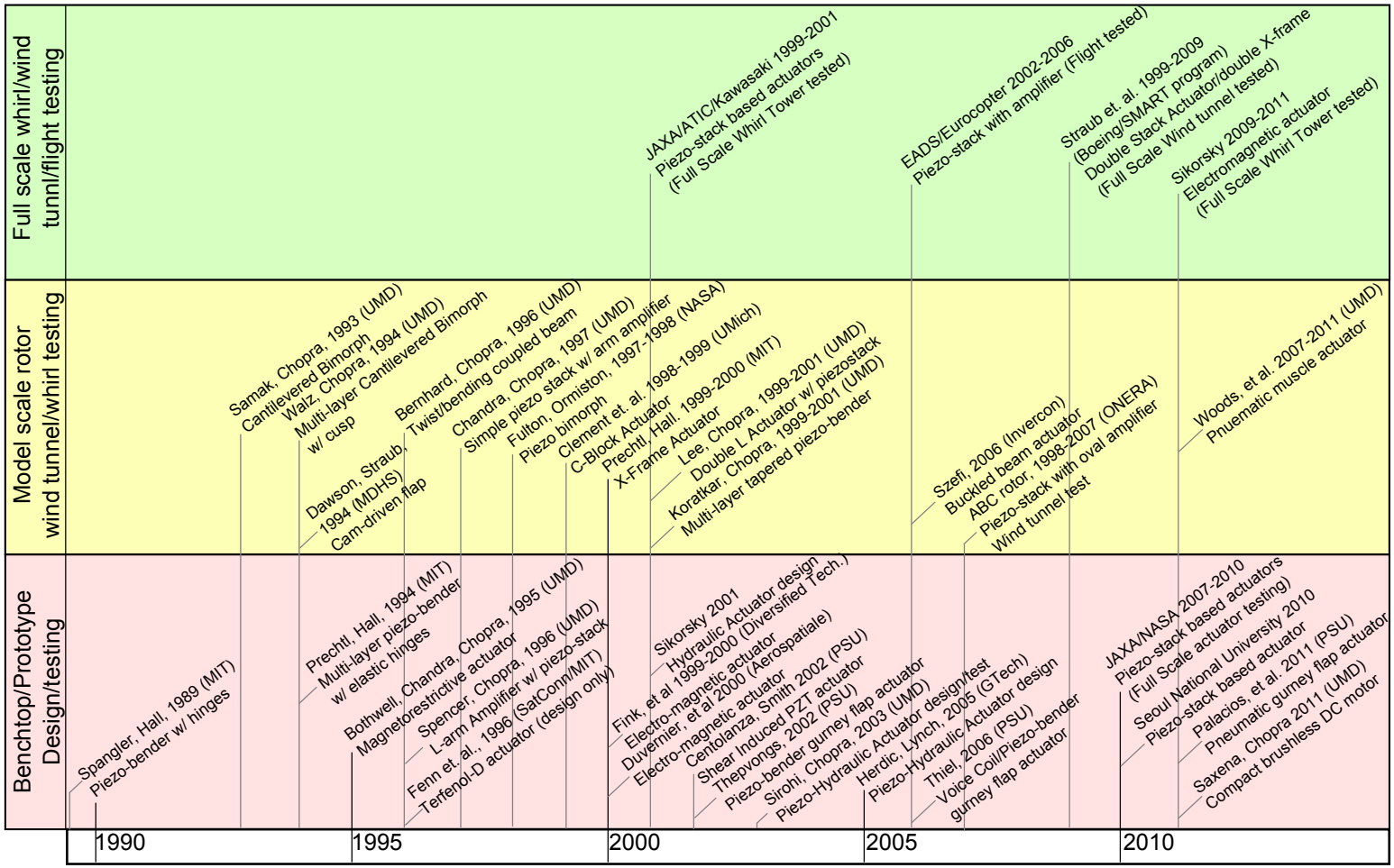

Figure 1.4. Timeline of Active Flap systems

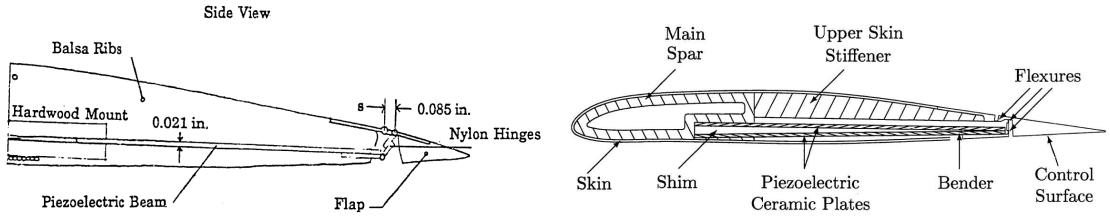

(a) Spangler and Hall [34] (b) Prechtl and Hall [35]

Figure 1.5. Piezo-bender flap actuator design evolution at MIT

and to increase actuation authority which resulted in better actuation characteristics.

Simultaneously in 1993, Samak and Chopra [1] at the University of Maryland developed a piezo-bender device which utilized linkages at the free end to connect to a 20% chord flap (Fig. 1.6). This device was built into froude scaled blades, between 85 and 97 % of blade span and tested on the hover test stand at the university. The experiment showed a degradation in flap performance with an increase in rotor RPM (dynamic pressure).

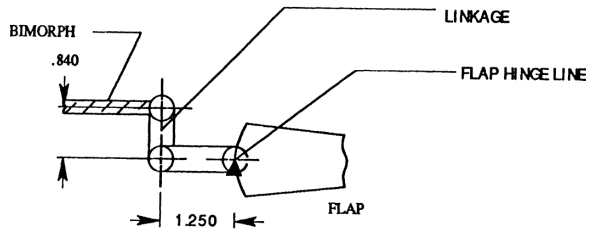

Figure 1.6. Samak and Chopra flap hinge design [1]

In 1994, Ben-Zeev and chopra [37] suggested the use of a thrust collar for the bender tip in order to reduce the degradation due to friction. This design feature is later adopted by other actuator designs as well. During the mid 1990's, Walz and Chopra[2] modified the piezo-bender design to introduce a cusp. This cusp was intended to solve the problem of the different arc motion of the bender and the flap as shown in Fig. 1.7(a) which lead to parasitic friction forces. A further modification to the original design was the use of a multi-layer bimorph to increase the control authority of the device (Fig. 1.7(b)).

Fulton and Ormiston [3, 38] developed and tested (hover and wind tunnel) a two bladed active flap rotor system using an actuator design similar to the cusp design

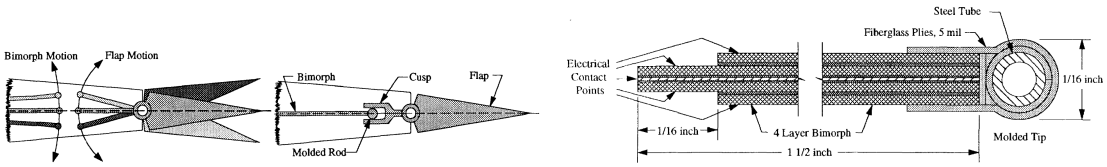

(a) Cusp design (b) Multi-layer bender

Figure 1.7. Walz and Chopra Piezo-bender design modifications[2]

(Fig. 1.8) proposed by Walz and Chopra. The 10% chord flap was designed and situated between 75 to 87% of the blade. The authors observed considerable blade flap response of the rotors to active flap actuation in hover and as a result suggest the possiblity of noise and vibration reduction in forward flight, a hypothesis which was later confirmed during wind tunnel tests.

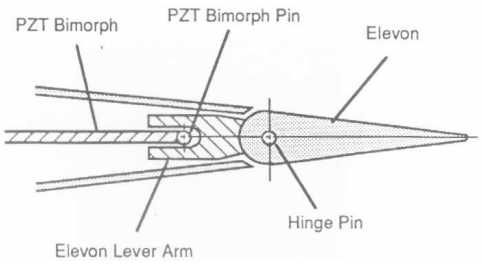

Figure 1.8. Fulton and Ormiston flap actuator design [3]

The last major body of work on Piezo-bender technology was undertaken by Koratkar and Chopra at the University of Maryland in the late 1990's early 2000's [39, 40, 41, 4]. For this research work a tapered multi-layered piezo-bender with a cusp (Fig. 1.9(a)) was designed, built and tested in both froude scale hover tests and mach scaled wind tunnel tests. Note the use of a thrust collar in the design, a design adopted from work done be Ben-Zeev and Chopra [37]. The blades were designed for a 20% chord and 8% span flap at 75% radial location (Fig. 1.9(b)). The location and sizing was determined by numerical parametric study conducted using the University of Maryland Comprhensive Analysis Code (UMARC). The wind tunnel test showed upto a 90% reduction of 4/rev hub loads for a four bladed rotor system.

The development and maturity of the piezo ceramic devices also lead to the development of a plethora of piezo-stack devices for active trailing flaps, starting in

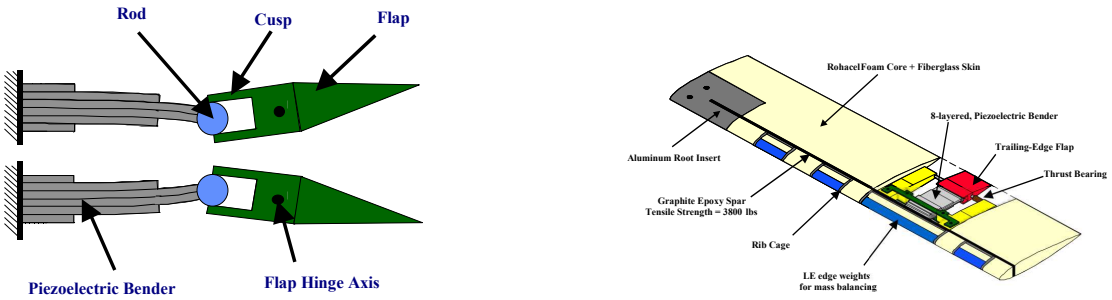

(a) Flap schematic (b) Mach scale blade schematic

Figure 1.9. Koratkar and Chopra multi-layer tapered piezo-bender flap actuator design[4]

1996 with Spencer and Chopra [5] at the University of Maryland. Piezo-stack devices, unlike piezo-benders, utilize out-of-place displacements of the piezo-ceramics as the mode of actuation. This enables for higher force capabilities albeit at the cost of lower amplitudes. Therefore, in order to meet the force and stroke actuation requirements, piezo-stack actuators are used in cohort with a mechanical amplification device. For this particular case, Spencer and Chopra, used a single column piezo-stack actuator in conjunction with a L-arm mechanical amplifier and a restoring spring to actuate a pushrod connected to the flap (Fig. 1.10). The open jet wind tunnel test of this first generation design concept showed a reduction in flap authority with increasing free-stream velocity. Furthermore the flap deflection measured was significantly lower than theoretically expected. This degradation was attributed to mechanical issues related to the system.

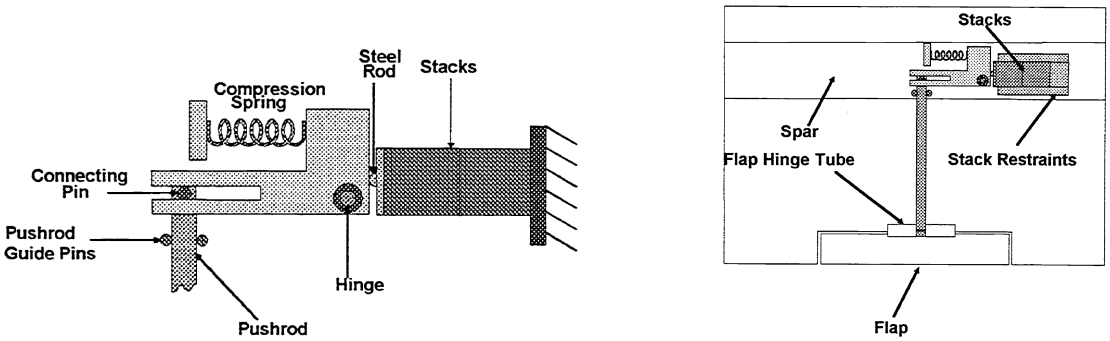

(a) Actuator Schematic (b) Flap schematic

Figure 1.10. Spencer and Chopra piezo-stack actuator with L-arm amplifier [5]

In the late 1990's, Chandra and Chopra [6] used a commercially available piezo-stack actuator with an integrated amplification arm (Fig. 1.11) along with a restoring spring and a push-rod device similar to Spencer and Chopra [5] to actuate a wind tunnel model flap. A reduction in the flap actuation with increasing free-stream velocities was observed. However, an analytical assessment of various commercially available stack actuators by authors concluded that with a proper redesign a piezo-stack based device for full scale rotor blades is feasible.

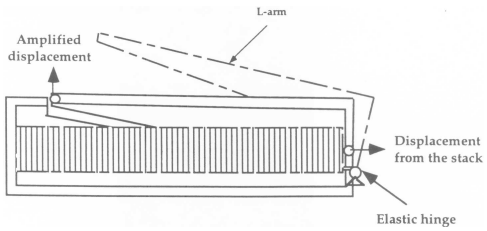

Figure 1.11. Chandra and Chopra flap actuator [6]

At the University of Maryland, between 1999 and 2001, Lee and Chopra worked on various designs for stack actuators and corresponding displacement amplification mechanisms [42, 43, 44, 7, 8]. The focus of this research work was the development of a full-scale active trailing edge flap actuator. As part of this research three different prototypes of a L-L amplification device were developed. The first design shown in Fig. 1.12, was whirl tested at the University of Maryland vacuum chamber where it was shown to work in a centrifugal field. However, as part of the testing, the authors notice several issues relating to the mechanical assembly of the device.

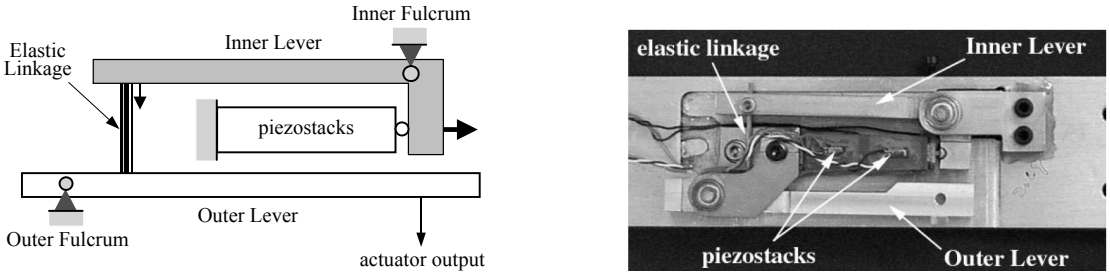

(a) Schematic (b) Actuator

Figure 1.12. Lee and Chopra 1st prototype of L-L amplifier arm integrated piezo-stack actuator [7]

Upon the successful testing of the first prototype, a second device was built with special consideration given to losses due to the elastic hinge and the stack actuator contact surface. Figure 1.13 shows the second generation L-L amplification piezo-stack actuator that was built. The major redesigns for the second generation prototype was inclusion of a curved contact surface for the piezo-stack and a specifically designed elastic hinge. This device underwent both vacuum spin tests as well as open jet wind tunnel tests. Wind tunnel test observations showed the system is incapable of providing the required restoring force for a wide range of operating frequencies [44].

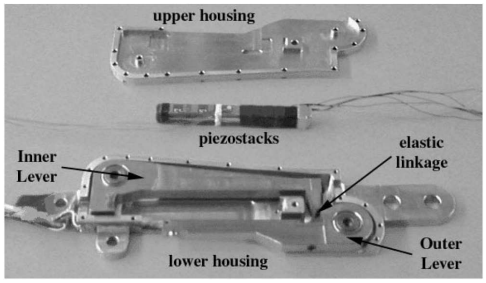

Figure 1.13. Lee and Chopra 2nd prototype of L-L amplifier arm integrated piezo-stack actuator [7]

Based on the observation from these experiments a third generation bidirectional piezo-stack actuation device was proposed (Fig. 1.14). As can be seen in this figure, the major new feature is the addition of another piezo-stack device which allowed for a power stroke in both directions of flap actuation. This design eliminated the need for an external restoring spring and allowed for better actuation authority for a wider frequency bandwidth [44].

Starting in the late 1990's there was also significant efforts undertaken at the Massachusetts Institute of Technology by Prechtl and Hall [9, 45] on the development of piezo-stack based full scale active flap actuators. This body of work was focused on a double stack actuator X-frame actuator (Fig. 1.15), and included rotor hover tests. The actuator was designed to produce a displacement perpendicular to the orientation of the stack actuation. This concept was further developed by Hall et. al. [46] to include two X-frame devices to provide higher force stroke capability.

The Boeing Company, in the late 1990's started work on the development of

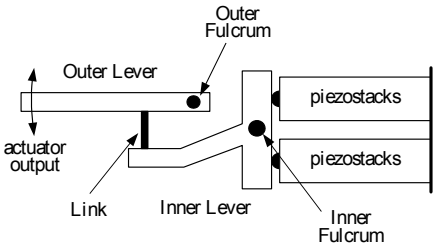

(a) Schematic

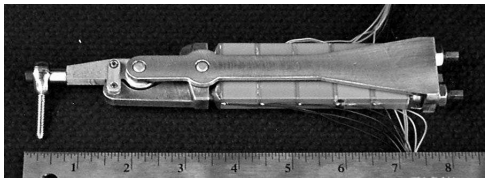

(b) Actuator

Figure 1.14. Lee and Chopra 3rd prototype of L-L amplifier arm integrated bi-directional piezo-stack actuator [8]

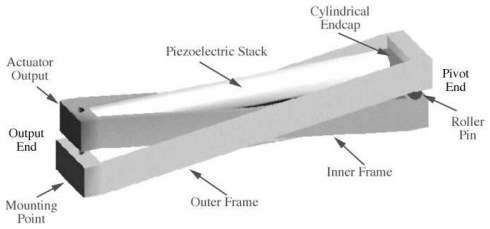

Figure 1.15. Prechtl and Hall double stack X-frame actuator [9]

a active trailing edge flap system for a full scale helicopter rotor system. The goal of the project was the full scale rotor system flap actuator development for whirl, wind tunnel and eventually flight tests. As part of this program several different actuation designs were analyzed as possibilities [47, 48], with two concepts eventually selected for benchtop prototype development and testing. These two concepts were based on the double stack L-L concept developed by Lee and Chopra [44, 49, 50] and the double X-frame actuator by Hall et. al. [46]. The double X-frame was finally down selected for use in the Smart Material-actuated Rotor Technology (SMART) program which involved the hover [51] and wind tunnel [29] testing of the MD-900 light utility helicopter rotor system (Fig. 1.16) in the NASA 40x80 wind tunnel. This program marked the first full scale active flap rotor testing in the United States.

Besides bender and stack actuator designs other piezo based designs were also explored, the earliest of which was the work done by Bernhard and Chopra at the University of Maryland in the mid 1990's [52, 53]. This unique concept utilized a bending-twist coupled composite beam which was installed within the rotor blade and was actuated via the use of piezo ceramics bonded to the beam surface. The

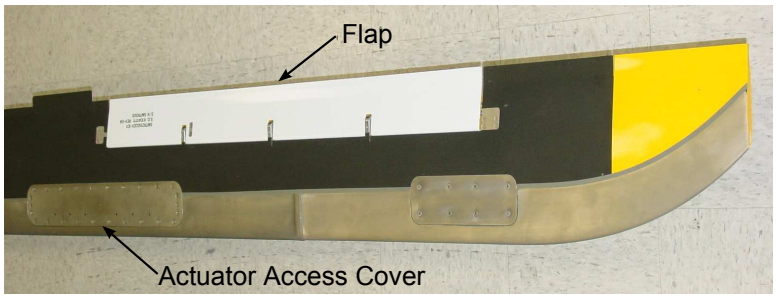

Figure 1.16. SMART program rotor blade [10]

accumulated twist of the beam tip due to the strain of the piezo actuators was used to rotate a flap. The concept was hover tested and was proven to work for small scale tests but further work of this actuation concept was diverted towards other rotor morphing technologies.

Clement et. al.[54], at the University of Michigan, worked on another innovative piezo-based actuator technology for active flap rotors. Dubbed C-block actuators by the authors, the actuators used were arc shaped piezo-ceramics bonded to a similarly shaped substrate which upon the application of a voltage field would produce a change in the distance between the ends of the arc. A row of these single arc devices were actuated in unison to produce a collective axial strain which was used to actuate the flap. This research project concluded in the development of a prototype which was wind tunnel tested [55].

At the Pennsylvania State University, Centolanza and Smith worked on unique induced shear piezo ceramic actuator for active flap systems [56, 57]. This device was built using radially placed bonded piezo ceramic rods which would undergo shear strains when actuated. The accumulate effect of the shear strains resulted in a tip-twist which was transfered to the flap. Although the concept was not wind tunnel or rotor tested, the project did involve the design, build and test of a benchtop prototype under simulated aerodynamic loads.

Another concept for active flap actuation was developed by Szefi et. al. [58], wherein two parallel piezo-stack actuators produce the end rotation of an axially pre-stressed beam which is amplified due to the specific placement of pivot pins. The actuator was designed to fit along the chordwise axis of an MD-900 rotor blade. This concept underwent benchtop and preliminary rotor testing as well.

By the late 1990's the idea of Individual Blade Control using active trailing edge

flap had caught the attention of international researchers as well. The Japanese Aerospace Exploration Agency (JAXA) in conjunction with The Advanced Technology Institute of Commuter Helicopter (ATIC) and Kawasaki Heavy Industries designed, built and tested a full scale active flap actuator for the ATIC rotor system [59, 11]. This concept utilized two parallel piezo-stack actuators to produce the rotation of a bell crank which in turn was used to actuate the flap. This project culminated in the first full scale whirl tower testing of an active flap rotor system (Fig. 1.17).

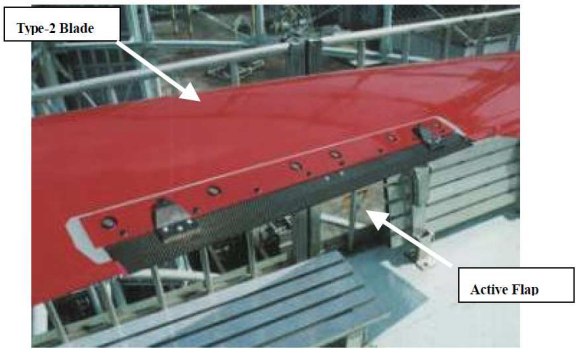

Figure 1.17. JAXA/ATIC/Kawasaki Industries full scale ATIC rotor flap [11]

Simultaneously, the French Aerospace Lab (ONERA) began work, starting in 1998, on the development of their Active Blade Control system which used a piezo-stack based device [60]. The actuation system design for this project was based around a commercially available piezo-stack manufactured by CEDRAT (APA 230). This device comprised of a set of stack actuators which are pre-stressed by an elliptical structure. The design used the Poisson's effect of the elliptical structure to amplify the strains produced by the stack actuators, which in turn were used to rotate the flap [60, 61]. As a part of this program a mach scaled rotor system with the active flap system was wind tunnel tested to prove the effectiveness of the flap system to reduce hub vibrations [62].

The European Aeronautic Defense and Space (EADS) Company in conjunction with Eurocopter, between 2002 and 2006, developed, full scale whirl [63] and flight tested [30, 31] a piezo-stack based actuator for the BK-117 rotor system named Adaptive Dynamische Systeme (ADASYS) (Fig. 1.18). This unique design also used the Poisson effect of an oval structure to amplify the strain of the piezo-stack,

furthermore, two such actuators are used to produce a power stroke in both flap directions. This program also involved significant design work for the optimization of the elliptical amplifying structure and the flap module design for rotor blade installation. This program marks the first time a full scale active flap system was flight tested: a significant step closer to commercial mass-production. The flight tests of the actuation mechanism was a success with experimental measurements showing significant reduction in both and noise and vibration emanating of the main rotor.

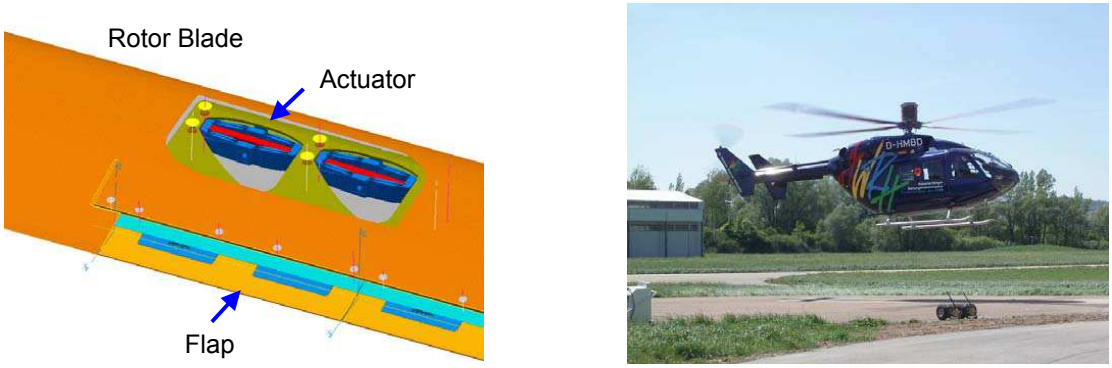

(a) Flap system schematic [63]

(b) Flight test [30]

Figure 1.18. Lee and Chopra 3rd prototype of L-L amplifier arm integrated bi-directional piezo-stack actuator

More recently, further development of a commercially available APA 200M piezo-stack actuator based active flap concept was undertaken by researchers at the Seoul National University in 2010 [64]. The blade design and actuator placement is similar in concept to that of the ONERA [60] and EADS/Eurocopter [63] designs.

Lastly, JAXA in conjunction with NASA is working on the development of a full scale piezo-stack based active flap actuator device for whirl testing at the Kawasaki Industries hover test stand [65, 66, 67]. The actuator design for this program is similar to the double piezo-stack used for the full ATIC rotor system [11].

1.2.1.2 Non-piezo based trailing edge flap actuation technologies

While there is a significant body of work done on piezo-based actuators for rotor active trailing edge flaps both in the United States and abroad, select research

groups have also explored alternative methods of actuation. In the mid 1990's the McDonnell Douglas company under the direction of Dawson and Straub [68] developed a cam driven tip mounted rotor flap system. This program involved the design, build and test of the first mach scaled active flap rotor system. The program was intended as a testbed for active flap systems and to experimental determine their effectiveness of reducing noise and vibration and as such involved extensive wind tunnel testing [69]. The actuation system used a fixed cam mounted at the hub along which the cam follower for the flap would ride. Different cam schedules were used to measure the effects of flaps on the noise and vibration of the rotor system.

At the University of Maryland, Bothwell, Chandra and Chopra [70] worked on a magnetorestrictive based actuator in conjunction with extension/twist coupled beams to produce the flap rotation. Benchtop tests of the design were undertaken, however, the actuator was found to have insufficient force and stroke capabilities to provide the reasonable twist outputs for flap deflections.

Fenn et. al. at SatCon Technology Corporation in conjunction with MIT developed the design of a Terfenol-D based actuator [71]. At the center of the actuator design were Terfenol-D tubes which would produce axial strain under a magnetic field. This actuator was design to transfered this axial strain into a chordwise motion of a pushrod which in turn would rotate the flap. The program only involved the design of the actuator system and as such no prototype of the concept was built.

Between 1999 and 2000 Fink et. al. at Diversified Technologies worked on the development of an electromagnetic actuator based system for an active flap rotor system [72]. The details of the actuator design are not found in literature and are therefore not presented. This program ended with a full scale whirl test of the active flap system on a derivative rotor system based on the OH-58 aircraft. Simultaneously, at Aeropastiale, Duvernier et. al. worked on the development of another electromagnetic actuator for active flap system [73]. Again, the details of the actuator design of this project are not available in literature and are therefore not presented.

The Sikorsky Aircraft Company in conjunction with the United Technology Research Center (UTRC) worked on the development of a hydraulic system for

the trailing edge flap deployment to improve rotor performance under the Army Variable Geometry Rotor Technology (VGART) program [74]. The device used a set of hydraulic bellows which were pressurized via hydraulic slip rings. This system was designed and built for a mach scaled rotor which was subsequently hover tested.

During the early 2000's various research groups were exploring the concept of hybrid-piezo actuation systems. The earliest was by Sirohi and Chopra [75] (University of Maryland), wherein a hydraulic system was used to amplify the strains of piezo-electric stacks via principle of work advantage. Herdic and Lynch at Georgia Institute of Technology also worked on a similar concept [76]. These type of actuators were also considered by the Boeing company as prospective candidates for active flap system actuators.

Around the same time the Sikorsky Aircraft Company during the late 2000's worked on the development of a unique electro-magnetic actuator for an active flap rotor system based on the Sikorsky Global Helicopter (Schweizer) 434 rotor system. This device comprised of an electric motor which is connected to a roller screw enclosed in an oil reservoir [77] (Fig. 1.19(a)). As part of the program the actuator design underwent full scale whirl [78] and wind tunnel tests [78](NASA 40x80 wind tunnel). This is the second full scale wind tunnel test of an active flap rotor system in the United States.

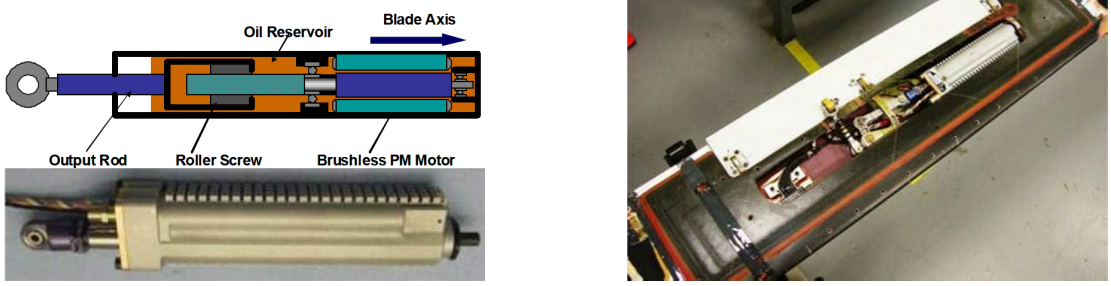

(a) Flap system schematic [77]

(b) Flight test [79]

Figure 1.19. Sikorsky Aircaraft Company electromagnetic active flap system

Woods et. al., around the same time, at the University of Maryland in conjunction with Techno-Sciences began work on the development of a novel pneumatic

actuator system for rotor trailing edge flaps. The design of this system was based on the Pneumatic Artificial Muscles (PAM) actuators, itself a derivative of Mckibben actuators. These devices comprise of a braided outer skin and inner elastic bladder which are cuffed at both ends. Actuation is achieved by the pneumatic inflation of the inner bladder which would expand radially. This radial expansion causes an axial contraction of the actuator due to the Poisson's effect experienced by the braided outer skin (Fig. 1.20(b)). As part of this program the actuation device underwent wind tunnel [80, 81, 82] (Fig. 1.20(b) and whirl tests [83] to prove their effectiveness in commanding flap actuation under the influences of external aerodynamic and dynamic forces.

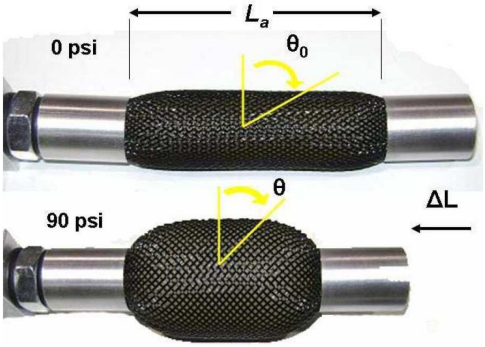

(a) PAM Actuator [83]

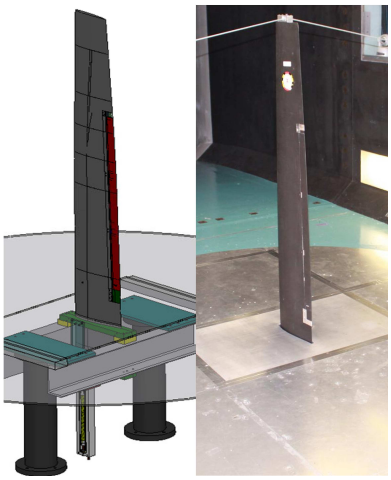

(b) Rotor blade embedded wind tunnel test [82]

Figure 1.20. Pneumatic Artificial Muscle (PAM) active flap design

More recently, in 2011, Saxena and Chopra at the University of Maryland have begun work on the development of a compact brushless active flap device for primary aircraft control [84]. Currently as part of the project, the actuator design has been spin tested and has shown promise. The authors state future work will include a mach scaled hover test of the actuation system.

1.2.1.3 Gurney flap actuation devices

Gurney flaps were invented by well known race car driver and team manager Dan Gurney in 1971 for use on his teams cars to produce more traction for better handling. The device was subsequently introduced to the aeronautic community by Liebeck in 1976 [85]. Since then they have been used on commercial aircraft as a high lift device. Recently, interest in the use of actively deployable gurney flaps for use in the rotor systems has garnered momentum. Research has shown the effectiveness of gurney flap systems in rotorcraft performance improvement [86]. The earlier work done in the area of actuation designs for gurney flaps on rotor systems was by Thepvongs at the Pennsylvania State University [87] in 2002. This project was aimed at the development of full scale prototype which was modeled after the work done at MIT on piezo-bender active flap actuation (Fig. 1.5). Following that Thiel and Lesieutre developed two separate gurney flap actuation design: The first employed the use of a voice coil connected to a mechanical amplifier and the second utilized a tapered piezo-bender. Prototypes of both devices were built and benchtop tested [88]. Following this work, Palacios et. al. in conjunction with Invercon Technologies developed and wind tunnel tested a pneumatically actuated active gurney flap system [89]. This concept used a pair of pneumatically inflatable bladders embedded in the blade to actuate a hinged gurney flap.

1.2.2 Variable/Active Twist rotor systems

Active flap systems attenuate the forces produced by the rotor systems by two means, the first is via the direct lift increment due to the flap deflection, the second is the increase in pitching moment which leads to the elasticly twisting of the rotor blade. Another way to produce this control of the rotor forces is via direct active variations of the blade twist. This variation of blade twist can be both dynamic (N-1, N, N+1/rev frequencies) or quasi-static (change per flight condition). While dynamic variation of twist is directly intended to reduce the noise and vibration of the rotor system [15, 90, 91], quasi-static twist changes can both be used for performance improvement and vibration reduction [92, 93, 94, 95, 28]. Figure 1.21 shows the timeline of the various projects on the development of technologies to actively vary blade twist on the horizontal axis and their respective maturation on

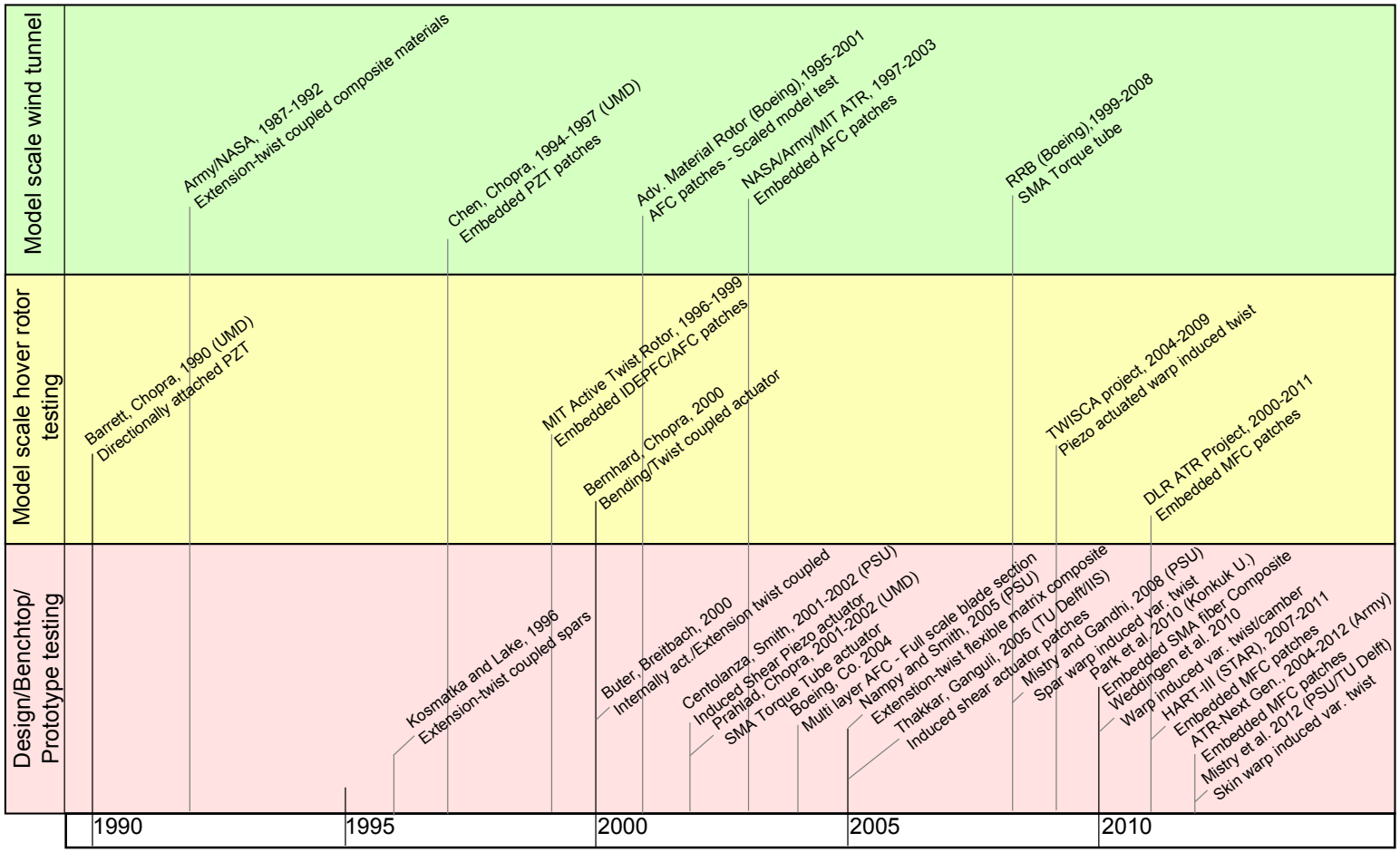

Figure 1.21. Timeline of Variable twist rotor systems

the vertical axis. As active twist technologies change the planform of the entire rotor blade the major challenge is to develop a system that can overcome the aerodynamic and dynamic forces experienced by the blade while maintaining the required stiffness to carry the rotor aero loads.

1.2.2.1 High frequency Active Twist Rotor designs

High frequency actuation has garnered larger attention and will be discussed first. These type of systems can be further catogerized into surface mounted actuation systems and internal actuation systems.

The basic premise of surface mounted active twist technologies was to introduce a shear in the blade which would result in a twist of the cross-section. To that effect, longitudinal strain produced at ±45 degrees from the spanwise axis of the blade would need to be produced using piezo ceramics. Considering that piezo ceramic sheets produced strain along both planar directions when an applied field about thickness is introduced, the first problem that needed to be solved was how to introduce directional strain.

Surface mounted actuation: To resolve the issue of strain actuation directivity and also initiating the concept of active twist rotor blades Barret and Chopra [12] in the early 1990's developed and utilized Directionally Attached Piezos (DAP). It was found that elements with high aspect ratios would produce higher strains along one planar direction (along the axis of the larger dimension) as compared to the other due to transverse shear lag. Furthermore, attaching the piezo ceramic to the substrate via a narrow bank of adhesive allowed for free motion of the material along the unwanted direction, while allowing the strain generated along the larger dimension to be transfered to the substrate. Taking advantage of both these observation allowed for the majority of the strain introduced by the piezo to be along a prescribed direction. In the case of the prototype developed by the authors, piezo strips were attached at a ±45 degree angle with respect to the spanwise axis on the top and bottom surfaces of the blade respectively. The actual blade core incorporated grooves cut out on the top and bottom surfaces to accommodate the piezo ceramic strip banks. At this early stage of development the piezo ceramic sheets were brittle in nature and therefore did not have sufficient allowable bend radius. This property is primarily what warranted the need for ac-

tuator placement grooves in the blade core. The blade core was then wrapped with three layers of resin impregnated Fiberglass composite fabrics. Using this method a blade with a NACA 0012 cross-section, chord of 2.98 inches and a span of 2.25 ft was built (fairly small, based on 1/8 scaled Integrated Technology Rotor [96]).

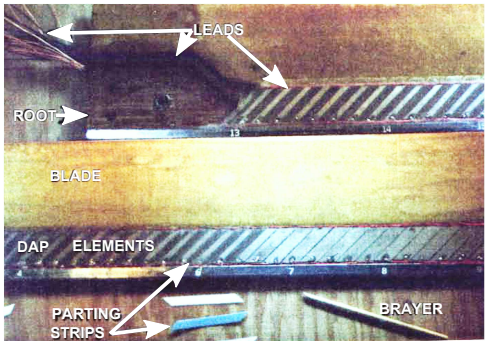

Figure 1.22. Barrett and Chopra Directionally Attached Piezo (DAP) Concept [12]

In order to produce the twist of the cross-section electrical fields with opposite phases were introduced to the top and bottom layers of actuators respectively. The end result was blade tip twist of up to ±2 degrees with an applied field of 500 Vrms at 147 Hz on the benchtop. These blades were subsequently rotor tested at the University of Maryland vacuum chamber. This concept was the first recorded effort of a piezo actuated active twist rotor blade concept and the starting point for many of the designs that followed.

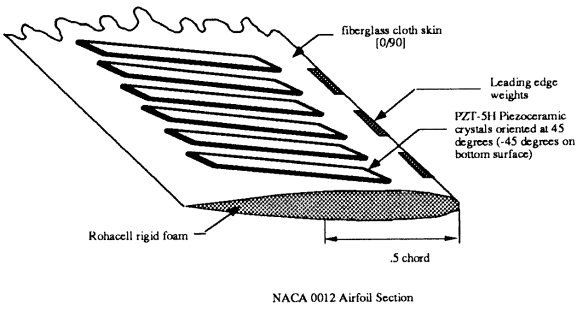

Figure 1.23. Chen and Chopra Active Twist Rotor concept [13]

Expanding on the idea of DAP in the mid 1990's, Chen and Chopra at the University of Maryland built a series of blades with several modifications [13, 97, 98, 99] (Fig. 1.23). Several generations of blades with varying actuator placement schemes, comparable in size and construction to the Barret and Chopra blade, were

built and tested on the hover stand as well as for the very first time in the wind tunnel. The first generation of blades examined the effect of varying the spacing between adjacent piezo strips. The results showed the detrimental 'interference' effect of a very dense packing of piezo strips. Since the piezo strips were attached above and below the blade elastic axis, the resulting added extension stiffness of the piezo contribute to the overall stiffness of the blade. The result is a loss of the maximum tip twist achievable of upto 38% as compared to the coarsely spaced actuator configuration. The researchers also considered the concept of multi-layer actuators and built and hover tested multiple sets of blades with varying spacing and layers of actuators embedded within the blade. The goal here was to understand wether it was possible to increase actuation authority while not significantly affecting blade stiffness by increascing actuator layers through the thickness rather than just along the span. Interestingly enough it was found that while large spacing with single actuators were able to obtain the highest tip twist on the benchtop, in the rotating frame due to the higher loads, the maximum tip twist achievable diminished significantly. Based on these the tests the maximum magnitude of blade twist achieved in hover was 0.5 degrees with dual layered actuators with fine spacing. These tests, however, did show the significant impact active twist rotors can have on the vibratory rotor loads. The last round of testing included wind tunnel testing which also showed a maximum 0.5 degrees tip twist in the rotating frame. Although the system produced smaller blade tip twists that required (design point was for 2 degrees), the researchers noted the significant variation in the unsteady loads produced due to active blade twist.

In parallel to the efforts at the University of Maryland on the Directionally Attached piezo strips to actively twist the rotor, researchers at the Active Materials and Structures Lab at the Massachusetts Institute of Technology (MIT) were developing the next generation of piezo actuators: Interdigitated Electrode Piezo Fiber Composites (IDEPFC). Commonly referred to as Active Fiber Composites (AFC), they are comprised of circular cross-section piezo fibers sandwiched between two layers of interdigitated electrode circuits [100]. This design had improved actuation strain capability because the interdigitated electrodes allow for the even distribution of the electric field and the piezo fibers operate in the more effecient d33 mode. The assembled actuators showed higher strain capabilities

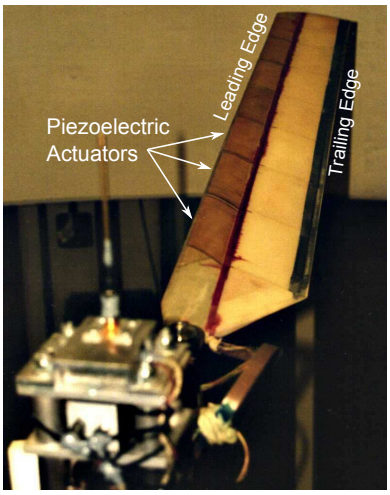

Figure 1.24. Massachusetts Institute of Technology first generation IDEPFC Active Twist Rotor concept [14]

compared to traditional piezo sheet actuators while also having higher structural conformability. The individual piezo fibers in the AFC results in a high degree of anisotropy, something that was achieved with the piezo sheets using directional attachment.

Using the AFC actuators MIT researchers Derham and Hagood [101] first built a relatively small (19 inch radius) blade and demonstrated the ability to produce a maximum tip twist magnitude of 1.4 degrees at resonance. This work was further extended by Rodgers and Hagood [14] who built and hover tested a rotor 51 inch radius rotor with embedded AFC actuators (Fig 1.24). There was no requirement for grooves in the base blade to attach the piezo actuators as AFC actuators had higher structural conformability. The tests on this prototype design showed the capability of the active twist technology of achieving twist variations of upto 0.4 degrees in hover.

The success of this first generation MIT rotor test spurred two additional active twist rotor projects, the first titled the NASA/Army/MIT active twist rotor (Fig. 1.25) project representing the Department of Defense interest and the second the Advanced Material Rotor headed by The Boeing Company (Fig. 1.26). The goals of each of the projects were very different, with the NASA/Army/MIT project focused on developing a sound understanding of the capabilities of an active twist rotor using a generic simple blade planform. The Boeing company project, on the

other hand, focused more on development and implementation issues of rotors with technology from a practical and operational standpoint.

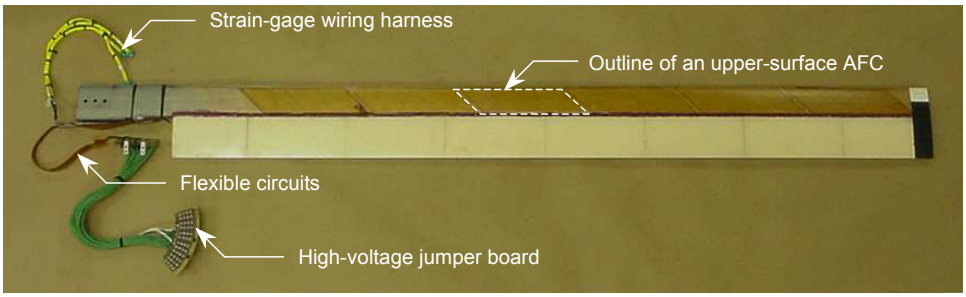

Figure 1.25. NASA/Army/MIT Active Twist Rotor Concept using AFC actuators [15]

The NASA/Army/MIT Active Twist Rotor (ATR) project, involved the development of a set of aeroelastically caled blades which employed the AFC patches embedded in the blade skin [15, 90, 91, 102, 103] (Fig. 1.25). These blades were to be tested on a rotor stant in the Transonics Dynamic Tunnel (TDT) NASA Langley. These blades had a moderately larger span length (55 in) as compared to the blades built by researchers at the University of Maryland and at MIT. The experimental effort was complimented with the development of aeroelastic models of the ATR the predictions of which were validated against experimental results. This validated analysis was later used as a design tool in the next generation ATR blade developed by the US Army Research Lab, which will be covered in later sections.

The NASA/Army/MIT blades underwent significant testing on the benchtop, and the rotor was tested in hover and in the wind tunnel as well. As a result of these tests, the relative insensitivity of the blade actuation as a function of operating condition (Forward velocity and blade pitch) was proven, with the blade capable of producing a tip twist magnitude of up to 1.5 degrees [90, 91]. This is in sharp contrast to the blades built by the University of Marlyand and is generally attributed to the relatively lower torsional stiffness and relatively lower actuation authority of the latter set of blades. This observation shows the marked improvement of the AFC actuation technology over the traditional piezo sheet driven (DAP) first generation active twist rotor blades in terms of actuation performance in less than a decade.

The testing of the ATR in the TDT showed a significant reduction in rotor hub

vibration observed over the entire flight envelope (upto 95%). While the 4/rev actuation input was shown to be effective in reducing the 4/rev vibratory hub loads, the authors noted a significant increase in pitch link loads at this operating frequency relating to an increase in the total fixed frame vibratory loads [90]. For all the successes of the NASAI/Army/MIT Active Twist Rotor program, operational issues of an AFC actuated system was also experienced. Researchers noted that during the initial testing phase a few of the AFC packs had been actuated beyond their maximum limit and as a result of this, these packs were shorted and unavailable as actuators for the remainder of the tests [103]. As the AFC packs were embedded within the blades themselves, they cannot be replaced and a malfunction of one of the packs would require the entire blade to be replaced.

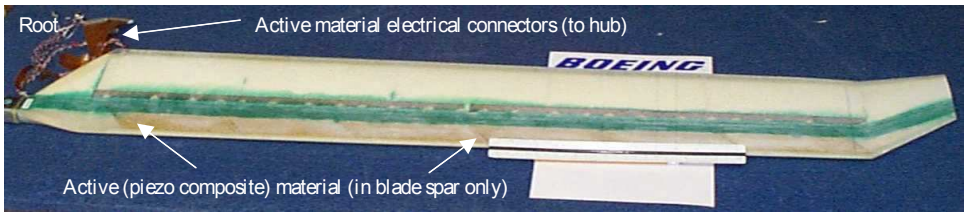

Figure 1.26. Boeing Advanced Material Rotor (AMR) program Active Twist Rotor concept [16]

The Advance Material Rotor project, under the direction of the Boeing Company, involved the development of mach scaled CH-47 Chinook blades with active twist capabilities (Fig. 1.26) [16]. This project also used AFCs but unlike the NASA/Army/MIT blades [15, 102] or the MIT blades [14] the blades had a more complex planform. The blades were hover and wind tunnel tested at the Boeing VTOL wind tunnel. As part of the overall project, the researchers also considered active flap actuators, and interestingly, reached the determination that an AFC driven active twist rotor system was more cost effective. In particular, the production and weight costs of the active twist rotor system was estimated to be lower to due to relatively simple blade integration procedure as compared to an active flap [16]. Although limited experimental data is available on these tests, the scaled Ch-47 blades were shown to be capable of producing comparable tip twists as the NASA/Army/MIT active twist rotor. Note, all AFC actuated concepts developed until this point included the application of actuators to the main spar only.

Following their initial investigations based on a scaled CH-47 rotor, the Boeing

company shifted their focus to a full scale CH-47 AFC actuated active twist rotor system [104]. As part of this effort, a section of a full scale blade was built with AFC actuators incorporated into the spar. Due to the size and stiffness of the blade, several layers of the AFC actuators were embedded to increase the actuation authority. While twist was demonstrated on the benchtop using AFC actuation the authority was lower than desired due to manufacturing issues wit certain layers of actuators. Their efforts highlight the difficulty of the mass production of such an active twist rotor blade.

In the AFC actuators used in the above studies the piezo fibers, fabricated using an extrusion process, had a circular cross-section. Imperfections in fiber spacing and diameter lead to non-uniformity in the field applied by the inter-digitated electrodes and the strain induced in the piezo fibers. Figure 1.27(a) shows a schematic representation of the applied electric field by the inter-digitated electrodes as well as magnified backlit view of an actual AFC pack showing non-uniform light intensity indicative of non-uniform induced strain. The labor associated with the fiber placement and the fabrication process, in general, and the performance degradation due to imperfections, are limitations of AFC actuator technology.

The limitations with AFC actuators discussed in the last paragraph led to the development of the next generation Macro Fiber Composite (MFC) actuators. The MFC actuators also use piezo fibers with inter-digitated electrodes applying an electric along their length but the key difference is that the fibers have a rectangular cross-section produced from piezo sheets sliced into thin strips. This process leads to more uniform cross-sections and fiber spacing, and Fig. 1.27(b) shows the more uniform strain consequently induced in the MFC actuator. In addition to the significantly improved actuation performance, the ease in manufacturing also makes MFCs more cost-effective. MFC actuatorss were originally developed by NASA Langley Research Center [105] but eventually the technology was licensed to Smart Material Corporation [106] and these actuators are now available commercially.

In addition to the vast amount of work in the US, researchers at the German Aerospace Center (DLR) in Braunschweig have also focused heavily on active twist rotor technologies. In the early stages they considered several actuation approaches including the use of directionally attached piezos, extension-

(a) AFC (b) MFC

Figure 1.27. Comparison of Active Fiber (AFC) and Macro Fiber (MFC) Composites

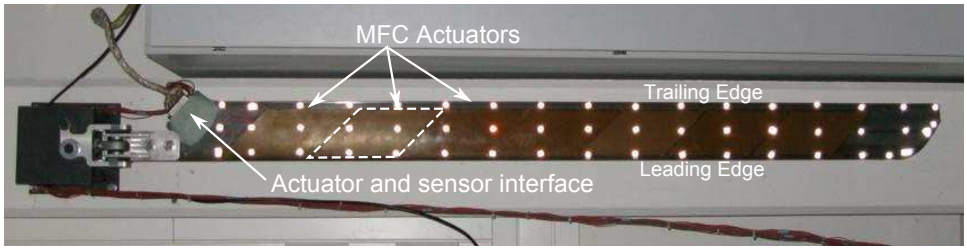

Figure 1.28. German Aerospace Center (DLR) 3th design iteration Active Twist Rotor blade

twist coupled composites and bimoment induced actuation [107]. Eventually, they converged on the use of MFCs as their actuation method of choice and went through several iterations of active twist blade design, fabrication and testing [108, 109, 110, 111, 112, 113, 114, 115]. The early prototypes underwent extensive benchtop testing but later prototypes were tested on the hover stand. The hover tests used a single blade with counter-balance, producing zero thrust, with the emphasis being the demonstration of actuator capability in a centrifugal field. Figure 1.28 is an image of their third design iteration blade which used a BO-105 like planform with a curved tip (Fig. 1.28), along with cambered airfoils and pre-twist [110]. The cross-section with C-spar was designed to have a first torsional frequency close to 4/rev and vibratory characteristics similar to the BO-105 rotor. The DLR tests demonstrated that the MFC actuators could produce impressive blade tip twists of up to 4 deg under a centrifugal field. To gain an understanding of the maximum magnitude of tip twist that could be achieved using MFCs, re-

searchers designed and built an additonal blade optimized for maximum twist while relaxing the torsional stiffness requirements. This blade was shown to be capable of producing a maximum of 8 degrees of tip twist. As with the NASA/Army/MIT blades [102] and the Boeing large scale twist demonstrator [104], however, replacement of a single or multiple MFC actuator(s) in the event of failure is not viable, and would require replacement of the entire blade.

After the NASA/Army/MIT Active Twist Rotor tests using AFC actuators reported in 2000-2002 [15, 90, 91], researchers at the US Army Research Labs and NASA Langley Research Center focused on the structural, aerodynamic and blade tip design of an advanced active twist rotor in the mid-2000s [92, 116, 117]. The parametric design studies were complemented with optimization efforts [118, 119], and led to the fabrication and benchtop testing of a prototype blade [120]. Using MFC actuators this time, the blade produced up to 6 deg of active tip twist, comparable with the DLR results. Like the DLR blades the MFC actuators covered most of the chord, differing from original AFC actuated blades (Fig. 1.25) where the actuators cover only the D-spar section. The 5.28 ft blade span is only slightly smaller than that of the DLR blades and the rotor is scheduled to be hover and wind tunnel tested in the future.

In addition to the above bodies of work, Thakkar and Ganguly [121] at the Indian Institute of Science worked on the preliminary design of an active twist rotor where piezo sheet actuators on the blade surface operated in the d15 shear mode. The idea was to exploit the high d15 induced shear strain authority and to directly shear the top and the bottom surfaces of the blade cross-section to produce twist (without resorting to +/-45 deg directional attachment of piezo strips or AFC or MFC packs that inherently produce extensional strain). The researchers computationally examined the aeroelastic behavior of such a rotor but unlike the studies above no prototype was built or tested. Although this design represents a departure from what the norm in blade surface actuation technologies for active twist rotors the manufacturing process of it is complex (very high voltages needed to pole the piezo ceramic) and would be expected to result in high production cost.

Figures 1.29, 1.30 and 1.31 present comparative data from the experimental efforts discussed in this section on DAP, AFC and MFC actuated active twist rotors. Presented chronologically, this allows an appreciation of the progressive

development and evolution of active twist rotor technology over the last twenty-plus years.

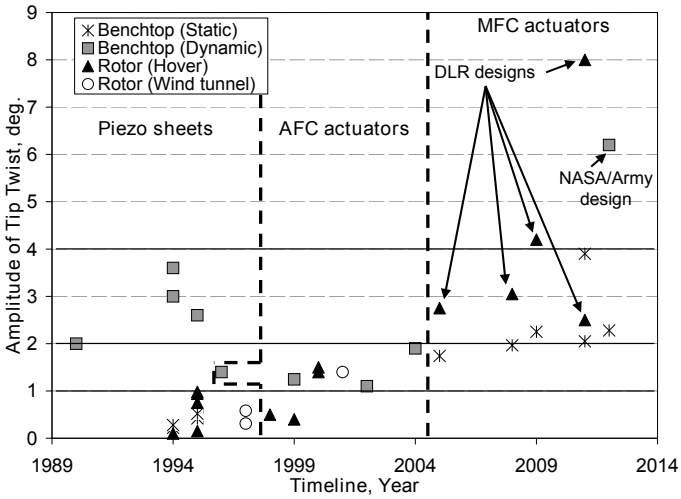

Figure 1.29. On blade surface actuator active twist rotor tip twist data

Figure 1.29 shows the amplitude of the maximum tip twist reported in the various tests. The symbols in the figure correspond to static and dynamic benchtop tests, and rotor tests on the hover stand and in the wind tunnel. The overall observation that can be made from Fig. 1.29 is that the first generation DAP driven rotors generally produced tip twist amplitudes in the range of a degree or lower, the exception being the results from the benchtop dynamic tests (this difference is discussed later). The AFC driven rotors in the NASA/Army/MIT tests generally produced tip twist amplitudes between 1-2 deg, and the MFC driven rotors tested at DLR easily produced increased tip twist amplitudes in the range of 3 deg, with a configuration optimized for maximum twist yielding as much as 8 deg in hover.

Figure 1.30 shows the torsional frequencies of the rotors in the various tests. With the exception of the NASA/Army/MIT tests, the rotor frequencies are generally seen to be in the range of 3.55/rev. Since the expected actuation frequency range on the rotor is 35/rev (for a 4-bladed rotor), these designs appear to take advantage of resonant amplification. The effect of resonant amplification is also evident in Fig. 1.29 when comparing the much higher tip twist in the benchtop dynamic tests to the lower values from static tests for the first generation DAP actuated rotors, and a similar difference is also observed between the hover test results and the static benchtop test results for the MFC actuated rotors at DLR.

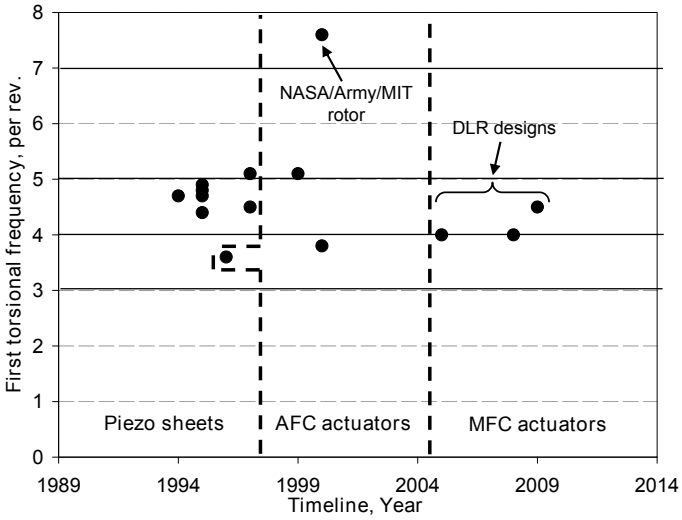

Figure 1.30. On blade surface actuator active twist rotor first torsional frequency data

While it is unclear whether the AFC actuated NASA/Army/MIT rotors first torsion frequency was in the 7/rev range by design (it may be the result of using of existing molds and fabrication techniques of passive blades with added AFC actuators), in a later study on the Advanced Active Twist Rotor (AATR) Sekula [92] suggests that for their particular configuration MFC actuation appears to be more efficient at reducing vibratory loads (higher ratio of change in vibratory loads to input twist actuation) if the rotor torsional frequency is higher.

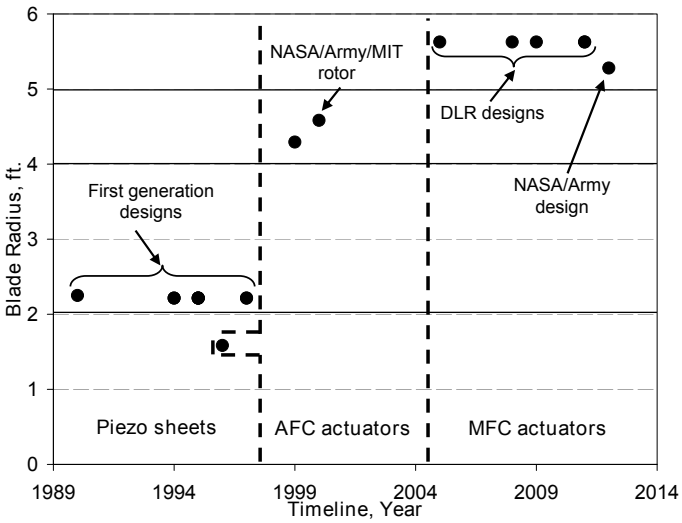

Figure 1.31. On blade surface actuator active twist rotor radius data

It is interesting to note that while the first generation DAP actuated active

twist rotors showed a large reduction in tip twist between the benchtop dynamic tests and the hover test, the differences were much smaller for the subsequent AFC actuated NASA/Army/MIT tests. This performance degradation in the hover tests in the case of the University of Marylands DAP actuated rotors is attributed to their lower stiffness. In the presence of aerodynamic and centrifugal stiffening in the rotating environment, the lower inherent structural stiffness and the lower authority of the DAP actuators was a liability. When the rotor stiffness was higher, and more powerful AFC actuators were used, a significant reduction in performance in the rotating environment was not seen in the NASA/Army/MIT tests. Table 1.2 indicates the rotor type (Froude versus Mach scaled) used in the different tests, as well as the actuation voltages required for the DAP, AFC and MFC actuators. Although the voltages in the case of MFC actuation are slightly higher than those for AFC actuation, the tip twist (Fig. 1.29) is significantly (disproportionately) greater, and this is attributed to the higher efficiency of the MFC actuators, as explained earlier in the section. Figure 1.31 shows how the size of the scaled rotors tested over the last two decades has increased from under 2 ft blade span to almost 6 ft span. However, no full scale tests have yet been conducted.

Table 1.2. Comparison of surface mounted active twist rotor technologies

Actuation concept	Organization	Voltage (V_{RMS})	Model scale
DAP	University of Maryland	150	Froude
AFC	NASA/Army/MIT	707	Froude and Mach
MFC	DLR	1002	Mach

While the tip twist performance has improved significantly over the years with higher authority MFC actuators and properly designed blades, the main challenge of "replaceability" in the event of actuator failure remains. Due to the high degree of integration, at the present time actuator failure would eventually require replacement of the entire blade. While this could be an option for small-scale rotors and UAVs, it is not cost effective for full-sized aircraft. If the question of actuator replaceability can be adequately resolved, the actuation authority is clearly sufficient for vibration reduction (as an example, the NASA/Army/MIT rotor was capable of reducing up to 95% of the vibration levels with only 1.5 deg tip twist).

Internally actuated technologies:

Apart from on blade surface actuation technologies using directionally attached piezo strips, AFC or MFC packs, researchers from various groups have also explored other actuation designs housed within the blade. Bernhard and Chopra at the University of Maryland introduced a bending-twist coupled beam running along the blade span, with alternate spanwise sections having opposite in nature elastic couplings. Piezo sheets at the top and bottom of each segment, operating in the d13 extension mode, induced bending moments such that the bending deformations over successive segments cancelled while the twist deformation added. The result was a beam that could have significant tip twist while being contained within the confines of the blade [52, 122, 17, 53].

The piezo actuated bending-twist coupled beam tip was first connected via a linkage to a drive a trailing-edge flap [52] and later reworked to actuate a blade tip in pitch in rigid body rotation [122]. This latter variation was referred to as the Smart Active Blade Tip (SABT) and is shown in Fig. 1.32. Bernhard and Chopra then further extended this concept by directly connecting the piezo actuated bending-twist beam tip to the fixed blade tip [17] with the net result of being able to actively twist the blade. The bending-twist coupled beam enabled active twist blade was tested on the benchtop and the rotor on the hover test stand at the University of Maryland and results showed an estimated 1.9 deg tip twist (amplitude) in hover, on a torsionally compliant (first torsion frequency 3.78/rev), 1.77 ft span blade. While interesting and innovative, the scalability of this concept is a question. A long bending-twist actuator beam required for a full-scale blade could be quite heavy as it would be required to be stiffer than the blade itself (or alternatively it would have much reduced actuation authority). The beam would also be susceptible to dynamic issues, and would have to be segmented into many small sections so local bending deformations are contained within the blade thickness.

As mentioned earlier, in addition to the vast body of work by researchers at the German Aerospace Center (DLR) on the use of MFC actuators for active blade twist, they considered other active twist actuation approaches as well [107]. One of the approaches considered using extension-twist coupled composites and actuators to introduce oscillatory axial forces in the spanwise direction that would in turn

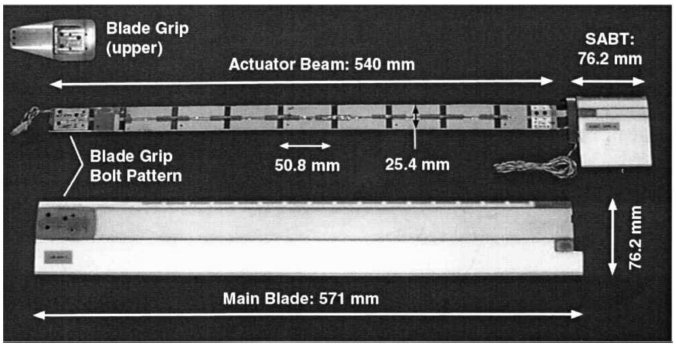

Figure 1.32. University of Maryland, Smart Active Blade Tip (SABT) concept [17]

result in blade twist. A prototype was built and tested on the bench-top as well in non-rotating conditions in a wind-tunnel [109]. In a rotating environment, though, the centrifugal forces are so large that the incremental axial forces the actuators introduce may not be particularly effective.

Another active twist rotor concept pursued by DLR's partner, the French Aerospace Lab (ONERA), was referred to as TWIstable Section Closed by Actuation (TWISCA) [123, 111, 18]. Open sections beams under torsional deformation are known to undergo cross-sectional warping. Conversely, if they're subjected to a warping actuation, they would twist. Exploiting this idea, the ONERA team slit the rotor blade cross-section, and used pizeo actuators to induce warping of the cross-section and a resulting twist. The original design had a slit along the trailing-edge but a bench-top demonstrator showed the center of gravity was too far aft due to the weight of the piezo actuator. To overcome this aft CG problem later designs had a slit starting at 10% chord from the leading edge and the piezo MFC shear actuator at 25% chord (Fig. 1.33). This design was built and whirl tested at DLR. Compared to the reference BO-105 blades, the TWISCA blades have a 20% lower torsional stiffness due to the slit [18]. The torsional stiffness of the classical rotor blades comes from the distribution of the shear flow through the walls of the blade and introducing a cut in the cross-section inherently reduces the torsion stiffness. In the TWISCA concept, the slit is closed by the piezoelectric actuator which is itself providing torsion stiffness. Due to this property, actuator structural failure could lead to reduction of the entire blade's torsional frequency leaving it susceptible to flutter instabilities. The problem would be further exacerbated in full scale blades where the actuators experience higher forces to maintain

the blade integrity.

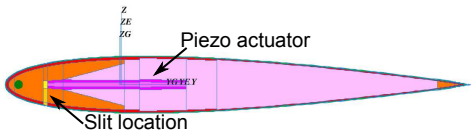

(a) Cross-section

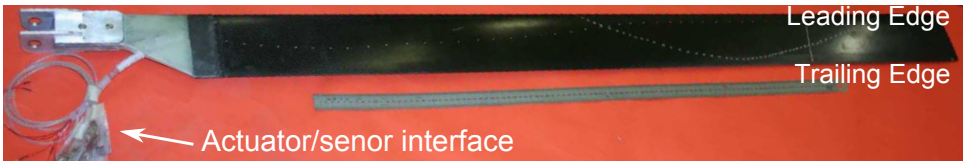

(b) Prototype blade

Figure 1.33. The French Aerospace Lab (ONERA) Active Twist Rotor blade [18]

Centolanza and Smith at the Pennsylvania State University analytically evaluated an induced shear piezo tube as an active twist actuator [124]. This induced shear piezo tube had been developed and previously explored for the actuation of a trailing-edge flap [56] but was later redesigned such that the tip of the tube would directly connect to the blade tip to twist the entire blade. Although no prototype of this twist actuation system was built, a finite element analysis indicated that a 48 inch long tube actuator sized for the MD900 helicopter would generate a tip twist of ± 1.1 deg, whereas an 18 inch long actuator would produce a tip twist of ± 1.50 degrees for a model scale blade. The induced shear piezo actuators operate at much lower voltages compared to the Kilo volts needed for AFC or MFC actuators. However, these actuators are much heavier, much more difficult to manufacture (requiring very high poling fields), and being brittle are susceptible to fracture and failure during application in rotor blades that undergo large deformation.

As can be seen there exist a plethora of innovative methods of producing the active twist of rotor blades. However, with the exception of the AFC actuator design, none of the programs discussed have developed full scale active twist rotor systems. This shows that despite the significant amount of work done in this area, there still remains significant room for developing innovative solutions for full scale active twist rotor designs. That being said, the designs in the current state, as mentioned earlier, are mature enough to be used for Unmanned Aerial Vehicle

(UAV) applications.

1.2.2.2 Quasi-static Active Twist Rotor concepts

Unlike the active twist rotor concept, Variable Twist rotors (quasi-static variation of twist; less than 1/rev) are not as well explored. The primary reason for this is the high amplitude required for these type of systems (up to 30 degree tip twist variation). Note that these type of technologies have to not only produce the required large twist variation but do so while maintaining the blade stiffness required to withstand the applied loads (inertial or aerodynamic). Interestingly enough the first published concept which explored the idea of variable twist rotors was also the first passively actuated concept as well.

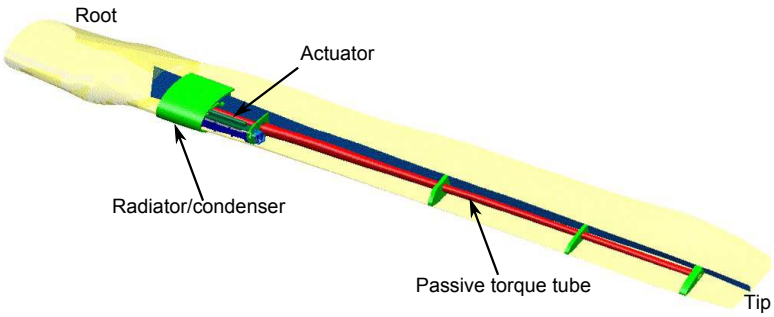

Figure 1.34. Boeing SMA torque tube based Reconfigurable Rotor Blade (RRB) program prototype [19]

Starting in the late 1980's and through the early 1990's, NASA in conjunction with the Army worked on the development of extension-twist coupled composite blades for the quasi-static variation of blade twist [125, 126, 127, 128]. This project was intended for tilt-rotor application where the aircraft inherently operates at two different rotor speeds for hover and forward flight cases respectively. The basic premise was to use this change in RPM and therefore centrifugal field to passively change the blade twist using tailored extension-twist coupled composites rather than physically introducing twist. The primary benefit of this method is the lack of requirement for an actuation device which would reduce the manufacturing and operating complexity. Starting with simple test specimens, this project culminated in the model scale testing of extension twist coupled blades at the Langley Transonic Dynamic Tunnel (TDT). This model was shown to be capable of producing

The analysis and testing conducted as part of this program concluded the feasibility of using such as system for passive blade twist variation. Following this work Kosmatka and Lake analyzed the use of extension-twist coupled spars for passive blade twist variation for tilt-rotors [129]. Their research work included exploration of various spar configuration which already have a pre-built twist. This latter body of work was focused on complex geometry configurations and as such represents development on the next stage of passively actuated variable twist rotors.

This type of centrifugally actuated variable twist rotor system garnered renewed interest in the mid 2000's. Nampy and Smith with the Pennsylvania State University (PSU) considered the development of an extension twist coupled composite tiltrotor blade with flexible matrix composite [130]. Traditionally composites are built with a stiff resin matrix which limit the maximum strain limits. However, replacing this stiff resin with one with higher strain capabilities would allow for larger strain limits. As part of this project small scale test specimens (non-aerodynamic) were built and tested on the benchtop which sufficiently showed the concepts capabilities. Note these type of solution also has effects on the stiffness bending stiffness as well and therefore poses a significant challenge when the design of a full scale blade is considered.These type of systems are very effective provided there is a mechanism to introduce a sufficient change in RPM. It should be noted, as this time all production manned aircraft have a fixed rotor speed design. The only exception to this is the Optimum Speed Rotor (OSR) concept developed by Karem Aircraft which is not embedded within the A-160 Hummingbird [131] in development with the Boeing Company. As such, such a centrifugal driven system would not be suitable as a retrofit for existing aircraft but rather for new aircraft built with advanced ending and transmission systems. However, judging from the recent interest of the rotorcraft community in the area of variable rotor speed concepts [132, 133, 134, 135, 136, 137, 138] this may likely be the trend of future aircraft.

While researchers at the Boeing Company worked on an AFC actuated active twist rotor, discussed earlier in the paper, another group at the company, along with other industry partners, focused on the development of a quasi-statically variable twist rotor under the auspices of the ONR-funded Reconfigurable Rotor Blade (RRB) program [139, 140, 141, 19, 142]. The goal was to apply the technology to tilt-rotor blades. The actuation system comprised of two Shape Memory Alloy

(SMA) tubes operating in a complimentary manner. When heated these SMA tubes undergo large strain and twist and can provide a large output torque. The SMA actuator was housed within the root of the tilt-rotor blade with the output end connected to a torsionally stiff torque tube. The other end of this passive torque tube (which spans the remainder of the blade) was attached to the blade tip (Fig. 1.34) to elastically twist the blade as the torque tube underwent rigid body rotation. The project resulted in the development of technologies for efficient heat transfer to the SMA tubes and the SMA actuator underwent several generations of design iterations to maximize efficiency before incorporation into the prototype blade. The blade/actuator system was tested in the wind tunnel the late 2000s on a 1/8th scale model three bladed rotor (similar to tilt-rotors). Being the first, and to date only wind tunnel test of an actuated variable twist rotor, this work represents a milestone. However, with the baseline blade structure undergoing only minor redesign to incorporate the actuation system it was much too torsionally stiff and the SMA actuators were only able to produce around 2 deg of static twist [19, 142]. Even if the SMA actuators could produce higher torque, the strains in the blade would increase. This work highlights the importance of suitably reducing the torsion stiffness and ensuring that the modified blade can withstand the strains associated with large quasi-static twist deformations.

During the early 2000s Prahlad and Chopra at the University of Maryland also explored an SMA tube based actuation system to quasi-statically twist rotor blades [143, 144, 145]. Their work included the development of SMA material models and bench-top tests with simulated external torque loads to determine the feasibility of such a system. Their efforts were similar to those of the RRB project in that an SMA tube would be directly responsible for the elastically twisting of the rotor blade. However, the SMA actuator tube was never actually coupled to a rotor blade leaving in question blade integration issues.

More recently Park et. al. at Konkuk University developed an alternative SMA based technology for variable twist tilt-rotor blades [146]. The design utilized SMA fibers embedded at angle (with respect to the spanwise axis) within a composite to produce a shear strain in the blade surface resulting in the twisting of the blade. The authors only explored the concept using mathematical models and no prototype was built or tested. Note this concept shares a similar design ideology with

the AFC and MFC active twist rotor concepts and would also face replaceability challenges in the event of actuator failure.

In an effort to consider alternative methods to quasi-statically change blade twist Mistry et. al. at the Pennsylvania State University, worked on the development of warp induced quasi-static variable twist rotor technologies. Two separate concepts were explored, both of which utilized the warp-twist coupling of open section beams to vary the blade twist. The first concept involved the direct twisting of an I-beam spar via the application of warp inducing bi-moments on the flanges [147, 20]. Since actuation involves the I-beam, which is the primary load bearing structure, this increases the risk associated with this technology. To reduce risk, the researchers envisaged applying the bi-moments and varying the twist only over an outboard portion of the blade span. While the idea of warp-induced twist actuation was earlier suggested by Buter and Breitbach [107] at the DLR, their emphasis was on high frequency actuation, whereas the Penn State effort focuses on spar design and quasi-static actuation. No prototypes were built but the design space of a reference variable twist blade was considered in fair detail.

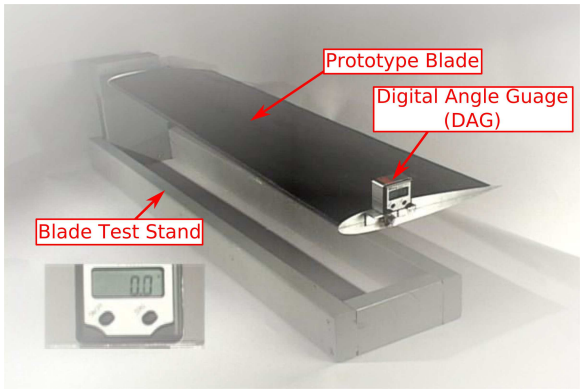

Figure 1.35. Skin warp induced variable twist rotor concept developed by Mistry et. al. [20]

The second concept considered by the researchers, was the warping of the skin itself [20]. The idea behind this concept was to have an open section airfoil skin shell, with a cut at the trailing edge. If the skin edges at the cut were forced to warp with respect to each other the end product would be an elastic twist of the cross-section. As an experiment one can induce warping of a rolled tube of paper at

the adjacent edges and clearly observe the twist of the cross-section. This concept was developed and refined in conjunction with the Delft University of Technology (TU Delft) where it was initially developed for fixed wing aircraft. As the skin in this concept was cut at the trailing edge, the resulting torsional stiffness of such a blade would be much lower if no restraint was applied between the two edges of the cut. To avoid the two edges was connected by a threaded rod assembly which prevented the unwarranted displacement of the two edges with respect to each other. This threaded rod mechanism was also responsible for the input actuation of warping. Note because the system used a threaded rod mechanism to induce warping, post actuation, the rod now provided zero energy lock capabilities (as it is inherently a non back drivable system). Note this is unlike the TWISCS concept developed by ONERA which joined the two cut edges using piezo-ceramic actuators intended for high frequency actuation. In addition to the threaded rod mechanism, the traditional spar of a rotor blade was replaced with a circular spar about which spanwise distributed ribs were allowed to rotate. In this case the ribs/skin interface allowed sliding to facilitate the input warping of the skin. As part of the project a prototype blade was designed, built and tested on the benchtop (Fig. 1.35) to ascertain the load requirements. Furthermore, a validated finite element model based on the experiments was used for a parametric study. The tests showed the capability of such a design to produce upto 16 degrees of tip twist with fairly low input actuation (0.15 in.). Note that these type of systems call for the entire redesign of the interior of the blade, thereby making it a very high risk concept. In particular, issues pertaining to maintaining the required blade stiffness (both bending and torsional) arise due to the presence of the sliding interface between the skin and the ribs and the additional rotational degree of freedom of the ribs. Furthermore, the presence of the actuator at the trailing edge would move the blade center of gravity further back resulting in possible rotor instabilities.

Around the same time (late 2000's) Weddingen et. al. worked on the development of a warp-induced variable twist rotor system [148]. This project was a collaboration between the Georgia Institute of Technology, NASA Ames Research Center and the Materials Technologies Corporation. As part of this project, initial benchtop tests on a warp induced camber system were undertaken, the design of which was later modified for a variable twist system. Interestingly, the final

full scale design for the variable twist concept incorporated a trailing edge and leading edge slit of a classical two cell D-spar blade cross-section configuration. Furthermore, the final design called for the use of the warp inducing actuator at the leading edge and an elastomeric seal at the trailing edge. This arrangement is in sharp contrast to earlier work done by Mistry et. al. wherein the slit was only at the trailing edge. The concept developed by Weddingen et. al. allows for a continuous spar wall has a potential of retaining a majority of the bending stiffness of the blade. However, in this design the elastomeric seal at the trailing edge and actuation system at the leading edge both have to provide sufficient resistance to maintain the torsional stiffness of the blade. Furthermore, this design requires to slits leading giving rise to two potential locations for failures.

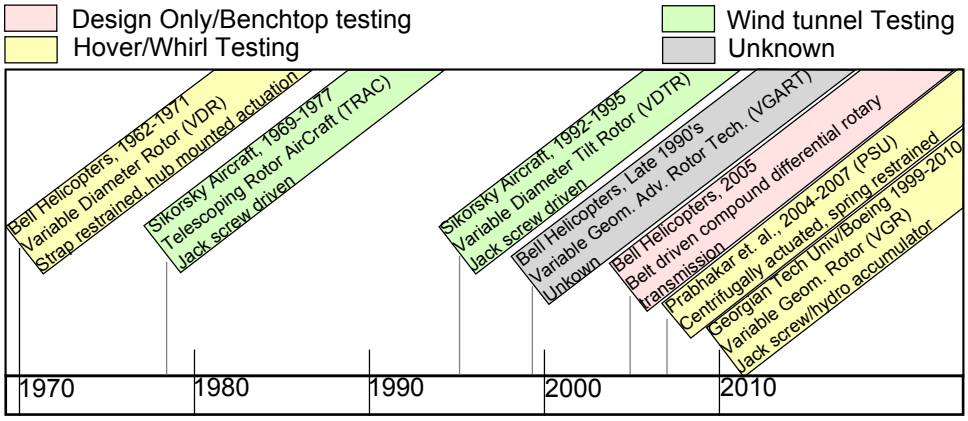

Figure 1.36. Timeline of Variable span rotor systems

1.2.3 Variable span rotor systems

Although a huge engineering challenge, and potentially very high-risk, rotor span variation has, and continues to, intrigue rotor designers due to the immense possibilities in terms of improvement in aircraft performance, operational flexibility and capability. Variable span rotor systems have been extensively researched, with patents dating as far back as the 1930's. A very good summary of variable span rotor technologies dated prior to the 1960's is presented in Ref. [149]. In an effort to avoid repetition, for the present literature survey, only technologies developed post the 1960's is presented. Figure 1.36 shows the timeline of variable span rotor research programs examined in this section.

(a) Extended (b) Retracted

Figure 1.37. Bell Helicopter Variable Diameter Rotor (VDR) program hover testing [21]

During the early 1960's, Young et. al. at Haig-K Helicopters developed a Variable Diameter Rotor (VDR) system for conventional edgewise rotors which was extensively hover tested [149, 21]. The systems used telescoping blades whose motion was controlled via an assembly of cable/straps. In 1967 this project was moved to Bell Helicopters for further development. As part of this project various design revisions were undertaken to resolve problems associated with the large centrifugal field of the rotor system and the subsequent locking of the rotor system. During the early 1970's full power tests of the latest revision of the project, the VDR-4 test article, were undertaken. This prototype design incorporated a locking mechanism to hold the blades in place during operation and later also included an innovative mechanism method to move the telescoping sections (Fig. 1.37). Following this testing of the VDR-4 prototype, the project was concluded and no further work was done until the mid 2000's when C. Fenny at Bell Helicopters [21] introduced a compound differential rotary mechanism for the cable system which allowed for increased system reliability, a major problem with the original VDR project mechanism.

Starting in the late 1960's the Sikorsky Aircraft Corporation started work on the Telescoping Rotor AirCraft (TRAC) rotor system [152, 149] (Fig. 1.38(a)). This project, unlike the Bell Helicopter VDR project, utilized a jackscrew mechanism to actuate telescoping blade sections. Furthermore, unlike the Bell concept, this design called for an inboard torque tube on which an aerodynamic blade section

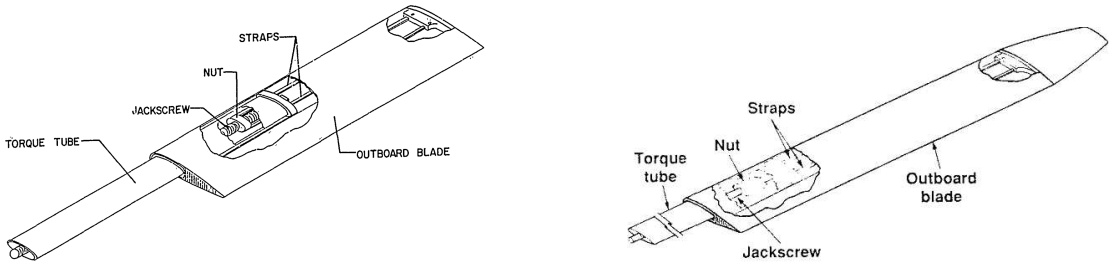

(a) TRAC Rotor [150] (b) VDTR Rotor [151]

Figure 1.38. Sikorsky Helicopter variable span rotor technology variants (TRAC and VDTR)

was allowed to slide. The design allowed for the jackscrew to be actuated via the main rotor power system itself. A scaled model of this concept was extensively wind tunnel tested and was shown to provide performance improvements [153, 154, 150, 155]. After trade studies on the impact of such a rotor system on tiltrotor aircraft [154], this design was later modified for a tilt-rotor aircraft configuration and was renamed the Variable Diameter Tilt Rotor (VDTR) project in the early 1990's [151, 156] (Fig. 1.38(b)). As part of this program significant wind tunnel and hover testing was conducted on a scaled prototype. The major difference for the scale rotor tests of this project was inclusion of a separate motor housed in the rotor hub which was used to actuate the jackscrew and hence the blade span variation.

Bell Helicopters again worked on variable rotor systems, during the late 1990's, as part of the Variable Geometry Advanced Rotor Technology (VGART) program in conjunction with the Army. The program was a closed door collaboration and such no detail description of the actuation mechanism is available in open literature.

Simultaneously during the late 1990's The Boeing Company in collaboration with the Georgian Technical University worked on the development of a Variable Geometry Rotor (VGR) design in conjunction with the International Science and Technology Center (ISTC). The first generation prototype of this program used a jackscrew system to directly actuate the blade span, however, the centrifugal field was found to be too large and therefore the inclusion of a secondary restraint system was proposed [157]. The second iteration utilized the jackscrew in conjunction with

a hydro-pneumatic accumulator to alleviate the loads experienced by the actuator system [158]. The concept developed as part of this program, unlike others, also included a mechanism to automatically vary the blade in-built twist as the span was varied. This was done via helically curved grooves on the main span of the blade along which the blade section attach points would slide causing a combined rotary and spanwise motion of the section.

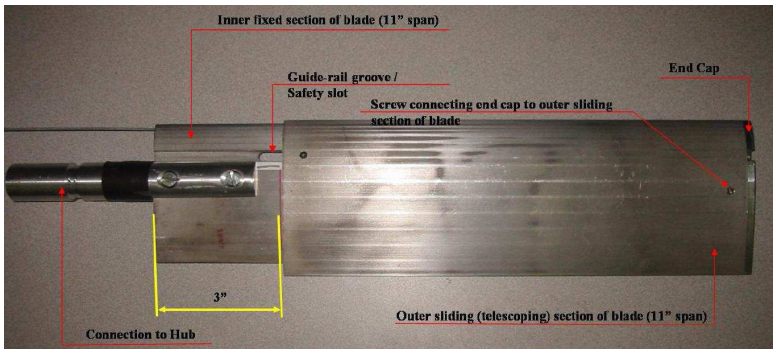

Figure 1.39. Prabhakar, Steiner and Gandhi centrifugally actuated variable span rotor demonstrator

More recently at the Pennsylvania State University, Prabhakar, Steiner and Gandhi, worked on the development of a centrifugally actuated variable span rotor system [159, 160] (Fig. 1.39). Unlike previous concepts which used powered systems to actuate the blade span variation, this concept utilized the centrifugal field itself to produce the spanwise motion of a spring restrained outer blade section. The authors envisioned a system wherein the rotor speed would be changed to control the blade spanwise location. A scaled prototype of the concept was designed and built to prove the feasibility of such a system. The concept design also incorporated a safety stop which would restrict over extension of the blades. Although the prototype was built using a commercially available linear spring, design work was conducted on the use of non-linear springs as well.

1.2.4 Emerging rotor morphing technologies

Since the 2000's, researchers have began to explore three relatively new types of rotor morphing technologies: Variable Camber systems, Variable Chord systems and Variable Nose Droop systems. Figure 1.40 shows a combined timeline of

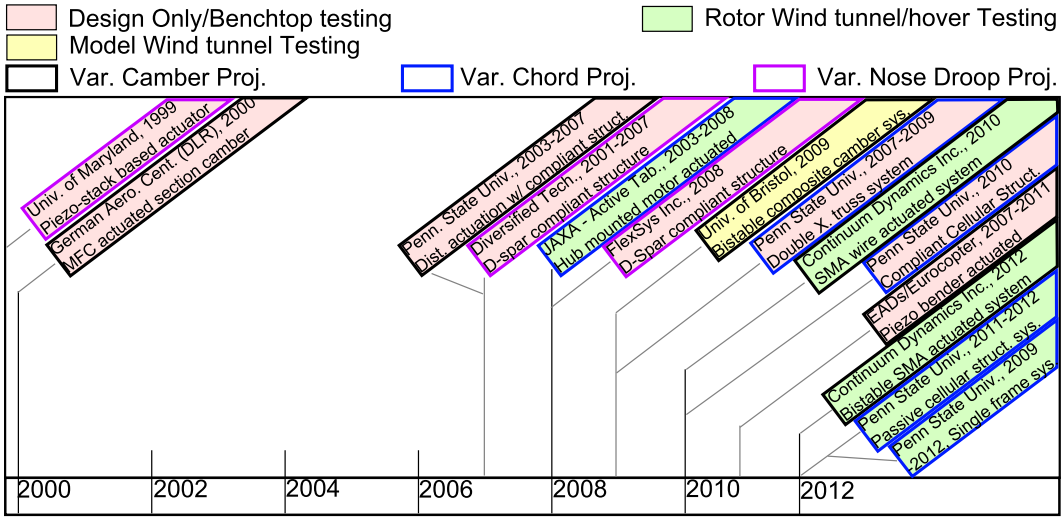

Figure 1.40. Timeline of emerging rotor morphing technologies: Var. Chord, Var. Camber and Var. Nose Droop

these emerging technologies. In the proceeding sections these technologies will be discussed individually.

1.2.4.1 Variable chord rotor systems

A relatively new concept for active rotor technologies, variable chord systems have been shown to provide significant improvement in aircraft performance when deployed quasi-statically [161, 32, 162] and in noise suppressions when deployed at higher frequencies [163]. Most of the work on actuator technologies for variable chord rotor systems were developed starting in the early 2000's with the Active Tab mechanism project undertaken by the Japan Aerospace Exploration Agency (JAXA) [164, 163, 67]. This program focused on the development and testing of a high frequency (N-1,N,N+1/rev) actuated rotor tab for noise reduction. The program included model scale wind tunnel tests of the concept. For this project, the authors used a motor housed within the hub of the rotor system to actuate the tab.

At the Pennsylvania State University, Leon et. al., developed a variable chord rotor system which utilized a double X truss system to amplify spanwise actuation to chordwise motion of the chord extension plate [161, 32] (Fig. 1.41(a)). A benchtop prototype of the concept was built and tested to prove the feasibility of

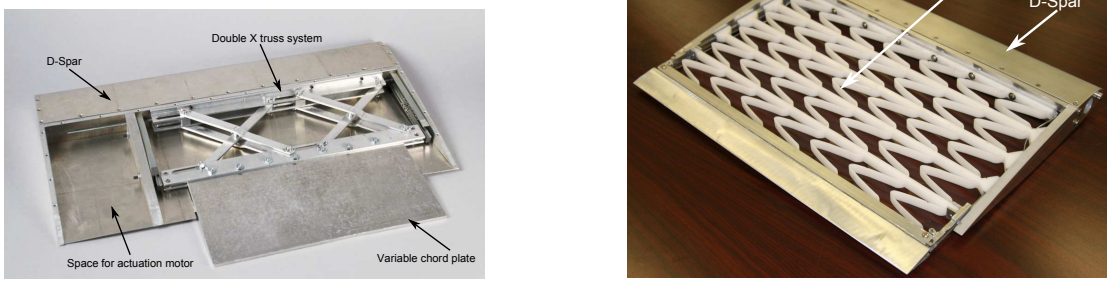

(a) Double X truss system [161] (b) Compliant cellular structure [165]

Figure 1.41. Evolution of Variable Chord systems at the Pennsylvania State University

the design. Simultaneously, Barbarino et. al. also worked on the development of a variable chord system that, unlike others, produced a continuous smooth aerodynamic airfoil when extended rather than a base airfoil with a tab [165] (Fig. 1.41(b)). This concept utilized a cellular structure as the basis of the restraining elastic structure to withstand the aerodynamic and dynamic loads experienced by the active rotor section. As part of this project, a benchtop prototype of the design was built and tested to prove the system feasibility. Further developing the double X-truss concept, Hayden [166] conducted rotor tests on an actuated variable chord system. As part of this study two different types of actuators were used to show the feasibility of the design. In parallel, Moser et. al. [167] at the Pennsylvania State University demonstrated the first passively actuated (rotor speed variation driven) variable chord concept on a rotor test stand. This concept utilized a Von-mises truss in conjunction with a biasing spring to realize the chord variation.

1.2.4.2 Variable camber rotor systems

Active flap systems are generally intended to produce an effective change in the camber of the system, however larger chord flaps can lead to increases in rotor profile power due to the discretized nature of these systems. An alternative is to directly change the camber of blade sections to produce the necessary changes in the aerodynamic characteristics of the blade section. These type of systems pose a challenge as they have to not only combat the same issues as that of active flap systems but within the additional constraint of smooth aerodynamic surfaces.

At the German Aerospace Center (DLR), Buter et. al. proposed the concept of using Macro Fiber Composites (MFC) to actively produce the camber of rotor blade sections [168]. Although no prototype of the concept was built, the concept was analyzed to prove its effectiveness in improving blade section aerodynamic characteristics.

During the mid to late 2000's, at the Pennsylvania State University researchers worked on the development of an active camber system based on a compliant truss assembly. The design used an active core aft of the D-spar wall to actuate the camber [169]. As part of this project compliant structure optimization studies were undertaken to show the feasibility of the concept [170]. Furthermore a benchtop model of the concept was built to further outline the concepts actuation capabilities. The authors also considered the design of deformable skins for the use of such active camber systems [171].

At the University of Bristol, Daynes et. al. have developed an active camber system which utilizes a bistable composite skin [172]. This skin is actuated via an electromechanical actuator placed within the D-spar section of the blade. This concept was wind tunnel tested to prove its effectiveness to successfully actuate in the presence of aerodynamic forces.

Researchers at Continuum Dynamics, Inc. [173] developed a Shape Memory Alloy (SMA) wire (with a restoring spring) based actuation scheme to realize variable blade camber. This system was hover tested on a scale rotor test stand.

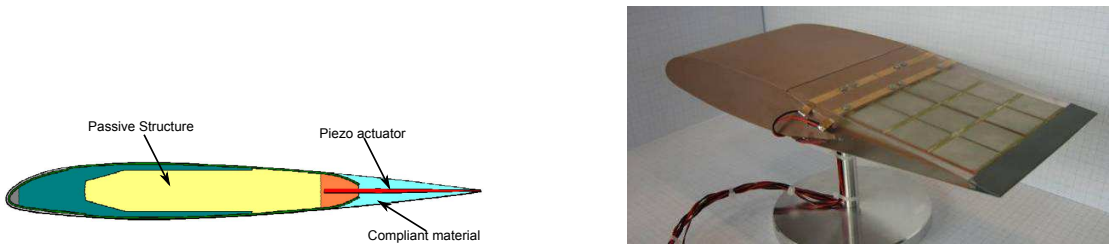

(a) System schematic (b) Prototype demonstrator

Figure 1.42. EADS/Eurocopter variable camber system

Another active camber concept project is under development in Europe, headed by a partnership of researchers from the European Aeronautic Defense and Space (EADS) company and Eurocopter [174, 175] (Fig. 1.42). This concept design uses

a piezo bender actuated via specifically design ceramics which are encased in a compliant material affixed to the trailing edge of a rotor blade section. As part of this project, a benchtop full scale blade section with these embedded systems was tested under full scale external loads. The successful completion of these tests have proved the effectiveness and reliability of this design to produce the rotor camber [176].

Considering an alternate method researchers at researchers at Continuum Dynamics, Inc. [177] developed a unique bi-stable structure which allowed for the variation of blade camber. This structure is envisioned to be actuated using Shape Memory Alloy (SMA) wires and was hover and wind tunnel tested (albeit as passive additions). The benefit of the design was the simple manufacturing process of the device and the ease with which it could be applied to existing blades.

1.2.4.3 Variable nose droop rotor systems

Rotor blades generally comprise of a D-spar or C-spar at the leading edge which contributes most of the blade stiffness. Nose droop systems pose a significant design challenge as they require the same real estate for operation. A possible way to combat this problem is to design a two wall system; one for the primary load bearing spar and the other outer wall to house the nose droop actuation system. For all their complication, nose droop systems can be used effectively to alleviate issues related to blade section dynamic stall [178].

Shaner and Chopra at the University of Maryland worked on the development of a piezo-stack based actuator for a leading edge nose droop system [179]. Their actuator arrangement was similar to that of earlier work done by Chandra and Chopra on flap actuation systems [6]. For the nose droop system design changes including the use of curved contact surfaces and elastomeric hinges which were based on the findings of Lee and Chopra [44] were also incorporated. However, in spite of these design changes, the actuator was not found to perform at the expected levels when benchtop tested. The authors determined a few sources of this observed lack of actuation including the inefficiency of the system to transmit the force and stroke output of the piezo-stack.

Fink et. al. at Diversified Technologies in conjunction with the Aeromechanics Division, Aeroflightdynamics Directorate (AMRDEC) developed the Leading Edge

Electro Magnetic Airfoil (LEEMA) actuator for a variable nose droop rotor system [180]. The system design was optimized to provide a smooth noose droop actuated via a linear electromagnetic actuator housed in the leading of the blade section. A benchtop prototype based on the actuator system was built and tested to show its effectiveness in producing the desired noose droop.

Another AMRDEC collaboration, this time with FlexSys Inc., was on the development of a conformable leading which was design using compliant structure optimization techniques [181]. This system comprised of a structure designed to convert the rotary motion of a motor into the effective rotation of the blade section of the leading edge. The relatively simplicity of manufacturing due to the reduced number of moving parts makes this design very viable. A benchtop prototype of the concept was built and tested to show the actuation characteristics of the system.

1.2.5 Variable rotor speed systems

Traditionally rotating wing aircraft are designed to operate at a fixed rotor speed (RPM). This design feature was chosen for numerous reasons, the most prominent of which is weight, as this type of system would not require a variable ratio transmission. However, recently the area of variable speed (variable RPM) rotors has also garnered much momentum, with the introduction of the A160 Hummingbird unmanned aerial vehicle and its optimum speed rotor system [131]. Apart from this work on unmanned aircraft, research work was also done at the Pennsylvania State University to examine the performance improvements with variation in rotor RPM only over the entire flight envelope [182, 132, 133, 183] of a UH-60A type aircraft model. This study showed the plausibility of using only a limited rotor RPM variation, to achieve a maximum power reduction of up to 14% for specified cases. Following this Bowen-Davies and Chopra [135] at the University of Maryland conducted an analysis on a similiar type of aircraft to understand both the performance benefits and the vibratory characteristics of a variable RPM rotor system. Simultaneously Berry and Chopra [136], also at the University of Maryland, conducted a model scale wind tunnel experiment to understand the behavior of a variable RPM system. Furthermore, an experimental study by Datta, Yeo

and Norman considered the effects of a slowed rotor configuration at high advance ratios [137]. This experiment was conducted for a full scale UH-60A rotor system at the NASA 40x80 wind tunnel. All of these bodies work showed the possibility of performance improvement with a variable rotor speed system.

1.3 Active control for performance improvement

In parallel with the efforts dedicated by researchers on the development of the various actuation systems presented, studies have also been undertaken that consider the impact these various type of actuation systems have on aircraft performance. These studies have considered the effects of the systems on power reductions as well as vibration reduction.

Over the years active flap systems have been thoroughly studied by various researchers. Liu et. al. [184] considered the use of single and multiple flap arrangements to reduce the aircraft power. This study showed that for an advance ratio of 0.35 it was possible to reduce the power by 1.73% (for single flap) to 1.76% for a two flap arrangmenet. However, this was at the expense of a 100% increase in the rotor vibrations. However, when the objective function considered both power and vibration, the power reductions obtained were limited to 0.67%. Alternatively, the use of gurney flaps on the rotor system was also considered by Bae and Gandhi [185].

Keys et. al. [94] considered the effect of twist on edgewise rotor performance over a wide range of forward velocities. This study showed that while a lower twisted rotor did provide for power reduction in high speed forward flight (compared to a blade with higher pre-twist), the magnitude was at best moderate. However, the primary benefit of using a blade with lower pre-twist is the significant reduction of the rotor vibration, i.e. a blade with higher pre-twist results in up to 126% increase in vibration (compared to the blade with lower pre-twist). McVeigh et. al. [186] showed that optimal twist distribution of tilt-rotor blades in hover varies signigificantly from that of forward flight (10-20 degrees), thereby highlighting the need for variable twist capability for tilt rotors.

Fradenburg and Matuska [151] showed that a power reduction of up to 30% was possible with a Variable Diameter Tilt Rotor (VDTR). As part of the study

significant rotor testing was conducted. An alterntive approach was taken by Khoshlahjeh [187] who considered the effect of variation of chord on the effect of rotor performance. This study showed power reductions upto 18% for high altitude and gross weight configurations.

Researchers at Continuum Dynamics Inc. [173, 177] considered the effects of camber on rotor performance. As part of this study significant numerical analysis and experimentation in the wind tunnel was conducted. This study showed the benefits of introducing a distributed camber (maximum at the root, no camber closer to the tip) in performance and rotor noise improvements.

1.4 Current research focus and dissertation layout

The subsequent chapters of this document present the research conducted on two separate quasi-static rotor morphing concept: Variable span and variable camber. Both concepts are analyzed from the perspective of the performance improvements they provide as well as their design requirements. The goal of this body of work is to develop a comprehensive understanding of the benefits and drawbacks of both systems.

Chapter 2 presents the power reductions possible as a result of variable span variation in conjunction with and without rotor speed variation in forward flight. This is followed by the variable span design analysis which is presented in Chapter 3.

Following this chapter 4 switches topics and presents the hover performance analysis of a variable camber system. Similar, to the variable span study, the following chapter (Ch. 5) covers the design of the variable camber system. Lastly, chapter 6 presents a summary of the major conclusions on the results presented followed by a detailed discussion of the future work.

CHAPTER 2

Variable span system performance analysis

The contents of this chapter explain in detail, the design concept of the variable span system considered followed by a description of the analysis model. The proceeding sections will cover the specific benefits of a variable span system both with and without rotor speed variation. In particular these results will be compared against the performance improvements calculated for a pure rotor speed variation case. Following this, a detailed discussion of specific benefits of variable span systems will also be presented.

2.1 Design Concept

The current work is focused on the applicability of variable rotor span technology to conventional edgewise rotor helicopter configurations. The mathematical model used in the current work is based on the UH-60A aircraft, which comprises of both non-linearly and linearly twisted blade sections. The sliding of the outboard

moving portion relative to the inboard fixed portion is allowed to occurs over the linearly twisted section of the blade (as this would be easier to realize in practice). Figure 2.1 shows a schematic of an implementation of the variable span rotor blade, in its completely stowed and deployed configurations, as envisioned in this study. The outer sliding section in the proposed layout undergoes a rotation simultaneously as its spanwise position is varied. This rotation is not due to a forced rotary actuation but due to the spanwise extension itself as both the sliding and fixed sections have the same constant twist rate. This kinematic motion is similar to that of a nut on a bolt whose position along the shaft can only be changed via rotation. Furthermore, the outer sliding section also has a smaller chord to enable it to slide into the inboard section. The inboard fixed section of the blade would incorporate a slide rail along which the outer section is allowed to slide. This slide rail would also be twisted to account for the twist of the blade. Note that the tip of the outboard sliding portion of the blade can have an arbitrary planform to best suit the aircraft performance, as it is not stowed within the inner fixed section. The result of the current assembly of the sections will result in a larger absolute blade tip twist as the radius is increased, despite a constant linear twist rate through the section.

The concept presented is intended to be capable of independent radius and RPM variation. This decoupling of the RPM and radius can be achieved via mechanical actuation which produces a radius variation. Possible solutions for a mechanical actuation system include, but are not limited to, the use of a jackscrew, hydraulic system or any other type of linear actuator. Another plausible method of achieving the decoupling of the rotor RPM and radius, is the use of a rotor radius locking mechanism for a centrifugally actuated rotor. An example would be where a decrease in rotor RPM is required with an increase in rotor radius. For this case, an initial increase in RPM causes an increase in rotor radius, after which the rotor is locked and RPM reduced to the desired value. The various actuation mechanisms considered for the presented concept will be discussed in detail in proceeding sections of this chapter.

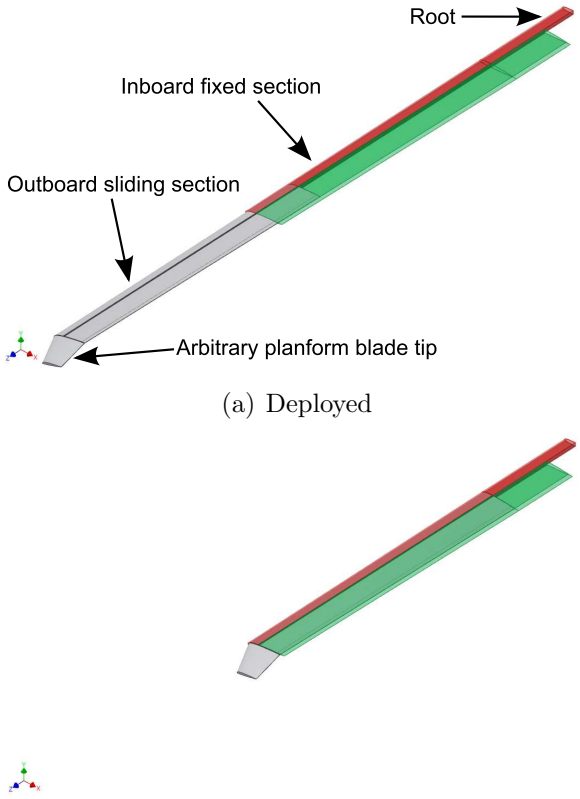

(a) Deployed

(b) Stowed

Figure 2.1. Schematic variable span blade concept with twist section in its completely deployed and stowed states

2.2 Analysis Model

The following sections describe various components of the analysis model that was used for the present study. A concise description of the mathematical aircraft model used for the present study is first presented and is followed by a detail description of the rotor model used.

2.2.1 Aircraft mathematical model

The analysis model used for the current study incorporates a four bladed articulated rotor system. The blades are assumed to undergo rigid-body flapwise rotation about an offset flap hinge. Since the focus for this research is on the possible improvements in rotor power requirements, and not rotor loads or vibration, this type

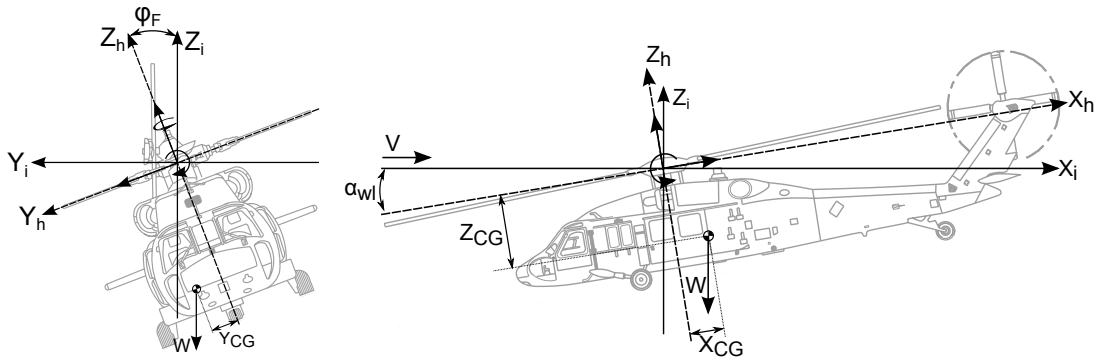

(a) Front view (b) Side view

Figure 2.2. Aircraft mathematical model free body diagram with pertinent properties highlighted

of rotor model was deemed sufficient. The blade twist and chord distributions are modeled within the code via the use of segmented blade sections. Furthermore, the airfoil (SC-1095 and SC-1094 R8) aerodynamic coefficients are obtained using look up tables. The current work uses a rigid prescribed wake to model the rotor inflow. The aircraft fuselage and horizontal tail aerodynamics characteristics are modeled using a least squared fit solution of wind tunnel test data [188]. The baseline rotor and fuselage parameters and the trim sequence used can be found within references of Leon and Gandhi [161, 32].

2.2.2 UH-60A type aircraft model details

As mentioned earlier, the current work focuses on the performance benefits of variable span and variable RPM systems for a UH-60A type aircraft. For the current study a window of ±11.11% RPM variation about the UH-60A's baseline of 257.8 RPM was considered; this corresponds to a maximum and minimum RPM of 286.5 and 229.2, respectively. The baseline UH-60A rotor chord, mass and twist distribution is shown in Fig. 2.3 and it can be seen that a significant portion of the mid span of the blade has a constant twist rate (linear twist variation). An implementation for a variable span twisted section would work best for a constant twist rate and therefore the variable span section of the blade was limited to the linearly twisted portion of the blade.

The initial specification on maximum and minimum radius limits were set to

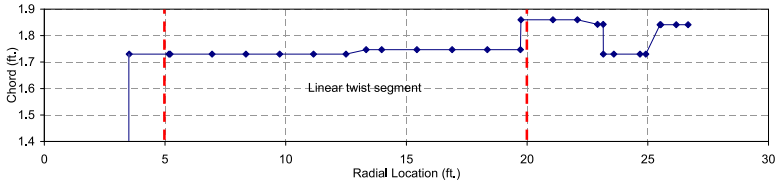

(a) Chord distribution

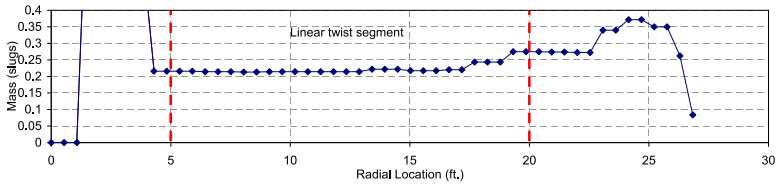

(b) Mass distribution

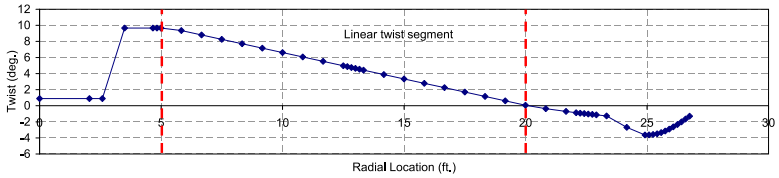

(c) Twist distribution

Figure 2.3. Blade parameter spanwise distribution for baseline UH-60A rotor

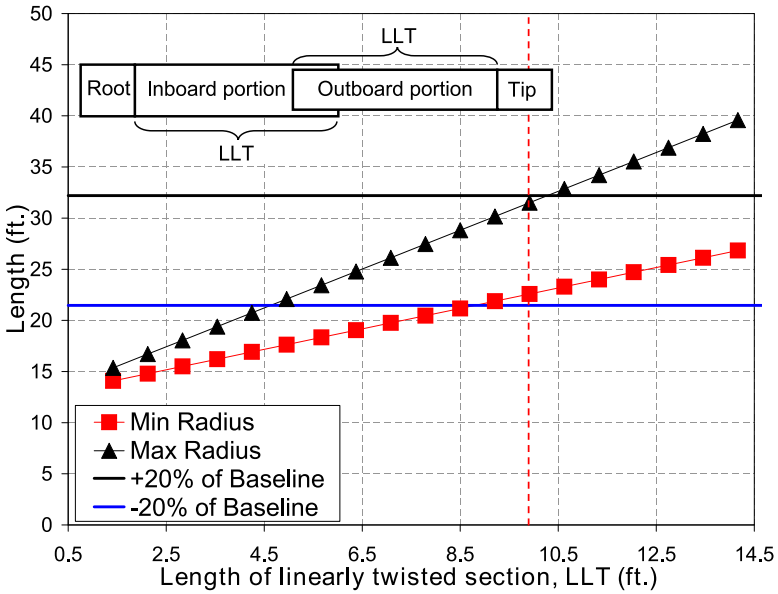

Figure 2.4. Maximum and minimum possible radius as a function of percentage of baseline linear twist portion of blade

be ±20% of the baseline radius using at least a 10% overlap of the inboard and outboard portions of the blade. It is assumed that the length of the linearly twisted section of the inboard fixed portion of the blade is the same as the linear twisted section of the outboard sliding portion. In the completely stowed condition the entirety of the linearly twisted section of the outboard sliding portion of the blade is within the inboard fixed portion. Figure 2.4 shows the variation of minimum and maximum possible radii of the blade as a function of the length of the linearly twisted section of the inboard fixed portion. As can be seen from the figure to obtain a maximum and minimum radius values closest to the set requirement a length of 9.91 ft for the linearly twisted section of the inboard fixed portion (and hence the outboard sliding portion) of the blade must be used. In Fig. 2.4, the region marked Root and Tip have constant lengths (5.83 ft and 6.75 ft respectively).

Based on these calculations, the baseline rotor was segmented to comprise of an inboard and outboard section whose chord, mass and twist distribution for the minimum, baseline and maximum radius cases are shown in Fig. 2.5. The final minimum and maximum radius was set to be 22.6 ft (−15.8% with respect to baseline) and 31.5 ft (+17.4% with respect to baseline) respectively, with a minimum overlap of 9%. The baseline radius corresponds to the UH-60A baseline rotor radius of 26.83 ft. As can be seen in Fig. 2.5(a) the outboard section was modified to have a lower chord for the section that will slide within the inboard section to allow for tolerances. Furthermore, the mass of the inboard section corresponding to the overlap section is increased by 60% (Fig. 2.5(b)) to account for the mass increase due to the inclusion of the actuation mechanism or the spring and locking assembly and possible increased stiffening. Note that although the twist rate of both the inboard and outboard section is the same as the baseline UH-60A rotor, a variation in the rotor radius results in a variation in the absolute tip twist of the rotor, as depicted in Fig. 2.5(c). For every trim case analyzed, the above rotor properties are varied to account for the variation in rotor radius. For the current study, the location of the tail rotor was not varied with rotor span, this was done in an effort to maintain a basis of comparision with the baseline aircraft configuration.

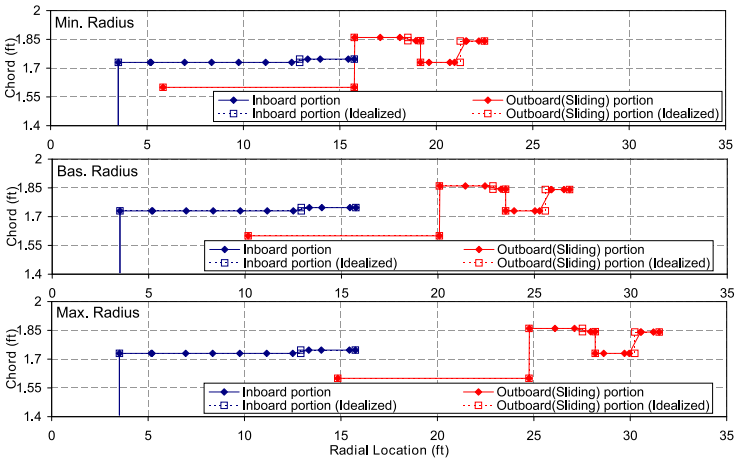

(a) Chord distribution

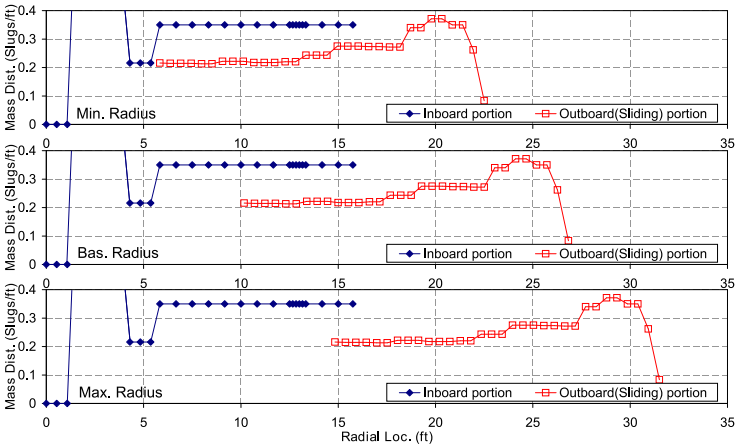

(b) Mass distribution

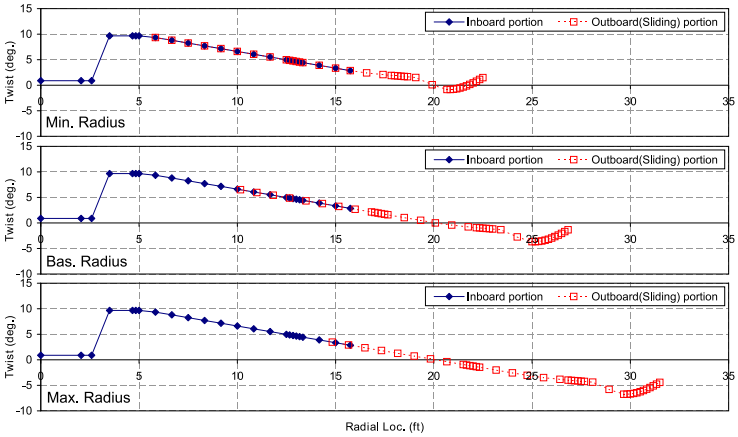

(c) Twist distribution

Figure 2.5. Blade parameter spanwise distribution for min, baseline and max radius values

2.2.3 Analysis/study details

The trim and power requirements of the helicopter with the modified rotor were analyzed for three gross weights: 16000 lbs, 18300 lbs (baseline) and 24000 lbs. Furthermore, each gross weight was analyzed at four different altitudes (Sea level, 4000 ft, 8000 ft and 12000 ft) and varying forward velocities (30-150 knots, 10 knot increments). For each combination of gross weight, altitude and forward velocity, the aircraft model was trimmed for all combinations of radius and RPM values within the window considered. In order to obtain a relatively fine resolution within the radius/RPM window considered, both radius and RPM were divided into 16 steps over the respective ranges of variation. A summary of the aircraft model used and the flight conditions considered in this study are presented in Table 2.1.

Table 2.1. Summary of aircraft model and analysis properties

Prop. Name.	Val.	Min. Val.	Max. Val.
No. of Blades	4		
Twist	UH-60A dist.		
Chord	UH-60A dist.		
Airfoils	SC-1095, SC-1094 R8		
Gross weight		16000 lbs	24000 lbs
Forward Vel.		30 kts	150 kts
Altitude		Sea Level	12000 ft
RPM (Bas.=257.8)		229.2	286.5
Radius (Bas.=26.83 ft)		22.6 ft	31.5 ft

In order to clarify the sources of power reduction, it was important to separate the components of the total power calculated in this study. Historically, there has been some debate with regards to the proper definition of induced power and for the current analysis the method laid out by Ormiston [189] is used. Equation 2.1 was used to calculate the total power required by the main rotor which comprised of constitutive components as shown. Profile power in this case is directly calculated using equation 2.2, whereas propulsive power is calculated using equation 2.3. Note that the propulsive force is largely associated to the fuselage drag force. Lastly, the induced power component is calculated as the difference between the total power and the sum of the profile and propulsive power as shown in equation 2.4.

$$P_{Tot} = \Omega \frac{N_b}{2\pi} \int_{\Psi} \int_{y} (\phi dL + dD) r d\Psi \tag{2.1}$$

$$P_{Tot} = P_{Profile} + P_{Induced} + P_{Propulsive}$$

$$P_{Profile} = \Omega \frac{N_b}{2\pi} \int_{\Psi} \int_{y} (dD) r d\Psi \tag{2.2}$$

$$P_{Propulsive} = F_{Prop} V \tag{2.3}$$

$$F_{Prop} \approx D_F$$

$$P_{Induced} = P_{Tot} - (P_{Profile} + P_{Propulsive}) \tag{2.4}$$

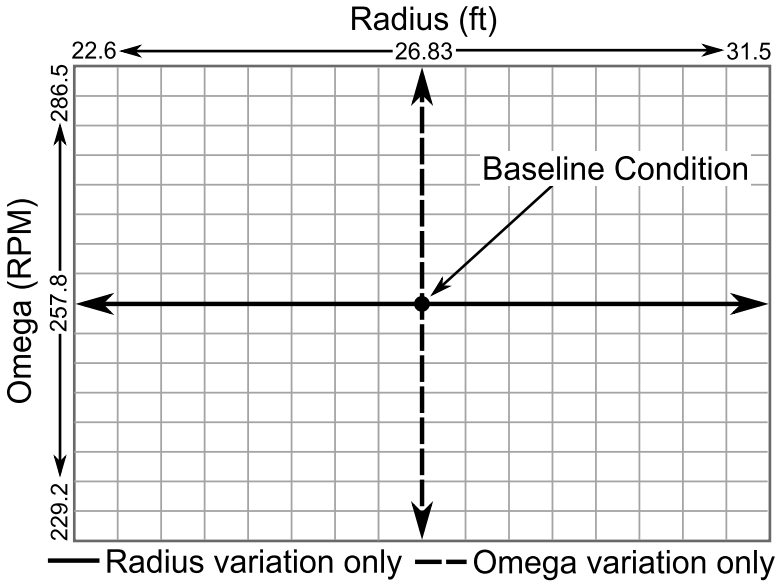

Figure 2.6. Data window considered for current study

Figure 2.6 is a graphical representation of the RPM/Radius variation window considered in the present study. Considering only the effect of RPM variation amounts to moving along the vertical axis through the origin. Similarly, considering only the effects of radius variation amounts to moving along the horizontal axis through the origin. The former case is similar to research conducted by Guo and Horn [132], Steiner and Gandhi [133, 183] and later followed by Bowen-Davies and Chopra [135]. For the current work, the effects of both RPM and radius variation

individually and in combination, will be considered in detail.

2.3 Results

2.3.1 Modified rotor comparison to baseline UH-60A rotor

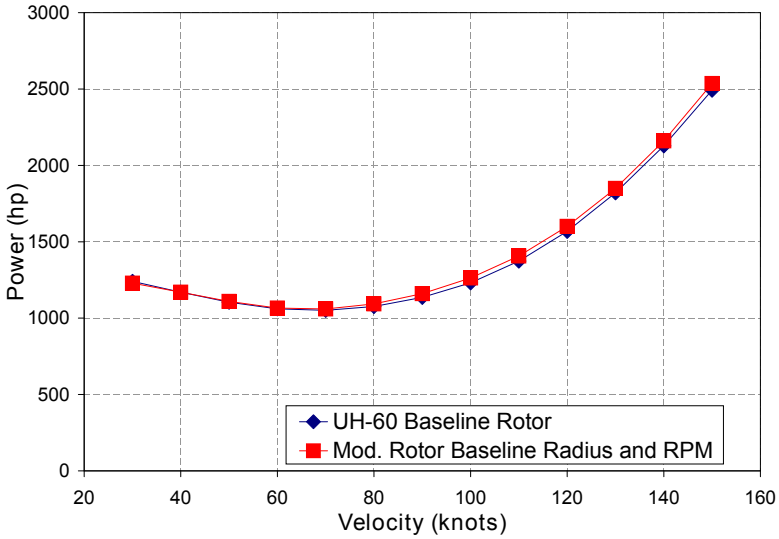

Figure 2.7. Trim power values for UH-60A baseline rotor as compared to modified rotor with baseline UH-60 radius/omega combination

With the main rotor undergoing modifications as described to practically realize span variation, the performance of the modified rotor for the baseline radius and RPM of the UH-60A is first examined. Figure 2.7 shows the variation of the total power required as a function of forward velocity for an aircraft gross weight of 18300 lbs at sea level. As can be seen in this plot, the power curves of the baseline UH-60A rotor compare well to those of the modified rotor operating at the baseline UH-60A radius and RPM. The baseline UH-60A results used in this figure is from a validated model used by Leon, Hayden and Gandhi [161, 32].

Figure 2.8 shows the variation of primary collective and cyclic control input $(\theta_0, \theta_{1c}, \theta_{1s})$ and aircraft orientation (α, ϕ). As can be seen in these figures overall both rotor models correlate well with few observed deviations. These differences are largely associated with the difference in the blade properties, i.e., the chord and mass distribution of the modified rotor. Based on these observations for all the

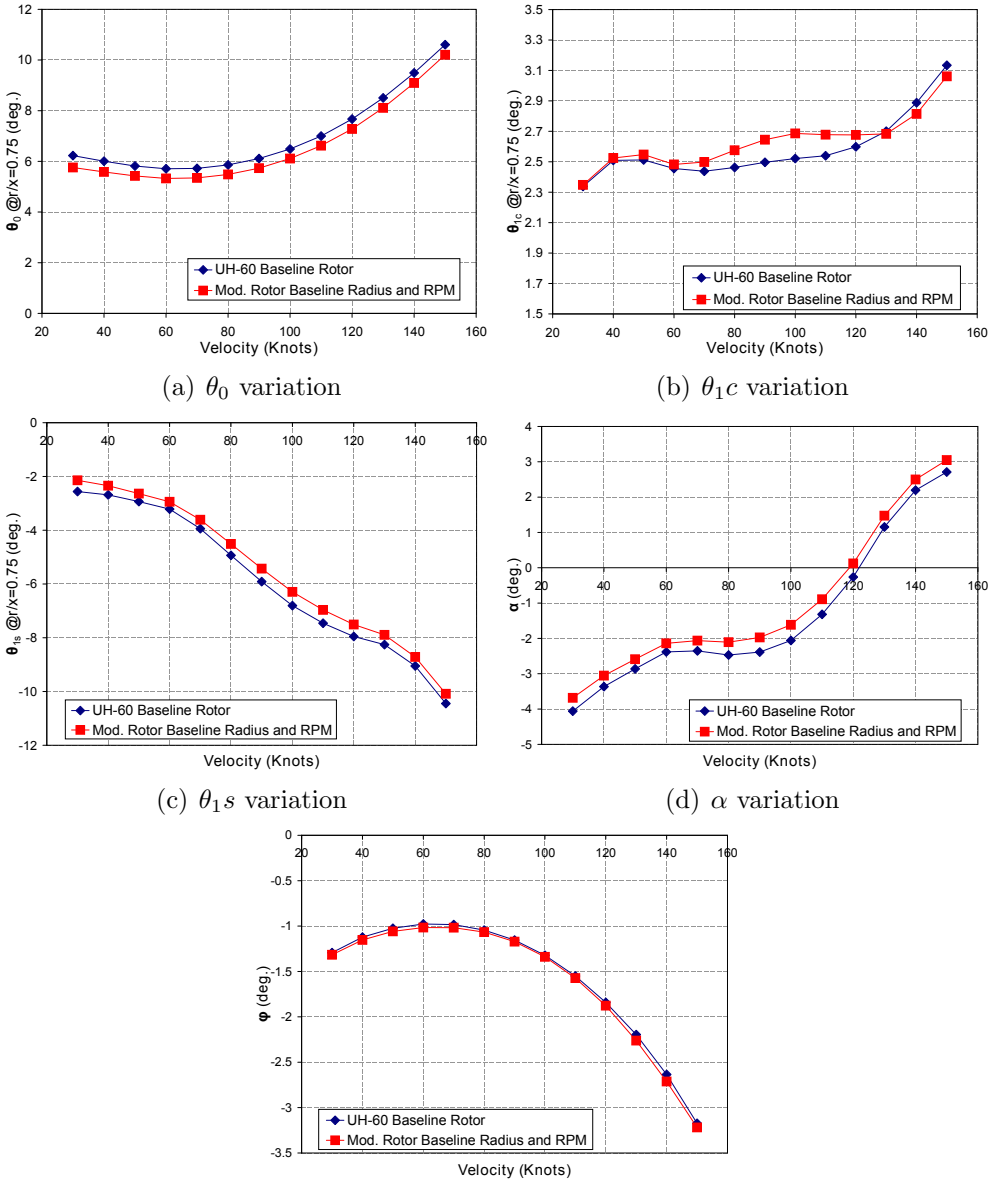

(a) θ_0 variation

(b) $\theta_1 c$ variation

(c) $\theta_1 s$ variation

(d) α variation

(e) ϕ variation

Figure 2.8. Aircraft trim control and attitude values for a UH-60A baseline rotor and modified rotor with baseline UH-60 radius/omega combination

proceeding sections, the modified rotor at the baseline UH-60A RPM and radius is defined as the baseline case.

2.3.2 Power reduction results

The power reduction percentage values presented are with respect to the power required for the baseline RPM and radius. For certain cases, in particular for high gross weight, altitude and forward velocity, no trim solution could be obtained corresponding to the baseline radius and RPM and therefore the power reductions are not calculated even though changes in radius and RPM would allow for the aircraft to operate at the envelope extremes and beyond.

2.3.2.1 Variation of RPM only

Figure 2.9 shows the percentage reduction in total power as a function of forward velocity and altitude for various gross weights. As can be seen in the figures, the largest power reduction is seen for low gross weight and altitude conditions for cruise velocities (80-100 knots), with lower power reductions calculated for low and high speed flight cases. The calculated performance improvement is also seen to diminish with increasing gross weight and altitude. Figure 2.10 shows that the RPM value corresponding to the minimum power increases as the forward velocity, gross weight or altitude increase. As can be seen in the figure, the RPM for minimum power is generally lower than the baseline for the low to mid range gross weights (16000 lbs and 18300 lbs), while larger than baseline values become preferable for the high gross of 24000 lbs. Note for a wide range of velocities and altitudes for the low gross weight considered (16000 lbs) the rotor speed for minimum power is at the lower limit of the variation considered for this study. This observation suggests potentially even higher performance improvements if the rotor speed was allowed to vary within a wider range.

Although not shown as figures, it was observed that the power reduction calculated as a result of RPM variation was dominated by profile power reduction for most flight cases. The exception for this observation are high gross weight (24000 lbs), high altitude (8000 ft and above) and low forward speed (30 knots and below) cases, wherein induced power reduction dominates the performance improvements calculated. Furthermore, it was also observed that the propulsive power has negligible variation between the baseline and minimum power cases. Both observations on the magnitude and the source of the power reduction are in agreement of anal-

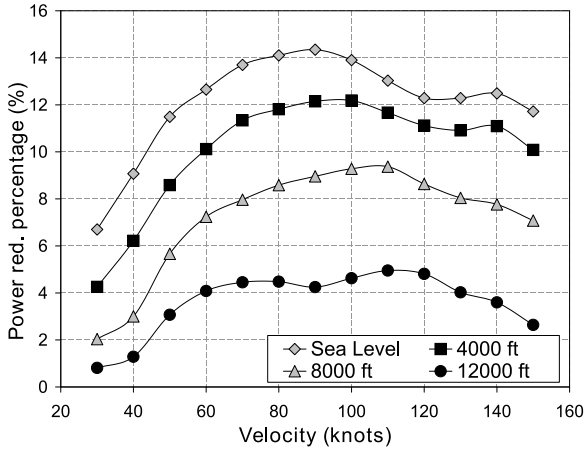

(a) 16000 lbs

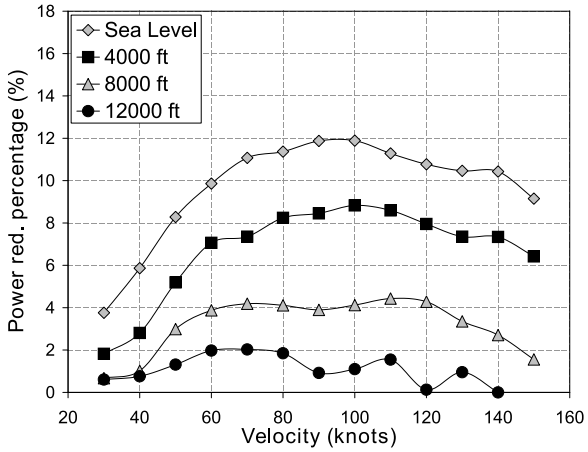

(b) 18300 lbs

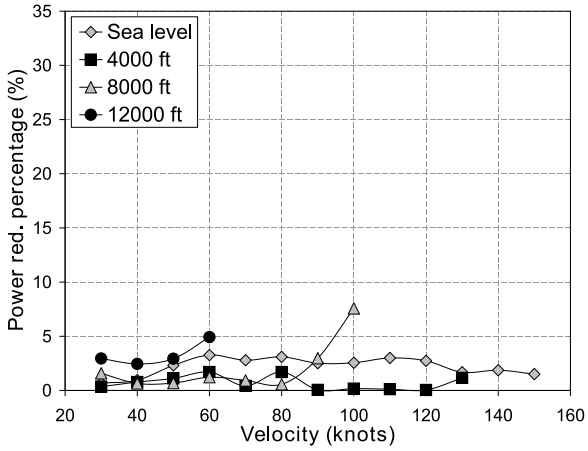

(c) 24000 lbs

Figure 2.9. Power reduction percentages due to RPM variation only

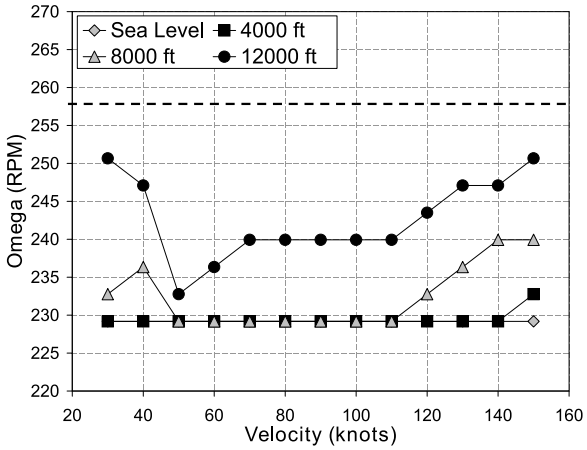

(a) 16000 lbs

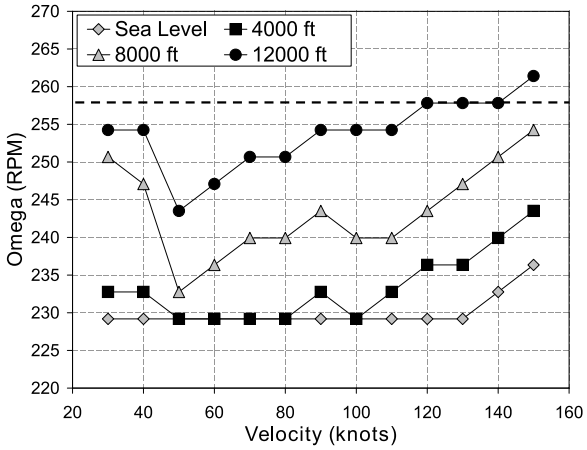

(b) 18300 lbs

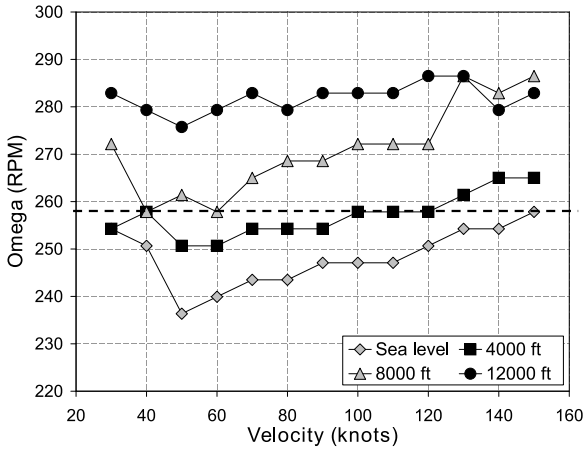

(c) 24000 lbs

Figure 2.10. RPM values corresponding to minimum power case for RPM variation only

ysis conducted by Steiner and Gandhi [133, 183] and Bowen-Davies and Chopra [135].

Variation of RPM directly effects the dynamic pressure the rotor blade operates in, this in turn affects the required blade pitch to produce the thrust levels needed for a specified flight condition as well as the profile drag of the blade. For the mid range forward velocities, reducing the RPM allows for the rotor to operate at the best possible power loading by reducing the profile drag experienced by the blade sections, thereby reducing profile power. For high gross weight, high altitude or high speed cases where the rotor is approaching stall, increasing the RPM allows for lower pitch values, thereby allowing the rotor to produce the required thrust, however, this comes at the cost of increased profile power due to the increase in dynamic pressure which is seen in the lower power reduction percentages for high gross weights and altitude cases. For low speed flight since profile power itself is a smaller component of the total power, reduction of the RPM has a more limited effect in reducing total rotor power.

2.3.2.2 Variation of Radius only

Figure 2.11 shows the power reduction variation due to the change in blade span only as a function of forward velocity and altitude for various gross weights. As seen in the figure the overall power reduction percentage values are lower than those observed with RPM variation only for low to mid range gross weights (compare Fig. 2.11(a) and 2.11(b) to Fig. 2.9(a) and 2.9(b)). However, for the 24000 lbs case, the power reductions observed are significantly larger than those with RPM variation only (compare Fig. 2.11(c) to 2.9(c)).

The power reduction trends for the radius only case are far more complex as compared to the RPM only variation case. For gross weights in the low to mid range (16000 and 18300 lbs), the forward speed range considered can be separated into two regimes. The first is where an increase in forward velocity relates to diminishing improvements. This type of behavior is exhibited for low forward speed values ranging from below 30 knots to below 100 knots for sea level case and 12000 ft case respectively for the 16000 lbs gross weight configuration. Furthermore, increasing the gross weight amplifies this behavior, i.e. the range of forward velocities where this behavior is exhibited increases (consider Figs. 2.11(a) and 2.11(b)) in

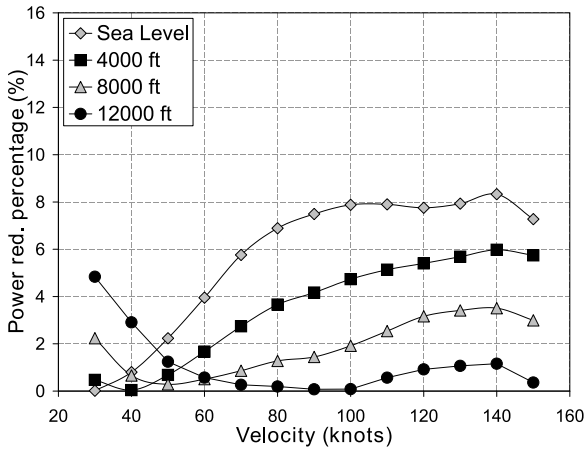

(a) 16000 lbs

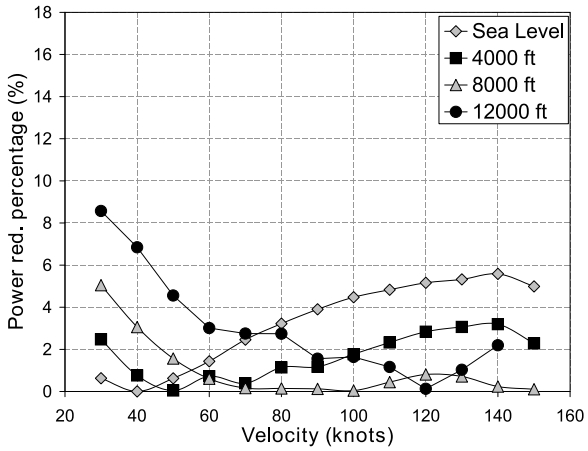

(b) 18300 lbs

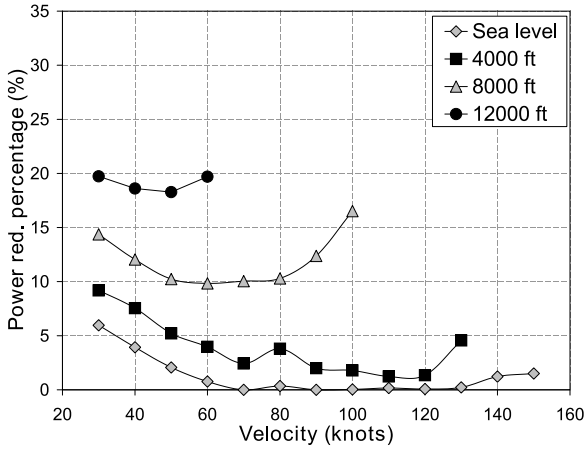

(c) 24000 lbs

Figure 2.11. Power reduction percentages due to radius variation only

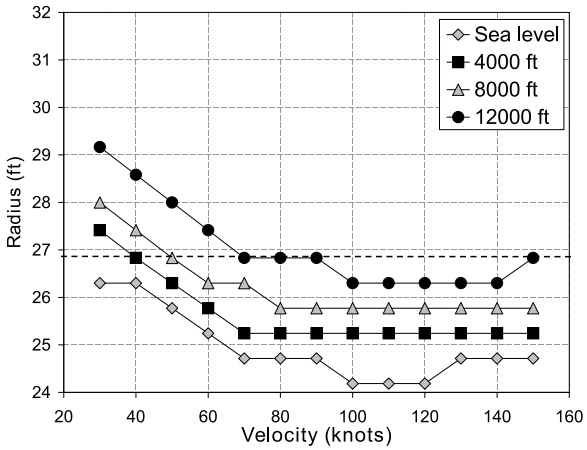

(a) 16000 lbs

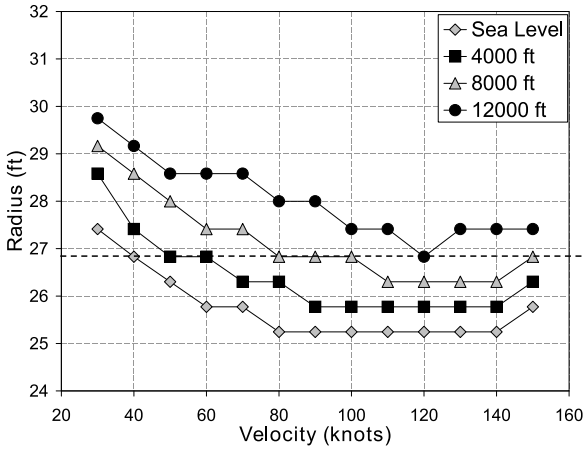

(b) 18300 lbs

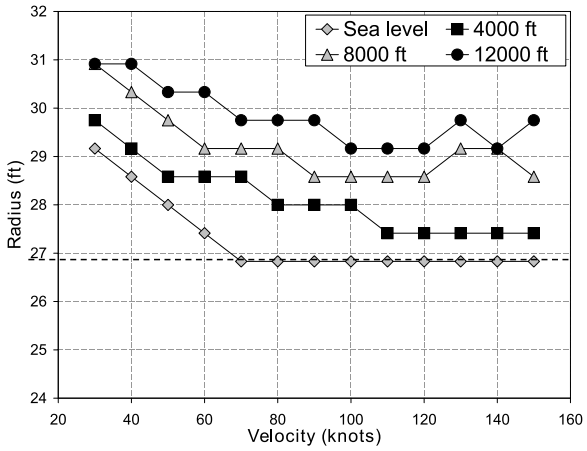

(c) 24000 lbs

Figure 2.12. Radius values corresponding to minimum power case for Radius variation only

particular for low speed values ranging from below 40 knots to below 120 knots for sea level case and 12000 ft case respectively for the 18300 lbs gross weight configuration. For the high gross weight configuration, as can be observed in Fig. 2.11(c), the specified regime encompasses the entire forward flight speed range considered. Note that for the corresponding forward speed range, power reductions increase with altitude, a trend which is in sharp contrast to that of the RPM only variation configuration (wherein power improvements diminish with altitude increments).

The second regime (corresponding to the remainder of the forward speed range considered) is where the power reductions increase with forward speed. This regime, as seen in Figs. 2.11(a) and 2.11(b) is only seen for the low and mid range gross weights (16000 and 18300 lbs). Interestingly within this range of forward speed, the power reductions decrease with altitude, a trend comparable to the RPM only variation case. Overall, for the case of radius only variation the best possible power reduction is observed for low velocity, heavy and high conditions.

Figure 2.12 shows the variation in radius corresponding to minimum power as a function of forward velocity, altitude and gross weight. Overall, as seen in the figure, increasing gross weight increases the required radius for minimum power, starting with lower than baseline values for the 16000 lbs case increasing to the generally higher than baseline values for 24000 lbs. Note that the required radius also increases with altitude and generally decreases with forward velocity.

Table 2.2 shows the power reduction and their corresponding sources for specific combinations of gross weight, altitude and forward velocity due to radius only variation. The highlighted cells in the table refer to cases where the profile power reduction dominates the performance improvement, whereas the other cells refer to cases where induced power reductions dominate. As can be seen in this table for low gross weights at low altitudes profile power reduction dominates the performance improvement for all three flight speeds considered. As gross weight is increased for low to mid range forward velocity cases the induced power reduction begins to dominate the improvements calculated.

In general, cases for which the smaller than baseline radius is preferred, profile power reductions dominate, whereas cases where larger than the baseline radius is required induced power reductions dominate. Note that for the case of lower than baseline radius while a profile power reduction is observed due to the reduction

Table 2.2. Power reductions and the corresponding reductions sources (Profile, Induced and Propulsive) for selected gross weight, altitude and forward velocity combinations due to radius only variation

Gross wt. (lbs)	Alt. (ft)	40 Knots					80 Knots					120 Knots				
		P.R.	Prof. R.	I.R.	Prop. R.	Rad.	P.R.	Prof. R.	I.R.	Prop. R.	Rad.	P.R.	Prof. R.	I.R.	Prop. R.	Rad.
16000	SL	8	24	-16	0	↓	67	114	-42	-5	↓	117	183	-56	-10	↓
	4K	0	0	0	0	–	35	76	-38	-3	↓	76	111	-32	-3	↓
	8K	7	-24	31	0	↑	12	43	-29	-2	↓	43	66	-23	0	↓
18300	SL	0	0	0	0	–	35	84	-45	-4	↓	83	122	-37	-2	↓
	4K	9	-28	37	0	↑	13	27	-13	-1	↓	43	71	-28	0	↓
	8K	40	-80	120	0	↑	0	0	0	0	–	12	26	-15	1	↓
24000	SL	69	-96	165	0	↑	0	0	0	0	–	0	0	0	0	–
	4K	145	-101	246	0	↑	62	-11	70	3	↑	28	11	18	-1	↑
	8K	259	-135	394	0	↑	194	33	156	5	↑	N/A				

P.R. – > Power reduction (HP), Prof. R. – > Profile power reduction (HP)

I.R. – > Induced power reduction (HP), Prop. R. – > Propulsive power reduction (HP)

Rad. – > Radius change (↑ for increase, ↓ for decrease, – for no change)

□ – > Profile power reduction dominated cases

in blade area, an increase (in some cases significant increases) in induced power is also seen due to the increase of disk loading. Furthermore, the converse is also true for cases which require a larger than baseline radius. If a reduction in one component of power is possible with a negligible negative impact on the complimentary component, larger overall power improvements are possible. For low to mid range gross weight cases due to the lower thrust requirement a reduction in profile power is favored and hence a reduction in radius is required. Conversely, for high gross weights due to the increase in the required thrust levels, increases in radius are preferred to reduce the induced power component albeit at the cost of increased profile power. Overall a negligible variation of propulsive power was observed between the baseline and minimum power cases.

2.3.2.3 Variation of Radius and RPM

Unlike the RPM or radius only variation cases, the power reduction values in this section represent the largest possible power reductions calculated over the range of variation in both RPM and radius considered. Figure 2.13 shows the total power reduction as a function of forward velocity and altitude for varying values of gross weight. Overall it can be clearly seen that the power reductions due to the simultaneous variation of RPM and radius leads to larger power reductions as compared to the each parameter variation individually. Another general trend, that is a departure from that of RPM or radius only variation, is the overall increase in performance benefits calculated with increasing gross weight for the range of forward velocities considered. For low gross weights and altitude, as seen in the figure, the best possible performance improvement is seen for mid range velocities. However, as gross weight and altitude are increased the best possible performance improvement is observed for lower velocities, with performance improvement generally decreasing as forward velocity is increased (the exception being the 24000 lbs gross weight case at 8000 ft and 12000 ft).

The optimum radii for minimum power as a function of gross weight, altitude and forward velocity is shown in Fig. 2.14. The corresponding optimum RPM was found to always be the minimum value (229.18 RPM) and is therefore not presented graphically. A few key trends observed in this figure are: First, unlike radius only variation, for most cases a radius larger than the baseline is preferred.

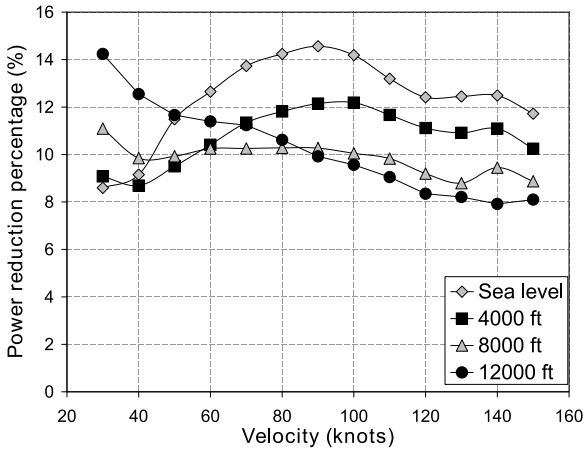

(a) 16000 lbs

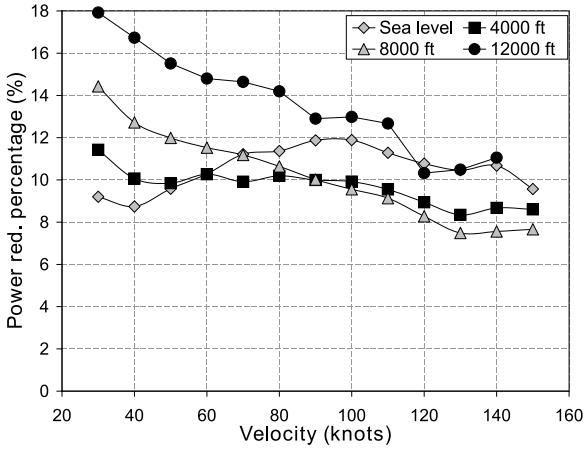

(b) 18300 lbs

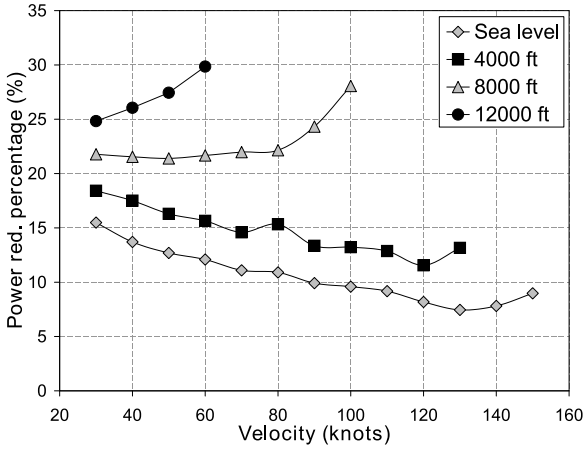

(c) 24000 lbs

Figure 2.13. Power reduction percentages due to combined radius and RPM variation

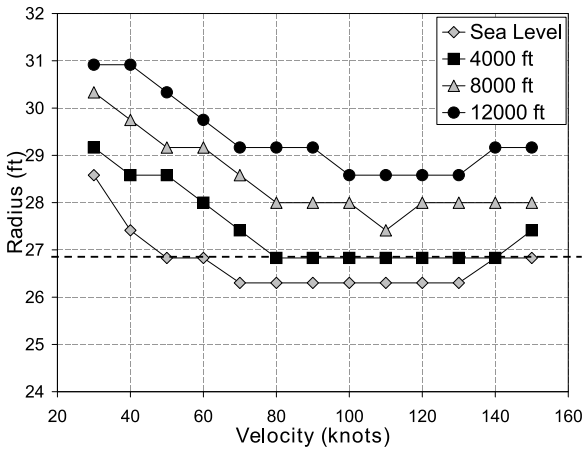

(a) 16000 lbs

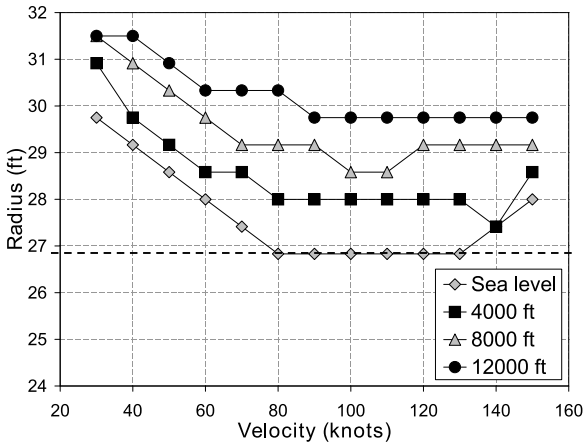

(b) 18300 lbs

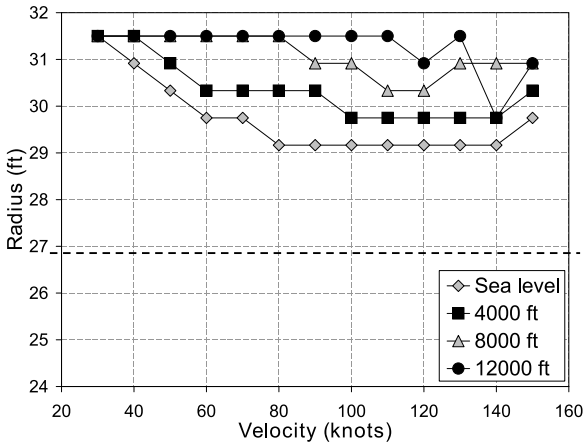

(c) 24000 lbs

Figure 2.14. Radius values corresponding to minimum power case for combined radius and RPM variation

However, similar to radius only variation as gross weight and altitude is increased, the optimum radius increases, and as velocity is increased the corresponding radius for minimum power reduces.

Figures 2.15, 2.16 and 2.17 show the power reduction breakdown corresponding to 16000, 18300 and 24000 lbs gross weights, respectively, for varying forward velocities and altitudes. For low gross weights and altitude, as can be seen in the figure, profile power reductions dominate the performance improvement for most of the forward velocity range considered (the exception being low forward speeds: 30-40 knots). Increasing gross weight and altitude results in induced power reduction dominating the total power reduction for the low to moderate forward velocities. This phenomenon is very similar to that observed for the radius only variation. However, unlike the radius only variation case, for simultaneous radius and RPM variation no significant increase of the complimentary power component was observed, which allows for higher overall power reductions. To illustrate this observation compare the data presented in Table 2.3 to that of Table 2.2. For radius only variation when profile power dominates the performance improvement there is a corresponding increase in induced power and vice versa (Table 2.2). However, this phenomenon is greatly diminished for the case of simultaneous RPM and radius variation as can be seen in Table 2.3 (highlighted cells correspond to cases where profile power reduction dominates power reduction). Lastly, overall no significant variation in the propulsive power relative to the baseline was observed for most cases considered.

Similar to the case of radius only variation, increases in radius generally tend to correspond to cases where induced power reduction dominates. The mechanism for induced power reduction for cases where a larger radius is preferred is similar to that of the radius only variation, i.e., larger than baseline radius decrease disk loading as compared to baseline and therefore reduce induced power. However, unlike the latter case, due to the simultaneous RPM reduction, the profile power increase associated with the increase in blade radius is reduced and as a result leads to higher power reductions than compared to either radius or RPM only variation cases. This phenomenon is especially true for low/mid (low velocity and high altitude) to high (all considered forward velocity and altitude cases) gross weights as seen in table 2.3. To understand the source of power reduction for the

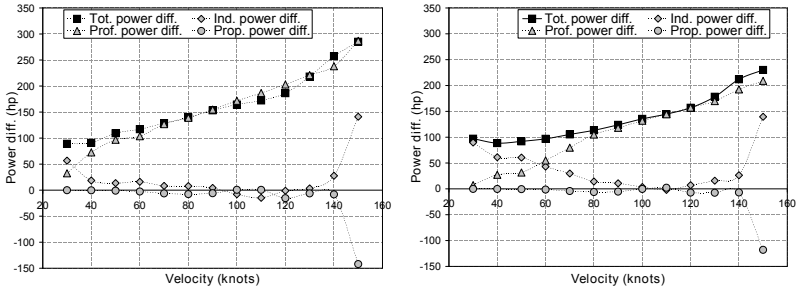

(a) Sea level (b) 4000 ft

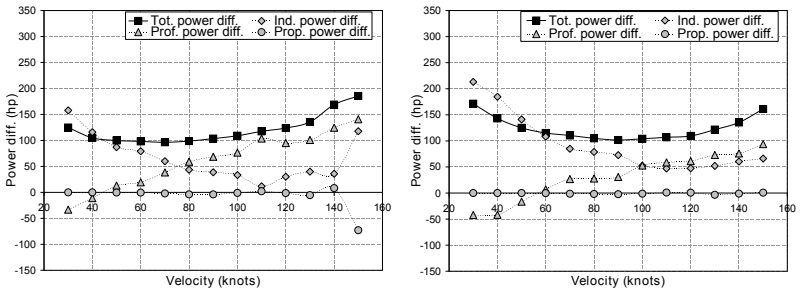

(c) 8000 ft (d) 12000 ft

Figure 2.15. Power reduction source components for a gross weight of 16000 lbs at various altitudes

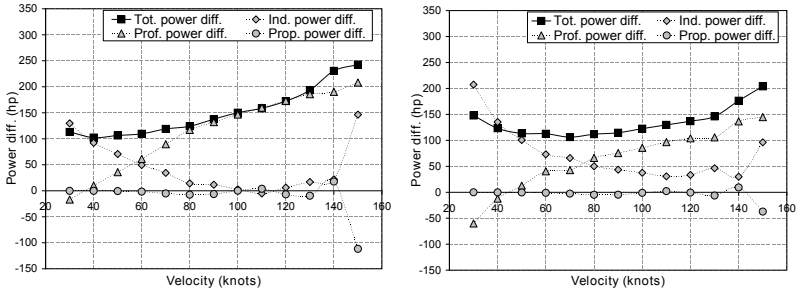

(a) Sea level (b) 4000 ft

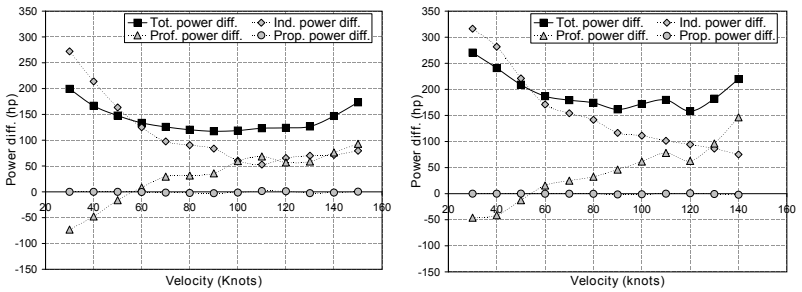

(c) 8000 ft (d) 12000 ft

Figure 2.16. Power reduction source components for a gross weight of 18300 lbs at various altitudes

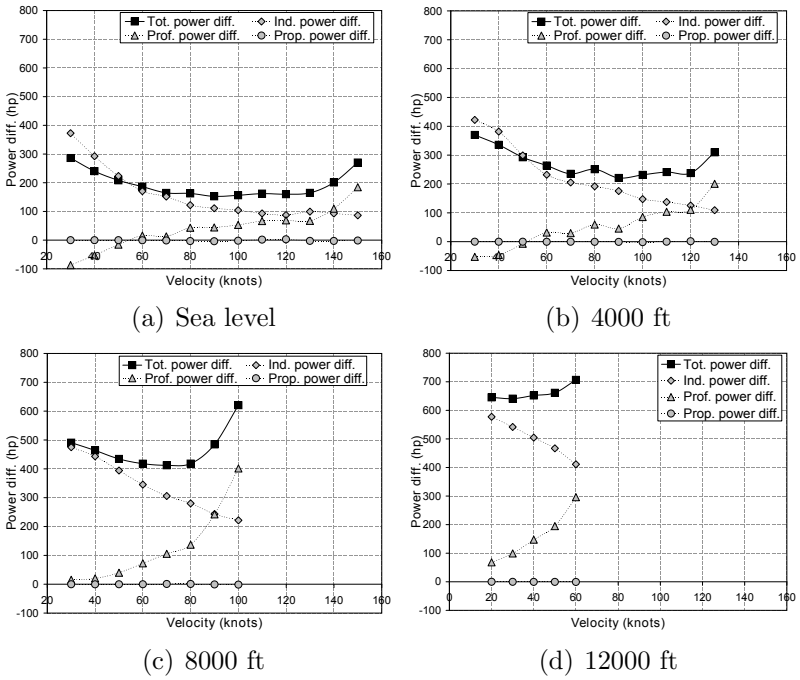

(a) Sea level (b) 4000 ft

(c) 8000 ft (d) 12000 ft

Figure 2.17. Power reduction source components for a gross weight of 24000 lbs at various altitudes

remainder mid to low gross weight and altitude conditions consider table 2.4, which lists the power reduction obtained via radius and RPM only variation alongside those obtained via simultaneous parameter variation. As can be seen in this table for these cases, the power reduction of the RPM only case are comparable to the simultaneous case. This observation implies that for these cases RPM variation dominates the power reduction and as such variation in radius has a minor effect and is such dominated by profile power reduction (Table. 2.3).

Table 2.3. Power reductions and the corresponding reductions sources (Profile, Induced and Propulsive) for selected gross weight, altitude and forward velocity combinations due to simultaneous RPM and radius variation

Gross wt. (lbs)	Alt. (ft)	40 Knots					80 Knots					120 Knots				
		P.R.	Prof. R.	I.R.	Prop. R.	Rad.	P.R.	Prof. R.	I.R.	Prop. R.	Rad.	P.R.	Prof. R.	I.R.	Prop. R.	Rad.
16000	SL	91	72	19	0	↑	140	139	8	-7	↑	186	203	-1	-16	↑
	4K	88	27	61	0	↑	113	105	14	-6	–	157	157	7	-7	–
	8K	105	-11	116	0	↑	99	59	44	-4	↑	124	95	30	-1	↑
18300	SL	102	10	92	0	↑	124	117	14	-7	–	172	173	6	-7	–
	4K	123	-12	135	0	↑	111	66	50	-5	↑	137	104	33	0	↑
	8K	166	-48	214	0	↑	120	32	90	-2	↑	124	57	66	1	↑
24000	SL	240	-53	293	0	↑	162	43	122	-3	↑	160	69	88	3	↑
	4K	336	-46	382	0	↑	251	59	192	0	↑	237	110	125	2	↑
	8K	463	20	443	0	↑	418	137	280	1	↑	N/A				

P.R. – > Power reduction (HP), Prof. R. – > Profile power reduction (HP)

I.R. – > Induced power reduction (HP), Prop. R. – > Propulsive power reduction (HP)

Rad. – > Radius change (↑ for increase, ↓ for decrease, – for no change)

□ – > Profile power reduction dominated cases

Table 2.4. Percentage power reductions due to simultaneous and individual RPM and radius variation for selected gross weight, altitude and forward velocity combinations

Gross wt. (lbs)	Alt. (ft)	40 Knots			80 Knots			120 Knots		
		C.R.	O.R.	R.R.	C.R.	O.R.	R.R.	C.R.	O.R.	R.R.
16000	SL	9.15%	9.07%	0.8%	14.24%	14.10%	6.89%	12.41%	12.29%	7.76%
	4K	8.69%	6.22%	0.04%	11.81%	11.81%	3.66%	11.12%	11.12%	5.4%
	8K	9.85%	3.00%	0.66%	10.28%	8.59%	1.28%	9.19%	8.64%	3.17%
18300	SL	8.74%	5.86%	0.00%	11.37%	11.37%	3.22%	10.77%	10.77%	5.16%
	4K	10.07%	2.80%	0.76%	10.19%	8.25%	1.14%	8.94%	7.95%	2.84%
	8K	12.72%	1.02%	3.06%	10.64%	4.11%	0.14%	8.28%	4.28%	0.81%
24000	SL	13.71%	0.95%	3.93%	10.9%	3.09%	.35%	8.18%	2.73%	0.08%
	4K	17.50%	0.78%	7.55%	15.33%	1.70%	3.80%	11.56%	0.04%	1.35%
	8K	21.55%	0.65%	12.04%	22.15%	0.56%	10.30%	N/A		

C.R.- > Combined Radius/RPM reduction, O.R - > Omega only reduction,
R.R - > Radius only reduction

2.3.3 Specific case analysis

2.3.3.1 Variation of gross weight and forward velocity

Figure 2.18 shows the total power contour plots within the radius/RPM window considered for this study for various gross weights and flight speeds at sea level. As can be seen for low gross weight (16000 lbs) at all forward velocities considered, and for moderate gross weights (18300 lbs) for mid to high velocities (80 knots, 120 knots), the maximum power reduction is largely due to RPM reduction. This is attributed to a reduction of the profile power as stated earlier. However, for the remainder mid to high gross weights (18300 lbs, 24000 lbs), the maximum power reduction is achieved with a combination of RPM reduction and radius increase, which is apparent in the figure. Areas, at the bottom left and top right, of the contour plots correspond to RPM-radius combinations where trim of the aircraft was not possible. The regions at the top right are of little interest as the power increases over the baseline and eventually exceeds installed power. The regions at the bottom left correspond to rotor stall due to the simultaneous reduction of RPM and radius, whereas the regions at the top right correspond to the compressibility effects due to the simultaneous increase in RPM and radius. Due to these two effects note the increased narrowing of the power contour valley as the forward velocity and gross weight is increased, relating to the increased sensitivity of the total power to RPM and radius. A visual representation of the effects of radius and RPM variation can be seen for the contour plot for the 24000 lbs gross weight at 80 knots. A reduction in RPM alone corresponds to a total power reduction of only 50 HP (Point A), as the rotor is approaching stall. However, a reduction in RPM with a simultaneous increase in radius results in total power reduction of 150 HP (Point B).

For the case of 18300 lbs at 80 knots sea level, the angle of attack distribution through the rotor disk for the baseline and minimum power configuration (baseline radius, reduced RPM) is shown in Fig. 2.19. As can be seen in the figure, due to the reduction of the RPM only to achieve the minimum power condition, the blade angle of attack distribution required to provide the necessary thrust is higher for the minimum power case as compared to the baseline, thereby operating the blade at a better power loading. Figure 2.20 shows the drag distribution for the baseline

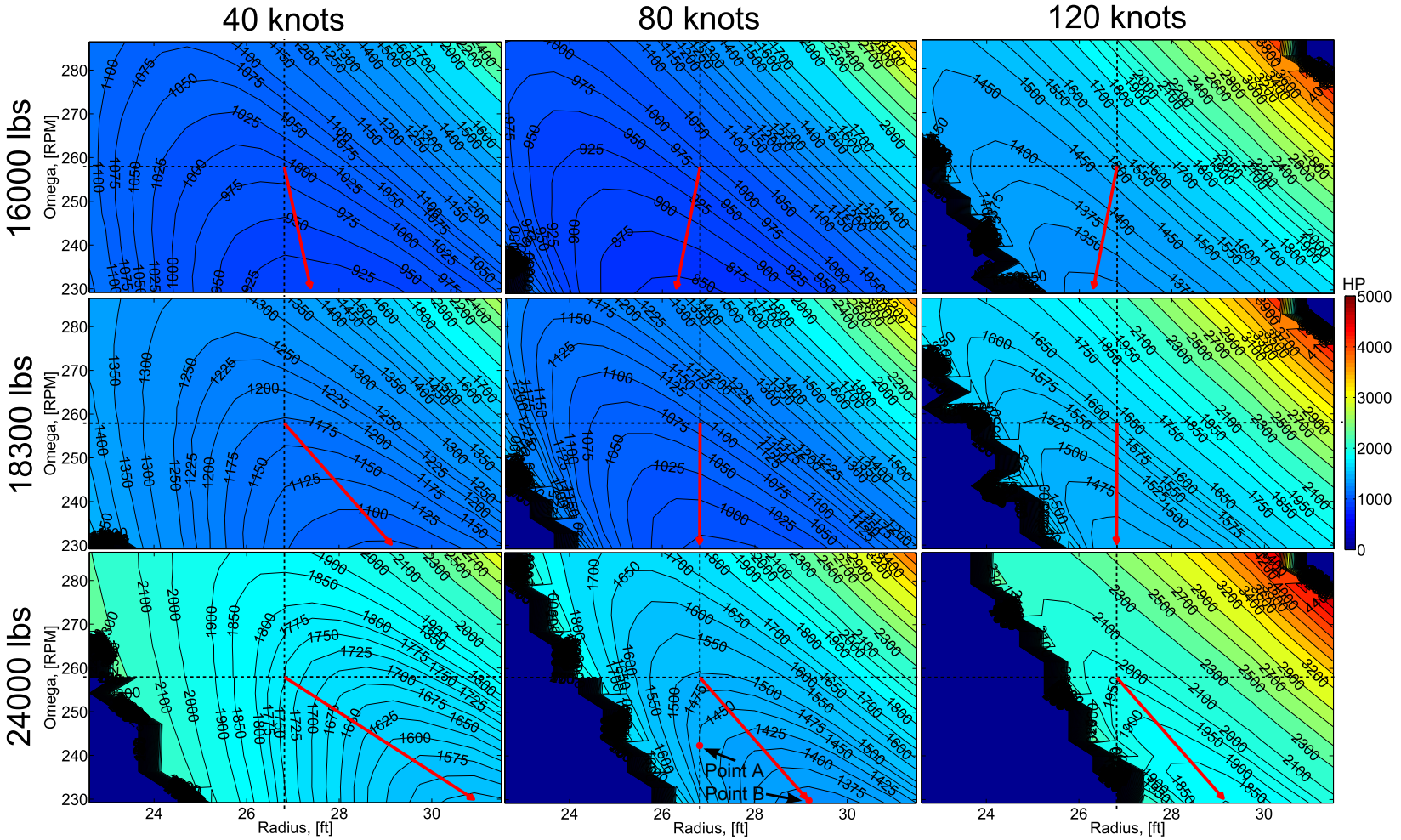

Figure 2.18. Total power contour plots for various gross weights and forward velocities at sea level

and the difference between the minimum and baseline power drag distribution for the same specified case (negative values correspond to drag reduction). As can be seen, due to the reduction in RPM only, the total drag experienced by the rotor deceases for a larger portion of the advancing side of the rotor disk, leading to a reduction in power.

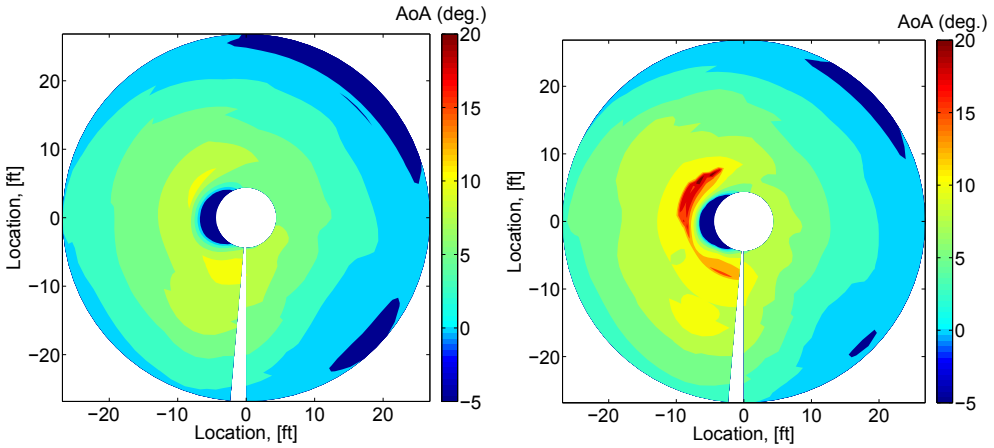

(a) Baseline (b) Minimum power

Figure 2.19. Angle of attack distribution through rotor for baseline and minimum power cases (18300 lbs, 80 knots, Sea Level)

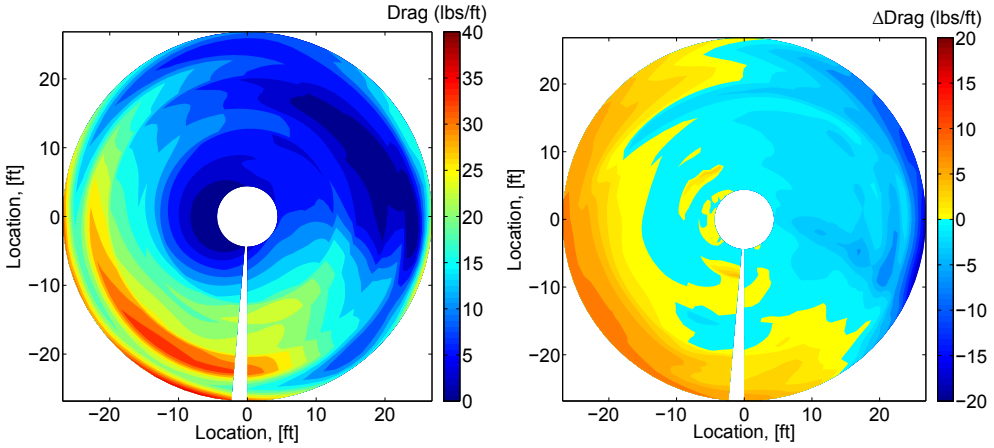

(a) Baseline (b) Difference

Figure 2.20. Drag distribution through rotor for baseline case and drag distribution difference between baseline and minimum power case (18300 lbs, 80 knots, Sea Level)

As stated earlier, for the highest gross weight considered, the total power re-

duction is due to a combination of radius increase and RPM reduction. Figure 2.21 shows the baseline and minimum power configuration induced velocity distribution through the rotor disk for the case of 24000 lbs, 40 knots at sea level (positive values correspond to downwash). As can be seen here, the overall values of the induced velocity are lower for the minimum power case as compared to the baseline, which leads to a reduction in the induced power.

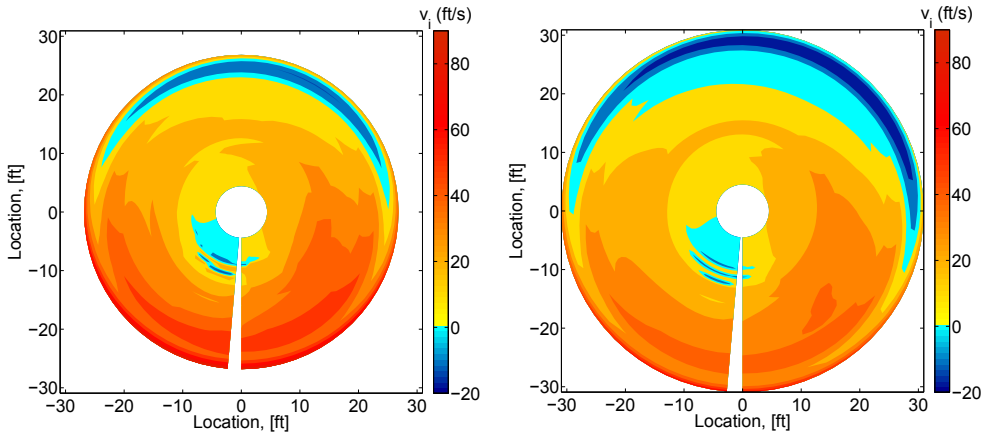

(a) Baseline (b) Minimum power

Figure 2.21. Induced flow distribution through rotor disk for baseline and minimum power cases (24000 lbs, 40 knots, Sea Level)

2.3.3.2 Variation of altitude

Figure 2.22 shows the total power contour plots for the the 18300 lbs case at 80 knots for various altitudes. The minimum power condition requires minimum RPM and increasing radius values for as the altitude is increased. This observed effect is similar to that of an increase in gross weight, i.e. to obtain the minimum power condition for high altitude and gross weight cases, the induced power must be reduced via the increase in radius and decrease in RPM. This observation is further noted in Figs. 2.15, 2.16, 2.17 and Table 2.3 which show that the power reduction contribution from the induced power increases with gross weight and altitude for low to mid range gross weights. Note the fast growth of the rotor stall regime at bottom left corner of the contour plots as a function of altitude. This observation is associated with the decrease in density with altitude increments, thereby making

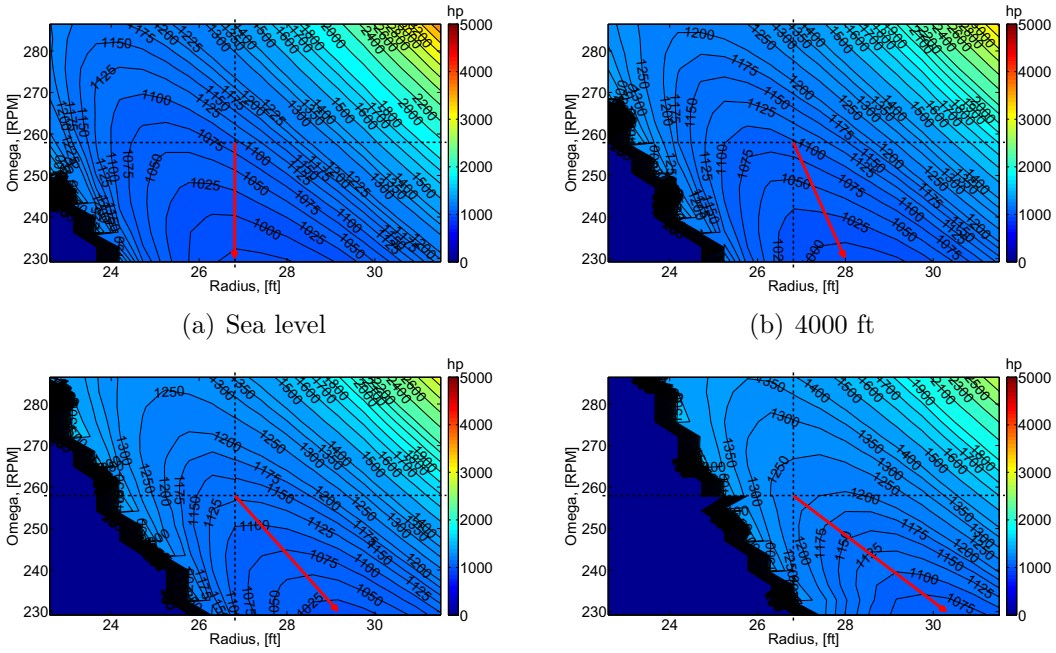

(a) Sea level

(b) 4000 ft

(c) 8000 ft

(d) 12000 ft

Figure 2.22. Total power contour plots for 18300 lbs at 80 knots for various altitudes

the rotor more susceptible to stall especially for the low RPM/small radius cases.

2.3.3.3 Effects on aircaft flight parameters (Horsepower, Maximum Range and Endurance)

While the previous sections show the power reductions possible and their corresponding sources if variable span and variable RPM capabilities were used (individually or in combination) for the UH-60A type aircraft they do not present the direct benefits in terms of possible maximum range and maximum endurance increases. The following section identifies these parameters in detail for specific nomial flight conditions.

Figure 2.23 shows the variation of power for the lowest (16000 lbs) and highest (24000 lbs) gross weights considered as a function of forward speed at sea level and at a density altitude of 8000 ft. As seen in the figure, the power reductions in terms of horse power is relatively constant throughout the range of forward velocities at sea level. For the specific case of 100 knots (which closely corresponds to the velocity for maximum range) for both the low and high gross weights the

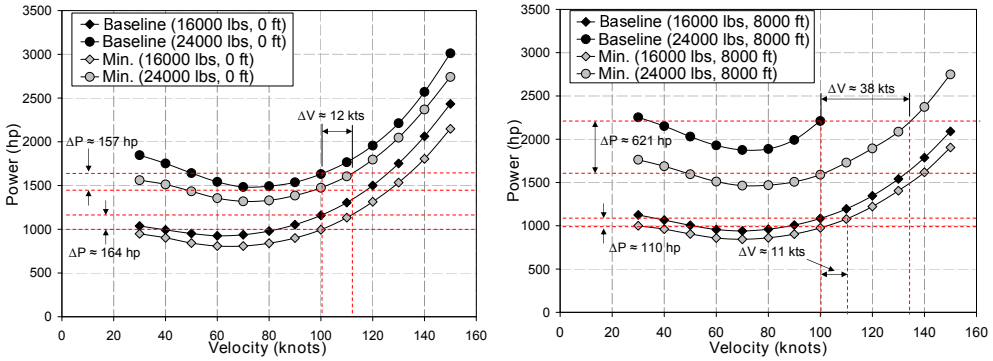

(a) Sea level (b) 8000 ft

Figure 2.23. Power curves for low (16000 lbs) and high (18300 lbs) gross weights at varying altitudes

approximate increase of forward velocity for the same power rating is 12 knots (12%). Correspondingly, for the same forward velocity a power reduction of 164 and 157 hp (14% and 9%) is possible for the respective low and high gross weights. For the case of 8000 ft the power reduction is also approximately constant for the range of forward velocities. However, for the higher gross weight case (24000 lbs) the magnitude of reduction is significantly higher (621 hp). This observation, as mentioned earlier is largely attributed to the rotor stall alleviation which is possible due to the combined variation of RPM and span for the high altitude and gross weight case. For the baseline forward velocity of 100 knots, this observed trends correlate to an increase of only 11 knots (11%) for 16000 lbs and upto 38 knots for the 24000 lbs case. Note that for the baseline radius and RPM case, for 24000 lbs at 8000 ft, aircraft trim condition past the 100 knots case could not be calculated; this convergence issue is another indicator of rotor stall.

$$I_{E_{max}} = (\frac{P_{min_{bas}}}{P_{min_{var}}} - 1)100 \tag{2.5}$$

$$I_{R_{max}} = (\frac{(\frac{V}{P})_{var}}{(\frac{V}{P})_{bas}} - 1)100 \tag{2.6}$$

Another important indicators of aircraft performance is their maximum endurance and range capabilities. Leishman [28] states that the velocity for minimum power corresponds to the maximum possible endurance whereas the velocity

for the minimum ratio of power to velocity corresponds to the maximum possible range. Using these definitions (and the corresponding equations for range and endurance found in Ref. [28]) the percentage increases in maximum possible endurance and range were calculated using equations 2.5 and 2.6 respectively. Note that these equations are based on the assumption of constant total fuel load weight as a function of gross weight and constant specific fuel consumption (SFC) as a function of forward speed.

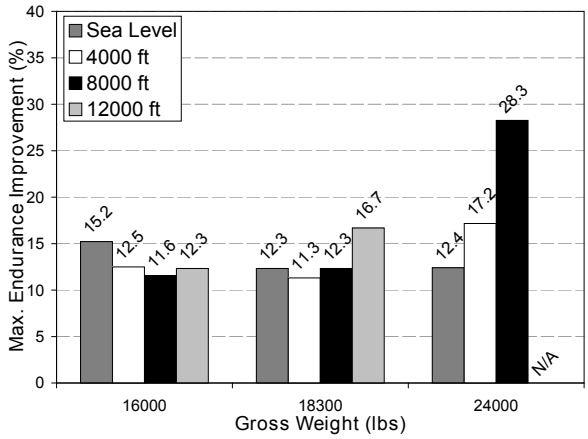

Figure 2.24. Maximum endurance percentage increases for the gross weights considered at various altitudes

Figure 2.24 shows the percentage increases in the maximum endurance for the various altitudes and gross weights considered. Note that the velocity for the maximum endurance ranges between ±10% of 69 knots. Furthermore, due to the assumption of constant fuel weight and SFC equation 2.5 is only a function of minimum power and therefore the trends follow that of the power reduction percentages. For the case of 24000 lbs at 12000 feet, the percentage increases could not be calculated as the aircraft could not be trimmed for the baseline radius and RPM cases past 60 knots.

The calculated maximum range percentage increases for the various gross weight and altitude cases are shown in figure 2.25. The velocities for maximum range were found to be within a range of ±7% about 105 knots As can be seen in the figure, the percentage increases are on the order of the performance improvements for the low (16000 lbs) and mid (18300 lbs) range gross weights for all the altitudes considered. However, for the case of the high gross weight, a significant increase

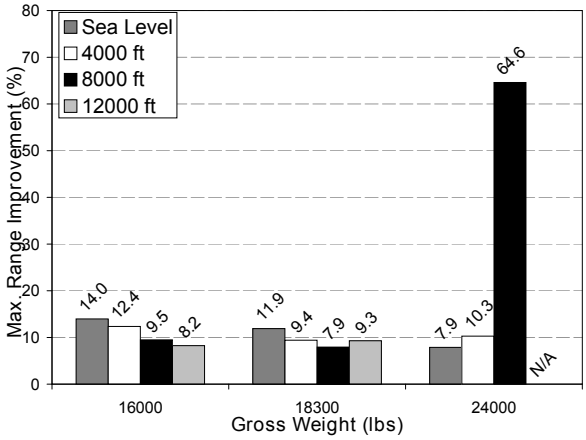

Figure 2.25. Maximum range percentage increases for the gross weights considered at various altitudes

of 64.6% in the max possible range was calculated. This observation, again, is primarily attributed to the power reduction due to the alleviation of rotor stall for this high altitude and gross weight condition. As the aircraft maximum range is a function of the minimum ratio of power to forward velocity and since the rotor is impending stall for the baseline case, variation of the radius and RPM produced a significant improvement as not only was the power required for max range reduced (by 621 hp) but the forward velocity for maximum range was also increased (by 17 knots).

CHAPTER 3

Variable span system design

As shown in the previous chapter, rotor span variation in conjunction with rotor speed variation is capable of significantly improving the performance of helicopters. However, in order to take full advantage of such a system, a mechanical system which is capable of performing adequately needs to be devised. The following section presents the design guidelines used for the variable span system proposed. This is followed by a description and analysis of the various designs considered.

3.1 Design guidelines

As there are a plethora of possible design solutions, a few standard design specifications are set in place, as listed below.

- The blade comprises of only two sections, an inboard fixed section and an outboard sliding section.
- Both inboard and outboard sections are to be aerodynamically viable (i.e., no significant distortion of blade airfoil shape).

- Incorporate guide rails and an emergency restraining device.
- Entire actuation system should be confined within the blade.
- System weight and complexity would be considered in the design.
- Preference is for a passive actuation design.

In the following sub-sections various system designs based on the above standards will be presented and analyzed individually.

3.2 Radius variation design space redefinition

As noted in section 2.3.2.3, for the case of combined variation of RPM and span, the optimal RPM tends to be the lowest within the considered window whereas the radius for most cases is larger than the baseline radius (Fig 2.14). Therefore, from a design point of view, the actuation system would only be required to extend the span (with respect to the baseline). This reduces the required span variation from -16% – $+17\%$, to 0% – $+17\%$. In order to further reduce the design space, understanding the effects of reducing the maximum radius extension possible is important.

Figure 3.1 shows the variation of the maximum power reduction percentage possible for the 100 knots case for all the gross weights and altitudes considered (assuming no reduction of the RPM design space). For the following study the 100 knots case was chosen as it is close to the maximum range speeds for the cases considered (Section 2.3.3.3). As can be seen in the figure, an overall trend is the asymptotic approach of the power reduction to its maximum value as the maximum possible radius is increased. Another important observation is that the trends are pronounced for increasing altitudes and gross weights. However, if the maximum radius increase possible were to be set to 10% of the radius, for most cases the maximum possible power reduction is achievable. Since this design analysis is based on the maximum range velocity, reduction of the maximum possible radius results in a degradation in the possible performance improvements calculated for other flight conditions. This is especially true at the lower range velocities (for all

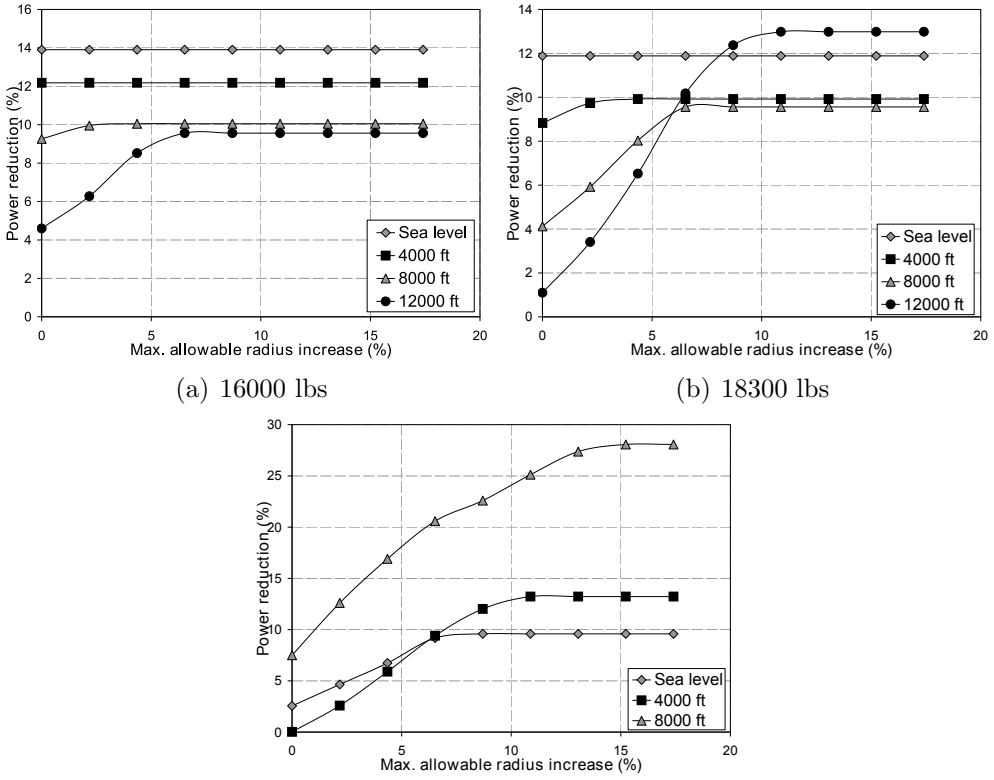

(a) 16000 lbs

(b) 18300 lbs

(c) 24000 lbs

Figure 3.1. Effect of reduction of maximum possible radius extension on power reduction percentages

altitude and gross weight cases) and for high speeds (for high altitude and gross weight cases).

Due to the possible reduction in weight of the sliding section, a second design point for the maximum possible radius of 10% is also chosen. For the following sections Design Case 1 corresponds to a maxmimum possible increase in radius of 17% whereas Design Case 2 corresponds to 10%. Due to the restriction of the design space to only radius increases, the chord, twist and mass distribution of the blade system were re-calculated using a similiar approach to that presented in section 2.2.2. However, unlike the previous analysis, the overlap was set to be a constant of one foot. Based on this analysis the total mass of the outboard sliding section was estimated to be 108 and 95 lbs for the design case 1 and case 2 respectively.

3.3 Blade design mass

The mass of the baseline UH-60A blade is 7.91 slugs (255 lbs). The design of the actuation system is heavily dependent on the weight of the outboard sliding section and therefore estimates of the blade section weights were developed. The originally proposed modified rotor which was capable of achieving a -15% to $+17\%$ change in radius was set to have an estimated outboard sliding section mass of 4.3 slugs (138.5 lbs). This mass value was calculated based on the estimated mass distribution presented in figure 2.5 and as previously stated is based on the baseline blade mass distribution.

Based on the analysis results presented, the radius variation required for the largest possible power reduction can be limited to a range between 0% and +17% as stated in section 3.2. This additional reduction in the range, corresponding to design case 1, results in a decreased mass of the outboard sliding section of 3.36 slugs (116 lbs). Furthermore for design case 2 the estimated mass of the outboard sliding section to be 2.95 slugs (95 lbs). Note that the mass distributions for both design cases proposed are still based on the baseline UH-60A mass distribtution.

3.4 Centrifugal force variation

An important consideration for variable span systems is the centrifugal forces on the sliding sections. Figure 3.2 shows the variation of these forces for the both design cases considered. As expected, increasing the rotor speed results in an increase in the centrifugal force. The deviation bands (vertical bars) presented in the figure show the variation of the forces due to the change in the position of the outer sliding section. As noted in the previous section, for maximum power reductions, the rotor speed was found to be the minimum of the RPM window considered. Therefore, for the active actuation designs, the forces required are limited to the lower end of the range. Note, that the force levels presented are based on the quasi-static analysis of the rotor dynamics and therefore only include the effect of the blade rotation about the main rotor shaft. In addition to the centrifugal forces the flap and lag motion of the blade can increase the total force on the outer-sliding section, but overall these increases represent a small component

of the total force acting on the blade section. Further, since the designs presented in the subsequent sections are preliminary concepts, this assessment of forces based on a quasi-static analysis considering only the centrifugal forces due to blade rotation about the rotor shaft is deemed sufficient.

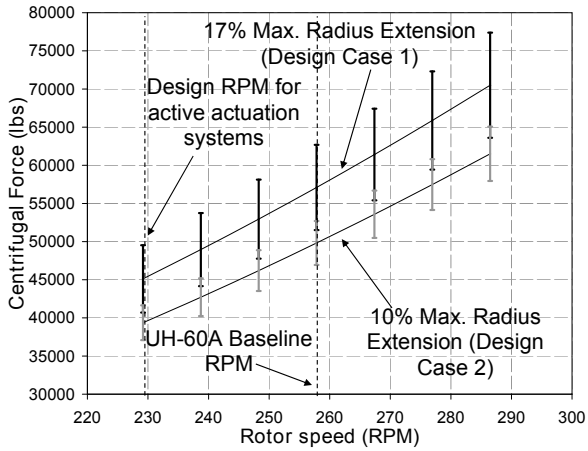

Figure 3.2. Quasi-static range of centrifugal forces required to hold outboard sliding section

Design case 1 corresponds to the outboard sliding section having a mass of 3.36 slugs (108 lbs), whereas case 2 corresponds to 2.95 slugs (95 lbs) as stated in section 3.3. This reduction in mass of the outboard sliding section in conjunction with the reduced spanwise variation results in significantly lower centrifugal forces, as seen in the figure. In particular, the upper range limit of the required centrifugal forces for case 2 are only marginally higher than the lower limit of design case 1. This reduction has the potential of significantly reducing the design simplicity and weight of the actuation mechanism used.

3.5 Blade interface design

As mentioned in section 3.1, a required standard for the proposed design was the inclusion of aerodynamically viable surfaces for both sections. Previous attempts by Prabhakar, Steiner and Gandhi [159, 160] utilized a guide rail on the exterior surface of the inboard blade section, thereby distorting the aerodynamic shape of the section. Whereas work done by the Sikorsky Aircraft Company on the TRAC

[153, 154, 150, 155] and VDTR [154, 151, 156] (Fig. 1.38(b)) rotor systems utilized an inboard elliptical cross-section torque tube. This inboard section while smooth did not provide lifting capabilities. Work done by the Georgian Technical University (GTU) and by Bell Helicopters both utilized aerodynamic surfaces for all their sliding sections and therefore adhere to the above mentioned design standard. However, for the case of the GTU system, the blade design incorporated multiple sliding sections and was specifically designed for tiltrotor type rotors. On the other hand, while the Bell Helicopters Variable Diameter Rotor (VDR) system incorporated smooth aerodynamic surfaces, the blades did not incorporate any specified sliding rails or an emergency restraining device.

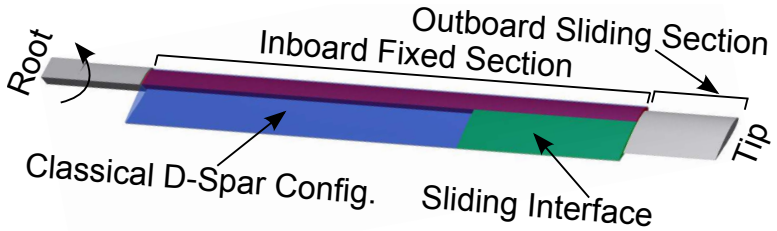

Figure 3.3. Isometric view of proposed variable span blade system schematic

In the current work designs for a variable span system which includes smooth aerodynamic surfaces while including guide rails and an emergency restraining device are considered. Note that the current design is presented as a schematic, detailed design of the structural components was not conducted and therefore not presented. Figure 3.3 shows an isometric view of the proposed design comprising of the two sections: the inboard fixed section and the outboard sliding section. As depicted on the figure, the inboard fixed section is further subdivided into two areas: the classical D-spar configuration section and the sliding interface section. The classical D-spar section follows standard rotor blade manufacturing designs, which comprise of the primary load bearing structure (the D-spar) and a classical honeycomb wafer or nomex foam core filled section aft of the spar web wall. The interface section on the other hand has been adapted to meet the current design specifications.

Figure 3.4 shows the detailed schematic of the sliding interface section of the inboard portion of the blade. This figure focuses on the sliding interface portion

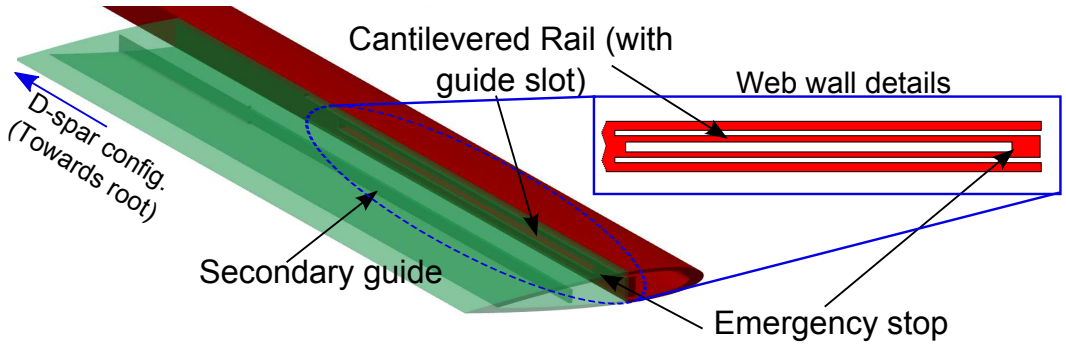

Figure 3.4. Detailed schematic of the sliding interface portion of the inboard fixed section of the blade

of the inboard fixed section of the blade. As can be seen in this figure, the D-spar web wall of the classic blade configuration is extended to a cantilevered rail comprising of a guide grove which terminates with a stop. This portion of the interface slides within the outboard sliding section of the blade, and acts as both the guide rail as well as an emergency stop in case of an actuation system failure. A secondary guide rail is included which provides additional support and is aimed at preventing possible binding issues. This secondary rail works in a similar fashion as the primary, with the exception of a guide slot or an emergency stop. Note that this secondary rail primarily acts as a supporting structure and is not strictly necessary for the operation of the design. In particular, for actuation systems which require additional blade volume this secondary rail can be removed. While the rails act as guides for the outboard sliding section, they also provide an additional load path for transferring the outboard blade section loads to the inboard blade section.

The details of the outboard sliding section are shown in figure 3.5. As can be seen here, in locations corresponding to the primary and secondary rails, a set of vertical walls are placed which interface with the inboard fixed sections. The area corresponding to the primary rail also includes a guide pin which slides along the guide slot and in case of actuation system failure, prevents from the over-extension of the outboard section. The double walls provide both an interface for the rails as well as provide the necessary blade stiffness of the outboard blade section. Overall, while detailed sizing and analysis of the blade components has not been conducted, the presented blade design incorporates the first three design specifications set in section 3.1.

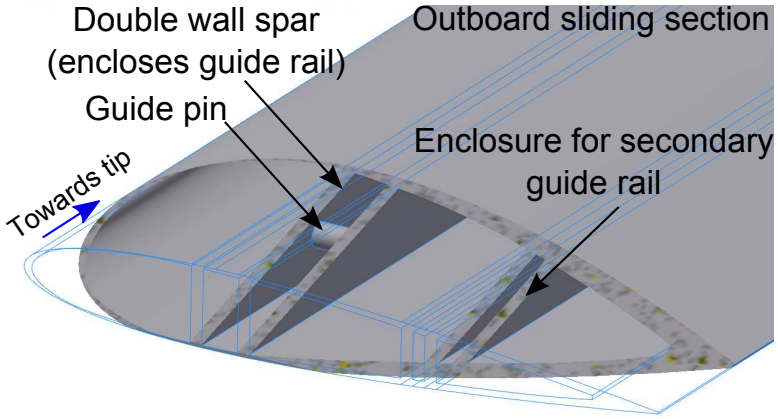

Figure 3.5. Detailed schematic of the outboard sliding section of the blade

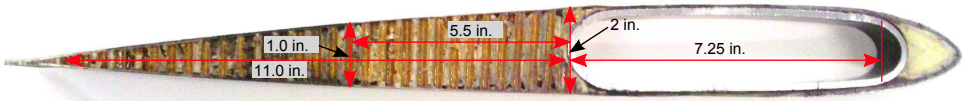

Figure 3.6. UH-60A blade cross-section view

Selection of an actuation system to satisfy the design standard of a completely incorporated system requires consideration of appropriate internal available space within the blade. Figure 3.6 shows an image of the actual cross-section of a UH-60A rotor blade annotated with dimensions of the possible locales for actuator placement. As can be seen in this figure, aft of the web spar, a maximum width of 11 inches with a tapering height ranging from 2 in is available if the secondary rail is not included in the design. The height of this volume reduces in an approximately linear fashion corresponding to a height of 1.0 in at a location 5.5 in aft of the spar wall. Furthermore, a maximum width of 7.25 in (max height of 2 in.) is available within the D-spar itself.

3.6 Actuation systems

A major component of variable span concepts is the actuation system used to realize the variation of the blade radius. A plethora of design options exists, however, in order to satisfy the design standards set in place, four separate concepts were chosen for further analysis. These actuation concepts can be sub-divided into

categories: Active and Passive actuation system. The following sections present the feasibility of such systems with detailed analysis of their capabilities.

3.6.1 Active actuation systems

Active actuation systems are defined as designs which require actuation force and power. Due to the high force levels required in this application, only two possible actuation technologies were selected for further analysis. The first concept involves the use of a hydraulic actuation system, whereas the second comprises the use of a jackscrew/ballscrew. Note, as stated in section 2.3.2.3, as the RPM for minimum power was found to be the smallest in the range considered (229.2 RPM), the centrifugal force requirements are limited to be approximately within 40000 to 50000 lbs for design case 1 and 37000 to 42000 for design case 2 (Fig. 3.2).

3.6.1.1 Hydraulic systems

Considering the high force and stroke requirement of the variable span system, one feasible actuation system would be the use of a hydraulic cylinder/piston assembly to actuate the outboard section. Figure 3.7 presents a schematic of the proposed arrangement of the hydraulic system within the active span system as described previously. Note that in this schematic, the secondary rail is not present to increase the volume available for the placement of the cylinders.

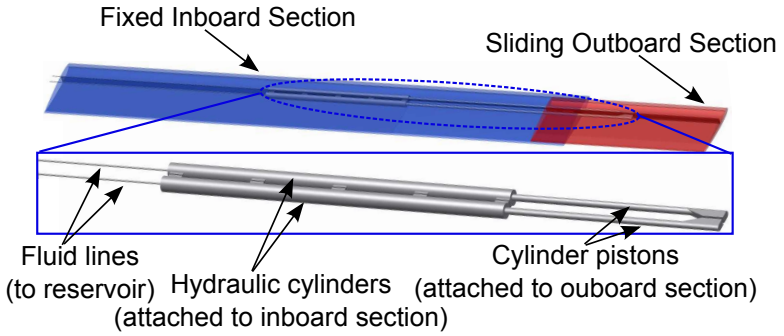

Figure 3.7. Schematic layout of a hydraulic actuation system

The proposed design would comprise of two hydraulic cylinders (to reduce the applied loads on an individual hydraulic cylinder) which are attached to the spar

wall of the fixed inboard section of the blade. The piston ends on the other hand would be affixed to the exterior of the double wall assembly of the outboard sliding section. In this fashion the hydraulic cylinders can be used to specifically position the outboard section at any position within the radius variation range possible. In the current setup the cylinders are intended to be pressurized by hydraulic fluid fed by fluid lines which run along the span of the blade through a hydraulic slip ring into the fixed frame.

In this configuration each cylinder is required to withstand forces in the range of 20000 to 25000 lbs for case 1 and from 18500 to 21000 lbs for case 2 (half of the total centrifugal force requirement). Note that these force ranges correspond to the outboard section center of mass location of 4.6 ft and 2.7 ft respectively (from the inboard side of the outboard sliding section in stowed mode). Since the blade is rotating, the hydraulic system is required to always operate as restraining device. Therefore, for the current layout, the maximum pulling force of the designed actuator is the key design parameter, in particular this maximum puling force should meet the maximum force requirement calculated earlier (i.e., 25000 lbs for case 1 and 21000 for case 2).

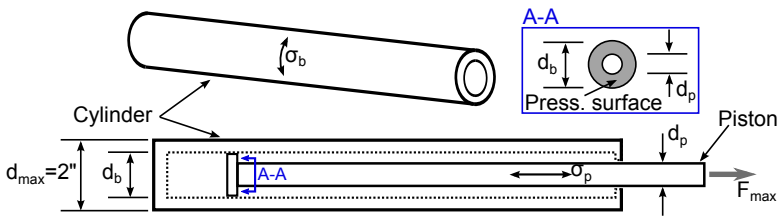

Figure 3.8. Schematic layout of a hydraulic cylinder system with pertinent system parameters annotated

Figure 3.8 shows a schematic of a hydraulic cylinder with pertinent system parameters highlighted. They work on the basis of the force applied by a pressurized hydraulic fluid on the effective piston head surface (as marked in the detail view of section A-A presented in the figure). For the case of pulling force the piston surface is limited to the area between the cylinder bore and the piston diameter. Assuming that the hydraulic fluid is incompressible and the piston/cylinder seal is perfect, the maximum restraining force of the hydraulic cylinder can be calculated using equation 3.1. As can be seen, the pulling force is a function of the cylinder

bore (d_b), piston rod diameter (d_p) and the pressure exerted (p) by the hydraulic fluid. Furthermore, the stresses experienced by the piston rod and the hydraulic cylinder can be calculated using equation 3.2 and equation 3.3 (hoop stress for a cylinder) respectively. Note, due to the restricted space available the maximum outer diameter of the hydraulic cylinder is limited to two inches as is reflected in equation 3.3.

$$F_{max} = \frac{p\pi}{4}(d_b^2 - d_p^2) \tag{3.1}$$

$$\sigma_p = \frac{4F_{max}}{\pi * d_p^2} \tag{3.2}$$

$$\sigma_b = \frac{pd_b}{2 - d_b} \tag{3.3}$$

Figure 3.9(a) shows the variation of the required hydraulic pressure required to obtain the necessary maximum force (25000 lbs) for case 1 as a function of cylinder bore diameter and piston rod diameter. As can be seen, as the cylinder bore diameter is increased, the required hydraulic pressure reduces. This trend is due to the increase in piston head surface corresponding to the increase in bore diameter. In sharp contrast, as the piston rod diameter is increased, the required hydraulic pressure increases exponentially. The latter is due to the corresponding decrease in piston effective surface as the rod diameter is increased.

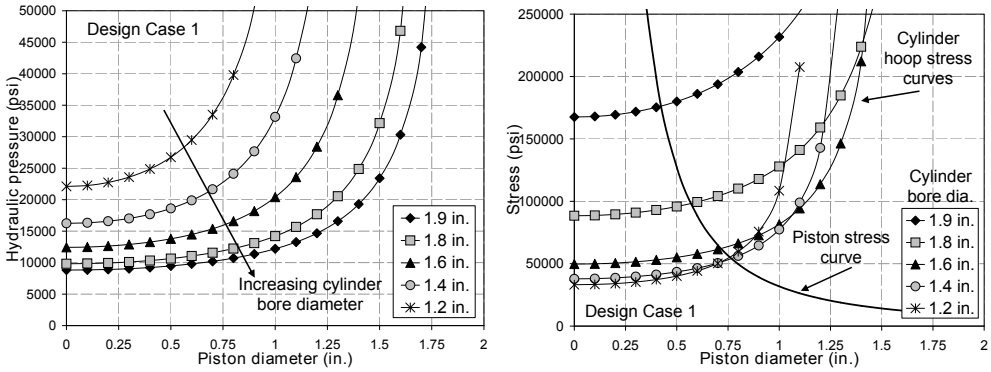

(a) Req. hydraulic pressure variation (b) Stress variation

Figure 3.9. Variation of required hydraulic pressure and piston tensile and cylinder hoop stresses as a function of cylinder bore and piston rod diameters for design case 1

Figure 3.9(b) on the other hand shows the variation of the cylinder hoop stresses and the piston tensile stresses as a function of cylinder bore and piston rod diameters. Note that only a single curve for the piston rod stresses is shown, as it is only a function of the rod diameter as seen in equation 3.2 and not a function of the hydraulic fluid pressure. The figure clearly shows an exponential decrease of the piston stress and an exponential increase in the hoop stresses as the piston rod diameter is increased. Furthermore, decreasing the bore diameter corresponds to a decrease in the cylinder hoop stresses. As seen in the figure the design point corresponding to the simultaneous minimization of both the cylinder hoop and piston tensile stresses is determined to be for a piston diameter of approximately 0.8 in. and a bore diameter of 1.4 in. This design point corresponds to a stress level within both the piston and the cylinder of approximately 51000 psi which is lower than the yield stress of steel (103000 psi). However, the corresponding hydraulic pressure required for this design point is over 10000 psi. The pressure and stress levels follow similar trends for design case 2 (Fig. A.4), with only marginally lower values of required pressure (9500 psi), and is therefore not further discussed in this section.

While this type of system was shown to theoretically be possibly, the hydraulic pressure level required for the design is significantly high. Therefore a design of a corresponding hydraulic slip ring for this pressure level would require a significant structure with large weight penalties. Furthermore, due to the high pressure level the system is prone to leaks at the pressure seals which may compromise the robustness of the system. The current analysis was based on static assumptions, however, when in a rotating environment, the fluid itself would experience centrifugal acceleration and therefore increasing the required levels of pressure. The accuracy of the hydraulic system to precisely place the outboard sliding section can also be an issue as even minute imbalance in the pressure lines for the individual blades can cause differences in the outboard section position.

3.6.1.2 Threaded rod systems

An alternate method of actively varying the radial position of the outboard sliding blade section is to use a threaded rod (Jackscrew/Ballscrew) along with a rotary actuator. Previous efforts to develop variable span rotor technologies have relied

on such a mechanism to achieve the span variation [154, 151, 156, 157, 158]. Such type of systems provide an inherent benefit, in that due to the friction between the thread surfaces the system has a zero energy lock capability (when a jackscrew is used). For the current concept however, to satisfy the design standard of including all the components of the actuation system within the blade, the goal is to include the rotary actuator within the blade itself. In order to do this, the torque required to actuate the threaded rod has to be minimized while maintaining safe stress levels within the threaded rod.

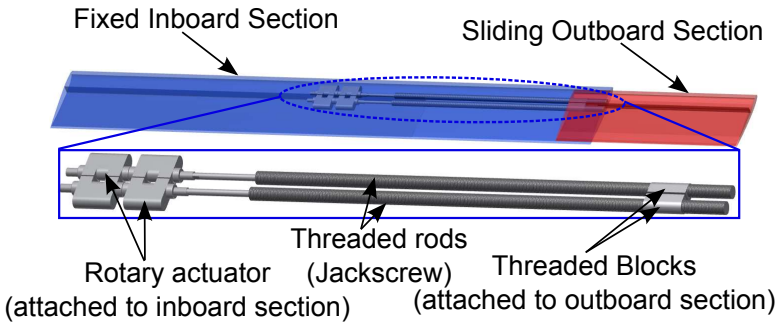

Figure 3.10. Schematic layout of a threaded rod (jackscrew) based actuation system

Figure 3.10 presents the schematic layout of the threaded rod actuation system as conceptualized for the present analysis. As shown, the system can be setup to have two threaded rods (jackscrews) in order to reduce the load on each rod. This setup is expected to reduce the actuation torque requirements. Each threaded rod is affixed on one end to a rotary actuator and on the other end (threaded portion) to a threaded block. The motor is directly attached to the web wall of the inboard fixed section of the blade, whereas, the threaded block is directly attached to the exterior of the double wall of the outboard sliding section. Altogether, the system is setup such that a rotation of the threaded rod by the actuator results in the spanwise motion of the outboard sliding section. Although not shown, cables would be routed from the rotary actuator down through a slip ring into the fixed frame. These cables can both be used to power the actuator as well as to return sensor data for a possible automatic blade position controller. A possible problem with such a system is the binding of the threaded rod due to the unequal actuation of the two rotary actuators. Alternatively, the system can be redesigned with one threaded rod to circumvent the binding issue albeit at the cost of a larger direct

load on the system.

For the purpose of the proceeding analysis, it is assumed that the system would have two threaded rods and as such would require each threaded rod/rotary actuator/threaded block assembly to perform with applied axial forces within the range of 20000 to 25000 lbs for case 1 and from 18500 to 21000 lbs for case 2. The motor selection is based on the maximum levels of the required actuation torque.

$$T_e = F_{max}\left[\frac{\left(\frac{d_{pt}}{2}\right)(\cos\theta_n \tan\alpha_a + \mu_f)}{\cos\theta_n - \mu_f \tan\alpha_a}\right] \tag{3.4}$$

$$T_r = -F_{max}\left[\frac{\left(\frac{d_{pt}}{2}\right)(\mu_f - \cos\theta_n \tan\alpha_a)}{\cos\theta_n + \mu_f \tan\alpha_a}\right] \tag{3.5}$$

$$\begin{aligned}\theta_n &= \tan^{-1}\left(\cos(\alpha_a)\tan\left(\frac{\beta_a}{2}\right)\right)\\ \alpha_a &= \tan^{-1}\left(\frac{1}{\pi d_{pt}}\right)\end{aligned} \tag{3.6}$$

$$\sigma_{tr} = \frac{4F_{max}}{\pi d_{p2}^2} \tag{3.7}$$

Assuming only an axial force is applied on the threaded blocks and using a classical friction model for a single-thread jackscrew, the required actuation torques were calculated for the extension (T_e) and retraction (T_r) of the outboard section using equation 3.4 and 3.5 respectively [190] (supported by equation 3.6). The model further assumes, that the entire magnitude of the axial load is transfered to the inboard fixed blade section via the attachment points of the motor, to clarify this assumption implies the absence of a thrust collar. Note, equations 3.4 and 3.5 are a function of the maximum applied axial load (F_{max}) as well as various properties of the threaded rod (d_{pt} - Pitch diameter, β_a - Thread angle, μ_f - Friction coefficient) and therefore the values calculated are very dependent on the type of thread rod used. Furthermore, since the threaded rods carry the axial load between the inboard and outboard sections of the blade, the tensile stress experienced by the threaded rod also has to be monitored (calculated using equation 3.7). A detailed description and formulation of the model and the pertinent thread properties is

presented by Hamrock et. al. [190].

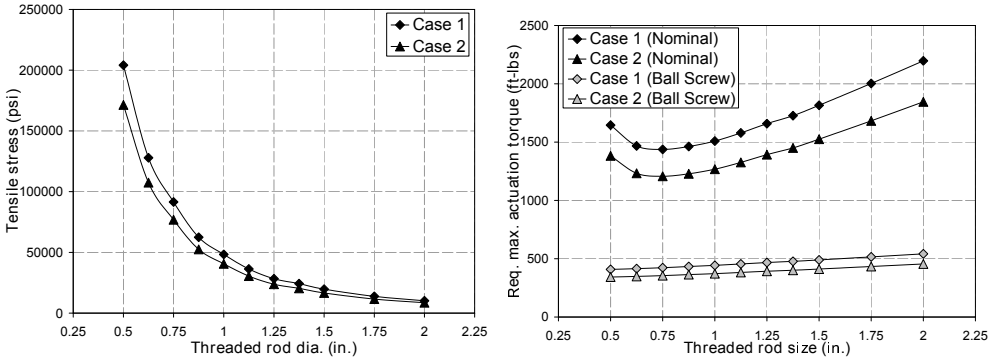

(a) Rod tensile stress (b) Actuation torque

Figure 3.11. Variation of rod tensile stress and required actuation torque as a function of rod diameter for both design cases and different rod operation methods

Figure 3.11(a) shows the variation of the tensile stress experienced by the each threaded rod when undergoing the maximum axial loads for both design cases (corresponding to the maximum deployed position, i.e., 25000 and 21000 lbs respectively) as a function of the threaded rod diameter. The rod diameter values selected in this figure correspond to standard single thread Acme screw sizes [190]. As expected, increasing the thread diameter leads to a reduction in the tensile stress experienced. Note, the nominal yield stress for steel is approximately 103000 psi. For the design to work effectively, assuming the threaded rod is made of steel, the rod diameter has to be at least 0.7 inches. However, for the design to have a safety margin this value would be further increased.

Correspondingly, figure 3.11(b) shows the variation of the required actuation torque for both case 1 and case 2 assuming a nominal thread ($\mu_f = 0.78$ - steel/steel surface) and for a simulated ball-screw type device ($\mu_f = 0.1$). Ball screw type devices have been used previously by Sikorsky Aircraft Co. for their active flap system, albeit for smaller displacements [77]. As shown, for the case of the nominal jackscrew system, the required actuation torque are lowest for a threaded rod radius of approximately 0.75 in and as expected, the torque values for case 2 are lower than that of case 1. Overall, for the simulated ball screw type device, the torque requirement is significantly lower. However due to the reduced thread surface friction these type of devices would require the use of an external lock-

ing mechanism to maintain the position of the blade post actuation which would increase the complexity and weight of the system.

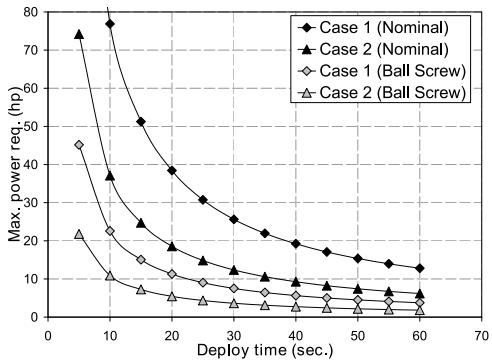

Figure 3.12. Maximum required power as a function of variable span deployment time for both design cases and different rod operation methods

For a thread rod diameter of one inch, which corresponds to stress level which is half of the nominal yield stress of steel, figure 3.12 shows the variation of the required maximum horsepower as a function of outboard blade section deployment time (assuming constant threaded rod rotation speed and no mechanical losses). As can be seen in the figure decreasing deployment time corresponds to increased maximum required power of the rotary actuator. Furthermore, in order for the maximum power required to be lower than 5 hp, the deployment time has to exceed 50 seconds (191 rotor revolutions) for either design cases or for either actuation device (Nominal or Ball Screw). For a lower deployment time of 15 seconds (57 rotor revolutions), the required maximum power increases to a between a range of 51 to 7 hp (depending on the design case and the threaded rod operation type). Based on the analysis due to the high deployment times/high maximum horsepower requirement, for the current variable span configuration a threaded rod actuation system is an impractical solution regardless of the design case or the operation mode.

3.6.2 Passive actuation systems

An alternative to active actuation systems is the use of passive systems, wherein, instead of providing direct power to an actuator to actuate the blade span, vari-

ations in the dynamic or aerodynamic environment are used as the driving mechanism for the span change. Prabhakar et. al. [159, 160] first outlined a passively actuated variable span system directly aimed at powered rotating wing aircraft. The model scale prototype developed in their work comprised of a linear spring which allowed for span variation due to the change in the rotor rotation speed.

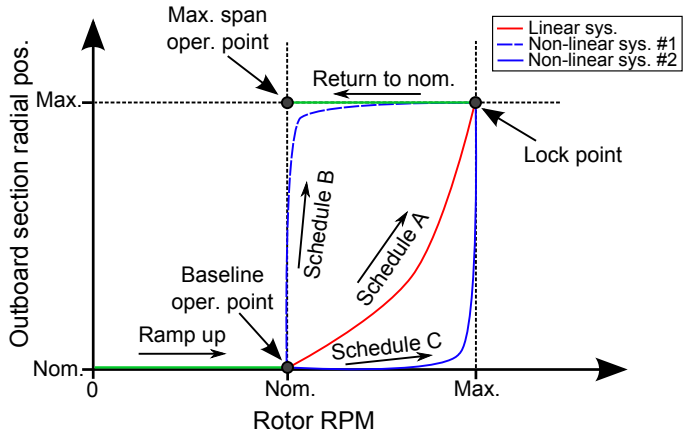

Figure 3.13. Ideal deployment schedule for a passive variable span actuation system

Figure 3.13 shows the ideal representations of three deployment schedules for a passive actuation system based on RPM variation. During the initial ramp up of the rotor from rest to the nominal operating RPM the outboard section ideally would not undergo any extension. However, post the baseline operating rotor speed, the outboard section may take one of three possibly different schedules to achieve the designed maximum radius. Schedule A corresponds to the span variation schedule of a linear spring (this corresponds to the type of system tested by Prabhakar et. al. [159, 160]). Note, while the spring stiffness of the system is linear, the extension as a function of rotor RPM varies in a quadratic manner, since the centrifugal force is proportional to the square of the rotational speed.

Correspondingly if the span were to be varied in a fashion represented by schedule B, the actuation system would need to have a non-linear stiffness. In particular, this type of system can, starting with a relatively low stiffness, have either a progressively increasing stiffness or a bi-linear increase in the stiffness value. Note, this stiffness schedule can be designed such that the variable span deployment schedule is linear as a function of rotor speed. Due to this variation of the system stiffness,

the outboard section, as seen in the figure, would undergo a rapid initial extension followed by a slow asymptotic approach to the maximum spanwise location.

Lastly, schedule C is an alternative solution which also corresponds to a system encompassing a non-linear spring system stiffness where the stiffness is initially relatively high followed by either a progressive reduction, or a bi-linear change to a lower stiffness value. This schedule, unlike A or B, would result in relatively small initial extension in span, followed by a rapid extension to the desired maximum radius location (as shown in figure 3.13).

Upon attaining the maximum radius, regardless of the expansion schedule, the outer blade section would be locked in place and the rotor speed then progressively reduced to the operating value. This last step completes the span variation deployment schedule of the proposed passive actuation system. For the case of stowage on the other hand, the system can be designed to simply unlock the blade position which would cause the blade to retract back albeit in a very rapid motion which may cause blade damage. Alternatively, the RPM may be initially increased to the maximum value following which the blade position is unlocked and the rotor speed progressively reduced to the baseline value, thereby completing the outboard section stowage cycle in a gradual manner.

Schedule A provides the benefit of having a mechanically simple actuation system, in that it requires only a linear spring whose stiffness has to be guaranteed to be the same for all the blades. However, the draw back of such a system is that it requires a significant amount of pre-strain to guarantee the blade extension would only take place for larger than baseline rotor speeds.

Alternatively schedule B, beside providing the benefit of a possible linear change in radius (as a function of RPM), provides no other direct benefit. Furthermore, the design complexity of such a system would increase, as the non-linear stiffness of the system would now need to be precisely defined and be guaranteed for all the blades simultaneously for proper operation in addition to the pre-strain constraint imposed.

Schedule C, similar to schedule B, would incorporate additional design complexity as the non-linearity of the system stiffness would need to be precisely the same for all the blades. However, this type of system, unlike schedule B, can be designed to have a relatively low pre-strain to compensate for the centrifugal

acceleration during baseline RPM operation for the stowed outboard radius.

Based on the design benefits and drawbacks discussed above, due to the additional design complication with no direct benefit of using schedule B, only schedule A and C were selected for further analysis. In the following sections the detailed analysis of three separate passive actuation systems based on selected schedules are discussed. Since the driving component of these concepts is the system stiffness, the primary focus of the presented analysis is on various methods of achieving the desired system stiffness properties and not on the locking mechanism.

3.6.2.1 Schedule A - Linear system stiffness

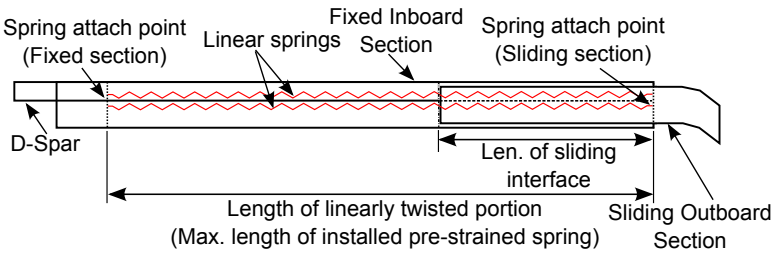

Figure 3.14. Schematic layout of a linear spring based passive actuation system

As previously stated, the primary benefit of schedule A is the simplicity of the required linear system stiffness. A feasible way to achieve this desired stiffness is to use linear springs. Figure 3.14 shows a schematic layout of such linear springs within the variable span blade (assuming two parallel springs) to achieve a schedule A type deployment path. As can be seen for such a configuration, an end of the spring would be attached to the fixed inboard section and the other to the outboard sliding section. Furthermore, as annotated in the figure, the maximum possible length of the installed length of the spring (including pre-strain length) is set to not exceed the length of the linearly twisted portion of the fixed inboard section (14.2 ft). This restriction is set as additional room for the attachment points for the spring and the blade hub interface is required. Although shown for a two spring assembly, based on the available volume estimated for actuator placement (Fig. 3.6) a maximum of four spring may be placed in parallel. The active actuation systems considered would require additional volume for placement brackets for the actuators or other secondary structures and therefore were limited to only two

system in parallel. However, for the case of a linear spring no such additional volume requirement is foreseen with the exception of a locking mechanism which could be potentially placed within the core. Therefore for the current analysis the feasibility of both configurations (two and four parallel springs) will be considered.

$$K_{req} = \frac{F_{max} - F_{bas}}{R_{inc_{max}}} \tag{3.8}$$

In order to guage the feasibility of such a system, the required linear system stiffness was calculated using equation 3.8. As noted, the equation is a ratio of the difference in the required centrifugal force between the minimum and maximum rotor speed cases (for corresponding spanwise locations of the outboard section) and the maximum increment in rotor radius ($R_{inc_{max}}$).

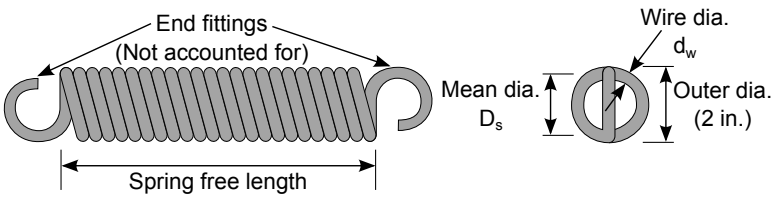

Figure 3.15. Annotated schematic of the helical (coiled wire) extension spring model used in the analysis

The focus of the current analysis is on helical extension springs (made of a coiled wire), an annotated schematic of which is shown in figure 3.15. Assuming a constant spring wire diameter (d_w) and spring mean diameter (D_s) (prevalent design) the installation length (sum of the required pre-strain length and free length) is calculated using equation 3.9 (N_{sp} - No. of springs used, K_{req} - Req. sys. stiff., G - Mat. shear modulus). Note that this length does not include the length of the end fitting of the springs required for attachment. As the spring undergoes extension, the coiled wire undergoes both bending and torsion. The maximum shear stress in the spring wire due to this combined loading is given by equation 3.10 for the maximum deployed length (F_{max} - Max. reqd. centrifugal force). The following equations assume the springs are placed in a parallel fashion. A detailed description of the spring parameters and derivation of the linear spring model is presented by Hamrock et. al [190].

$$L_{inst} = \frac{F_{bas} N_{sp}}{K_{req}} + d_w \left(1 + \frac{d_w^4 G N_{sp}}{8 K_{req} D_s^3}\right) \tag{3.9}$$

$$\tau_{max} = \frac{8 D_s F_{max}}{\pi d_w^3 N_{sp}} \left(1 + \frac{d_w}{2 D_s}\right) \tag{3.10}$$

Helical extension springs are commonly built using various elastic materials, with the most prevalent being high carbon steel alloys. In particular, for high fatigue life and high strength the ASTM-A228 steel alloy is most prevalent [190]. Therefore for the proceeding analysis, the material properties of this high carbon steel alloy will be used (Table 3.1).

Table 3.1. Helical extension spring material properties

Prop. Name.	Value
Material	ASTM-A228 High carbon steel
Elastic modulus*, E (psi)	30.0e6
Shear modulus*, G (psi)	11.5e6
Tensile yield stress$^+$, σ_{yield} (psi)	10.3e4
Shear yield stress^o, τ_{yield} (psi)	5.19e4

$()^*$ - Hamrock et. al. [190]
$()^+$ - Average value [191]
$()^o$ - Based on MSST ($\tau_{yield} = \frac{\sigma_{yield}}{2}$)

Since the nominal operating rotor speed for maximum power reduction was found to be 229.2 RPM (which also corresponds to the minimum RPM considered for this study), only increases of the rotor speed from this value can be used to vary the blade span. A graphical representation of equation 3.8 for both design case 1 and case 2 is shown in figure 3.16. As seen, as the rotor speed corresponding to the maximum radial position is increased so does the required system stiffness. This is an expected trend as an increase in the rotor speed corresponds to a larger centrifugal force requirement (Fig. 3.2). Note that the rotor speed range shown is set for 237.8 RPM and above as this provides a buffer RPM range (between 229.2 and 237.8 RPM) to prevent unwanted deployment.

As the range of required system stiffness varies widely with the RPM for maximum span, for the proceeding analysis only the minimum (238.7 RPM) and maximum (286.5 RPM) rotor speed cases. Note that restricting the proceeding analysis to the ends of the range of rotor speed considered does not affect the conclusions

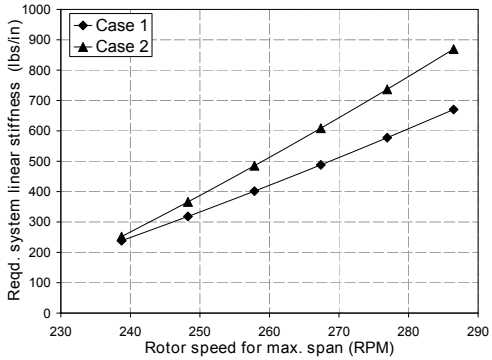

Figure 3.16. Variation of required passive actuation system stiffness as a function of rotor speed corresponding to maximum span

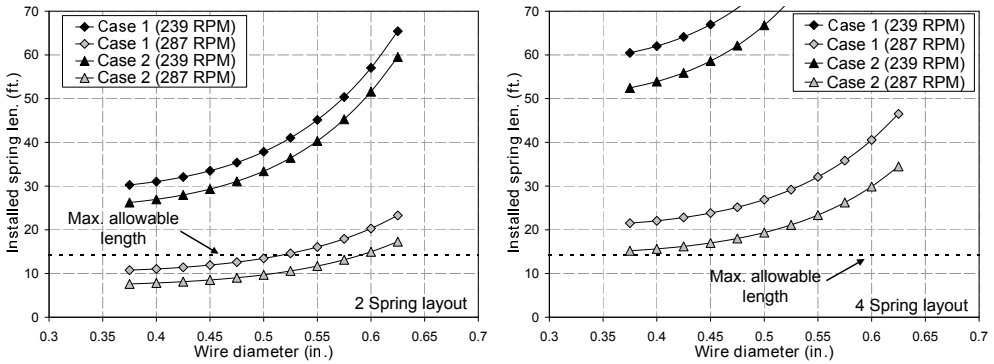

(a) Two parallel springs (b) Four parallel springs

Figure 3.17. Variation of the installed spring length as a function of wire diameter for both design cases considered (at the minimum and maximum rotor speed considered)

drawn (229.2 to 286.5 RPM). The two important consideration for the feasible design of the proposed linear stiffness spring system are the installed spring length (including pre-strain) and the maximum shear stress induced within the wire during maximum radius deployment. In particular, the installed spring length has to be lower than the maximum available length which corresponds to the length of the linearly twisted portion of the inboard fixed section of the blade (14.2 ft). Furthermore, the maximum shear stress induced must be lower than the shear yield stress as calculated using Maximum Shear Stress Theory (MSST) (τ_{yield} = 5.19e4 psi). Figures 3.17(a) and 3.17(b) show the variation of the length of the installed spring (including the pre-strain length of the spring) as a function of the wire diameter for both design cases at the minimum and maximum rotor speeds

considered for a configuration with two and four parallel springs respectively. As seen, for increasing coil wire diameters the installed length increases. As the wire diameter is increased the stiffness provided by a unit coil also increases as the local torsion and bending moment of inertia increased. However, to maintain the required system stiffness the number of coils would have to be increased (as they essentially act as springs in series). The increment of the number coils results in an increased free length of the spring and thereby requiring a larger installed spring length.

Another observation recorded from the figure, is the overall increase in the installed spring lengths for the minimum rotor speed considered (as compared to the maximum case). For the lower rotor speed, as the centrifugal force required variation is smaller the required stiffness is also lower (consider figure 3.16). Therefore, to provide the required centrifugal force for the stowed blade condition at the operating rotor speed (229.2), the required pre-strain length is larger. Lastly, the overall values of the installed spring length were observed to be lower for design case 2 as compared to case 1. This trend is primarily attributed to the reduced mass of the outboard sliding section for design case 2 (as compared to case 1) which correlates to lower centrifugal force values (as seen in figure 3.2).

Also shown in the figures is the maximum allowable installed spring length as defined by figure 3.14. As can be seen, for both design, rotor speeds for maximum span and number of parallel springs considered, this design criteria is satisfied for a very small range of cases. In particular, for wire diameters smaller than approximately 0.52 inches and 0.59 inches for design cases 1 and 2 respectively for the maximum rotor speed considered (two parallel spring configuration).

Figures 3.18(a) and 3.18(b) present the variation of the maximum shear stress induced in the wire as function of the wire diameter for the various design cases and rotor speeds for the two and four spring layout configurations respectively. As seen, increase in the wire diameter results in a reduction of the maximum shear stress. This trend is expected as the torsional moment of inertia increases with wire diameter resulting in lower values of stress. Furthermore, overall larger shear stress values are observed for higher rotor speeds for maximum span. This trend is due to the increase levels of centrifugal forces required of the actuation system at the higher rotor speeds. Correspondingly, increase in the required centrifugal forces

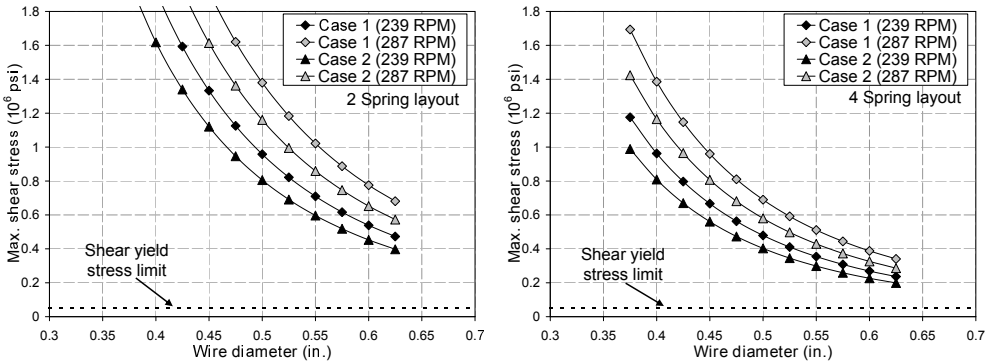

(a) Two parallel springs (b) Four parallel springs

Figure 3.18. Variation of the maximum induced shear stress as a function of wire diameter for both design cases considered (at the minimum and maximum rotor speed considered)

for design case 1 (as compared to case 2) results in subsequent higher induced shear stresses within the wire as seen in the figures. Lastly, the reduced levels of the required centrifugal forces for the reduced mass outboard sliding section, corresponding to design case 2, results in lower induced shear stresses as seen in the figures.

As stated earlier, the maximum shear stresses produced have to be lower than the shear yield stress level for this type of design to be feasible. As shown in the figure, for all physically feasible combinations considered in this analysis, all of the cases result in the plastic deformation of the spring wire. In particular, the maximum shear stress values calculated are significantly higher than that of the tensile yield stress of the material as well.

In conclusion, due to blade actuator placement space constraints and material load limit constraints, the proposed linear spring passive actuation system is not a viable design for the current configuration and materials used. However, such a design may prove to be viable for lighter smaller aircraft (e.g. Unmanned Aerial Vehicles - UAV) and/or with advanced materials which maybe developed in the future.

3.6.2.2 Schedule C - Non-linear system stiffness

Due to the unique stiffness variation requirements of variable span deployment schedule C, and the limited availability of existing solutions, a unique design comprising of bistable structures was developed.

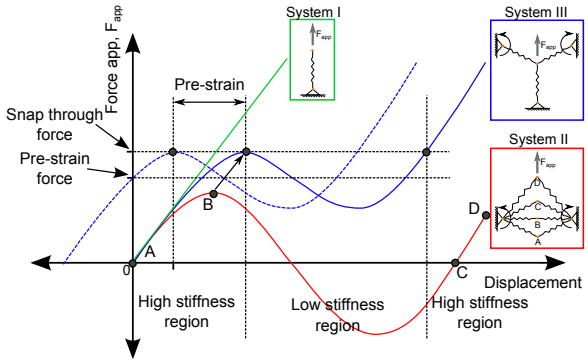

Figure 3.19. Schematic force versus elongation curve of several elastic systems

Figure 3.19 shows a reference schematic of the variation of the force required for actuation as a function of the system elongation for various elastic structures. System I corresponds to a structure with a linear stiffness and as the name suggests portray a proportional relationship between the force applied and the resultant elongation (and vice versa). This type of behavior is portrayed by most engineering materials and is also true for the linear spring used as the basis for a blade span variation schedule of type A.

System II, on the other hand, corresponds to the classic bistable truss. In this arrangement, as can be seen, two linear stiffness systems are diagonally attached such that their unstrained shape corresponds to point A (as marked in the figure). An initial increase in the applied force corresponds to a proportional increase in displacement until point B, which corresponds to the snap through point. At this point, the two spring are in compression and are position in a horizontal line (as shown in the schematic). Post this point, due to the arrangement of the spring, a reduction in the applied force is required for the further elongation of the structure, effectively reducing the system stiffness. This cycle terminates in the second stable state of the structure, as noted by point C. Elongation post this point requires the application of a proportional force and would result in the structure over-extending

(point D).

Lastly, as can be seen, structure III is the classical bistable structure with an additional linear spring arranged in a Y-formation. The addition of the third spring results in the biased behavior of the structure to an applied force. Furthermore, given a sufficiently stiff third spring (relative to the diagonal springs) the bistability of the structure would be completely eliminated, as shown in the figure. However, due to the arrangement of the springs, three separate regions of system stiffness now exist. From the undeformed state to the point of snap through, the system has a relatively high stiffness, as seen in this figure. Post this point, the system exhibits a lower stiffness which is followed by a third range of high stiffness. Note that the addition of a pre-strain on such a structure would only result in a translation of the force/elongation curve to the right with no other property disturbed (snap through force, high and low stiffness region slope). Therefore, to satisfy the unique stiffness requirements set forth, structure III is used as the basis for the proceeding analysis.

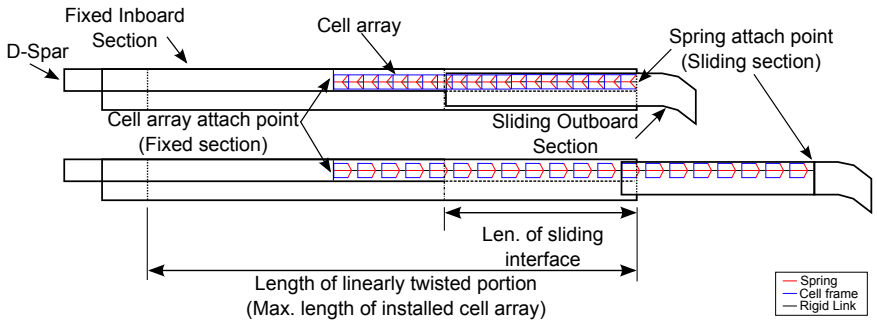

Figure 3.20. Schematic layout of the cell array based non-linear stiffness passive actuation system

Figure 3.20 presents the schematic layout of the proposed passively actuated variable span system. In this configuration, cells comprised of three linear springs in a 'Y' formation (as discussed above) are attached in a serial fashion. An end of this column of cells is attached to the inboard fixed section of the blade, whereas the other end to the outboard sliding section. Note, due to the limited space available, this cellular structure array is only confined to the D-spar section of the blade. As the blade slides the cells undergo translation in the spanwise direction as well. The cells are only intended as restraining devices and as such are not designed to function as a secondary spar.

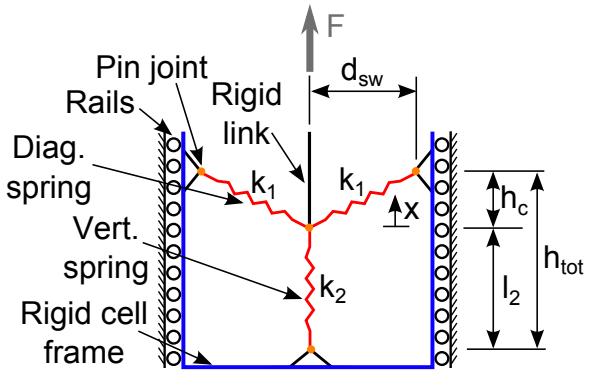

Figure 3.21. Schematic of one cell of the proposed array

A schematic view of a cell, along with pertinent properties highlighted, is shown in figure 3.21. As shown, each spring is pinned at both ends, with the middle junction free to move (primarily in the longitudinal direction as drawn). Furthermore, the fixed ends of each spring share a common frame and therefore are not allowed to move with respect to each other. Note the diagonal springs are constrained to have the same stiffness (k_1). Each spring is only assumed to perform as a simple compression or extension spring, i.e. the cells are not intended to undergo bending. Therefore, the system force/elongation relationship is a function of the geometric position of the junction point only and can be calculated using equation 3.11. In order to satisfy the blade D-spar geometric constraints, the cell semi-width (d_{sw}) is set to be 3.25 inches.

$$F(x) = k_2 x + 2k_1 \left(\frac{\sqrt{h_c^2 + d_{sw}^2}}{\sqrt{(h_c - x)^2 + d_{sw}^2}} - 1 \right) (h_c - x) \tag{3.11}$$

During operation, the vertical spring would only undergo tension and therefore was modeled as simple helical coil extension spring as shown in figure 3.15. Equation 3.12 presents the relationship of such a spring to its wire diameter (d_{sp_2}), material shear stiffness (G) and prescribed vertical spring height (l_2).

$$k_2 = \frac{G d_{sp_2}^5}{8(l_2 - d_{sp_2})(2 - d_{sp_2}^3)} \tag{3.12}$$

However, the diagonal spring undergoes both compression (through the snap through point) followed by extension (during cell over-extension) and is therefore

modeled as such. In particular, the spring solid height (fully compressed height), is constrained to be the cell semi-width, which corresponds to a spring stiffness calculated by equation 3.13 (d_{sp_1} - diagonal spring wire diameter). Note both equations 3.12 and 3.13 include the maximum constraint of two inches for the outer spring diameter (to satisfy space constraints).

$$k_1 = \frac{G d_{sp_1}^5}{8(d_{sw} - d_{sp_1})(2 - d_{sp_1}^3)} \tag{3.13}$$

The cell installed length is the sum of the length of the additional pre-strain required and the free-length of the cell array and is defined by equation 3.14. Note the presented equation is a function of the pre-strained cell elongation (x_{min}) and the cell elongation at the maximum radial location (x_max) as well (ΔR_{max} - Maximum change in radius for the specified design case). These cellular elongation values are calculated using a numerical iterative procedure due to the non-linear nature of the force/displacement curve of the proposed cell spring arrangement.

$$L_{ins} = \frac{\Delta R_{max}}{x_{max} - x_{min}} (h_{tot} + x_{min}) \tag{3.14}$$

Due to the large array of design parameters (i.e., cell, spring and blade system variables) the proposed design analysis was formulated as an pseudo-optimization problem. As such four design parameters, namely diagonal spring stiffness (k_1), vertical spring stiffness (k_2), diagonal spring vertical dimension (h_c), vertical spring height (l_2) and the rotor speed corresponding to the maximum radius (Ω_{max}). The range of the parameters considered are summarized in table 3.2. The objectives of the study was to minimize the passive actuation system installation length (L_{ins}) and the maximum shear stresses induced within the both the diagonal and vertical spring coil wire (calculated based on equation 3.10). As with the case of the linear spring actuation system, for a feasible design the installed length of the passive actuation system cannot exceed 14.2 ft. Furthermore, the maximum shear stress within the spring coils cannot exceed the yield sheer stress of the high carbon steel alloy as defined in table 3.1. A complete description of the spring model and its derivation is presented by Hamrock et. al. [190].

In order to determine a feasible system design, the following primary blade system constraints were defined:

Table 3.2. Cellular array design study parameter ranges considered

Prop. Name.	Min. Val.	Max. Val.	Inc. Val.
Diag. spring height, h_c (in.)	2	8	1
Vert. spring height, l_2 (in.)	2	8	1
Diag. spring stiff., k_1 (lbs/in.)	125	10000	125
Vert. spring stiff., k_2 (lbs/in.)	125	10000	125
Max. rotor speed, Ω_{max} (RPM)	239	286.5	9.5

- The cell snap through force must be greater than and the lower than the apparent centrifugal force experienced by the outboard section when stowed (at operating rotor speed $\Omega = 229.2RPM$) and at the maximum deployed radius position and corresponding rotor speed ($\Omega = \Omega_{max}$, $R = R_{max}$).

- The outboard sliding section must be at the maximum radius position when operating at the prescribed maximum rotor speed ($F = F_{max}$, $x_{sys} = (\Delta R)_{max}$).

Furthermore, a set of constraints to obtain a feasible cell design were also set in place as follows:

- Spring wire diameters (d_{sp_1}, d_{sp_2}) must be smaller than one inch (to satisfy space constraint).

- Prescribed spring stiffness must be guaranteed within defined cell dimensions.

Based on the constraints provided, within the design range considered, multiple solutions were tabulated to satisfy the set design constraints. The process used to calculate these solutions is outlined in Fig. A.5. Figure 3.22 presents multiple views of possible design solutions pareto front calculated for design case 1 and as such represent the best possible family of solutions. The pareto front was calculated using an open source tool developed for matlab [192]. The three axes represent the objective functions used in this analysis (Diagonal spring maximum shear stress - τ_{max_1}, vertical spring maximum shear stress - τ_{max_2} and the installed cell array length - L_{ins}). The ideal solution is represented to be as close to the origin of the presented plot. Note, to improve the clarity of the presented figure, only design points corresponding to installed cellular array lengths lower than 30 ft are shown.

Due to the discretized nature of the parametric analysis and the non-linear effects of the constraints the pareto surface is not continuous. However, a few

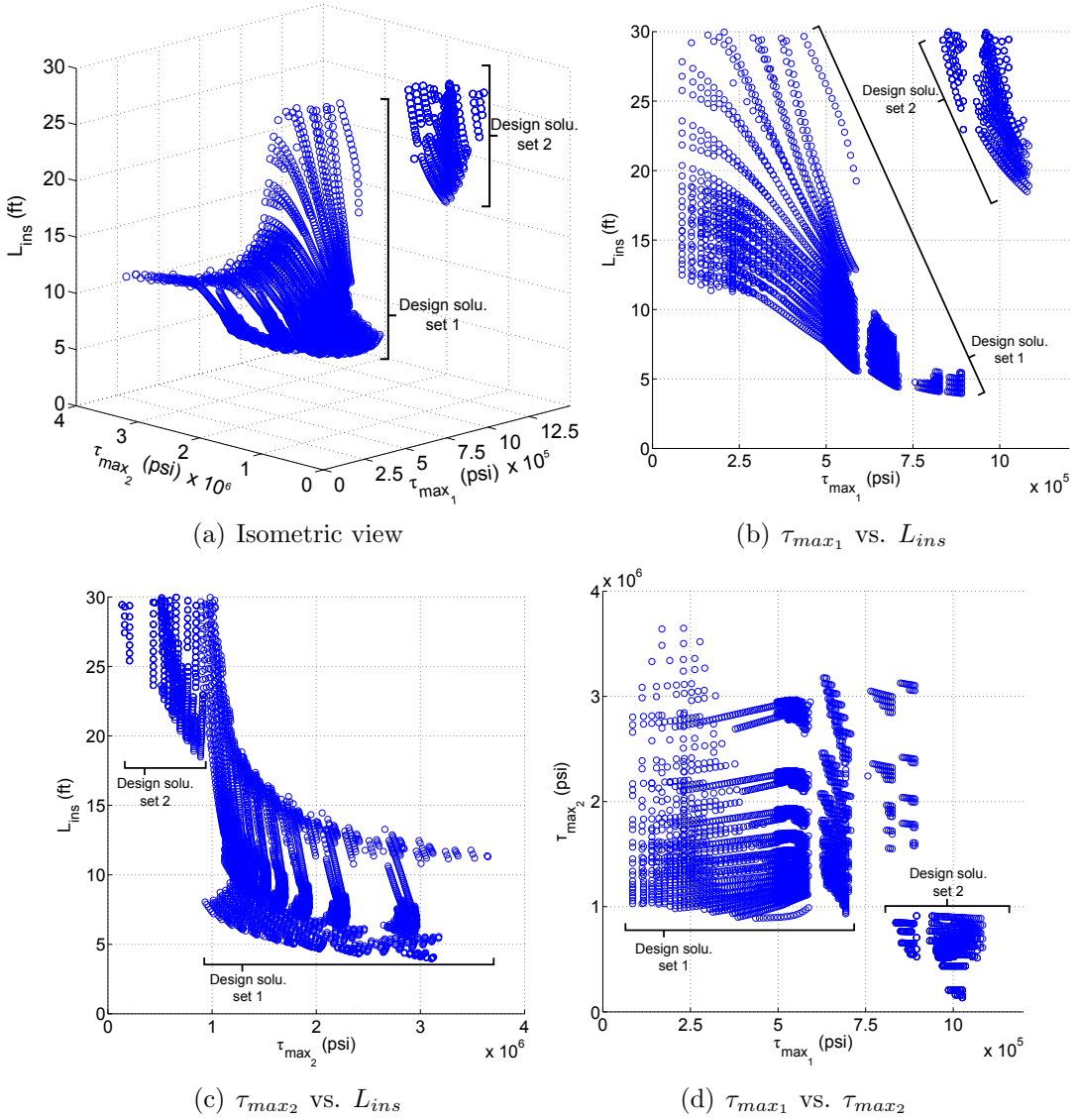

(a) Isometric view

(b) τ_{max_1} vs. L_{ins}

(c) τ_{max_2} vs. L_{ins}

(d) τ_{max_1} vs. τ_{max_2}

Figure 3.22. Multiple views of the design case 1 cellular array solution pareto surface

notable trends are apparent in the figure as well. As can be seen in the figure, the installed cellular array length is a strong function of both the maximum shear stresses induced within the diagonal and vertical springs. In particular the installed length of the array increases in an exponential fashion as the maximum shear stresses within the vertical spring are reduced (Fig. 3.22(c)). However, for the case of the diagonal spring, as the maximum shear stresses are reduced the maximum installed length of the array increase to an asymptotic limit (Fig. 3.22(b)). For the

case of the maximum shear stresses induced within the springs, no clear dependence is apparent as see in figure 3.22(d). Overall, as can be seen in the figure, there exists a multitude of solutions which are shorter than 14.2 ft. However, as also seen in the figure for all the possible design solutions tabulated neither the maximum shear stress within the vertical nor diagonal spring is lower than the yield shear stress of the high carbon steel material for the design variable range considered.

As marked in figure 3.22(a), the pareto surface solutions were observed to group into separate solution sets. Furthermore, the division shows the second set to incorporate designs solutions which would allow the lowest level of the maximum induced shear stresses within the vertical spring (Fig. 3.22(d)). However, this set of design solutions also result in the highest levels of maximum shear stresses within diagonal springs as seen om the figure, along with high installed spring lengths (Fig. 3.22(b)).

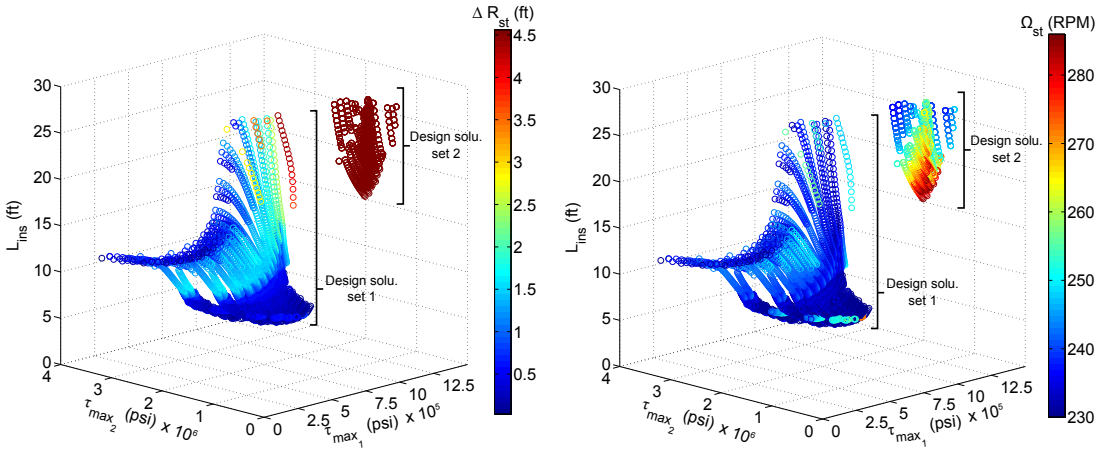

(a) ΔR_{st} variation (b) Ω_{st} variation

Figure 3.23. Design case 1 solution pareto surface isometric views with ΔR_{st} and Ω_{st} variation highlighted

Figure 3.23 presents isometric views of the pareto surface well with the variation of the change in radial position at which snap through of the cell array occurs (ΔR_{st}) and the critical rotor speed at which the snap through occurs (Ω_{st}). Note the value of Ω_{st} can only be between the minimum (229 RPM) and maximum rotor speed (286.5 RPM) considered. As can be seen in figure 3.23(a), the second design set corresponds to cases wherein the snap through occurs at the larger limit

of the radial position change ($\Delta R_{st} = \Delta R_{max} = 4.6ft$ (Design case 1)). However, the first data set corresponds to design solutions wherein the snap through occurs with minimal change in radius.

Correspondingly, for solutions within the first set, the snap through occurs at the lower limit of the range of rotor speeds considered as seen in figure 3.23(b). However, the second solution set has a wider of range snap through rotor speeds as clearly seen by the spread presented in the figure. Note, for the lowest shear stress levels within the diagonal spring, lower snap through rotor speed and change in radial location is preferred. As noted the distinction between the two sets corresponds to the magnitude of the change in the radial position of the outboard section where the snap through occurs. Due to the high maximum shear stresses induced within the diagonal spring for the second design set, the respective design solutions are not viable and will therefore not be further discussed.

Figure 3.24 presents the isometric view of the pareto surface corresponding to design case 1 with variation of the corresponding design variables. As highlighted by figures 3.24(a) and 3.24(b) for the first design set, the variation in either diagonal (k_1) or vertical spring (k_2) stiffness has a negligible effect on the maximum shear stress induced within the vertical spring stiffness. However, for the cases of lower maximum shear stresses within the diagonal springs, a combination of soft vertical spring and stiff diagonal spring is preferred. Note that this is also the combination that corresponds to the lowest possible installed cell array length. Recall design solutions corresponding to this range correlated to cases which required the lowest snap through rotor speed and radial location change (Fig. 3.23).

As stated earlier, the snap through force of the cell is restricted to be between the ranges of the corresponding minimum and maximum apparent centrifugal forces experienced by the outboard section and therefore requires an initial system stiffness. For design solutions with soft vertical springs, the diagonal spring array is required to compensate. As stated in equation 3.11, the component of the total spring force contributed by the diagonal springs is proportional to the diagonal spring vertical height and spring stiffness. Therefore, as seen in figure 3.24(c), for the range of high diagonal/low vertical spring stiffness, the diagonal spring height (h_c) varies widely. Due to the high possible snap through force because of the high stiffness of the diagonal spring, a higher initial stiffness is possible,

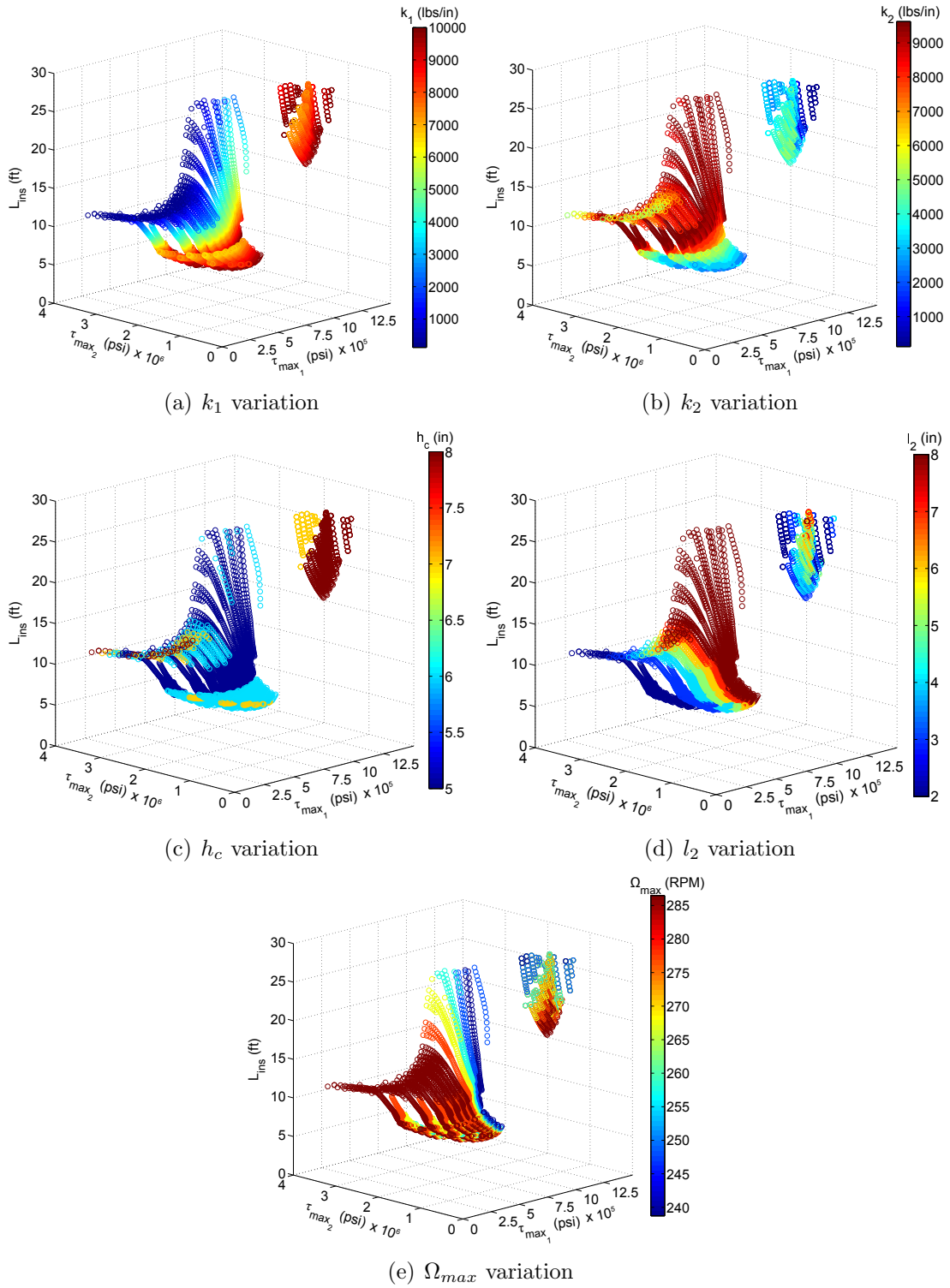

(a) k_1 variation

(b) k_2 variation

(c) h_c variation

(d) l_2 variation

(e) Ω_{max} variation

Figure 3.24. Design case 1 solution pareto surface isometric views with design parameter variation highlighted

which results in lower installed lengths of the cell array (due to the lower required pre-strain).

Figure 3.24(d) presents the vertical spring height variation for the pareto surface design solutions. The variation of this property, as shown has a minimal effect on the maximum shear stiffness induced within the diagonal spring (for the first design set). However, increases in the vertical spring height correspond to decreases in the vertical spring induced shear stress at the cost of increased installed cell array lengths. As the vertical spring length is increased, the free length of the cell array increased (due to increased in the cell height h_{tot}) which correlates to the increases in the installed length (L_{ins}).

Lastly, as seen in figure 3.24(e), overall, the rotor speed corresponding to the maximum radius is preferred to be close to 286 RPM (corresponds to the upper limit considered). However, as also seen in the figure, for lower values of the rotor speed the induced maximum shear stress within the vertical spring also reduced (albeit at the cost of increased installation length). Note the maximum shear stresses induced within diagonal spring, however, are relatively unaffected by the variation by the maximum radius rotor speed.

As shown, design solutions for which the installed length was lower than the maximum available (14.2 ft) are possible. However, for all of the design solutions tabulated, none were capable of reducing the maximum shear stresses induced within the either spring (diagonal or vertical) below the shear stress yield limit of the high carbon steel material used. Therefore, the limiting factor for this design is not space constraints, but rather the material properties.

The pareto surface corresponding to the solutions for design case 2 also follow similar trends as design case 1 (Fig. A.6). The solutions tabulated showed an overall lower installed length requirement. However, only marginal reductions in both the diagonal and vertical maximum induced shear stresses were calculated (for the corresponding design solutions) and therefore the pareto front is not presented in this section.

3.6.3 Actuation system scaling

Based on the presented results it is observed that the current actuation concepts are not feasible for a full scale aircraft similar to the UH-60A or larger. The primary issues for each of the proposed solutions stems from the centrifugal forces that the actuation system has to withstand. These forces are the result of the combined effect of the centrifugal field the rotor system operates in and the the mass of the outer sliding section.

Prouty [193] states that the mass of the blades is a strong proportional function of the aircraft gross weight (among other parameters). Therefore as the aircraft gross weight is scaled down so will the mass of the blades and hence the mass of the outboard sliding section. Correspondingly, however, assuming that the tip speed is kept constant, the centrifugal acceleration would also increase, for e.g. if the radius is halved for the same tip speed the centrifugal acceleration at the tip will be doubled. Overall, however, the centrifugal forces withstanding capability requirement of the actuation system would reduce and this is what may allow the proposed systems to become more feasible for smaller aircraft. Note while this is a general statement, each concept would need to be individually analyzed for smaller aircraft to ensure feasibility.

CHAPTER 4

Variable camber system performance analysis

The sections presented in this chapter explain the concept of the variable camber system developed. Furthermore, the sections will also cover the aerodynamic effects of such airfoil morphing. This is further followed by the effectiveness of such a system on an edge-wise rotor system in hover.

4.1 Design Concept

While the focus of the current body of work is on the application of a variable blade camber technology for a morphing rotor aircraft, the genesis of this concept can be traced backed to variable twist rotors and as such a discussion of this rotor morphing technology is important. Variable twist technology can be implemented one of two different ways, the first being high frequency actuation, wherein the blade twist is varied at a rate in the order of N-1,N,N+1/rev with relatively low amplitude (usually less than 3-4 deg.). This type of actuation is applicable for

noise and vibration reduction of rotating wing aircraft. The alternate to this type of technology is the quasi-static variation of the blade twist, wherein the blade twist is varied at a much lower frequency (less the once per revolution) albeit for higher amplitudes (10 deg. and greater).

There exist a plethora of concepts which have been significantly explored by academia, the government and industry alike for the high frequency blade twist variation. The most prominent of which being the work done with Active Fiber and Macro Fiber Composite (AFC and MFC) actuators (Sec. 1.2.2.1). Comparatively, however, there has been very limited focus on quasi-static variable twist blade technologies (Sec. 1.2.2.2). The focus of the current concept is on the development of a quasi-statically actuated technology for edge-wise rotors. However, such a technology may potentially also applied to any rotating wing vehicle type including tiltrotors.

The majority of the solutions proposed for quasi-statically twisting rotor blades included the use of an actuator to introduce a torque (either distributed or discrete). In particular, the state of the art quasi-static rotor blade systems (Reconfigurable Rotor Blade program) utilize a Shape Memory Alloy (SMA) based actuator to produce spanwise twist of the blade. Although significant resources were dedicated towards the development of the actuator, minor modifications were made on the blade structure itself. This was done primarily to maintain the blade stiffness (in particular the torsion stiffness). Due to this design choice the actuators were only capable of producing a tip twist of 2-3 degrees for model scale rotor blades. The concept presented in the following sections, therefore, unlike the majority of previous designs, considers the redesign of the blade cross-sections itself. In particular the concept utilizes the unique warp-twist relationship of beams to introduce the required blade deformation.

To illustrate, this warp-twist relationship further, consider a slender (length is at least ten times the maximum cross-section dimension) cantilevered beam with an applied tip torque as shown in figure 4.1 (closed rectangular cross-section). As expected, under such a torque load, the beam would undergo a macro scale twisting deformation. However, along with with the twisting deformation, the local cross-section of the beam also undergoes an out-of-plane deformation in the spanwise direction. This local cross-section displacement is what is commonly re-

ferred to as warping and is especially pronounced for thin walled beams (maximum cross-section dimension is over 10 times beam wall thickness). Note the warping deformation shape of the beam is purely a function of the cross-section shape for thin walled slender beams while the magnitude is purely a function of the load.

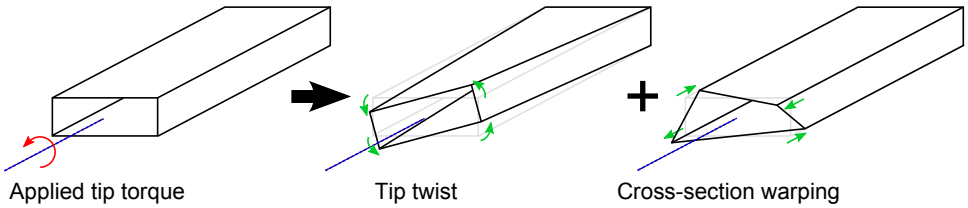

Figure 4.1. Closed section beam twist kinematics

If the same slender thin-walled beam were to be cut at a point on the cross-section through the entire length (Fig. 4.2) it would now behave as an open-section beam. This results in a significantly lower beam torsion stiffness as compared to the closed-section counterpart. Furthermore, the warping displacement shape would also vary significantly, as illustrated in the figure. In particular, the warping shape would now be discontinuous at the point of the cut (Fig. 4.2). As stated earlier, the twisting of the cross-section and the corresponding warping, as presented, is due to the application of a tip torque. However, an introduction of warp inducing cross-section forces would also correspondingly produce a twisting of the cross-section. The primary benefit of twisting a beam in such a manner relates to the relatively simple linear input actuation.

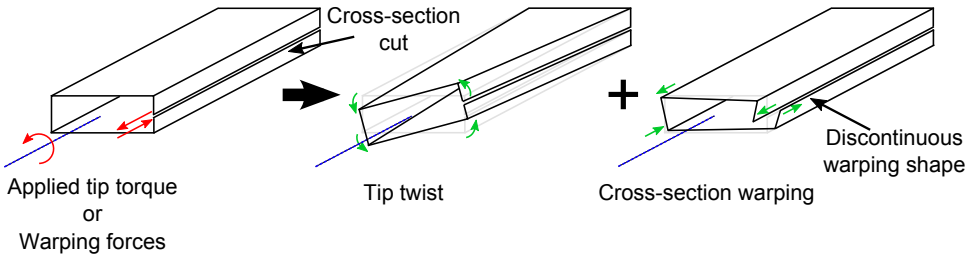

Figure 4.2. Open section beam twist kinematics

This basic warp-twist relationship of beams is the underlying physical mechanism used by Mistry et. al for a concept for quasi-statically varying the blade twist [20] (Fig. 4.3(a)). The design incorporates an airfoil shaped blade skin shell which

is slit at the trailing edge. This skin is affixed to ribs in a manner which allowed for the free sliding of the skin in spanwise direction, while restricting motion in the chordwise plane. Furthermore, the ribs themselves were allowed to rotate about a circular spar without being allowed to move in the spanwise direction.

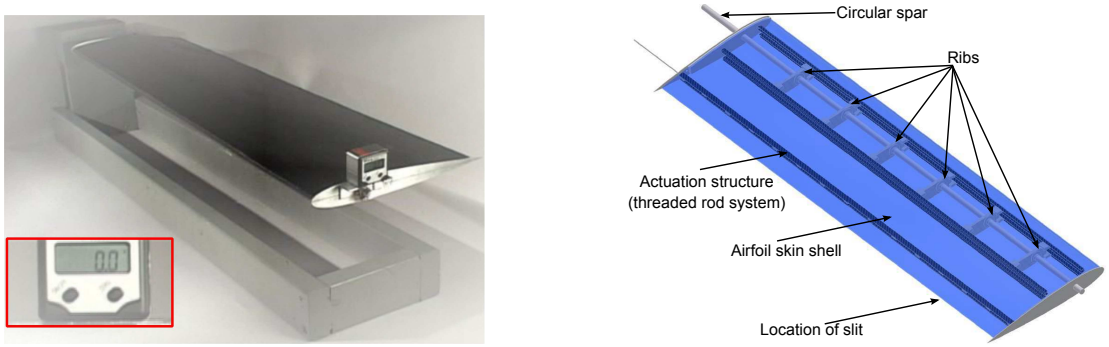

(a) Prototype (b) Design schematic

Figure 4.3. Warp induced blade twist prototype and design schematic [20]

As stated, open section beams are generally torsionally softer than the closed-section counterparts, therefore the loss of the stiffness due to the slit at the skin trailing edge would need to be addressed. For this particular warp-twist blade design, a threaded rod mechanism running along the span in proximity of the trailing edge and attached to the inner surface of the top and bottom of the airfoil skin shell (Fig. 4.3(b)) at regular intervals was used. This design feature, allowed for the prescribed warping of the skin in a manner similar to that of an open section beam, however, when not actuated the skin would behave as a closed section beam. In particular, the airfoil skin shell torsion stiffness is now directly related to the axial stiffness of the actuation mechanism as it prevents the unactuated warping of the cross-section. Due to the unique re-design of the blade, a prototype device based on the prescribed design was able to show a variation of ± 16 degrees of tip twist for a maximum input warping actuation of 0.15 in.

However, while the design presented by Mistry et. al. was shown to be capable of producing large twist variations, it also incorporates significant inherent risks. The primary risk is related to the blade bending and torsion stiffness which are now decoupled. In particular, the blade bending stiffness is contributed primarily by the circular spar. Therefore, for a full scale design the spar diameter would need

to be impractically large (and heavy) in order to have the appropriate stiffness to withstand the aerodynamic and dynamic forces experienced by the blade section. Furthermore, as the skin is allowed to rotate about the circular spar, it is the primary source of the blade torsion stiffness. Correspondingly, in order to obtain the appropriate stiffness required for a full scale design, the airfoil skin thickness would need to be increased significantly, effectively making it a thick walled beam thereby increasing the force required for actuation.

The secondary risk relates to the actuator structure itself, in particular with its axial stiffness and its placement. As the airfoil skin shell is a large contributor of the blade torsion stiffness, the actuator axial stiffness would need to be sufficiently large to provide the required resistance to warping due to external twisting loads. Furthermore, as the actuator structure is placed at the trailing edge it poses two major issues, the first being the shift of the blade center of gravity further aft due to the mass of the actuator which relates to significant blade dynamic instabilities. The second issue, is in regards to the volume constraints of placing an actuator in the confined locale of the trailing edge. Note the center of gravity shift can potentially be compensated for via the use of leading edge weights, albeit at the cost of increased blade weight.

Therefore, in order to scale up the concept of a warp induced variable twist blade system significant revisions to the design would need to implemented. Rotor blades cross-sections are generally comprised of two cells: the D-spar cell and the airfoil shaped cell aft of the spar web wall. The D-spar cell is designed to be the primary load bearing structure of the blade and as such provides the majority of the blade stiffness (both bending and torsion). Based on the risks associated with the original design two major design revisions were pursued in the current work:

- The D-spar cell is intact (no cuts through the cell walls)
- The slit is placed on the bottom skin just aft of the D-spar web wall

The first design revision is incorporated to abate the risk associated with the required full scale blade stiffness. Whereas the second design revision is introduced to overcome the challenges related to the actuator structure design and placement. Due to the incorporation of this design revisions, the system would now produce a

variation of blade camber instead of the direct variation in blade twist (Fig. 4.4). This is the idea which is further explored in the current work.

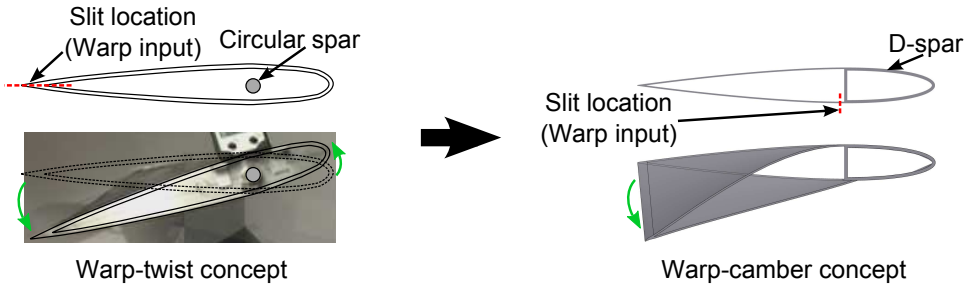

Figure 4.4. Comparison of warp-induced twist and camber concepts

Figure 4.5 shows the proposed layout of a rotor blade incorporated with the presented active camber concept. As seen in the figure, active camber can be incorporated both at the root or the tip of the blade for only a partial length of the blade. It can also be incorporated over the entire length of the blade span, albeit at the cost of increased system weight and design complexity. As the proposed system utilizes the warp-twist relationship of open section beams, the introduction of cross-section warping would relate to an approximately linear distribution of the blade camber through the active section. As such for partial span active camber blade systems, the system would be designed such that the blade cross-section continuity is maintained (i.e. cross-section has no camber at active section end). This would require the top skin to be integrated with the passive section of the blade while the bottom skin is slit along the chordwise direction to allow for spanwise motion.

Since the proposed design revision would cause a change in blade camber rather than direct blade twist, the direct aerodynamic effects of such a cambered airfoil section and its potential benefits on the rotor system need to be examined. The proceeding sections present the camber changes from a structural stand point followed by the aerodynamic effects at the airfoil level. Following this, the effects of the active camber technology on a BO-105 type rotor system in hover is examined (preluded by a description of the rotor model used in the study).

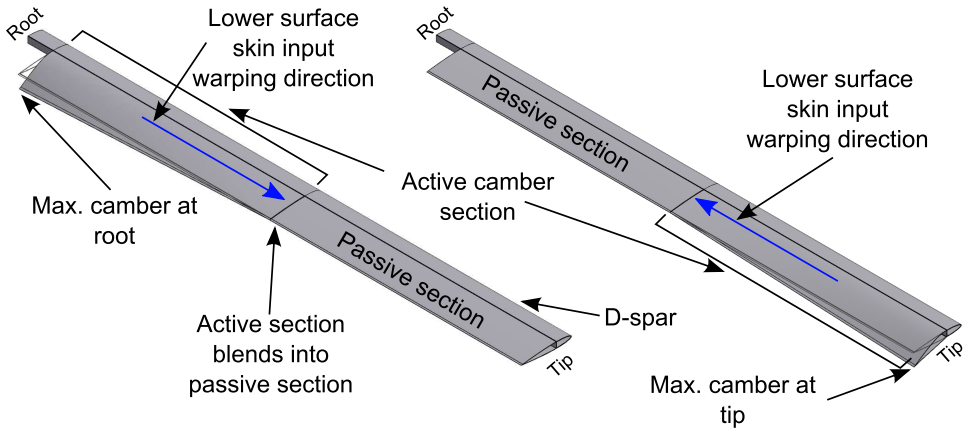

Figure 4.5. Proposed variable camber system layout

4.2 BO-105 rotor model

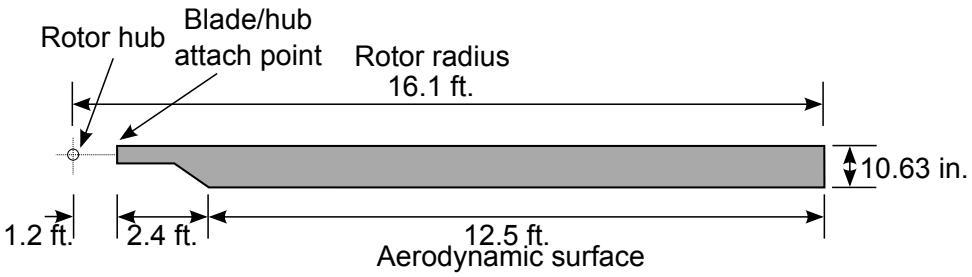

Figure 4.6. BO-105 blade schematic [22]

Figure 4.6 presents a schematic of the baseline BO-105 blade planform [22]. As indicated in the figure, the baseline BO-105 rotor system has a 16.1 ft radius and a constant 10.63 inch chord. The blade incorporates a linear twist distribution of -8 degrees and uses a NACA 23012 airfoil. Note that due to the airfoil cut off and the blade root/hub interface, the aerodynamic portion is limited to the outer 12.5 ft of the blade. Due to the relatively simple baseline blade planform, this rotor type provides the ideal configuration on which an active camber system can be applied. Table 4.1 presents key properties of the the BO-105 type rotor model used in the current study. The BO-105 has a total installed power of 840 hp (at sea level),derived from the two installed turbines.

The rotor blade properties including, but not limited to, the blade mass and

Table 4.1. BO-105 rotor properties

Prop. Name.	Min. Val.
Radius	16.1 ft
Aerodynamic surface length	12.5 ft
Root Cut out	3.6 ft
Chord	10.63 in.
Baseline Twist (linear)	-8 degrees
Baseline Rotor speed	421 RPM

stiffness distribution is based on the data presented by Staley [194]. As the baseline BO-105 blade has a C-spar type internal structure, the representative blade cross-section used for the current analysis is based on BK-117 aircraft as it includes a two cell cross-section (Fig. 4.7(a)). Therefore, the blade cross-section presented in figure 4.7(b) is used for the proceeding analysis (internal layout dimensions are based on ratios of corresponding locales of the BK-117 rotor cross-section). As shown in the figure, the slit was placed just aft of the spar web wall and therefore only the highlighted section of the cross-section is expected to undergo deformation. Note, although the BK-117 blade cross-section (Fig. 4.7(a)) shows a filled cross-section, for the proceeding analysis the aft cell of the representative cross-section is assumed to have no filler.

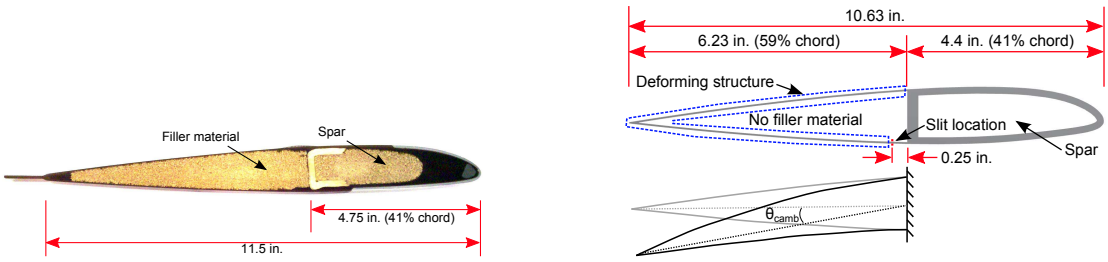

(a) BK-117 cross-section

(b) Proposed cross-section

Figure 4.7. Representative (BK-117) and proposed blade cross-section

4.3 Warp-camber relationship

In order to determine the effects of the camber on the airfoil aerodynamics, the basic cambered shape of the cross-section due to warping would need to be identified.

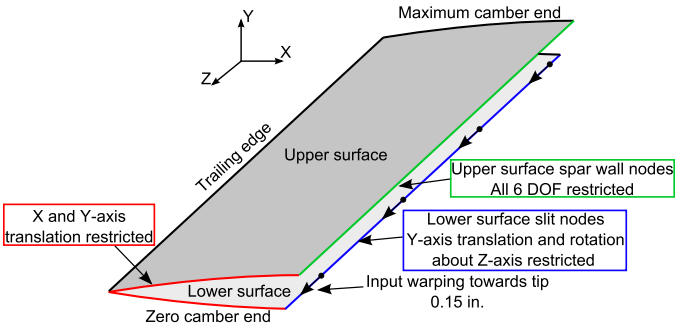

Figure 4.8. Finite element model schematic with boundary conditions annotated

As stated earlier, the warping shape is a function of the beam cross-section only. As such, the cross-section deformation due to the input warping can be determined using arbitrary material properties. Furthermore, since the active section involves deformation aft of the web spar, only the highlighted section in figure 4.7(b) is pertinent to the analysis. Figure 4.8 presents a schematic of the active section of the blade. A Finite Element (FE) model (ANSYS® Ver. 12.1) of this section was developed using shell elements which incorporated four nodes each with six degrees of freedom for the partial span case (6.25 ft). Based on the expected implementation, boundary conditions were applied as listed below (graphically represented in figure 4.8).

- Zero camber end nodes constrained to move only along spanwise axis.
- Model upper skin surface web wall nodes restricted in all six degrees of freedom.
- Rotation about spanwise axis and vertical motion restricted for model lower skin surface slit nodes.

The zero camber end constraint is intended to emulate the interface between the active and passive section of the blade which would ensure the smooth variation of the cross-section shape through the blade. The upper skin wall nodes are restricted for all six degrees of freedom (DOF) as this represents the transition to the skin which wrapped around the D-spar itself, which in itself is assumed to be rigid for this analysis. The rotation about the spanwise axis (Z-axis) of the lower surface slit nodes is restricted to emulate the actuation system which would ensure smooth

deformation of the skin across the slit interface. Lastly, the vertical axis (Y-axis) motion of the slit nodes is also restricted to again emulate the presence of an actuator system which would prevent peeling of the two ends of the slit.

Furthermore, the lower surface slit nodes were constrained to move a maximum of 0.15 inches (towards the zero camber end along the spanwise axis). The material properties and thickness properties are irrelevant since the objective is to determine the deformed shape and not the force required. However, for the finite element model a material stiffness of 10.3e6 psi was used along with a skin thickness of 0.125 inches. Furthermore, the element width was uniformly adjusted to be an average 0.1 inches. The model was evaluated using the ANSYS®non-linear solver which accounts for large displacements (to capture any geometric non-linearities due to deformation). The camber (θ_{camb}) introduced into the system was calculated as the rotation of the mean chord line between the trailing edge of the airfoil and the airfoil web wall (Fig. 4.7(b)).

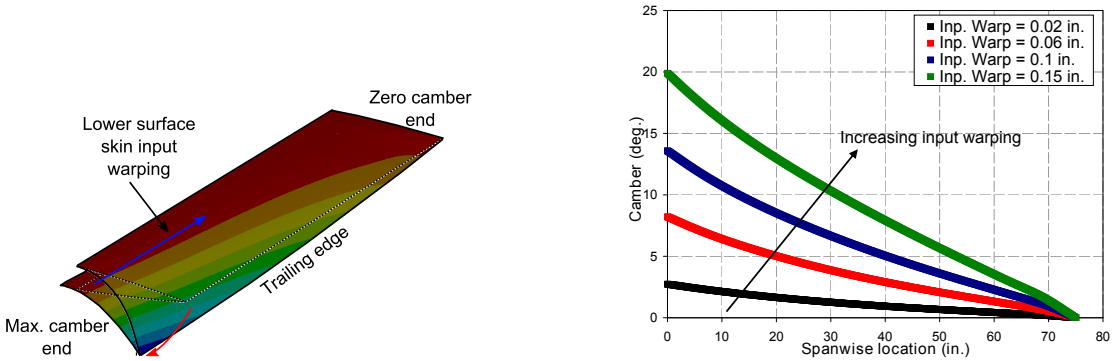

(a) Deformed FE model (b) Spanwise camber variation

Figure 4.9. Global active camber section deformation kinematics

Figure 4.9(a) presents the deformed shape corresponding to the maximum input warping (0.15 in.). As seen the deformed section shows a smooth variation of the camber through the span. Furthermore, the camber variation is approximately linear along the span for a given input warping, as seen in figure 4.9(b) (presents the span variation of camber for a variety of different input warping).

As seen in figure 4.10, the deformed shape of the cross-section shows smooth contours on both top and bottom surfaces. Note that for this particular case, unlike traditional beam twisting, the cross-section itself deforms due to the specific

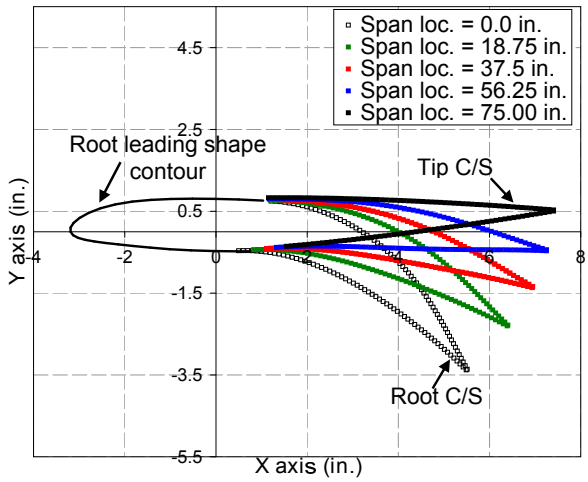

Figure 4.10. Cross-section deformation due to warping

boundary conditions applied. Due to this behavior classical linear Vlasov beam theory or St. Venant's theory cannot be directly applied to the current case [195] to get deformation results and therefore modeling using finite elements was the only viable approach. Figure 4.11 presents the maximum blade camber as a function of input warping for the calculated half span case. As shown, the output maximum blade camber is a linear function of the input warping. This is a favorable result from an actuation view point as it would correlate to simple actuation control schedules.

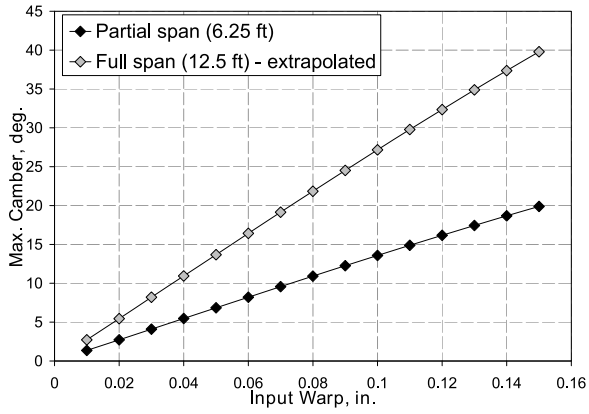

Figure 4.11. Maximum (root) camber variation as a function of input warping

While St. Venant's theory cannot be directly applied to the current case, the general trends represented by this theory provide an estimate of the expected warp camber relationship of a blade with a larger span active camber section. Equation 4.1 shows the expected cross-section twist (θ_t) to be a function of input warping(Δw), beam length (L_b) and enclosed cross-section area (A_e). Based on this equation while the current finite element model is for a partial span (6.25 ft) active camber system, for a full span (12.5 ft) active camber system the maximum blade camber is expected to be 200% larger (with respect to the half span case) for a given input warping (Fig. 4.11).

$$\theta_t = \int_0^L \frac{d\theta}{dz}\, dz. \; = \frac{L_b}{2A_e}\Delta w \tag{4.1}$$

4.4 Effects of camber on airfoil aerodynamics

The deformed trailing edge section greatly affects the aerodynamic properties of the cross-section. In order to quantify this effect, the deformed trailing edge shape along with the corresponding leading edge curve was used as an input for the MSES airfoil analysis software. This software uses Euler discretization along with a two-equation boundary layer formulation (includes viscosity effects) and a full Newton method to solve for the airfoil cross-section aerodynamic performance (this tool also includes compressibility effects). Note the shape for a specified camber angle for any point along the blade span was not found to differ significantly. Therefore, the deformed trailing edge shape corresponding to the maximum camber end was used for the aerodynamic analysis. The analysis was conducted for a Reynolds number of 3.9e6 (corresponding to the blade average operating Reynolds number). The analysis was carried out for Mach number between 0 and 0.8 (0, 0.2, 0.4, 0.6, 0.8). The airfoil mesh was created using the built in mesh tool (H-type mesh).

Table 4.2 presents the analysis matrix for the current study. The camber values present correspond to the maximum camber calculated for the blade section for a a given input warping. Due to the limitations of the MSES software, only select combinations of Mach number and airfoil camber could be calculated (the remaining cases could not be solved for due to convergence issues with the stall model). As can be seen for camber of upto 10.92 degrees, solutions were calculated for all

Table 4.2. NACA 23012 cambered airfoil analysis matrix

Camber (deg.)	M = 0.0	M = 0.3	M = 0.4	M = 0.6	M = 0.8
0.00	X	X	X	X	X
2.78	X	X	X	X	X
5.47	X	X	X	X	X
8.21	X	X	X	X	X
10.92	X	X	X	X	X
13.58	X	X	X	X	
16.18	X	X	X		
18.68					
19.89					

X − > Completed analysis

the considered Mach numbers. Therefore, for the proceeding rotor performance analysis the maximum camber values possible will be limited to 10.92 degrees (as highlighted in the table).

Figure 4.12 shows the variation of the airfoil coefficient of lift as a function angle of attack for various camber angles at different Mach numbers. The baseline NACA 23012 airfoil , as expected (due to the asymmetric shape), is shown to have a non-zero coefficient of lift at angle of attack of zero degrees. Furthermore, as seen in the figure, increases in camber in general do not change the slope of the linear portion of the curve but rather increase the coefficient of lift value at zero degrees (corresponding to an upward shift of the lift curve). Increasing camber also corresponds to the earlier offset of the stall point as seen in the figure, however, there is also a notable increase of Cl_{max}. Increasing the Mach number, on the other hand, causes the earlier onset of stall (compare figures 4.12(a), 4.12(b) and 4.12(c)).

Corresponding to the coefficient of lift curves, figure 4.13 presents the variation of the coefficient of drag for the range of angle of attacks, Mach number and camber considered. Increase in camber corresponds to an increase in the rate of change of coefficient of drag as a function of angle of attach within the drag bucket (corresponds to the linear range of the coefficient of lift). Whereas, an increase in the Mach number corresponds to the reduction of the angle of attack range of the drag bucket, eventually leading to a very small range for large camber high Mach number case (compare figure 4.13(a), 4.13(b) and 4.13(c)). Overall, increasing

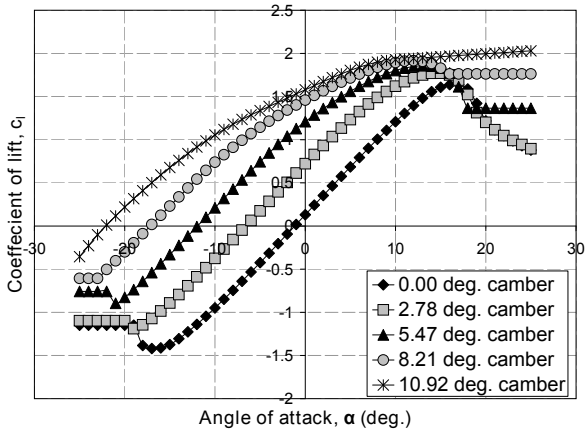

(a) Mach 0.0

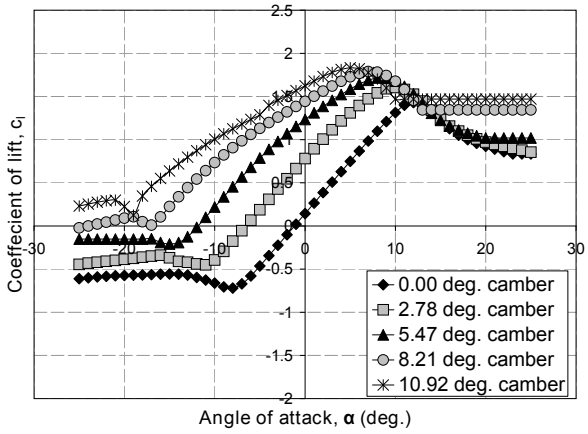

(b) Mach 0.4

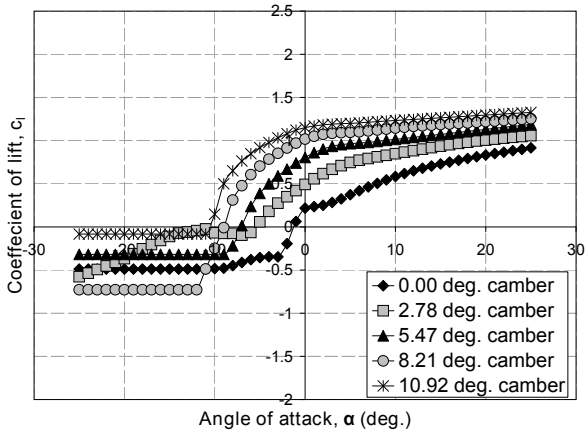

(c) Mach 0.8

Figure 4.12. Variation of the airfoil coefficient of lift as a function of angle of attack, camber and Mach number

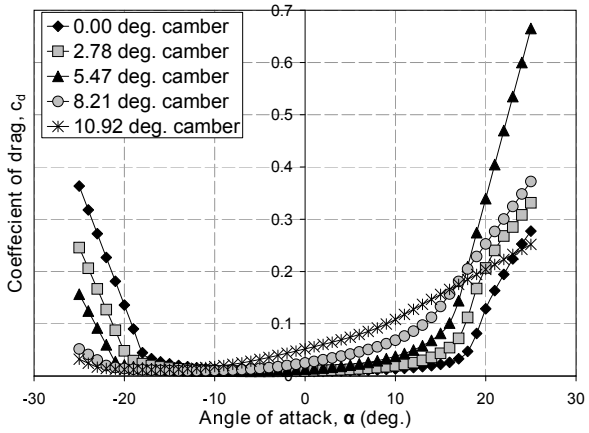

(a) Mach 0.0

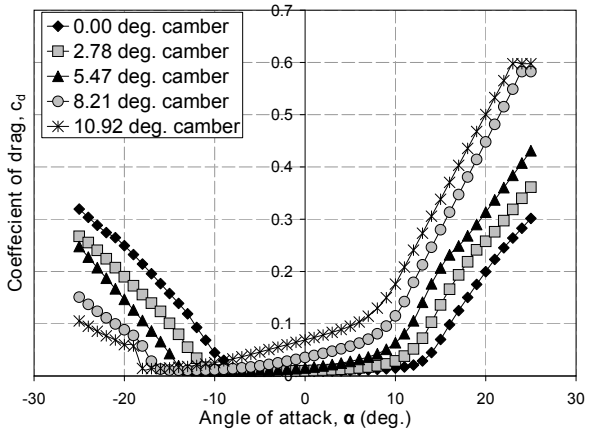

(b) Mach 0.4

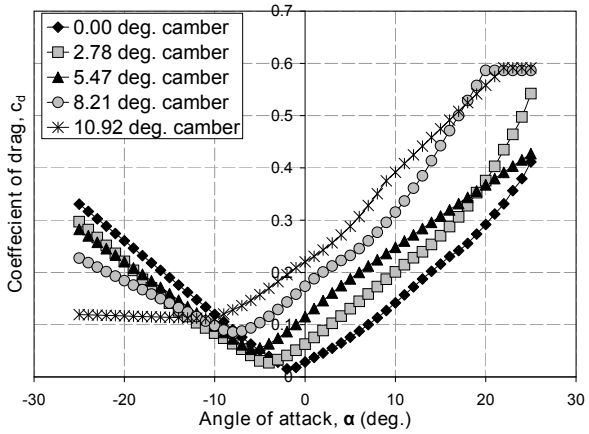

(c) Mach 0.8

Figure 4.13. Variation of the airfoil coefficient of drag as a function of angle of attack, camber and Mach number

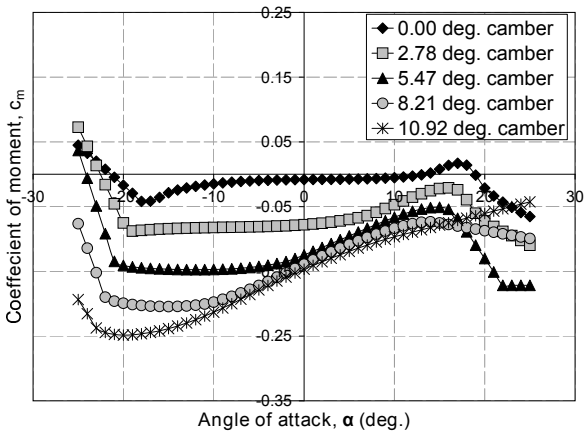

(a) Mach 0.0

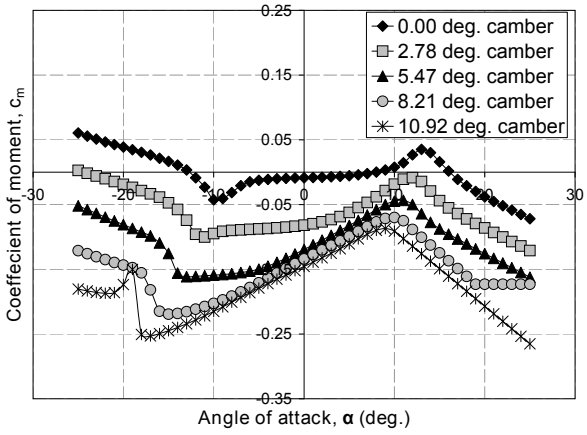

(b) Mach 0.4

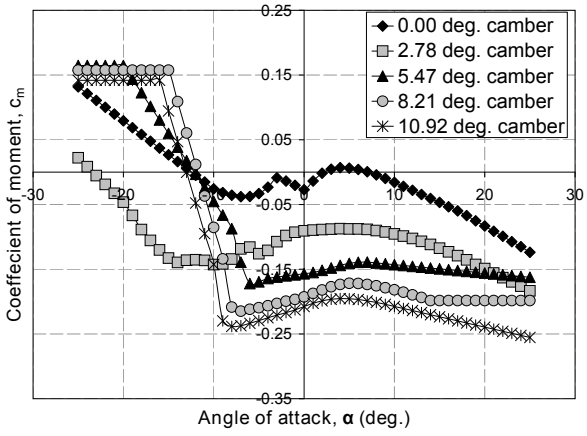

(c) Mach 0.8

Figure 4.14. Variation of the airfoil coefficient of moment as a function of angle of attack, camber and Mach number

Mach number also correlates to an increase in drag, as seen in the figures. The drag polars corresponding to this data is presented in appendix section C.1.

Lastly, figure 4.14 shows the variation of the coefficient of moment (as measured about the 25% chord mark) as a function of angle of attack, Mach number and camber. Similar to the coefficient of drag variation, increase in camber relates to the increase in the rate of change of coefficient of moment (corresponding to the linear range of the coefficient of lift). Furthermore, it also relates to an overall magnitude increase of the coefficient of moment. Although, in general a nose down moment is produced (negative), note that for the baseline NACA 23012 cross-section, variations in the angle of attack can result in both a positive (leading edge up), and negative (leading edge down) moments. The range of angle of attacks at which this switch occurs corresponds to the stall of the airfoil. Due to the earlier onset of stall as the Mach number is increased, the angle of attack at which the switch of the direction of moment occurs is reduced (compare figure 4.14(a), 4.14(b) and 4.14(c)).

4.5 Effects of active camber section on rotor performance

The present section describes the model developed to understand the effects of the proposed camber system on the rotor performance for the hover condition. Following this, the calculated effects of the proposed system on a rigid and torsionally elastic blade will be presented (for various thrust levels and altitudes).

4.5.1 Rotor model description

The following sub-sections present the rotor blade model, along with the rotor inflow model and the analysis process. The rotor, blade and aerodynamic modeling parameters are based on the BO-105 rotor parameters (Sec. 4.2) and the cambered airfoil aerodynamics (Sec. 4.4).

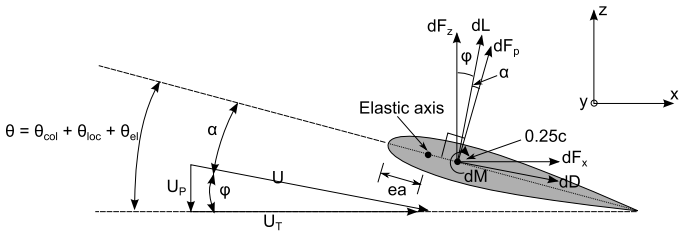

Figure 4.15. Blade cross-section aerodynmic model schematic

4.5.1.1 Blade aerodynamic model

Figure 4.15 presents the blade cross-section schematic with the pertinent aerodynamic parameters annotated. As seen in this figure the θ parameter is defined as the sum of the input pitch (θ_{col}), local pitch due to blade twist (θ_{loc}) and the elastic blade twist (θ_{el}). Based on the figure and assumptions laid out by Leishman in [28], the rotor thrust (T) and power (P) is calculated using equation 4.2 and 4.3 (P_{pro} - Profile power, P_{ind} - Induced power) respectively.

$$T = \frac{N_b \rho \Omega^2}{2} \int_{R_{co}}^{R} c y^2 c_l dy \tag{4.2}$$

$$\begin{aligned} P_{ind} &= \frac{N_b \rho \Omega^2}{2} \int_{R_{co}}^{R} c y^2 c_l v_i dy \\ P_{pro} &= \frac{N_b \rho \Omega^3}{2} \int_{R_{co}}^{R} c y^3 c_d dy \\ P &= P_{ind} + P_{pro} \end{aligned} \tag{4.3}$$

The rotor wake structure was modeled using a deformable free vortex model based on the work of Bagai and Leishman [196, 197]. However, the model used in this analysis was simplified for the hover axis-symmetric flow assumption. This simplification allowed for significant improvement in solution convergence time and therefore allowed for the solution of a larger number of operating conditions with relatively low computational expense. Note, while simplifications were made to the model, the basic underlying physics of the wake solution remains unchanged and hence maintains validity. A detailed explanation of the rotor wake model, its benefits and the trim algorithm used for the current study is presented in Appendix B.

In order to calculate the effects of altitude on the performance of the rotor, the standard day atmosphere model was used to calculate the air density ([198]). Furthermore, the available installed engine power was assumed to only vary based on the air density and such is corrected based on the ratio of the sea level and altitude density ([28]).

To simplify the analysis, only the torsional elasticity of the blade was modeled (blade assumed to be rigid in both flap and lag motion). The torsional elasticity was modeled using a simple two node finite element model (with linear shape functions) as presented in section 4.5.1.2, with corresponding element torsional stiffness varied as a function of radius based on data provided by Staley [194].

4.5.1.2 Blade elastic model

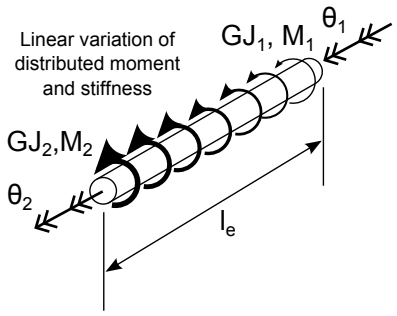

Figure 4.16. Torsional element schematic

The rotor blade is modeled to only be torsionally elastic (i.e. it is rigid in flap and lag) and for this a simple linear shape function based torsional element was used. Equation 4.4, presents the stiffness matrix and equation 4.5 presents the load vector for a blade element (Fig. 4.16) used in the present study. As seen in the figure and the equation, the stiffness and the applied distributed moment is assumed to linearly vary through the element. Note the blade inertia was not considered as the rotor analysis were to be conducted for the hover condition (with no azimuthal variation in blade pitch or aerodynamic forces). The blade model is set to be clamped at the root which coincides with blade attachment point as presented in figure 4.6. The torsional elastic axis is set to be at 20% chord (from the leading edge) based on the results of a parametric study presented in section B.9.3.2.

$$K_e = \frac{GJ_1 + GJ_2}{2l_e} \begin{bmatrix} 1 & -1 \\ -1 & 1 \end{bmatrix} \tag{4.4}$$

$$F_e = l_e \begin{bmatrix} \frac{M_2}{6} + \frac{M_1}{3} \\ \frac{M_2}{3} + \frac{M_1}{6} \end{bmatrix} \tag{4.5}$$

As the elastic axis is offset from the quarter chord location (Fig. 4.15) the total moment contribution at an element is defined using equation 4.6. As seen as the elastic axis moves forward the perpendicular force (dF_p) adds a nose down component to the pitching moment (ea - elastic axis offset from the leading edge, c - chord length).

$$\begin{aligned} dF_p &= dLcos(\alpha) + dDsin(\alpha) \\ dM_{tot} &= dM + dF_p(eac - 0.25c) \end{aligned} \tag{4.6}$$

4.5.1.3 Aerodynamic and structural element configuration

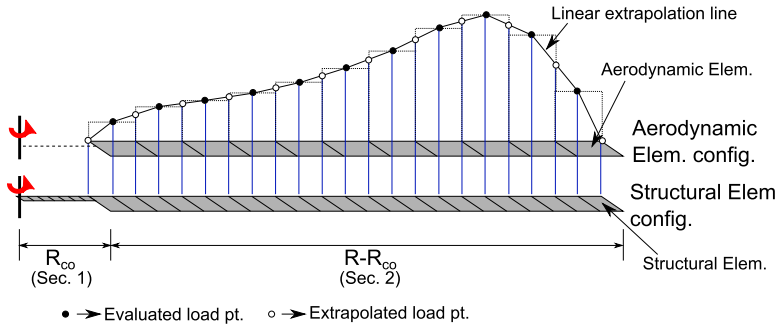

Figure 4.17. Schematic presenting difference and interface between the aerodynamic and structural element layout

Figure 4.17 presents a schematic representation of the aerodynamic and structural element layout. As can be seen the two can have an independent number of elements. The structural elements layout is grouped into two sections. Section 1 makes the region which does not carry any direct applied aerodynamic loads. This section connects the hub to the aerodynamic section of the blade (section 2). The nodes of the structural elements belonging to section 2 have the aerodynamic loads applied to them. In the event a location of a structural node does not line up with

an aerodynamic load calculation point, linear interpolation between to the closest aerodynamic calculation points is used to calculate the applied load. For the current analysis 40 aerodynamic elements were used, whereas 30 structural elements were used in section 2 and 10 elements in section 1. These values were selected as they provided sufficient solution resolution at a reasonable computational expense.

4.5.2 Results

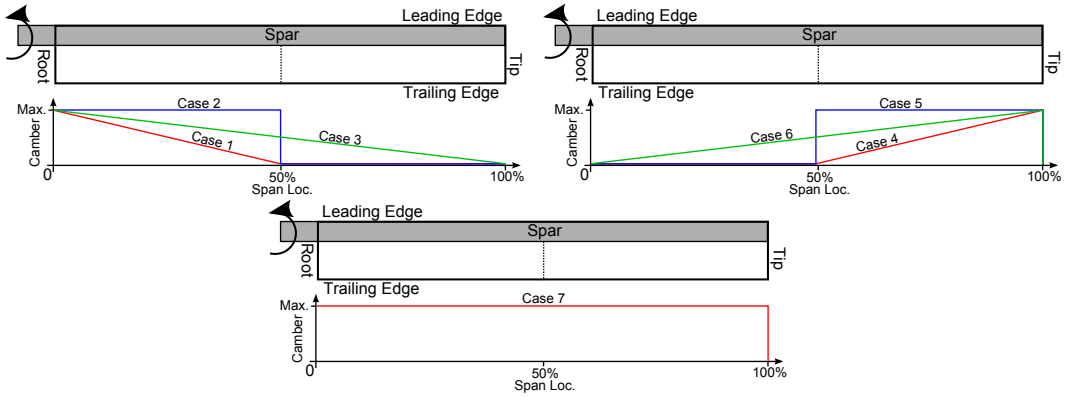

Figure 4.18. Schematic representation of the various active camber configurations considered

The rotor model was used to calculate the rotor power required for a variety of gross weights (4800 lbs, 5500 lbs and 6400 lbs) at varying altitudes (sea level to 18000 ft in 2000 ft increments). For the prescribed thrust levels and altitudes, various different rotor configurations were analyzed. Figure 4.18 presents a schematic representation of the various cases along with the case numbers assigned to them (these will be used to identify the configuration in the proceeding sections). Note that cases 2, 5 and 7 are for a constant camber distribution, which is not achieved via the current warp induced actuation concept. However, these configurations are included as reference cases for comparison. The characteristics of both an untwisted and twisted (-8 deg linear twist) baseline blades in conjunction with the active camber concept were also analyzed. The proceeding sections will present the results of this analysis. The rotor model used in this analysis was thoroughly validated (with regards to power predictions) using experimental data presented

by Warmbrodt and Peterson [199]. The details of this validation are presented in appendix section B.9.3.

4.5.2.1 Effect of camber configuration

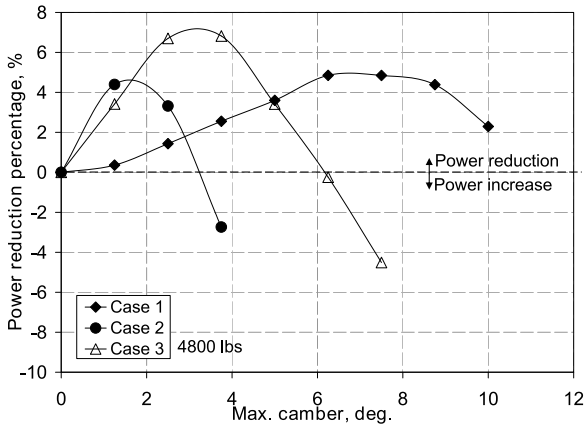

(a) Tip maximum camber cases (1, 2 and 3)

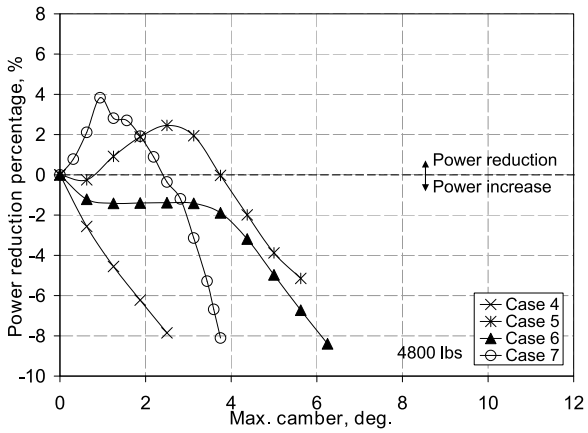

(b) Root maximum camber cases (4, 5, 6 and 7)

Figure 4.19. Percentage change in power (as compared to baseline blade) for various cambered blade configurations for 4800 lbs gross weight case at sea level

As stated earlier several different camber configurations were considered for the current analysis. Figure 4.19 shows the reduction of power (compared to baseline rotor) as a function of the maximum camber applied for the case of lowest thrust condition of 4800 lbs at sea level. Positive values signify a decrease in power and vice versa (compared to the baseline BO-105 rotor). Considering camber configuration cases 1-3 (Fig. 4.19(a)) reductions in power up to 7% can be observed.

The results show the existence of a camber value for which the maximum power reduction is observed (a phenomenon attributed to blade section stall due to high camber). Increasing camber beyond this value reduces the improvements and can even result in power increases relative to the baseline. For case 1, maximum power reduction of 5% is obtained with a camber amplitude of 6-8 degrees , whereas for case 3 an even higher power reduction of 7% is observed for lower camber amplitude (approximately 3 degrees). This observation is attributed to the lower span used for case 1 as compared to case 3. The modest improvement with case 2, for a constant distribution of camber along the inner 50% of the span is attributed to the vortex produced at the midspan due to the step variation in camber introduced at the interface of the active and inactive portions of the blade. The presented results are for the case of the baseline rotor speed, appendix section C.2 presents the effects of the variation of rotor speed in combination with camber variation.

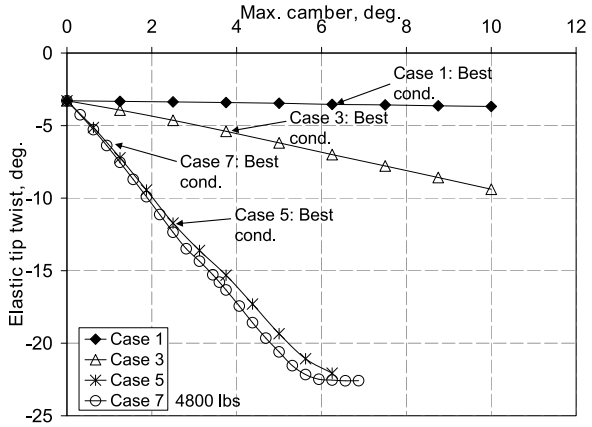

Figure 4.20. Elastic tip twist variation as a function of maximum camber for various camber configurations (Sea level, 4800 lbs)

The tip maximum camber (case 4-6) conversely show an opposing trend (Fig. 4.19(b)). For cases 4 and 6, power increases with increasing camber magnitude and no reductions at all are observed. Cases 5 and 7 (both with discontinuous camber distribution) produce only modest power reductions ($2-4\%$) at low camber magnitudes. To further understand this behavior figure 4.20 shows the elastic tip twist variation for cases 1, 3, 5 and 7 as the maximum camber is changed. As shown, both the tip camber configurations (case 5 and 7) trim at relatively high elastic tip twist (consider the pertinent best condition camber magnitudes

highlighted). Case 1 on the other hand shows almost negligible variance while case 3 exhibits a moderate increase. Interestingly, while the elastic nose down tip twist is higher for cases 5 and 7 the power reductions calculated are lower than those of cases 1 and 3. While the results presented are for the 4800 lbs thrust level at sea level, the trends hold true for the remainder of the parametric space under consideration.

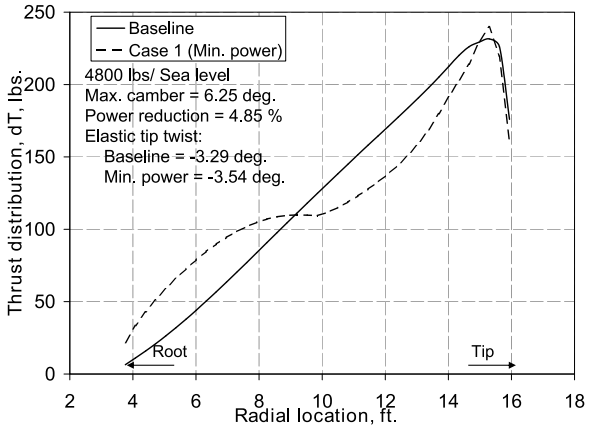

(a) Case 1

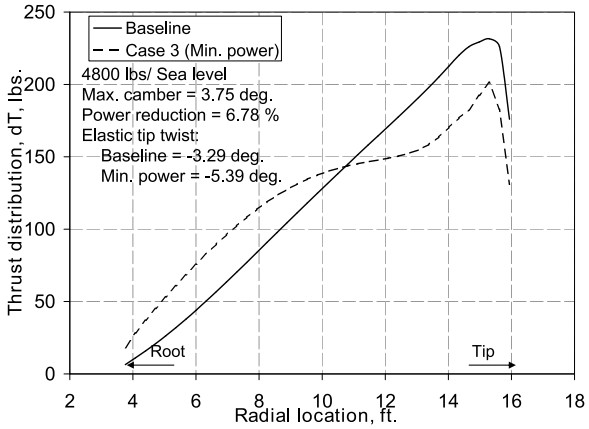

(b) Case 3

Figure 4.21. Thrust distribution for the minimum power configuration for root maximum camber cases in comparison with the baseline blade distribution (4800 lbs, Sea level)

Figure 4.21 presents the thrust distribution for the minimum power configuration for case 1 and case 3 as compared to the baseline rotor. These figures clearly show the increase in lift produced inboard due to the increase in camber in that re-

gion. The increase in inboard lift is accompanied by an offloading of the outboard section of the blade. Comparing case 1 (Fig. 4.21(a)) and 3 (Fig. 4.21(b)), the inboard increase in lift is clearly larger in magnitude and about a larger spanwise section for case 3 as compared to case 1. Furthermore case 3 produces a reduced loading at the tip of the blade (and correspondingly a weaker tip vortex and associated reduced performance penalty). This observation is attributed to an increase in the elastic tip twist observed for this case (5.39 degrees nose down). The increase in lift inboard lift and corresponding offloading of the tip is reminiscent of increasing the blade pre-twist which improves hover performance [28, 200, 201].

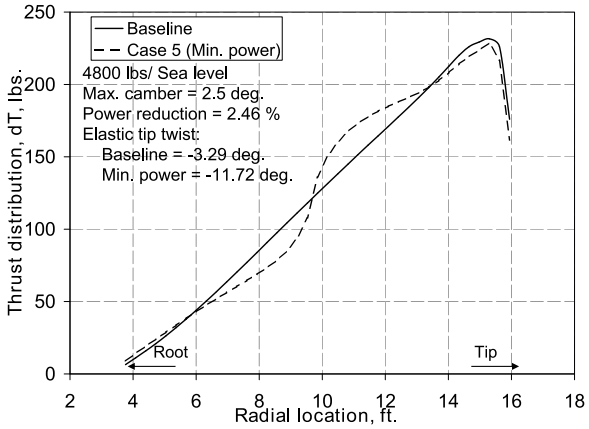

(a) Case 5

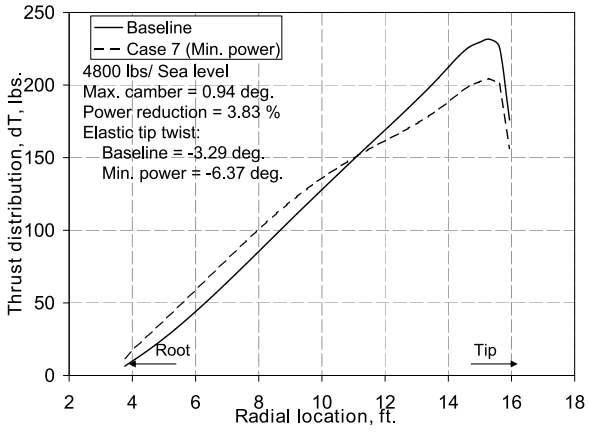

(b) Case 7

Figure 4.22. Thrust distribution for the minimum power configuration for tip maximum camber cases in comparison with the baseline blade distribution (4800 lbs, Sea level)

Conversely, figure 4.22 shows the thrust distribution for cases 5 and 7 as com-

pared to the baseline rotor. For case 5, an unloading of the inboard section of the blade is observed, accompanied with some increase in lift over the outer half of the blade. The tendency to move lift inboard due to nose-down twisting of the blade is negated by the direct lift effect of camber the outer 50%. Comparing case 7, to case 1 and 3, the similarity in the blade loading is clearly seen. In particular, the lift inboard is increased with a corresponding offloading of the tip. Note that the magnitude of the increase in inboard lift is lower than case 1 or 3, furthermore, the camber for minimum power is much lower than any of the other cases. For case 7, the elastic tip twist is very sensitive to increases in camber. Correspondingly, as the blade camber is constant along the span a significant increase in the drag at the blade tip is observed. As a result of this behavior, the minimum power configuration is limited to a smaller camber angle.

4.5.2.2 Effect of gross weight

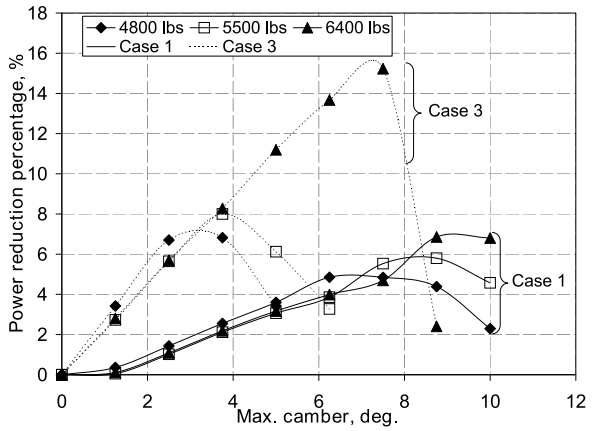

Figure 4.23. Percentage change in power (as compared to baseline blade) for case 1 and 3 for various gross weights (Sea level)

Figure 4.23 presents the variation of the reduction in power (compared to the baseline) as a function of magnitude of camber input for both cases 1 and 3 for varied thrust levels (gross weights). The power reductions due to case 1, as seen in the plot, are marginally improved as the thrust level is increased. Note, the corresponding camber for largest power reduction also increases, a phenomenon which is also echoed in case 3. It is observed that the improvement in power

requirements drastically improves as the thrust level is increased for case 3.

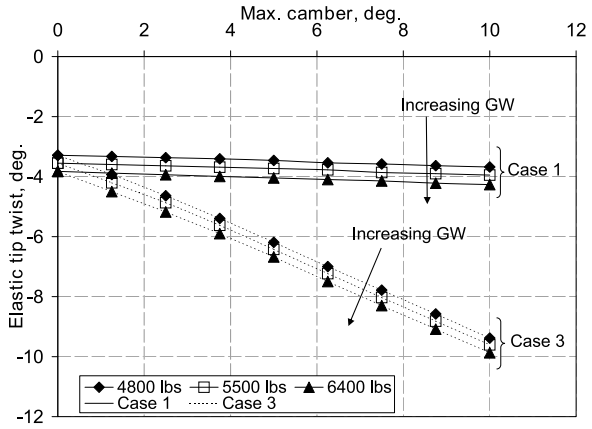

Figure 4.24. Elastic tip twist variation as a function of maximum camber (Case 1 and 3, Sea level, all gross weights)

Considering that the elastic twist can have a significant impact on the performance of the rotor blade, figure 4.24 shows the variation of the elastic tip twist for the same cases and thrust levels (in relation to Fig. 4.23). As highlighted variation in thrust levels results in minor changes in the elastic tip twist (for a specified camber angle) which is consistent for the range of the input camber magnitudes. However, as the gross weight is increased, for case 3, there is a significant increase in elastic tip twist at the minimum power configuration (ranging from approximately 5 degrees nose down for 4800 lbs to 8.5 degrees nose down for 6400 lbs).

4.5.2.3 Effect of altitude

Figure 4.25 presents power reduction changes with altitude (based on the difference of the minimum power required for a cambered blade and the baseline blade). Although most helicopters have a ceiling altitude of less than 10000 ft, the present simulation results are shown for altitudes up to 18000 ft to better understand the trends in behavior. As seen in the figure for both cases increases in altitude result in an increase in power reduction. However, due to the reduction of the available power as the altitude is increased the maximum power reduction (and hence the maximum altitude attainable) is limited as highlighted in the figure. Note that,

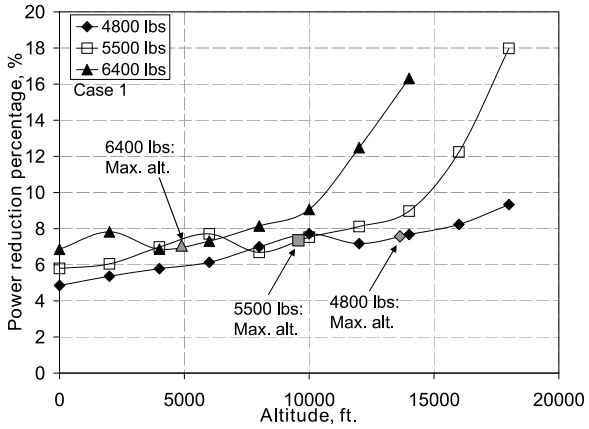

(a) Case 1

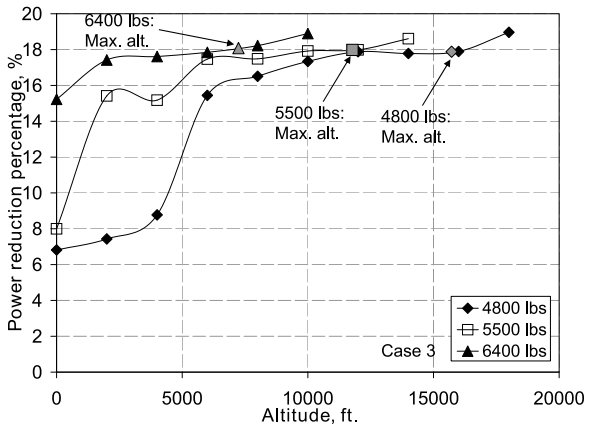

(b) Case 3

Figure 4.25. Percentage change in power as a function of altitude (All gross weights)

case 3 is capable of fairly high power reduction (Approx. 18%) as the altitude is increased when compared to case 1 (Approx. 8%) and is fairly consistent with gross weight.

To better understand the power improvements due to the blade camber the power curves corresponding to the best condition for the cambered blade are plotted alongside the baseline blade (as a function of altitude for all gross weights considered), Fig. 4.26. As seen here there is a consistent reduction of the power curve throughout the altitude range considered. In particular, as seen for case 3 (Fig. 4.26(b)) the minimum power curves perform at levels comparable to that of the next lower thrust condition. This reduction in power has an added benefit of extending the operating envelope as it increases the maximum altitude possible

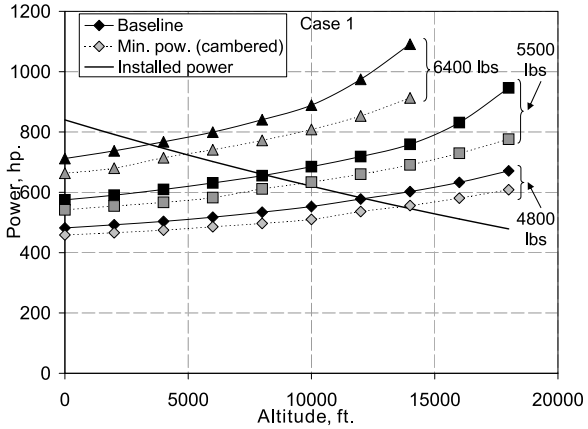

(a) Case 1

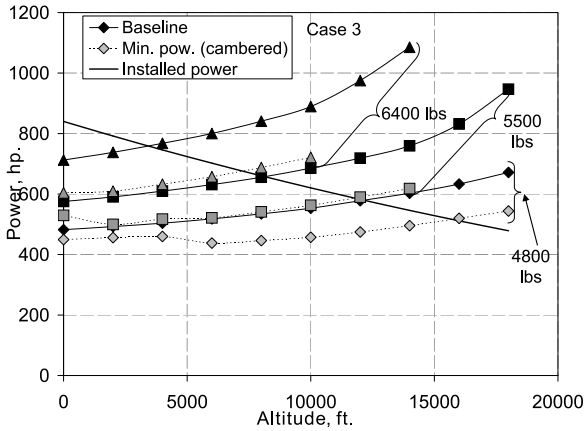

(b) Case 3

Figure 4.26. Change in power as a function of altitude (All gross weights)

for a given thrust level (as seen by the intersection of the installed power and minimum power curves) of upto 4000 ft for case 3 and upto 1500 ft for case 1 (6400 lbs thrust).

In general as the altitude was increased the camber required for minimum power also increased, in particular for case 1, the camber for minimum power increased from 6.25 degrees for 4800 lbs at sea level to 10 degrees at 6400 lbs at the highest altitude considered. Similar trends were observed for Case 3 as well, however, for the lower gross weight and altitudes (as expected) the magnitudes of the camber required were lower (3.25 degrees).

The results pertaining to the remainder of the cases are not shown as only marginal power reductions were observed (at most 5%) for case 4 and 6 at high

altitudes (well above the available horsepower limit) and high gross weights (with a corresponding power increase at lower altitudes and gross weights). Furthermore, power reductions were also observed for case 5 and 7 for the range of altitudes considered, however, these reductions came at the cost of significant elastic tip twist (greater than 10 degrees nose down). In addition, with the current warp induced camber concept, this constant camber cases cannot be implemented.

4.5.2.4 Effect of pre-twist

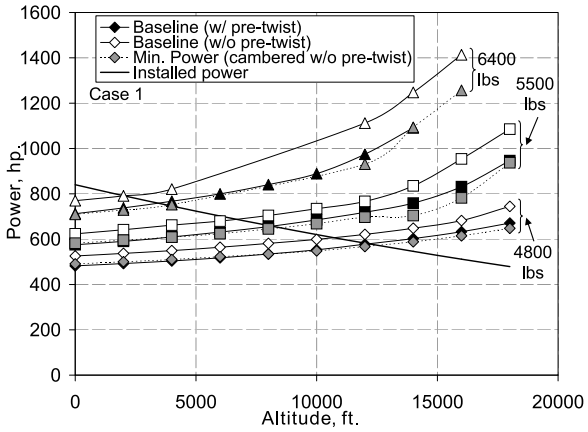

(a) Case 1

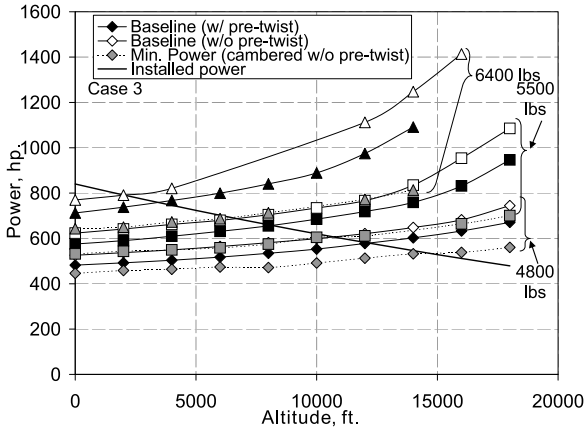

(b) Case 3

Figure 4.27. Change in power as a function of altitude for blades with no pre-twist (with and without camber for all gross weights)

The introduction of camber within blades as seen in the previous sections can result in a reduction in power requirement over the baseline blades. As shown

by Keys et. al. [94] and Wachspress et. al. [200], the optimal twist distribution for hover and forward flight differs greatly. In particular, while highly twisted blades are optimal from a hover performance standpoint, they produce significant vibration in forward flight (attributable to negative lift at the advancing blade, in addition to other factors). Therefore, if a lightly twisted blade was used in conjunction with camber, the result can possibly allow for good operation in hover (with respect to lower power levels) and in forward flight (with respect to vibration levels). This section explores the effect of blade pre-twist on the effectiveness of active camber for performance improvement.

Figure 4.27 presents the variation of the power curves of the baseline blade with and without pre-twist alongside the maximum power reduction achievable using active camber on blades without pre-twist. To clarify, the baseline with pre-twist corresponds to the baseline BO-105 blade (i.e. with a -8 deg. pre-twist), whereas the baseline without pre-twist incorporates the same planform of the BO-105 and is otherwise idetical with the exception of pre-twist. As expected, the baseline blade with no pre-twist requires more power for a given thrust level. For case 1 (Fig. 4.27(a)), the introduction of camber results in power levels comparable to that of the baseline blade with pre-twist (compare baseline blade with pre-twist curve with minimum power curve) for the range of thrust levels and altitudes considered. Furthermore, for case 3 (Fig. 4.27(b)) the power reduction due to camber results in performance levels better than that of the baseline blade with pre-twist. This shows the effectiveness of introducing root camber as a means to realize the performance levels comparable to pre-twisted blades.

Similar to the case of the -8 deg pre-twisted blades with camber, the camber required for minimum power increases as the gross weight and altitude are increased. Furthermore, case 1 in general requires more camber to obtain the minimum power condition. However, unlike blades with the baseline pre-twist, the camber required for minimum power is overall larger for blades without pre-twist. In fact, for case 1 the maximum camber considered for this study is required for minimum power, whereas for case 3 the camber required ranges from 8.75 degrees to 10 degrees (corresponding to 4800 lbs at sea level to 6400 lbs at the maximum altitude considered respectively).

Figure 4.28 presents the equivalency of pre-twist to input camber for both

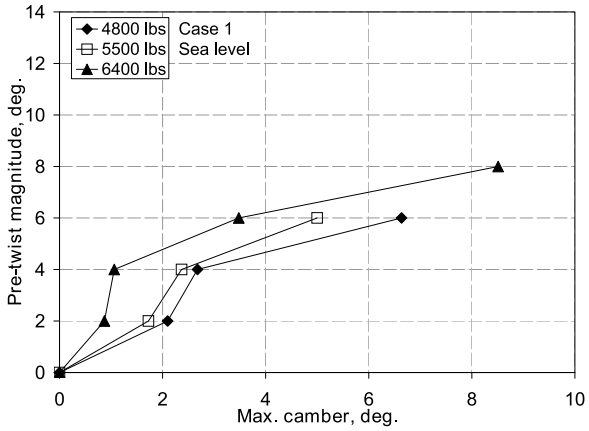

(a) Case 1

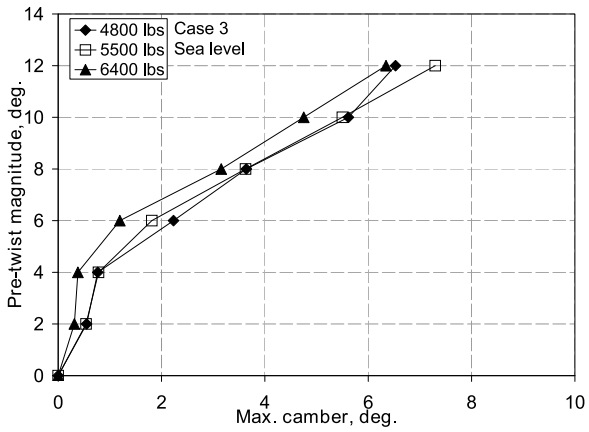

(b) Case 3

Figure 4.28. Pre-twist equivalency to input maximum camber (All gross weights, Sea level)

cases 1 and 3 (note the pre-twist presented refers to a linear distribution case). The equivalency is based on matching the power loading ($\frac{Power}{Thrust}$) of blades with the corresponding pre-twist with that of cambered blades with no pre-twist. As seen in Fig. 4.28(a), camber configuration case 1 is capable of achieving at least the baseline BO-105 pre-twist (i.e. -8 deg.). However, blades with camber configuration case 3 would be capable of operating at power loadings comparable to that of pre-twists upto -12 degrees (given the limit imposed of a maximum input camber of 10 degrees). Note the observed equivalency is relatively insensitive to thrust levels (limited dispersion of the curves). These observations further emphasize the wide range of capability of the active root camber (case 1 and 3) in successfully

being able to emulate the efficiency of pre-twisted blades.

4.5.2.5 Power reduction source

In order to understand the mechanism of the power reductions due to camber as well as the preference of root camber as opposed to tip camber consider figure 4.29 which shows the reduction in total, induced and profile power (compared to the baseline BO-105 blade) as a function of camber for case 1 and 4 (5500 lbs, Sea level). As seen clearly the total power reduction is apparent only for case 1 (note a positive change refers to a decrease in power and vice versa). Furthermore, for both cases the total power change is dominated by the change in induced power as the camber is varied (compare total power change curve to the induced power curve). Conversely, compared to the induced power change, the profile power of the cambered blade changes only moderately. The exception to this trend are high camber conditions for case 4 wherein the profile power increases due to the higher operating Mach number environment of the cambered section (i.e. blade tip).

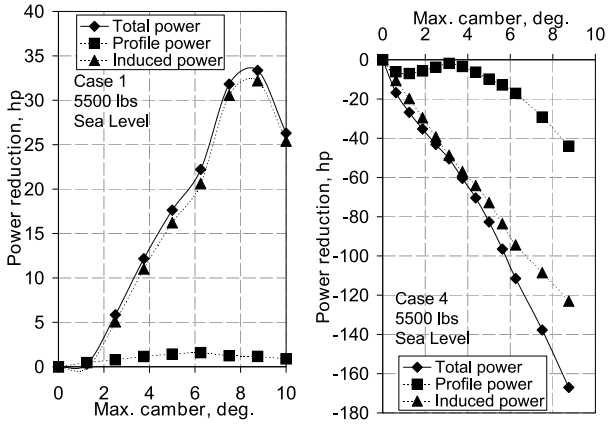

(a) Case 1 (b) Case 4

Figure 4.29. Change in total, profile and induced power (compared to the baseline) as a function of maximum camber (Sea level, 5500 lbs)

Figure 4.30 shows the change in the thrust distribution (compared to the baseline) for the best condition for case 1 (8.75 deg. camber) alongside the thrust distribution for case 4 with the same magnitude of maximum camber applied. As highlighted in the figure case 4 corresponds to a much higher elastic tip twist (-17.3

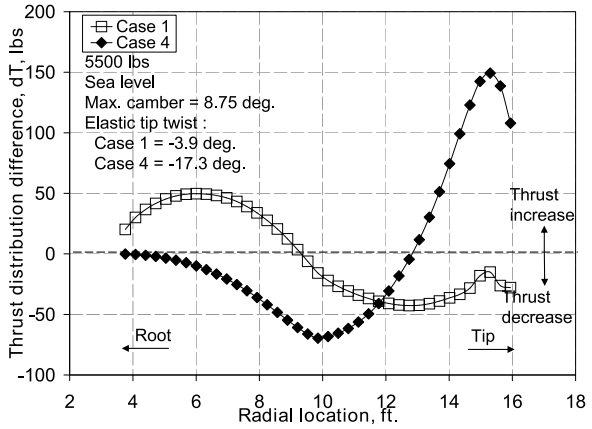

Figure 4.30. Thrust distribution difference (as compared to baseline) for case 1 and 4 at 8.75 deg. max camber (Sea level, 5500 lbs)

deg. compared to case 1: -3.9 deg.) which is a result of the nose down moment produced at the blade tip when maximum camber is at the tip. Conversely, there is also a direct increase in lift over the outer half of the blade which results in the net increase in outboard lift that is detrimental to both induced and profile power. Comparatively, for case 1 there is a significant increase in the lift produced at the root of the blade with corresponding decreases in the lift at the blade tip. This shift of the lift inboard relates to a better distribution of the inflow across the blade span and a corresponding decrease in induced power.

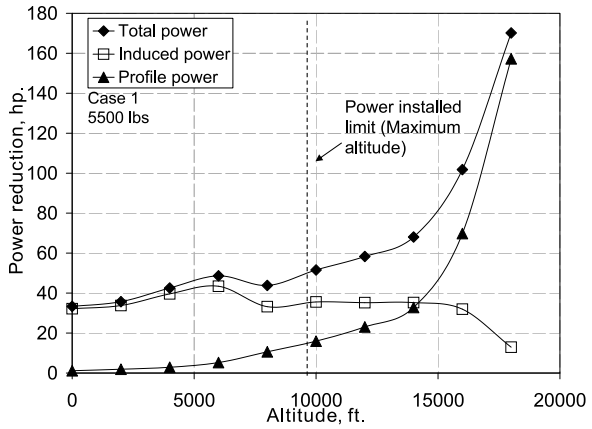

Figure 4.31. Change in total, induced and profile power (as compared to the baseline) as a function of altitude (Case 1, 5500 lbs)

As the altitude increases, the total, induced and profile power changes for case 1 are shown in figure 4.31 (5500 lbs). This figure clearly shows the dominance of the induced power reduction for a wide range of altitudes. Note the relatively insensitivity of the induced power change as the altitude is increased. The exception being at very high altitudes (notably outside the maximum altitude limit imposed by the installed power) wherein the profile power change begins to dominate. This phenomenon is attributed to the reduction in dynamic pressure due to reduced density at higher altitudes, bringing the baseline rotor closer to stall. Increases in the blade camber at the root results in the thrust inboard thereby requiring lower angle of attack which corresponds to profile power reduction.

Increases in camber produce increases in the lift coupled with a nose down pitching moment (due to the aerodynamic pitching moment as well as the offset of the elastic axis forward of the aerodynamic center). As seen from the previous figures induced power reductions tabulated are a result of shift of the thrust distribution towards the root of the blade. This inboard shift can be the produced by two separate mechanisms: elastic twisting (nose down) of the blade due to the pitching moment or the direct increase in lift due to camber. To highlight which of these two mechanisms dominate, the power reductions for three different configurations are examined in greater detail. The first is the minimum power condition for case 1 at the 4800 lbs thrust level (6.25 deg. camber, Sea level). The second is the minimum power configuration for case 3 for the same thrust level and altitude (3.75 deg. camber). Lastly, consider case 4 configuration with an input camber of 1.25 degrees which produces a comparable elastic tip twist to that of minimum power case for case 3. The elastic twist distributions for these three configurations are shown in figure 4.32 along with the baseline rotor distribution for the selected thrust and altitude as a reference.

In order to quantify the effectiveness of the elastic twist as compared to the direct lift increase due to camber variation, two separate conditions are compared. The first being where the blade is allowed to elastically twist due to the camber. The second condition is for a rigid blade (torsionally elasticity is removed) with an equivalent pre-twist applied to it (i.e. additional pre-twist equivalent to the elastic twist deformation calculated for condition one). Figure 4.33 presents the percentage of the induced power change of both conditions (compared to the base-

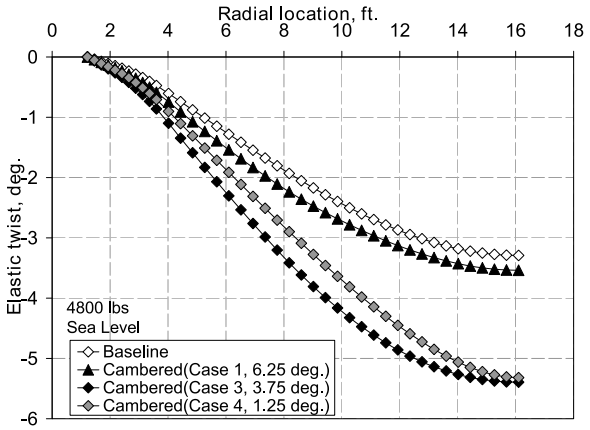

Figure 4.32. Elastic twist radial distribution for selected cambered blade cases as compared to the baseline (Case 1, 3, 4, Sea level, 4800 lbs)

line BO-105 blade), for all three cases. As can be seen for case 1, the introduction of camber (with torsional elasticity) produces a reduction of the induced power, whereas the rigid blade condition (with the corresponding equivalent pre-twist applied) results in a negligible variation of the induced power (note the elastic twist for this configuration varied very slightly from the baseline, Fig. 4.32). This shows the dominance of the inboard lift generated by the camber as the primary source of induced power reduction. Similarly, for case 3 we see a significant reduction in induced power for the cambered elastic blade configuration. However, the equiv-

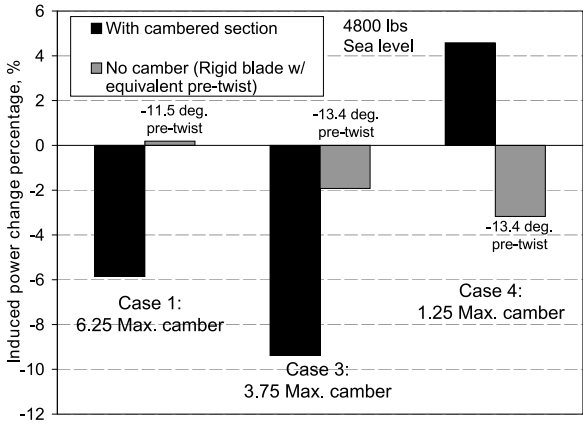

Figure 4.33. Percentage change in induced power (compared to the baseline) for cambered (elastic) and rigid blade with equivalent pre-twist conditions (Case 1, 3, 4, Sea level, 4800 lbs)

alently pre-twisted blade also results in the reduction of induced power, albeit by a much lower percentage. This phenomenon is further highlighted in Fig. 4.34(a) which shows the change in the thrust distribution (compared to the baseline BO-105) for the two different conditions (for the case 4 configuration). As seen here the thrust distribution change due to the cambered blade with elastic twist is observed to show a larger increase in the thrust at the root as compared to the blade with equivalent pre-twist. This further shows the dominance of the increased inboard lift due to camber as the source of the induced power reduction.

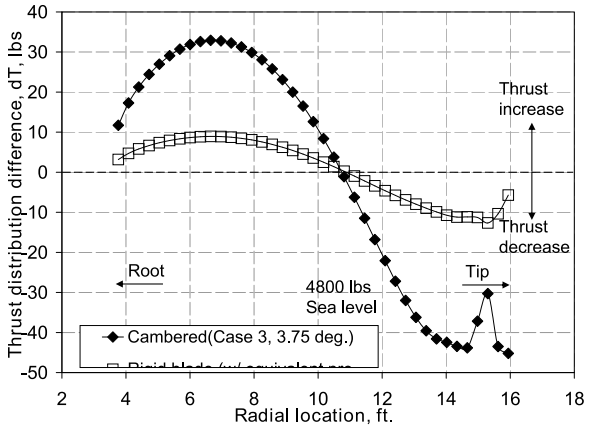

(a) Case 3

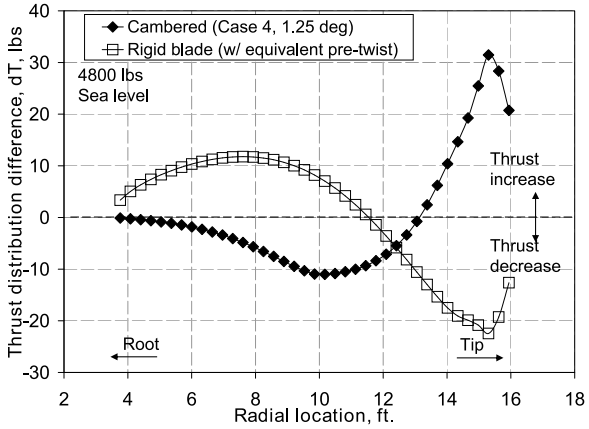

(b) Case 4

Figure 4.34. Change in thrust distribution (compared to the baseline) for cambered and superimposed elastic twist rigid blade configurations (Sea level, 4800 lbs)

Conversely, consider the case 4 configuration (1.25 deg. camber) wherein the elastic twist is comparable to that of the case 3 minimum power configuration. As

seen in the figure 4.33 the cambered blade with elastic twist actually results in an increase in the induced power whereas the rigid blade with equivalent pre-twist results in an induced power reduction. This phenomenon is further clarified by figure 4.34(b) which shows the thrust distribution change (compared to the baseline) for both the conditions. Clearly, as seen, the rigid blade with equivalent pre-twist results in a shift of the thrust towards the root which results in the induced power reduction. Whereas, the elastic blade with camber results in increased thrust at the tip of the blade, thereby resulting in an increase in induced power.

4.6 Deployment concept

Based on the results presented it is evident that the application of camber to a rotor blade can provide reductions in required rotor power over the baseline in hover. However, it can be argued that, based on the presented results, it is enough to design a blade with distributed camber that is not varied (i.e. the variation of camber is not needed). To clarify this notion, consider the results presented by Keys et. al. [94], which states that while a blade with lower pre-twist leads to power reduction (compared to a blade with larger pre-twist) in high speed flight, the magnitude of reduction is moderate at best. However, a blade with lower pre-twist corresponds to significantly lower vibration levels in forward flight (again compared to a blade with higher pre-twist). Therefore, based on this observation and the results presented in the preceding sections, the benefit of having the ability to vary the blade camber can be ascertained. In particular, a blade with little or no pre-twist can be used in conjunction with camber variation to operate at the best power loading level in hover, but as the aircraft transitions to forward flight a reduction in camber can correlate to lower vibration levels with relatively low performance penalty (as compared to a blade with fixed high pre-twist and/or camber).

CHAPTER 5

Variable camber system design

Based on the results presented in chapter 4 the benefits of a variable camber system is clearly evident. The next problem that needs attention is the design of the active camber which is realizable. The design developed in the following sections has its origins in the warp-induced variable twist mechanism developed my Misty et. al. [202]. The following sections explain the design guidelines and requirements used. This is followed by a detailed description of the actuation structure developed and the prototype construction. Lastly, the results of the experiments carried out on the prototype are discussed, along with a discussion on the effects of external loads on the system.

5.1 Actuation requirements

Based on the proposed warp-camber concept, a interesting kinematic relationship was observed. Similar to the warp-twist prototype developed by Mistry et. al. [20], the warp-camber concept also experiences a chordwise deformation along the slit line. Figure 5.1 presents a schematic diagram highlighting the effect of restraining

this deformation on the overall camber shape. As can be seen, unlike the warp-twist concept, the deformable section undergoes an undesirable 'potato chip' like deformation which would prevent its effective operation as a cambered airfoil. This phenomenon is largely attributed to the non-uniform boundary conditions of the warp-camber concept.

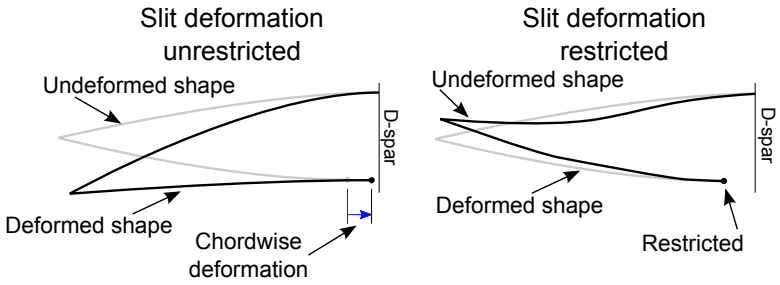

Figure 5.1. Schematic representation of the effects of chordwise slit deformation due to warping

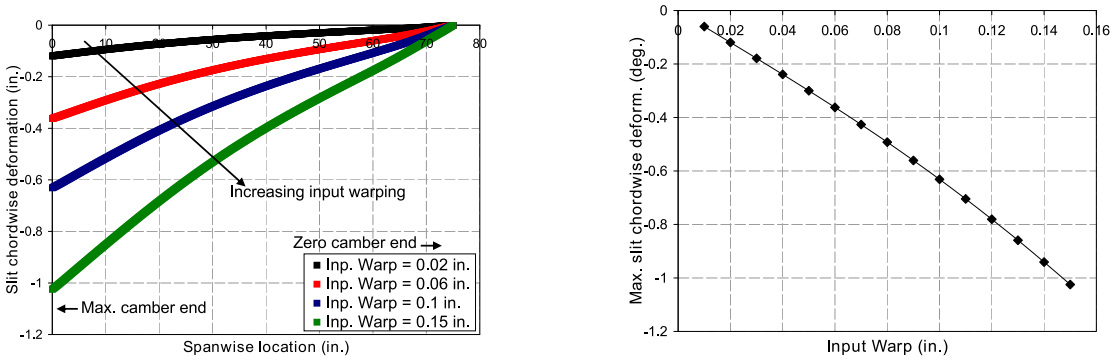

(a) Spanwise variation

(b) Max. deformation variation

Figure 5.2. Characteristics of the chordwise deformation of the slit (for the warp-camber system)

Figure 5.2 presents the spanwise variation of the chordwise deformation of the slit (if unconstrained) for various input warp values along with the variation of the maximum slit chordwise deformation as a function of input warp for the BO-105 configuration as used in the study presented in chapter 4 (the solution was obtained from the finite element model used in the corresponding chapter). As can be seen (Fig. 5.2(a)) the spanwise distribution is approximately linear in nature and is therefore is desirable from a design stand point. Furthermore, as seen in

figure 5.2(b) the variation of the maximum slit chordwise deformation also follows a linear relationship with the input warping.

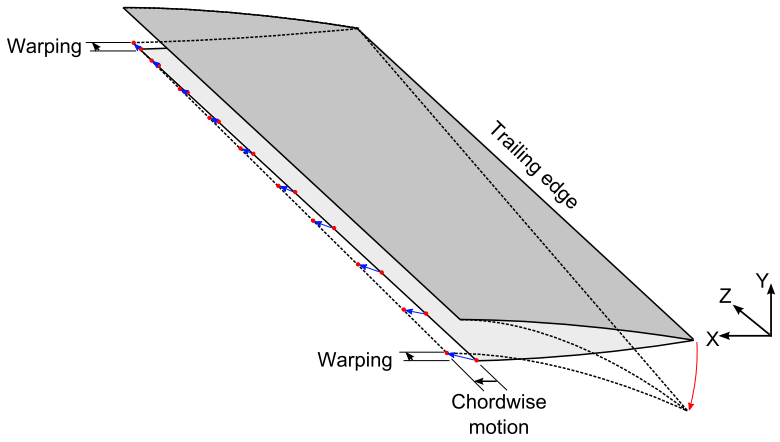

Figure 5.3. Schematic representation of the spanwise distribution of the required chordwise motion of the slit

Figure 5.3 presents a schematic of the motion the slit undergoes. As can be seen at the maximum camber end, a point on the slit undergoes chordwise motion in addition to the spanwise warping, whereas at the zero camber end the slit only undergoes the input spanwise warping. At intermediate locations in between the two end stations, the spanwise warping component remains the same, whereas the chordwise component of the motion varies in an approximately a linear fashion (as presented in figure 5.2(a)). Due to the direct effect of the slit kinematics on the camber deformation, the actuation structure must allow for such a displacement.

5.2 Baseline blade

A warp induced active camber prototype was built using a section of a decommissioned CH-46 rotor blade (Fig. 5.4). This hardware was donated by the US Navy Naval Air Systems (NAVAIR) Command's Vertical Lift Center Of Excellence (VLCOE). The pertinent dimensions of the donated blade section are listed in table 5.1. As seen in figure 5.4 the blade section has visible wear on the structure and hence was not deemed flight-worthy. Aside from these characteristics, the exterior coating of the blade leading edge was stripped away down to a metal surface (as-

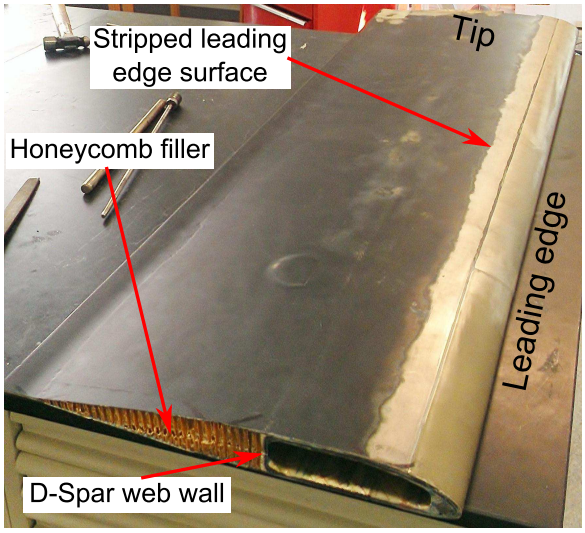

(a) Top surface

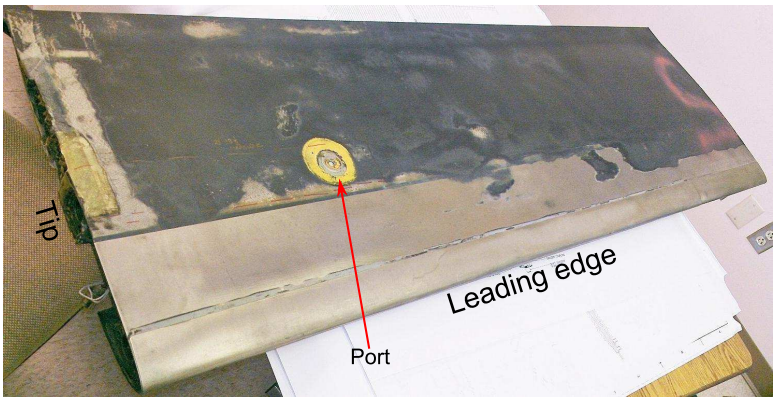

(b) Bottom surface

Figure 5.4. Isometric views of the top and bottom surfaces of the donated CH-46E blade section

sumed to be the blade tip leading edge reinforcements). As is clearly evident from the figures the section aft of the spar wall was filled with a honeycomb filler.

Furthermore, the blade section is stipulated to be from the tip of the blades, as seen in figure 5.5(a) (evident due to the presence of removable tip weights; see figure 5.5(b)). These tip weight slots were measured to extend a distance of at least 18.875 in into the blade. The blades incorporated a port (of unknown purpose) on the bottom surface close to the blade tip.

Based on the data presented in a report by the Boeing Vertol company [27] the pertinent CH-46 rotor properties are presented in table 5.2. The chord value

Table 5.1. Measured pertinent properties of the donated CH-46E blade section

Prop. Name.	Specification
Section length	59.875 in.
Section chord (constant)	18.75 in.
Section thickness (max)	1.75 in.
Spar wall location (aft side)	7.375 in.
Average Skin thickness (aft of spar)	0.03125 in.

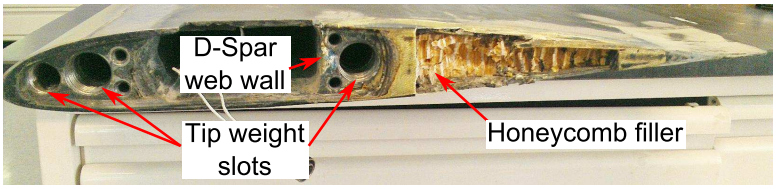

(a) Detail view of tip

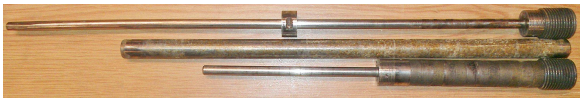

(b) Tip weights

Figure 5.5. Detail views of the components of the blade tip

presented in the report matched the physical hardware dimensions. The report also stated the inclusion of a 3 degree downward deflected tab with a width of 0.75 in . Note that blade does have a moderate amount of pre-twist.

Based on the information collected and the physical dimensions of the device, a Computer Aided Drafting (CAD) model of the hardware was created. The presence of the port and the tip weights aft of the web wall coincide with the intended

Table 5.2. Rotor system properties of the CH-46 presented by the Boeing Company [27]

Prop. Name.	Specification
Number of rotors	2
Number of blades (per rotor)	3
Radius	306 in
Chord (constant)	18.75 in
Pre-twist (root to tip)	-8.5 deg.
Airfoil	V23010-1.58
Tab width	0.75 in (0.04c)
Tab angle (downward)	-3 deg.

location of the variable camber actuator. Therefore, a 14.875 inch spanwise section of the blade was removed from the blade. This reduced the available active camber section to 45 inches. This section only includes a honeycomb filler aft of the spar wall, making this new configuration ideal for the application of camber actuation. Furthermore, a 1.25 inches wide cut was introduced in to the bottom skin, with the aft most cut of the slit set to be 2.25 inches aft of the D-spar web wall, along the entire span of the active section of the blade. This was done to allow room for placement of the interior actuation structure and to allow for the chordwise motion of the lower skin. A CAD representation of the final modified blade structure (with dimensions annotated) along with the details of the slits cut into the bottom skin are shown in figure 5.6 (Note the honeycomb filler is not shown in the CAD model). This is the starting point of the design and analysis conducted as part of the present research. While the report presented by the Boeing company [27] included macro dimensions of the rotor system, information regarding the specific materials (and layup) used in the CH-46E blade construction was not available in the open literature.

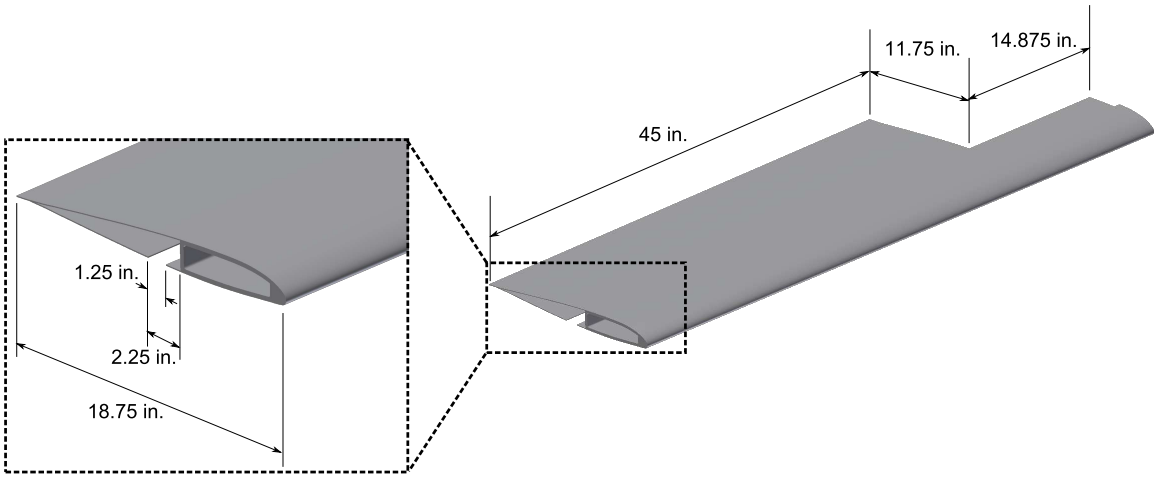

Figure 5.6. Computer Aided Drafting (CAD) model of the modified section of the CH-46E rotor blade used for the current analysis

5.2.1 Design guidelines

Similar to the variable span blade design analysis, a set of guidelines were set forth (listed below) to help in developing a feasible design.

- Entire actuation system should fit within the confines of the section of the blade aft of the D-spar web wall.
- System should require only a single actuation input (minimize complication). The design should allow for a minimum of 0.1 inches of input spanwise warping.
- Design should incorporate features which minimize the possibility of system jamming.
- The prescribed chordwise motion and warping of skin slit should be allowed by the actuation system.

5.2.2 Effect of actuation boundary conditions

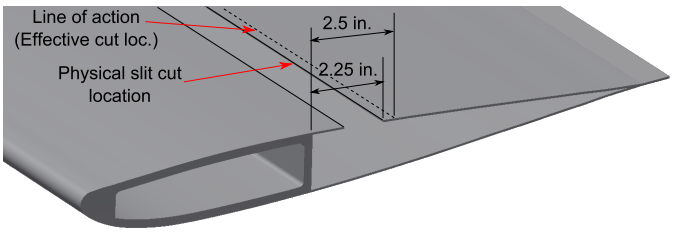

Figure 5.7. Schematic showing the line of action location (effective cut location)

The main purpose of the presented analysis was to determine the kinematic relationship of the chordwise motion to input warping of the specified blade section. The secondary purpose was to analyze the effect of various actuation schemes (via the use of corresponding boundary conditions). While the outer cut of the slit (in the blade skin) was placed at distance of 2.25 inches from the spar web wall, in order to allow for the proper dissipation of forces into the skin, the line of actuation was set to be at a distance of 2.5 inches from the spar wall (Fig. 5.7). Doing so allows for a buffer space of 0.25 inches from the line of action to the edge of the

skin which permit placement of holes in the skin for the attachment points while minimizing the risk of tearing the skin (this is a preventative measure taken purely from the standpoint of manufacturing). Since the actuation kinematics are based on the location of the line of action, a finite element model with a representative cut placed at the 2.5 inch distance from the spar web wall was used for preliminary kinematic analysis presented in this section. Furthermore, only the model of the active section (the region aft of the spar web wall) was used to reduce the number of elements required and thereby allowing for faster solution times. Note that the material properties used here are arbitrary (the model uses the average modulus of aluminum) since only the kinematic relationship is being considered.

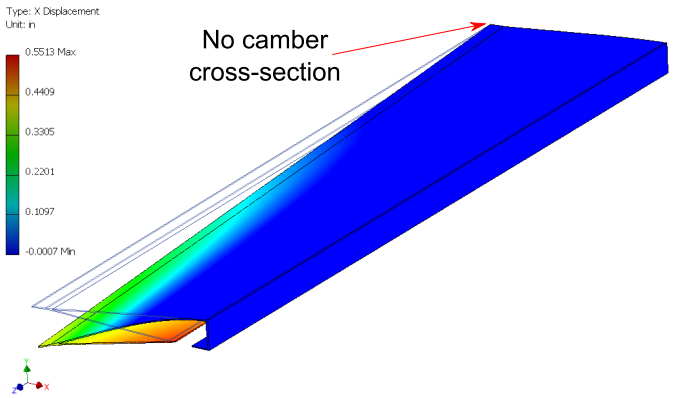

Figure 5.8. Calculated chordwise deformation with applied case 1 boundary conditions

Three cases were analyzed to represent three different actuation schemes. For all three cases the spar web wall is considered to be clamped (to represent the rigidity of D-spar). Case 1 encompasses the boundary conditions set forth in chapter 4 wherein the slit is allowed to move in the chordwise and spanwise direction while the zero camber cross-section is restricted from moving in the blade cross-section plane. In this configuration the input actuation is a specified warping of the slit by 0.1 inches (towards the zero camber cross-section). Based on this applied boundary condition, the resulting calculated deformation is presented in figure 5.8 (with contours marking the chordwise motion, i.e. along the x-axis). As can be seen here for an input of 0.1 inches of warping requires the slit to undergo 0.55 inches of chordwise motion.

Case 2 has similar applied boundary conditions in that the slit is only allowed to

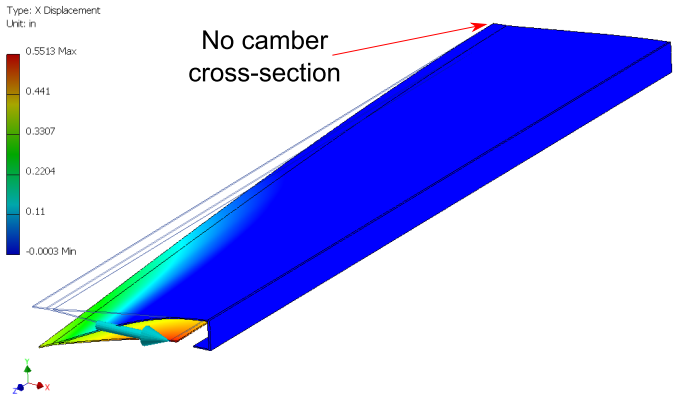

Figure 5.9. Calculated chordwise deformation with applied case 2 boundary conditions

move in the chordwise and spanwise directions while the zero-camber cross-section is restricted in the cross-section plane. The difference however is the application of the input displacement. For case 2, instead of an applied warp input at the slit the maximum camber end of the slit is forced to undergo a chordwise motion equal to 0.55 inches. The resulting chordwise displacement field is presented in figure 5.9. Comparing figure 5.9 to 5.8 it can be clearly seen that the deformation seen in the blade is comparable. In fact in this particular case the spanwise motion of the slit (warping) was calculated to be approximately 0.1 inches (not shown in figures). Therefore this method proves to be an alternative method of actuation wherein instead of input warping the skin itself is forced to move in the chordwise direction.

The boundary conditions used for case 3 were designed to showcase the effect of restricting the chordwise motion of the slit (as schematically explained in figure 5.1). To clarify for case 3, the slit is restricted to now move only in the spanwise direction while keeping all the other boundary conditions applied in case 1 the same. The resulting calculated through the thickness (along y-axis) deformation is presented in figure 5.10. As can be clearly seen, restricting the chordwise motion leads to an undesirable deformation profile of the skin. The presented results highlight the importance of having an actuation system which allows for this chordwise motion.

While case 2 presents an interesting alternative to actuating the blade camber (compared to case 1), it should be noted that this requires the input of chordwise

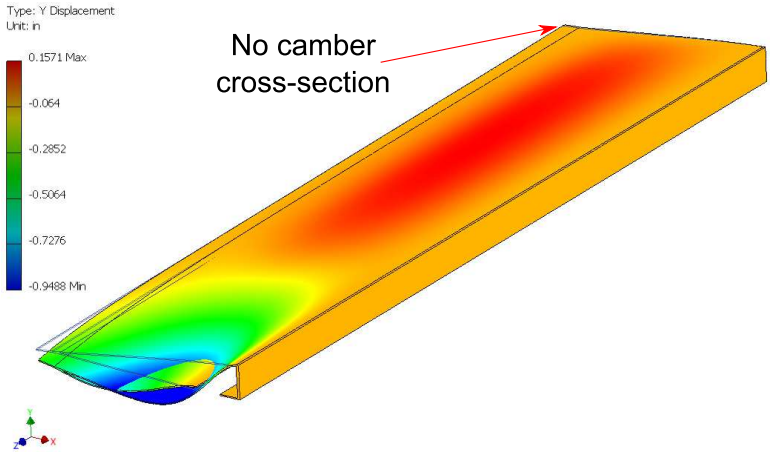

Figure 5.10. Calculated chordwise deformation with applied case 3 boundary conditions

motion. In this configuration either a linear actuator would need to be small enough to be placed along the chordwise axis or a series of mechanical linkages would be required to produce the required chordwise motion input. Case 1 on the other hand allows for relaxed limitations on the dimension of the actuator as the placement would be along the spanwise axis. Based on this observation the actuation system development presented in the proceeding sections follows the scheme presented by case 1.

5.3 Actuation structure design

As stated earlier it is imperative that the structure allow for the chordwise motion of the slit in order to produce a smooth cambered airfoil profile. However, while in operation, a rotor blade experiences significant external forces. These forces arise due to both the dynamics of the blade itself as well as the aerodynamic and centrifugal load environment it is operating in. Therefore, it is not sufficient for the actuation mechanism to just allow for chordwise motion but rather has to ensure that the slit follows the precise combined motion along the span (warping) and in the chordwise direction. In order to realize this requirement, a simple two bar linkage design was developed. Figure 5.11 presents a schematic of the actuation frame concept along with the pertinent dimensions annotated. This arrangement consists of two linkages affixed to each other via a hinge (point B). The larger

link (between point A and C; fr_{AC}) is the main part onto which the skin will be directly attached. One end of this linkage is restricted to move only in the spanwise direction (point A) where as the other end (point C) is free to move in the plane of rotation about point A (this equivalent to moving in the X-Y plane as marked in figure 5.11). This link has a length of l and is equal to the length of the active camber section (in the specific case of the presented prototype this value is 45 inches). Furthermore, this linkage is designed to be parallel to the skin slit in the undeformed configuration. The second smaller link, referred to as fr_{BD}, has a length of l_f and is oriented at an angle θ_{f_0} from the skin slit in the undeformed configuration. While it shares point B with fr_{AC}, the other end (point D) is pinned (spanwise distance d and chordwise distance h from point B in the undeformed configuration). Note that distance of point D from point A (l_D) has to always be greater than l_B for the system to work as prescribed. The end result of this arrangement of linkages ensures the skin (which is rigidly attached to fr_{AC}) undergo both the prescribed warp input of x_A along with the maximum chordwise motion at point C of y_C (the deformed configuration is also shown in the figure for comparison). To clarify, point C corresponds to the maximum camber end of the active camber section.

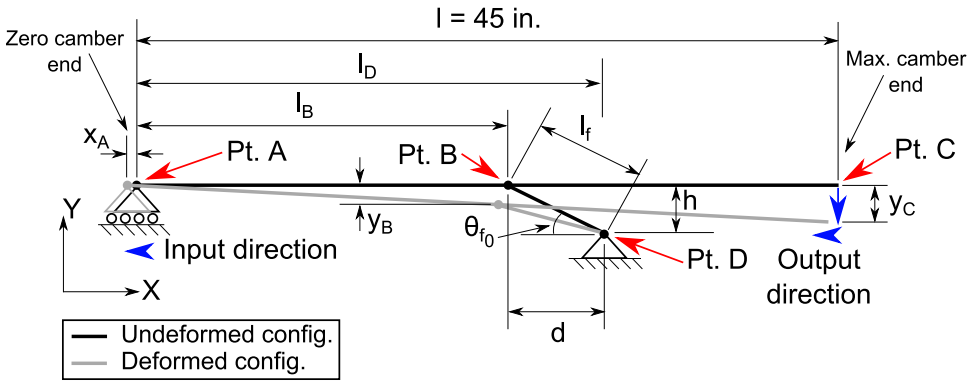

Figure 5.11. Actuation frame design schematic annotated with pertinent dimensions

Equation 5.1 present the kinematic equations corresponding to the system schematic presented in figure 5.11. Recall the line of action was set to be at a distance of 2.5 inches from the spar wall, however, in order to provide room for structure (including hinges and fasteners) h was set to be 1.875 inches. With this

restriction put in place the only two parameters that were unknown were l_f and l_B. For the current design in order to ease the machining requirements, the lengths of l_f and l_B were set to be round integers. In particular, l_B was varied from 12 to 36 inches in 4 inch increments, whereas l_f was varied from 3 to 9 inches in 1 inch increments. The constraint was to find the right combination unknown lengths that would produce vertical motion of y_C, prescribed to 0.55 inches to match the kinematics of the structure, for a given input of 0.1 inches (x_A).

$$\begin{aligned} d &= \sqrt{l_f^2 - h^2} \\ y_B &= h^2 - \sqrt{l_f^2 - (d + x_A)^2} \\ \theta_{f_0} &= sin^{-1}\frac{h}{l_f} \\ y_C &= \frac{y_B l}{l_B} \end{aligned} \tag{5.1}$$

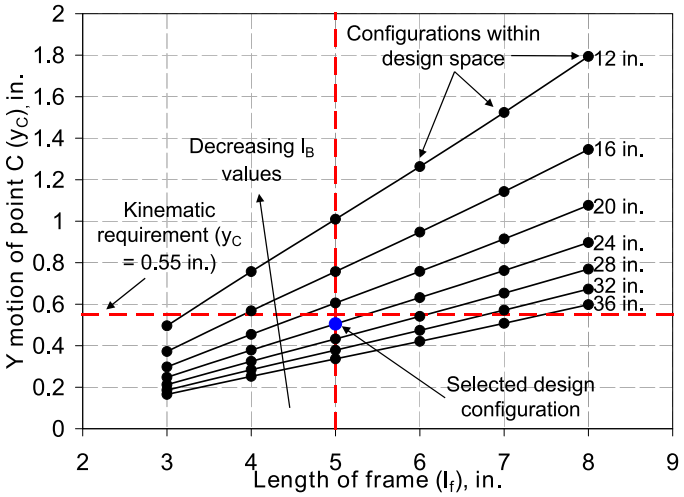

Figure 5.12. Actuation frame design selection chart for dimensions l_f and l_B given a warp input of 0.1 inch and requiring an output of up to 0.55 inch (chordwise motion)

Since there is one equation and two unknowns in general an infinite number of solutions exists. However, due to the physical limits placed on the maximum and minimum values of l_f and l_B and the discretizing of the possible solution space a visual approach was used to pick the design configuration. Due to manufacturing constraints it was generally preferred to have point B to be around the center of

fr_{AC} (corresponding to a value of l_B in the vicinity of 22.5 inches). Figure 5.12 presents the variation of the y_C value as a function of l_f for a varied range of l_B. Based on the design guidelines a length of l_B of 24 inches and 5 inches for l_f was picked from the possible configuration within the design space (marked as solid blade circles in figure 5.12). As seen in the figure this value is marginally lower than the required chordwise displacement, however due to the discretized nature of the design space this is the closest configuration possible. For future designs, the unknown lengths can be more finely tuned for a more refined configuration.

As the presented design only incorporates hinges that act in the same plane, the structure is expected to not be susceptible to jamming (when compared to designs that can involve sliding or telescoping members). Furthermore, as a result of the design only one linear actuator is required to introduce a warping input, as the structure itself ensures both the chordwise motion and warping of the skin slit. Due to this quality the presented design is thought to be better suited for a rotor blade.

5.4 Prototype design and construction

Having defined an actuation structure design which would satisfy the kinematic requirements of the blade structure now it was possible to conduct the detail design and construction of the variable camber prototype. The following sections outline the various components of the presented variable camber prototype.

5.4.1 Blade skin

In order to proceed further, the first task was to remove the honeycomb filler that was built into the blade. Figure 5.13 presents a view of partially removed skin exposing the interior honeycomb filler. The process of removing the honeycomb filler was started at the skin slit and then continued further towards the trailing edge. A combination of hacksaws and power tools were used to remove the filler

Figure 5.14 presents a detail view of the interior of the blade skin in its final state. As seen there is still little sections of low thickness filler remaining on the structure. As the filler had to be removed with care, so as not to damage the skin, it

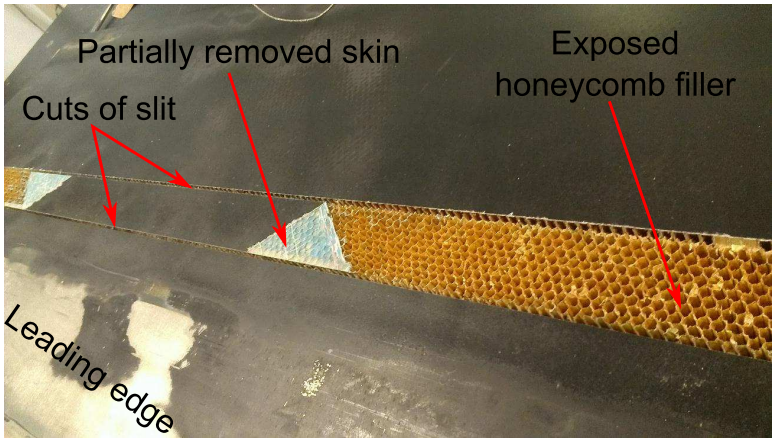

Figure 5.13. View of partial skin removed showcasing the honeycomb filler used in the construction

was very challenging to get tools into the low thickness regions of the trailing edge. Note that for a production blade this would not be an issue as the blade would be manufactured from the ground up to have the actuation mechanism rather than be a retro-fit as it the case for this blade.

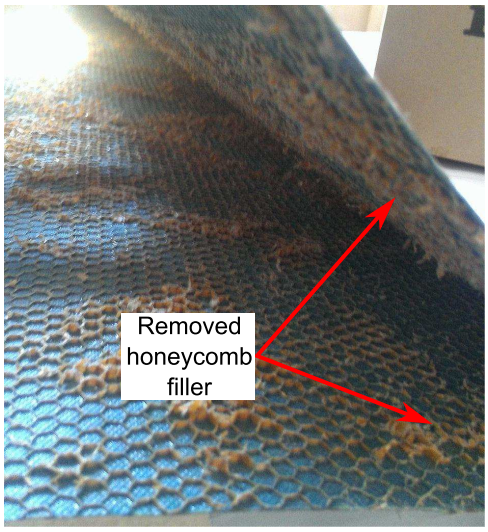

Figure 5.14. Interior view of the blade skin aft of the D-spar web wall with the honeycomb removed

Upon removing the honeycomb filler the effect it on the stiffness on the section aft of the D-spar wall is readily apparent (see figure 5.15). As can be seen the

Figure 5.15. Exterior view of the blade skin aft of the D-spar web wall with the honeycomb removed

skin is soft enough in bending to fall on itself. Therefore, while the current blade has no honeycomb filler, it is important to have some soft of a structure which maintains stiffness of the section through the cross-section thickness. While not shown explicitly in the presented pictures, there is a section of the trailing edge corresponding to the start of the 3% chord tab at the trailing edge which is observed to be significantly stiffer than the rest of the skin.

5.4.2 Actuation frame

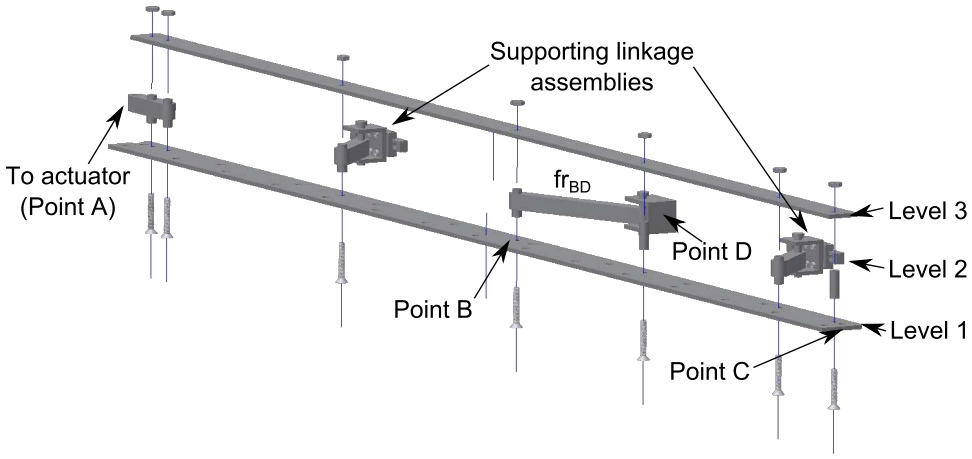

Figure 5.16. Exploded view of the actuation frame structure

Due to manufacturing and load path requirements, the actuation schematic design presented in section 5.3 is realized as a three level sandwich structure (Fig. 5.16). The three levels are designed to provide bending stiffness while allowing for hinges to be securely fitted between levels 1 and 3. All three levels are sandwiched

together via the use of an assembly of bolts and nuts. As seen in figure 5.17 level 1 consists of a 1.5 inch wide 0.125 inch thick plate with simple clearance holes intended for rivets and countersunk holes intended for bolts which will compress all three levels together. This is the level which is rigidly attached to the skin (which has a corresponding rivet hole pattern drilled into it). Similar to level 1, level 3 consists of a plate with simple clearance holes, however this place has a smaller width (1 inch compared to 1.5 inch for level 1). Both these levels have a span length equal to that of the active camber section (45 inches).

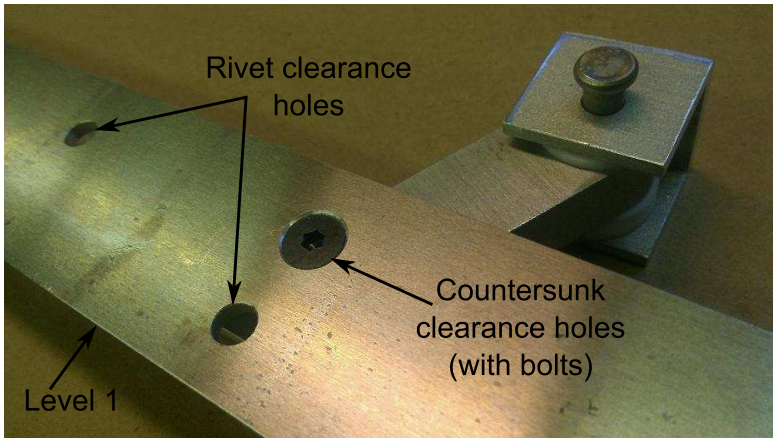

Figure 5.17. Detail view of the outer surface of level 1

Level 2 on the other hand consists of seven spacers which maintain the distance between level 1 and 3. Three of these spaces act as hinge for the actuation frame fr_{BD} (at point B) and two supporting linkage sub-assemblies. Another two spacers act as anchor points for the interface between the actuation structure and the actuator (at point A). Unless otherwise specified all the linkages shown here have a 0.5 inch square cross-section with 0.3125 inch holes at the connection points (this is an over-design to make the current assembly failsafe since it is a proof-of-concept design). The actuation frame fr_{BD} sub-assembly consists of the linkage itself and a supporting structure for point D (which includes a hinge comprising of a clevis pin) as shown in figure 5.18.

The two supporting linkage sub-assemblies (Fig. 5.19) are intended to provide bending load support (in the flapwise direction) to the actuation frame. These sub-assemblies do not affect the kinematic characteristics of the actuation frame

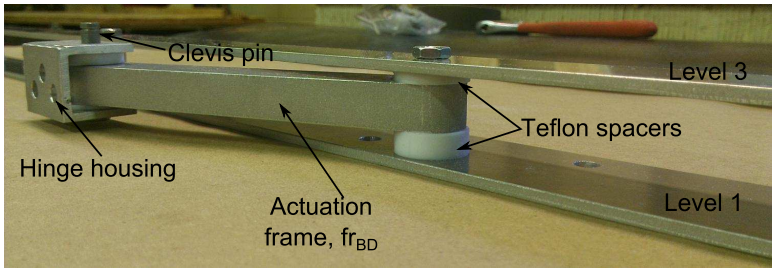

Figure 5.18. Detail view of the actuation frame fr_{BD}

at all. As such they contain a 2 inch long linkage connected to a hinge housing (similar in design as the actuation frame) which is affixed to a commercially available linear bearing. As the actuation frame undergoes motion the hinge housings of the supporting linkages are allowed to slide along the linear bearing. These two sub-assemblies are located at a distance of 13 and 40.5 inches from the actuation interface location (point A). The placement of these assemblies was based on distributing the supports as close to the ends as possible.

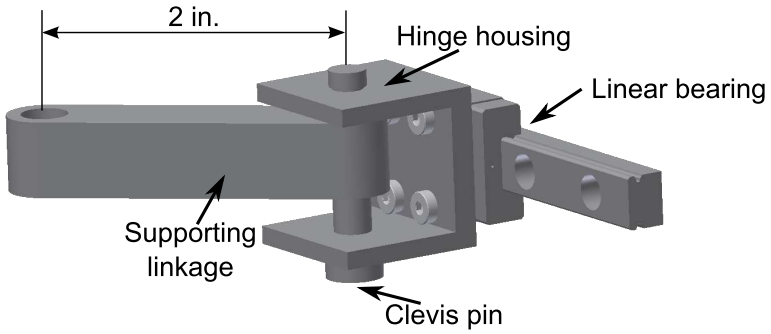

Figure 5.19. Detail view of supporting linkage sub-assembly

Lastly the actuator interface consists of a bar with two spacer slots (Fig. 5.20). This structure was designed to provide continuity of the load path from the actuator to the actuation frame structure. Note that between any two sliding surfaces Teflon spacers were sandwiched to provide some relief to internal friction forces while allowing for a snug fit of the components (as is evident in a number of the figures shown above).

Figure 5.21 presents a view of the final assembled actuation frame assembly (without the linear bearing of the supporting linkage sub-assemblies). Note the

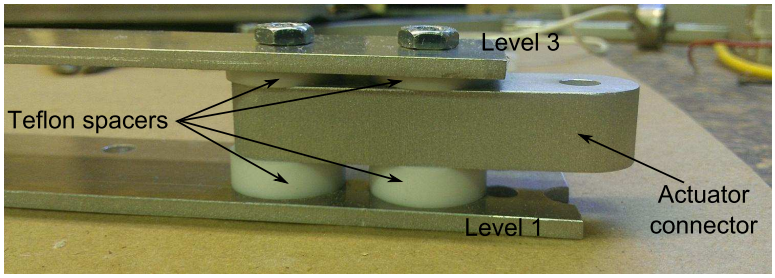

Figure 5.20. Detail view of actuator interface (at point A)

clearance holes on the top surface. These are the rivets locations which will connect to the lower skin of the blade section.

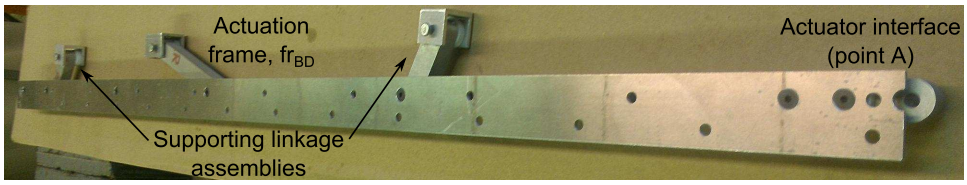

Figure 5.21. View of the completed actuation structure assembly

The entire actuation frame structure is affixed to the internal spar web wall using bolts which run through the spar itself (using clearance holes in the spar wall). As seen in figure 5.22 a mounting plate is placed along the surface of the spar web wall on the interior of the D-spar. This plate contains threaded holes through which the respective bolts of the various components (either for the actuation frame hinge housing or the supporting linkages linear bearings) are affixed. Using this assembly, the risk of the bolt threads stripping through the composite spar web wall under an applied load is reduced. This assembly essentially emulates the function of a doubler which is used to stiffen the structure around various holes within primary load bearing components of aircraft. All the components of the actuation frame structure (with the exception of the linear bearings) were built using Aluminum-6061. The components were built using a combination of water-jet and traditional milling and lathe manufacturing processes.

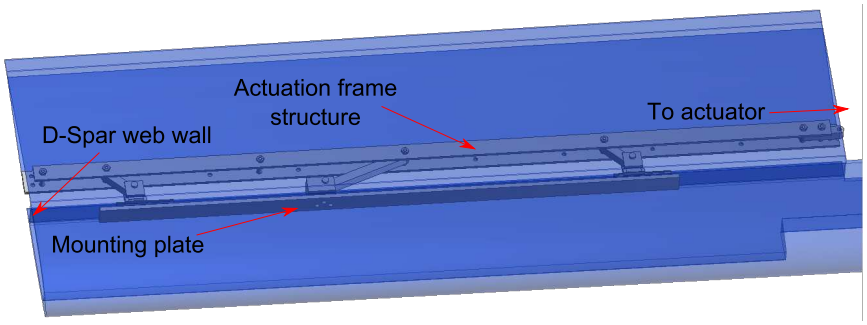

Figure 5.22. Schematic showing the actuation structure spar attachment assembly

5.4.3 Actuator sub-assembly

The second primary component of the presented design is the actuator sub-assembly. As shown in figure 5.23 this assembly consists of the actuator, sensors (load cell and actuator displacement) and various other supporting structures that ensures only pure spanwise warping input. Since the existing blade spar wall was removed for this section of the blade (due to the presence of tip weight slots and bottom surface port) a new replacement spar was affixed to which all the components of the actuator sub-assembly are attached. Note that the replacement spar is attached to the D-spar walls using three mounting blocks and is a retrofit measure for this specific prototype. Active cambers blades designed from the ground up are envisioned to have the actuator directly mounted to the actual blade D-spar web wall.

As seen in the figure load cell is positioned between the actuator and slide attach block. This assembly has been put in place to ensure that the load cell only measures (and therefore the actuator only experiences) the forces required along the spanwise direction. Furthermore, this arrangement also ensures that point A of the actuation structure (actuator interface bar) only moved along the spanwise direction as desired. In this configuration any chordwise load experienced is transferred directly to the spar. Therefore, for full scale blades, the spar would need to be specifically designed to carry these chordwise loads associated with camber actuation.

The specifications of the actuator used for the current study are presented in table 5.3 [23]. This is the same actuator used by Hayden for the rotor testing of

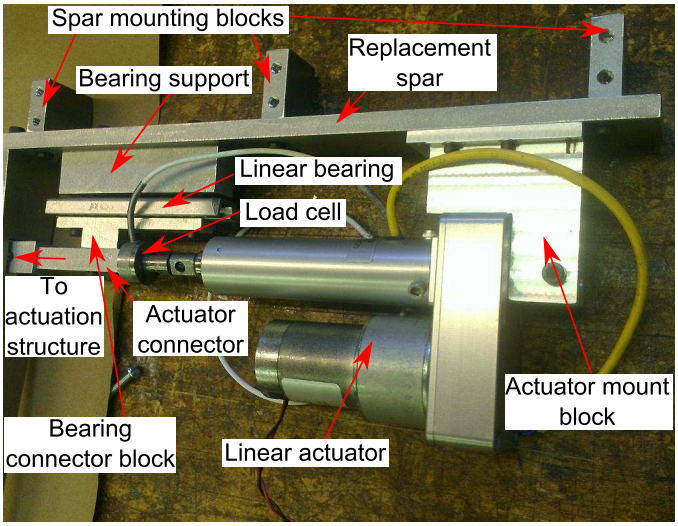

Figure 5.23. Actuator sub-assembly detail view with annotations

Table 5.3. Actuator specifications [23]

Prop. Name.	Specification
Max. Stroke	2 in.
Max. Force	500 lbs
Max. speed	0.12 in./sec
Weight	2.08 lbs

a variable chord rotor blade concept [166]. As can be seen in figure 5.24 the actuator has an built-in linear potentiometer which was used to measure the actuator linear input. This actuator was proven to work in a rotating frame [166] and is therefore suitable for operation on a rotor blade (with modifications applied). An Omega Engineering LC202-300 load cell was used for the current prototype. This model has a maximum load capability of 300 lbs and was used without a signal conditioner.

As can be seen in figure 5.25, which shows the completed internal structure assembly, the interface between the actuator sub-assembly and the actuation structure is a hinge. This allows for the fr_{AB} frame of the actuation structure to rotate independently of the actuator. Aside from the actuator, load sensor and the linear bearing (which was made of hardened steel) all the components of the actuator sub-assembly were made using Aluminum-6061. Similar to the actuation frame the components of the actuator sub-assembly were built using a combination of

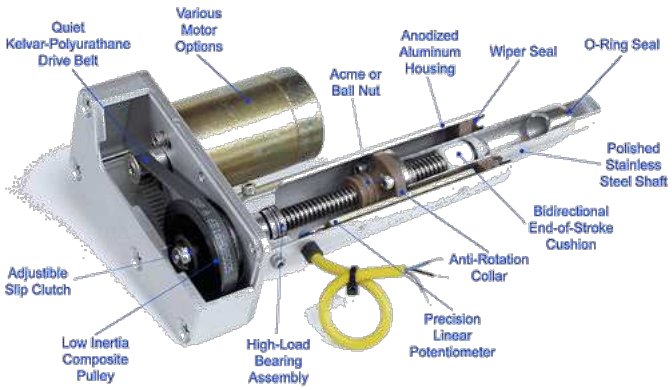

Figure 5.24. Bug actuator cut-away view [23]

water-jet and traditional milling and lathe manufacturing processes.

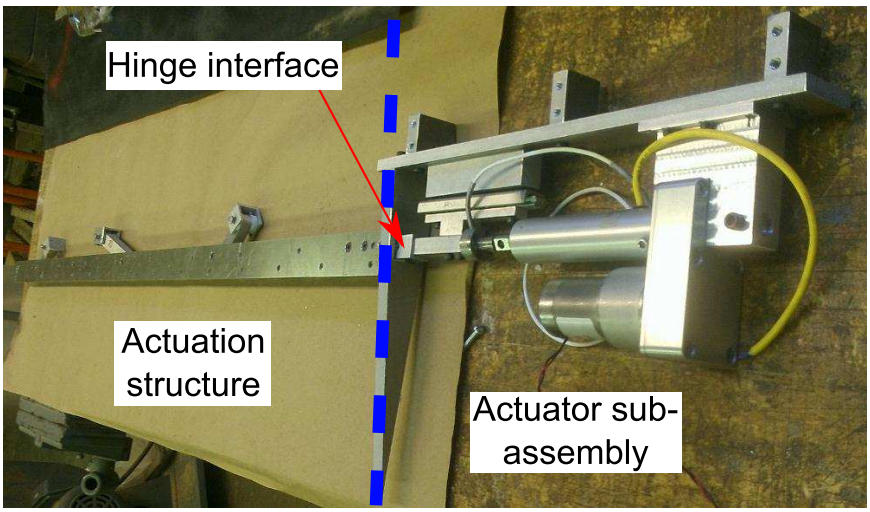

Figure 5.25. Completed internal structure with the actuator sub-assembly and the actuation structure highlighted

5.4.4 Slit cover lip

In order to complete the airfoil profile of the cross-section by covering the gap in the cross-section introduced by the slit a lip cover was installed. This cover consisted of a 3.5 inch plate (0.0625 inch thickness) which was affixed to the D-spar in such a position that is produced an overlap of 0.75 inches over the slit in

the undeformed configuration. In order to reduce sources of friction this slit cover lip was not installed during testing.

5.4.5 Camber sensor

Figure 5.26. Front view of the camber sensor (installed on the prototype)

Two separate techniques were used to measure the output camber of the presented prototype (Fig. 5.26). The first technique was the use of a digital angle gauge (digital level). The second method utilized a rotary potentiometer which was affixed to the D-spar web wall at the maximum camber end of the prototype (Fig. 5.27). In order to read camber angle produced by the prototype, the potentiometer was connected via an arm to a fixed point on the trailing edge of the blade cross-section, the digital level was then placed on this arm. Since the point on the trailing edge undergoes translation within the cross-section plane as the section undergoes camber, the angle of the connector arm (connecting the spar web wall and the trailing edge point) was equal to the camber angle of the cross-section. Note that a slot was placed in the arm to remove any jamming that may occur during testing.

The potentiometer was calibrated against the digital level. However, upon the installation of the potentiometer into the prototype, the data read from this sensor was shown to not be reliable (see section C.3.3). Therefore for the results presented only the data collected from the digital level was used as a measure of the camber produced.

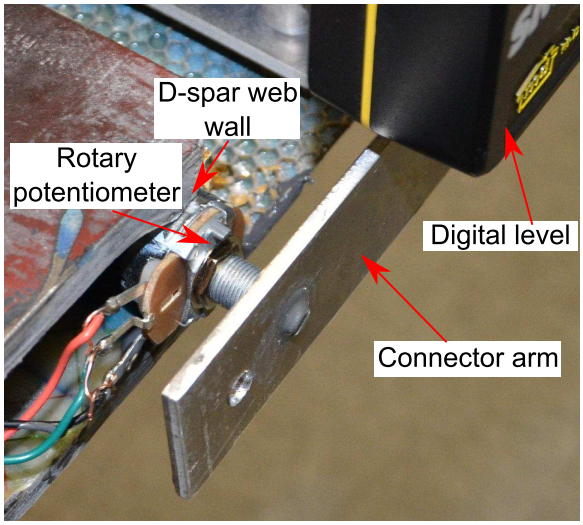

Figure 5.27. Detail view of the installed rotary potentiometer

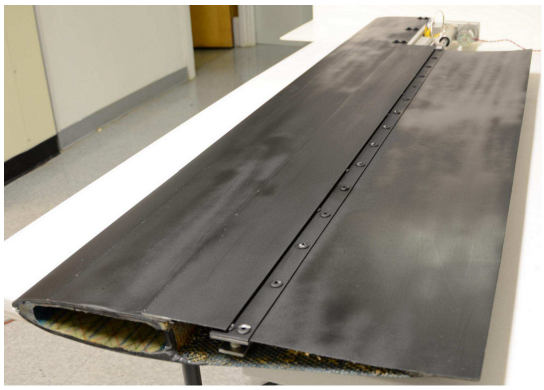

(a) Undeformed configuration

(b) Deformed configuration (maximum input warp)

Figure 5.28. Isometric views of the completed prototype in two configurations

5.4.6 Final assembled prototype

Figure 5.28 presents an isometric view of the final assembled prototype (with the slit lip cover) in the undeformed and deformed (maximum input) configurations. As can be seen an input warping is capable of producing an approximately linear distribution of camber. Figure 5.29 presents a front view of the blade cross-section at the maximum camber end of the prototype at varying levels of camber. As can be seen in the figure a significant variation of camber is possible with the current

prototype. The details of the camber angles and the forces required to actuate the device are presented in the following sections.

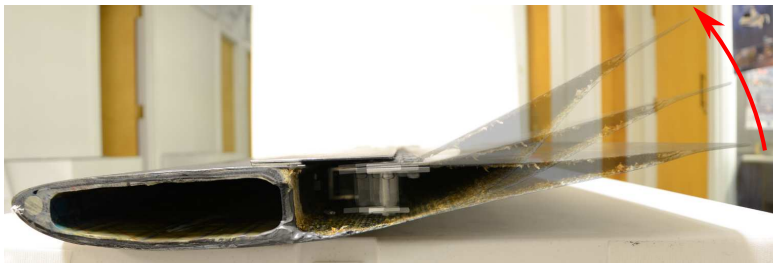

Figure 5.29. Front view of the maximum camber cross-section at varying levels of camber

5.5 Finite element model details

A finite element model of the assembled prototype was developed using ANSYS® Ver. 14.0. Figure 5.30 presents an isometric view of the final model. The model includes all the pertinent components of the actuation frame structure, however effective boundary conditions (motion only allowed in the spanwise direction, rotations about the X and Z axis not allowed) were applied at the actuation frame/actuator sub-assembly interface. This was done to reduce the number of elements in the design while maintaining model validity. The model is made of three different types of elements: Beam (BEAM188), Shell (SHEL181) and Brick (SOLID185) elements. The beam element used is the classic two node (with each node having 6 Degrees of Freedom, DOF) element. The shell element is comprised of four nodes, each with 6 DOF. Lastly, the brick element is modeled to have 8 elements each with 3 DOF (translation along three primary axis). Note that the brick element is only used for the case when the effect of a filler is considered. Overall, the elements were sized to have element size of 0.2 inches, resulting in a fairly fine mesh.

The actuation frame structure is entirely modeled using beam elements. Furthermore, as stated earlier, since all the components were made aluminum, all of the elements were set to have a corresponding modulus of 10.6e6 psi. Furthermore all the elements were set to have the same cross-section of the physical parts they were representing (note that details such as hinge holes and curved ends were not

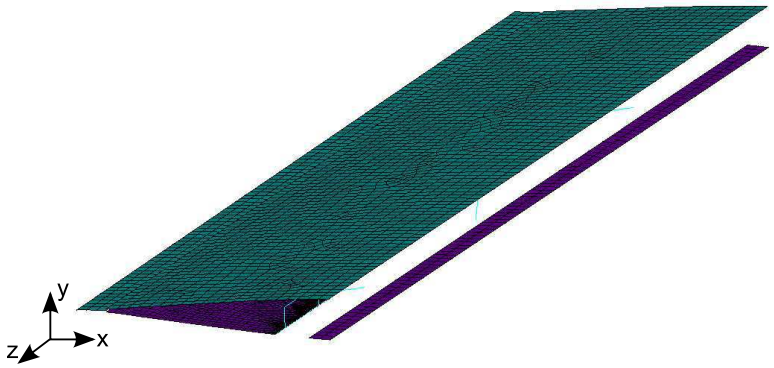

Figure 5.30. Isometric view of the variable camber blade prototype finite element model used for the current study

explicitly modeled).

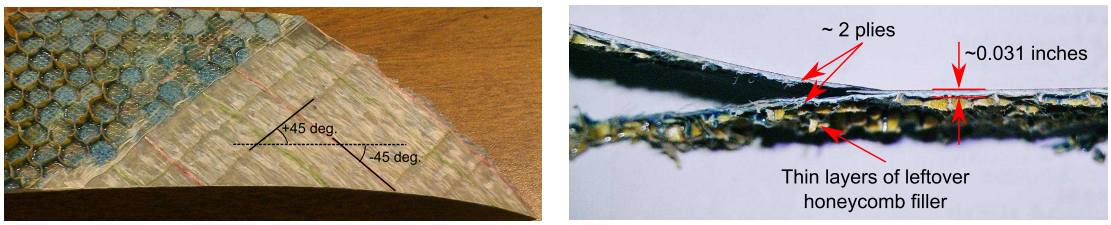

(a) Ply orientation (b) Number of plies

Figure 5.31. Visual inspection of the blade skin construction

The skin and the trailing edge tab of the blade were modeled using shell elements with various layups (pertinent to the section under consideration). Based on a visual inspection of the skin of the prototype (Fig. 5.31) it was observed that the skin was comprised of (approximately) ±45 degree plies (Fig. 5.31(a)). A closer inspection reveals that the top and bottom skin, on average, each consisted of two ply layers (Fig. 5.31(b)). Based on the average thickness of the skin of 0.031 inches, each layer was assumed to be 0.016 inches. As highlighted in figure 5.31(b) there were still thin layers of leftover honeycomb filler which can contribute to errors in the stiffness of the skin. The fiber material was approximated as glass fiber and the material properties approximated for each ply are listed in table 5.4. The moduli presented are based on the average values for glass fiber and glass fiber epoxy matrix found on Matweb [191]. Furthermore it is assumed that the plies are not weaved and hence the shear, matrix direction and thickness direction moduli

values correspond to that of the epoxy matrix.

Table 5.4. Approximated skin ply stiffness properties (along ply axes)

Stiffness	Value
E_{11} (Fiber extension modulus)	9.96e6 psi
$E_{22} = E_{33}$ (Matrix extension modulus)	5.85e5 psi
$E_{12} = E_{13}$ (Matrix shear modulus)	2.18e5 psi

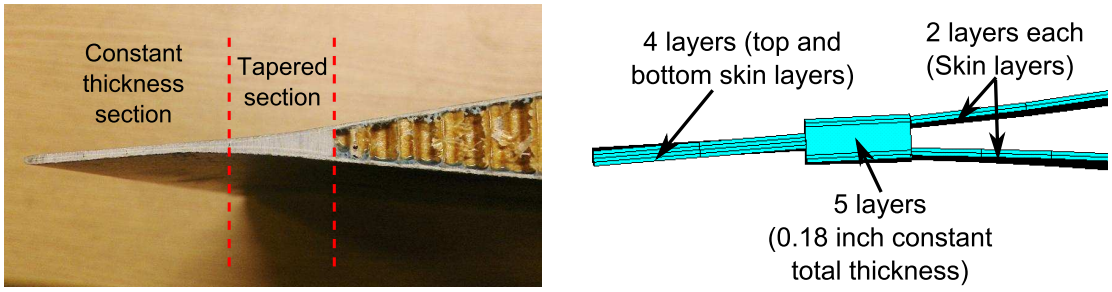

(a) Blade trailing edge

(b) FEM trailing edge

Figure 5.32. Comparison of physical blade trailing edge (with tab) to the corresponding finite element representation

A visual inspection of the trailing edge tab reveals the bonding of both top and bottom skin layers in two sections of varying and constant thickness respectively. Figure 5.32 presents a view of the actual tab on the blade alongside the finite element model representation of it. As can be seen in figure 5.32(a) the trailing edge of the model consists of a tapered section of length approximately 0.45 inches followed by a 0.9 inches (approximate) section of relatively uniform thickness. Correspondingly, in the finite element model (as seen in figure 5.32(b)) the tapered portion is modeled as a section of constant thickness (0.18 inches) which is comprised of 5 layers. The top and bottom two layers correspond to the same layup as the top and bottom skins respectively (i.e. ±45 deg., 2 plies) whereas the middle layer is assumed to be comprised of epoxy filler and therefore is set to have the corresponding moduli (see table 5.4). Lastly, the constant thickness section is modeled as a composite comprising of four layer corresponding to the two layers of the top and bottom skins respectively. This final layup is an approximation of the actuation structure based purely on visual inspection of the prototype. As the blade was from a commercial product, the actual blade layup materials was not

available in open literature and hence such an approximation of the stiffness was used (correspondingly this may be the source of some error in the calculation).

The nodes corresponding to the D-spar section of the blade are clamped (all 6 DOF constrained) to represent the stiff spar. Furthermore, as stated earlier the actuation structure/actuator sub-assembly interface location is allowed to only move along the spanwise direction. The input warping applied is up to 0.15 inches (away from the maximum camber section). Note that the maximum input warp is larger than the maximum input warp the structure was designed for. This was done to check for the effectiveness of the actuation structure beyond the design point.

5.6 Experimental setup

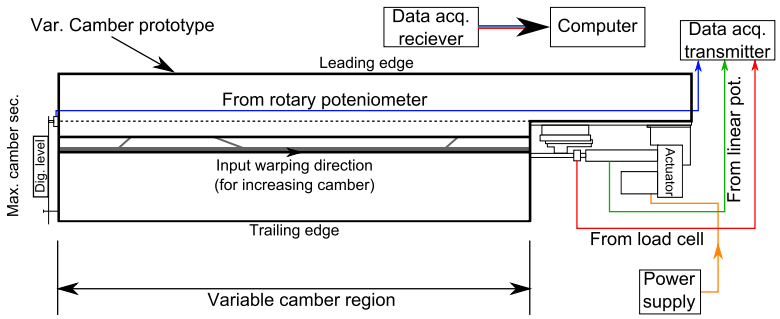

Figure 5.33. Schematic diagram of the experimental setup used

Figure 5.33 presents a schematic of the experimental setup used for the current analysis. The rotary potentiometer, linear potentiometer (from the the actuator) and the load cell signals were fed directly into the data acquisition transmitter unit (after digitization). The digital signal was then received by the data acquisition transmitter which was then fed to a computer with the appropriate software (which also recorded the data for further post-processing). The digital level measurements were recorded manually into the computer. Since the data acquisition system digitized the signal from the sensors the data was stored as bit values. This data was then converted to the equivalent physical measurement unit using the experimentally measured calibration curves (see section C.3). For the experiments

the D-spar was clamped for stability. Prior to the fully assembled prototype tests, the actuator structure by itself was tested to visually observe the frame kinematics, the result of this test is presented in section C.4. The input was cycled from zero to maximum warping (up to 0.18 inches) several times to understand the system hysteresis.

5.7 Results

The following sections present the experimentally measured data as compared to the numerical results predicted by the finite element model. Furthermore, using the validated finite element model, a study is conducted to understand the effects of various external forces on the actuation behavior of the system. Lastly, an explanation of the effect of a cross-section filler on the system behavior is presented along with plausible filler concepts. Due to the malfunctioning rotary potentiometer discussed earlier, all the camber measurements presented in the following sections are from the digital level.

5.7.1 Warp-camber relationship

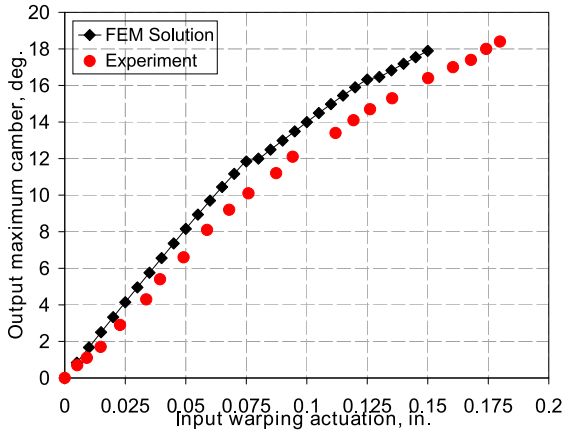

Figure 5.34. Comparison of the warp-camber relationship measured experimentally against the finite element model results

Figure 5.34 presents the output maximum camber as a function of the input warping, measured experimentally as compared to the finite element result. As

can be clearly seen the results agree very well. The minor deviations observed are attributed to the small imperfection in the hinge designs which introduce some play in the system. Due to the high ratio of output to input a small change in the frame movement relates to a relatively large change in the tip camber.

5.7.2 Warp-force relationship

Corresponding to the warp-camber relationship, figure 5.35 presents the actuation force measured as a function of input warping, as compared to finite element model results. This figure clearly shows the good agreement between the two results. The spike in the forces measured for input warping greater than 0.15 inches is due to internal binding between the actuation frame (fr_{AC}) and the hinge housing of the supporting linkage hinge housing. Note that the finite element model does not account for such a contact effect and therefore would not be able to predict such a spike.

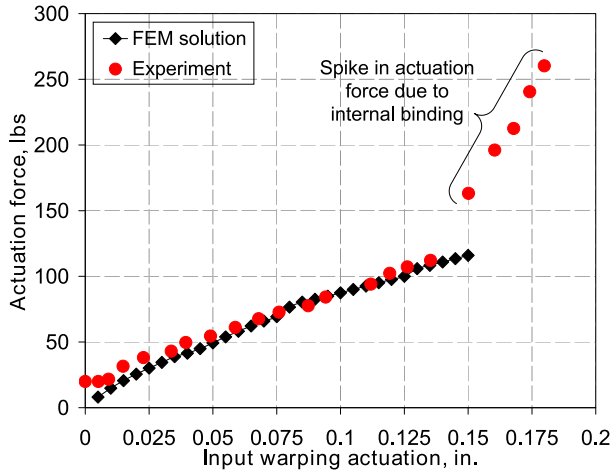

Figure 5.35. Comparison of the experimentally measured actuation force variation as a function of input warping against the finite element model results

5.7.3 System hysteresis

Figure 5.36 presents the warp-camber and warp-force hysteresis loops of the system for two separate complete actuation loops. As can be seen in figure 5.36(a)

there is exists hardly any hysteresis in the system for the case of the warp-camber relationship. However, while relatively low, there does exist a slight variation between loading and unloading portions of the warp-force relationship curve (Fig. 5.36(b)). This is primarily attributed to internal friction in the system as well as some effects of pre-strain introduced in the system as a result of human error during the assembly of the prototype. Note while there is a variation observed, it is fairly repeatable, as is evident by the matching of the curves of the two different experiment data sets.

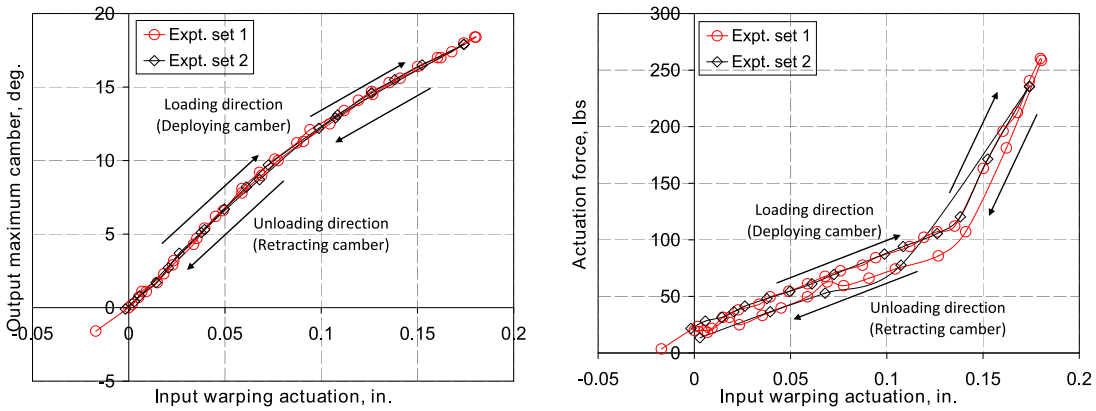

(a) Warp-camber var.

(b) Warp-force var.

Figure 5.36. Comparison of the operating cycles of two separate experiments sets to identify system hysteresis characteristics

5.7.4 Effect of applied loads

The proceeding results highlight the effect of both aerodynamic and dynamic forces acting on the variable camber blade kinematic behavior. Furthermore, the effect of variations in boundary conditions will also be presented. Each variation in applied load or boundary condition is treated as a new case and will be designated with increasing case numbers. For the following sections, the finite element model results for the benchtop experiments are used as a reference case for comparison to the results of the various cases. For the proceeding analysis the Y-axis is oriented through the thickness (positive towards the upper surface), X-axis is oriented in the chordwise direction (positive towards the leading edge) and the Z-axis is oriented

along the spanwise direction (positive is pointing outboard).

5.7.4.1 Centrifugal loads

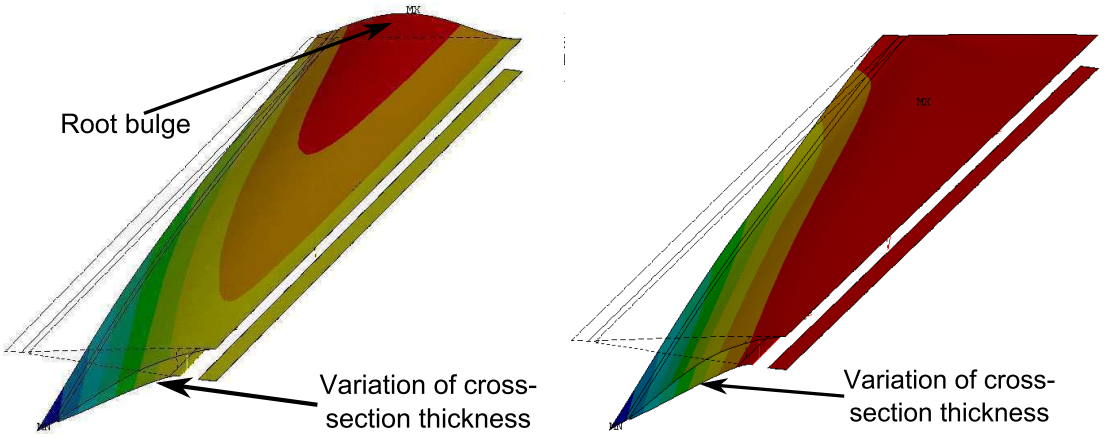

(a) Case 1 (b) Case 2

Figure 5.37. Isometric view of the displacement of the model nodes along the y-axis for the maximum input warping configuration for case 1 and 2

Using the CH-46E baseline blade configuration (and the results of the study presented in chapter 4) the maximum camber section of the blade was placed a distance of 67.6 inches from the center of rotation as this is the root cut-out location of the CH-46E [27] (the quarter chord location is placed along the radial axis emanating from the center of rotation; the blade is assumed to have a zero angle of attack at the root cut-out). The mass distribution used in the finite element model for this study is based on the physical device. The rotor speed was set to 263.7 RPM which corresponds to that of the CH-46E [27]. Case 1 presents the effect of centrifugal forces only on the blade behavior (that is the current variable camber prototype with no modifications on a rotor test stand in a vacuum chamber). Figure 5.37(a) presents an isometric view of the deformed configuration (with input warping and centrifugal forces) of the blade as predicted by the finite element model (the contours refer to the displacement along the Y-axis). As can be clearly seen the centrifugal forces acting on the structure has an detrimental impact on the camber distribution produced by the blade. The two clear features of this detrimental effect is the bulge which occurs at the zero

camber end of the blade and the variation of the cross-section at the maximum camber end. This cross-section variation is primarily due to the lack of a filler in the current setup.

While the current prototype is a stand alone proof-of-concept device, on a full scale blade the variable camber section would only be a part of the full blade. As such, the top surface at the outboard end of the active camber section (corresponding to the section with no camber) would be continuous with that of the passive portion of the blade that immediately follows. The effect of this continuity can be emulated via the application of the continuity boundary condition wherein the nodes of the top surface of the skin at the no camber cross-section are restricted for all 6 degrees of freedom. The result of this new applied boundary condition (Case 2) is apparent in figure 5.37(b) which shown an isometric view of the deformed configuration of the blade at maximum warp input of 0.15 inches. As can be clearly seen the addition of the continuity boundary condition causes the system to behave better. In particular, it removes the root bulge but does not alleviate the cross-section variation effect (as seen highlighted in the figure).

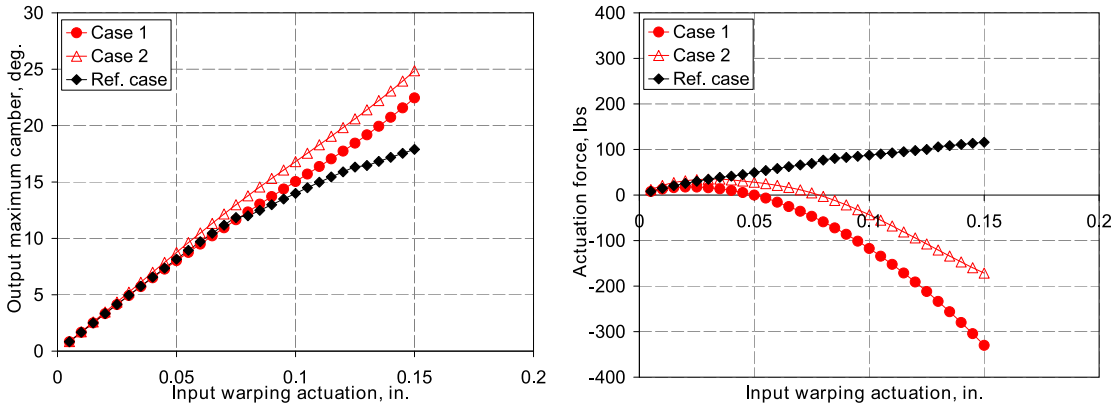

(a) Warp-camber var. (b) Warp-force var.

Figure 5.38. Comparison of the warp-camber and warp-force relationships (as a function of input warping) of case 1 and 2

Figure 5.38(a) shows the variation of the calculated tip camber as a function of warping for case 1 and 2 as compared to the reference case. As seen in this figure the addition of the continuity boundary condition removes some of the nonlinearities in the warp-camber relationship for the reference case (no centrifugal

forces applied). Note that the camber variation here is calculated using the translation of the trailing edge only and is therefore unable to capture the quality of the camber produced.

Alternatively figure 5.38(b) presents the variation of the actuation force as a function of the input warping for both cases. In this figure a clear departure in trends is observed, as compared to the reference case. This highly non-linear relationship is primarily due to the variation of the location of trailing edge of the cross-section. Starting with no camber as the warping is increased, the trailing edge of the blade is lowered below the chord-line of the baseline. This change in location results an outward pushing force acting on the trailing edge of the blade, which in turn results in a reduction of the net force required to produce incremental warping. In fact, at a critical warp value, the required actuation force crosses the zero mark and there is now aligned in the opposite direction of input warping. The application of the continuity boundary conditions aids at delaying the effect of actuation force reversal, however the overall trend still remains.

5.7.4.2 Centrifugal and aerodynamic loads

Case 3 considers the effects of representative aerodynamic loads applied to a rotating variable camber blade section with the continuity boundary condition applied. The aerodynamic effect here is implemented via the use of effective applied aerodynamic hinge moment. For the current model a representative operating condition of Mach 0.2 (recall the variable camber section is situated at the blade root) with a blade angle of attack of 4 degrees. Using XFOIL element model via the application of a distributed force at the trailing edge nodes which produce the representative moment at the 0.4c point. This method on applying the hinge moment was chosen for its relative simplicity. Furthermore, initial trials for the application a distributed pressure on the upper and lower surfaces lead to significant convergence instability issues of the model.

Figure 5.39(a) presents the deformed configuration of case 3 with contours highlighting the y-displacement of the model nodes. As can be clearly seen the skin begins to dimple at the root due to the application of the effective hinge moment. This effect is similar to the one presented by Mistry et. al. [202] in relation to the warp induced variable twist prototype. Apart from the issues highlighted, for

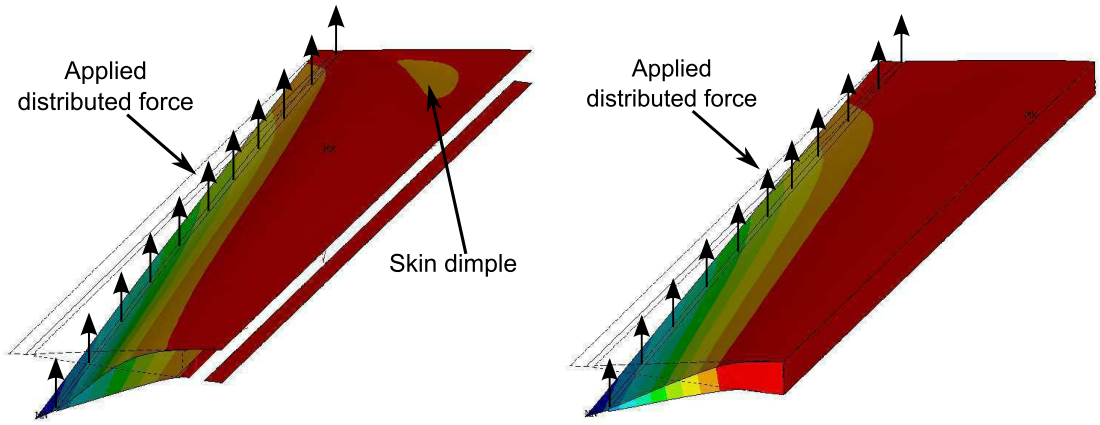

(a) Case 3 (b) Case 4

Figure 5.39. Isometric view of the displacement of the model nodes along the y-axis for the maximum input warping configuration for case 3 and 4

all the cases, the blade thickness varies to some degree when the cross-section is cambered due to the lack of a core (filler). Recall that since the variable camber works on the premise of warping, a filler with high shear stiffness would corresponds to undesirable deformations and high actuation forces. To abate this, case 4 (in addition to all the forces and boundary conditions used in case 3) considers the effect of a filler which has a very high extension stiffness along the Y-axis but is relatively soft in the remaining direction (in particular all three shear stiffnesses are relatively low). The representative filler material properties used for the current study is listen in table 5.5.

Table 5.5. Representative stiffness of hypothetical filler used in case 4

Stiffness	Value
$E_{xx} = E_{zz}$	1 psi
E_{yy}	1000 psi
$E_{xy} = E_{xz} = E_{yz}$	1 psi

Figure 5.39(b) presents the deformed shape of the variable camber blade for case 4. As can be clearly seen, no skin dimpling is occurring in the vicinity of the zero camber section. Furthermore, the variation of the blade cross-section thickness is also eliminated (note the solution presented is for a input warping of 0.08 inches, as the model convergence could not be achieved beyond this value).

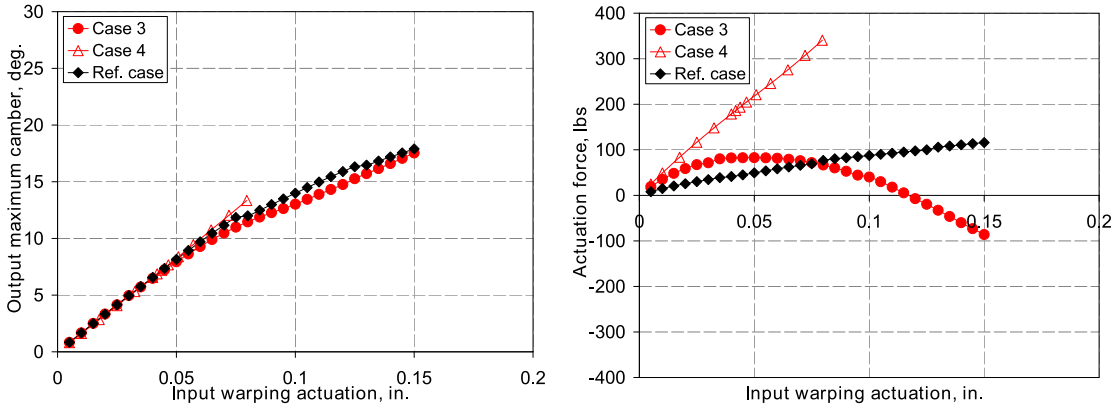

(a) Warp-camber var.

(b) Warp-force var.

Figure 5.40. Comparison of the warp-camber and warp-force relationships (as a function of input warping) of case 3 and 4

Figure 5.40(a) presents the variation of the output camber as a function of input warping for case 3 and 4 as compared to the reference case. As can be seen the variation of the tip camber with input warping is well behaved. Further comparing the actuation forces reveals the major effect of using a filler (Fig. 5.40(b)); i.e. using a filler corresponds to higher actuation force requirements. While this is an expected effect, the increase in actuation forces is not unreasonable and can be easily realized using the actuator used in the current prototype (albeit for a lower maximum camber angle).

5.7.5 Possible core design

As presented in the previous section, introducing a core filler which has high through the thickness stiffness (relative to stiffness along the other directions) produce a very clean camber of the blade cross-section even under aerodynamic and centrifugal loads. While a material with the desirable stiffnesses can be engineered for the specific application, another possible way to achieve this property for the filler is to use flexure ribs. A schematic representation of such a concept is presented in figure 5.41. The flexural ribs are envisioned to have a main spine which on one end is affixed directly to the D-spar web wall (Fig. 5.41(a)). From this spine several arms branch out which have tabs at the tips. Each of these tabs are fit into guides which are directly attached to the blade skin. The orientation

of these guides follow the prescribed motion of the skin which corresponds to the warp-chordwise motion kinematics specific to the blade (Fig. 5.41(b)). In this arrangement while the shear stiffness is minimized the extension stiffness provided by the branch arms of the ribs ensure the cross-section remains well behaved when a camber is introduced. Furthermore, this arrangement also resists undesirable deformations under the influence of aerodynamic loads. This type of concept is similar to the sliding ribs used by Mistry et. al. [202].

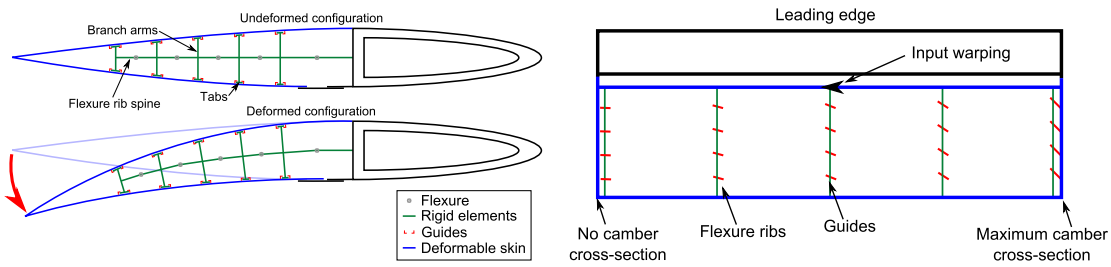

(a) Cross-section view (b) Top view

Figure 5.41. Schematic representation of a possible core filler concept

Considering the presented solution introduces several sliding elements, there is a high risk of jamming. Furthermore, due to the sliding, the actuation forces are expected to be higher due to friction. Lastly, the manufacturing and assembly of these types of ribs into the blade cross-section may be complicated and therefore can be cost-prohibitive. These challenges warrant the need for the further exploration of this and other methods to achieve the required properties of the filler.

CHAPTER 6

Conclusions

The sections in this chapter present the conclusions derived for the analysis conducted on two separate quasi-static rotor morphing concepts: Variable span systems and Variable camber systems. Following this, the future work direction will be summarized for both concepts.

6.1 Variable span system

The following conclusions pertain to the variable span system analysis. As part of this body of work, the performance analysis of a variable span system based on a UH-60A type aircraft was conducted. Variation in radius of $+17\%$ to -16% and in RPM of $\pm 11\%$ about the nominal is considered. Furthermore, various actuation concepts to achieve the proposed span variation were considered and analyzed. Based on the presented results the conclusions derived are grouped into ones pertaining to the performance anslysis, followed by points pertaining to the variable span system design which are presented in the following sections.

6.1.1 Performance analysis

With RPM variation only, power reductions of up to a maximum of 14% were obtained in cruise (80-100 kts). The power reductions become smaller at higher speed, altitude and gross weight. At very high gross weight, RPM variation alone is practically ineffective in reducing power. The power reductions come from reduced profile power associated with lower dynamic pressures when RPM is reduced. This phenomenon cannot be exploited at very high gross weight or altitude as it would increase the propensity for the rotor to stall. The effectiveness of RPM variation in reducing rotor power also diminishes at low speeds, as induced power (which dominates at these conditions) is not significantly affected by RPM variation.

With radius variation only, power reductions of up to a maximum of 20% were obtained at high altitude and gross weight (high-and-heavy conditions) with increase in rotor radius, which both decreases the disk loading (and induced power), as well as decreases the angle of attack around the disk (and hence decreases the drag coefficients or profile power). At low to moderate gross weight, the power reductions are generally lower than those observed due to RPM change, except at low flight velocities. For these conditions increases in radius reduce the induced power albeit at the cost of increased profile power.

With a combination of radius and RPM variation, the overall reductions in power are significantly higher than those obtained through use of RPM or radius variation alone. When used in combination, minimum RPM is always favored, with radius varying to allow this. At low and moderate gross weight for low to cruise velocity, power reductions at sea level are similar to those realized with RPM variation alone. However, with increasing altitude while the power reductions for RPM variation alone quickly decreased when RPM-radius variations are used in combination, an increased radius is favored with increasing altitude, and significant reduction in rotor power is achieved even at high altitude. While RPM-only showed the largest power reductions in cruise, and radius only appeared to be quite effective in low-speed operation, with the combination of RPM and radius variation good power reduction is realized over the entire airspeed range. At high gross weight and altitude, the combination of radius increase and RPM reduction gives power reductions of over 20% and up to 30%. Although radius increase only was effective for reducing power in high-and-heavy conditions, the power reductions quickly

diminished as the high gross weight aircraft operated at low altitude. In contrast, for high gross weight, the combination of radius and RPM variation shows power reduction even at low altitude.

For high and heavy conditions, the variable span system in conjunction with variable rotor speed were able to show significant improvement in the range and endurance of the aircraft. In particular, up to a 65% increase in range and 28% increase in endurance was calculated.

6.1.2 System design analysis

Four different variable span system design were proposed: Hydraulic system, threaded rod (jackscrew) system, linear spring and cellular structure based system. The systems were selected based on space and actuation constraints. Based on the analysis conducted, the proposed solutions were found to have significant challenges due to implementation issues (for the assumed blade weight).

Hydraulic systems were shown to be infeasible due to the high pressure required to actuate the pistons in the rotating environment. In particular, approximately 10000 psi would be required while maintaining the stresses within the cylinder structure below allowable limits. Analysis of jackscrew type devices showed the requirement of high power rotary actuators to allow for feasible deployment times. The major constraint for this type of system was the placement of the rotary actuator within blade housing.

Linear spring systems considered for a passive variable span system showed very high levels of stresses within the spring coil. Furthermore, the pre-strain levels required to maintain outboard blade section motion were shown to be larger than maximum allowable install length. A cellular structure based non-linear stiffness system was also considered for the variable span system. This type of system while apt from an install length (low pre-strain length) view point were shown to introduce larger than allowable stress limits within the internal components.

6.1.3 Future work

Based on the presented study, while the performance benefits of a variable span rotor system are significant, the design of the structure poses an equally significant

challenge. The design analysis showed the limitations of several active and passive concepts to realize the span variation of a full scale rotor system. However, it may be possible to apply the same designs to smaller aircraft as the centrifugal load requirements would be lower. Furthermore, considering the high risk of the variable span concept, using them for unmanned vehicles (including micro air vehicles) may prove to be the ideal configuration.

Therefore, as a possible path forward, the effects of the variable span rotor concept on the performance of smaller unmanned rotating wing vehicles should be considered. Furthermore, to improve the design efficiency, rather than treating the morphing concept as a retrofit to an existing design, it should be used as a feature that is considered from the ground up. Another avenue of exploration is the use of hybrid systems for active actuation, for e.g. the use of hydraulic cylinders in parallel with springs.

6.2 Variable camber system

The following conclusions pertain to the variable camber system analysis. As part of this body of work, the performance analysis of a warp induced variable camber system based on a BO-105 type rotor in hover was conducted. Variation in the active camber configurations were considered along with the effects of blade torsional elasticity and twist for a variety of thrust levels and altitudes. This was followed by the design, fabrication and testing of an actuation structure to realize the variable camber. Based on the results, the following conclusions are derived, grouped into those pertaining to the performance analysis, and those pertaining to the system design and hardware.

6.2.1 Performance analysis

Chapter 4 presents the comprehensive analysis of the effect of the quasi-static variation of camber on the performance of a rotor system in hover. The analysis was carried out using a thoroughly validated numerical hover rotor model which incorporates a deformable geometry rotor (free) wake model, airfoil aerodynamic table look-up scheme with a torsionally elastic rotor model. The rotor model was

analyzed for three different gross weights, range of altitudes and for various camber configurations (root and tip maximum partial and full span linearly varied camber along with root and tip maximum partial and full span constant camber used as reference cases). Based on the results presented the following conclusions were drawn:

- Camber variation can provide a means of reducing the operating power requirement of the prescribed rotor system in hover .
- Root maximum camber cases, in particular partial and full span linearly distributed camber (maximum camber at the root) are preferred over the tip mounted camber configurations.
- The power reductions observed for a variable camber configuration are shown to increase with gross weight and altitude.
- The full span linearly distributed camber configuration is shown to provide significant power reductions over the baseline rotor performance levels (upto 18% compared to the baseline) along with improvements in the maximum altitude capabilities for the range of thrust levels considered.
- The performance levels of blades with no pre-twist can be significantly improved using appropriate camber distributions. Furthermore, the ability of camber distributions to emulate the effect of pre-twisted of various magnitudes (upto 12 degrees at sea level) is also shown.
- The power reductions due to the distribution of camber are shown to be dominated by the reduction in induced power.
- Isolation of the effects of camber have shown that the reduction in induced power is primarily a result of the shift of the thrust produced towards the root via the direct increase of the lift due to camber and not the elastic twisting of the blade.

6.2.2 Design analysis

As part of the design analysis the kinematics of the blade warping were considered in fair detail. Based on this analysis it was observed that in order to obtain a

smooth clean camber profile it was imperative to allow the slit to deform in the chordwise direction. A unique actuation structure design was then developed based on the calculated kinematic relationship for the case of no external applied loads. This design was then realized in physical hardware which was installed in a CH-46E blade section. Sensors were installed in the blade to measure the actuation force and output camber as a function of the input warping. The prototype was able to realize up to 18 degrees of camber (on the benchtop) for an input warping of 0.18 inches.

Correspondingly a finite element model (FEM) based on the physical prototype was also developed. Comparison of the FEM results against the experimentally measured data showed very good agreement. The minor deviations observed were attributed to the play in the system due to minor manufacturing imperfections.

The validated finite element model was then used to develop an understanding of the effects of external centrifugal and representative aerodynamic loads on the system. The study showed that the absence of the filler would result in (for some cases significant) distortion of the output blade camber in the presence of centrifugal and aerodynamic loads. Furthermore, this study also showed that if the active camber section were to be installed with a filler with high through the thickness stiffness (compared to the other directions) satisfactory output camber at reasonable actuation forces can be realized even under external loads.

6.2.3 Future work

Based on the results presented it is clear that a variable camber system can provide significant performance improvements. However, while the presented study provides for the justification of using variable camber, significant effort must be dedicated to further develop a comprehensive understanding of the effects of a variable camber system. These possible future research paths are listed below:

- While the current work was focused on the performance benefits of variable camber in hover, the specific details to its implementation in cruise and high-speed forward flight still needs to be considered.
- The current study focuses on the effects of variable camber on a simple planform rotor system of the BO-105 only, therefore it would be interesting

to explore the effects of variable camber on different types of aircraft (either heavier or lighter than the BO-105) with varying blade planforms.

- So far the effects of variable camber on edgewise rotor has only be considered, therefore, the effects of variable camber on tilt-rotors as an alternative to quasi-static variable twist is also another interesting concept that needs significant consideration.

- As the BO-105 rotor system was used in the current study, the rotor blade torsional elasticity was fixed. However, changes in the torsional elasticity of the blade can have an impact on the effects of variable camber, for example, for a torsionally soft rotor perhaps tip maximum linearly distributed camber may be better suited as it would operate as a blade twisting device.

- As part of the current study the effect of rotor speed variation in conjunction with camber was explored for operation at sea level. Therefore the performance characteristics of rotor speed and camber variation at different altitudes needs to be considered in detail.

- The current study uses free vortex based wake to analyze the aerodynamic effects of camber. Therefore, to further increase the solution fidelity the use of a higher order methods (such as full CFD) for the rotor wake solution along with a comprehensive rotorcraft analysis model needs to be used.

Based on the design study undertaken for the variable camber system the following possible future research paths were identified:

- The design and implementation of a shear flexible core for the region aft of the spar wall to alleviate spurious deformation modes under centrifugal and aerodynamic loads is of paramount importance.

- In order to fully understand the effects of external loads, further testing of the design on a whirl tower and/or vacuum chamber much be conducted.

- While the current study shows the effects of variable camber numerically, it is important to ascertain the benefits directly through rigorous wind tunnel and whirl tower testing.

- The presented actuation scheme is a method to input the required warping (and hence realize camber), however, the development of other potentially passive (rotor speed variation driven) actuation systems also require attention.
- Along with static loads, the effects of external vibrations on the proposed actuation system would also need to be ascertained through a comprehensive array of tests.

APPENDIX A

Variable span concept supplementary materials

A.1 Alternative view of presented data

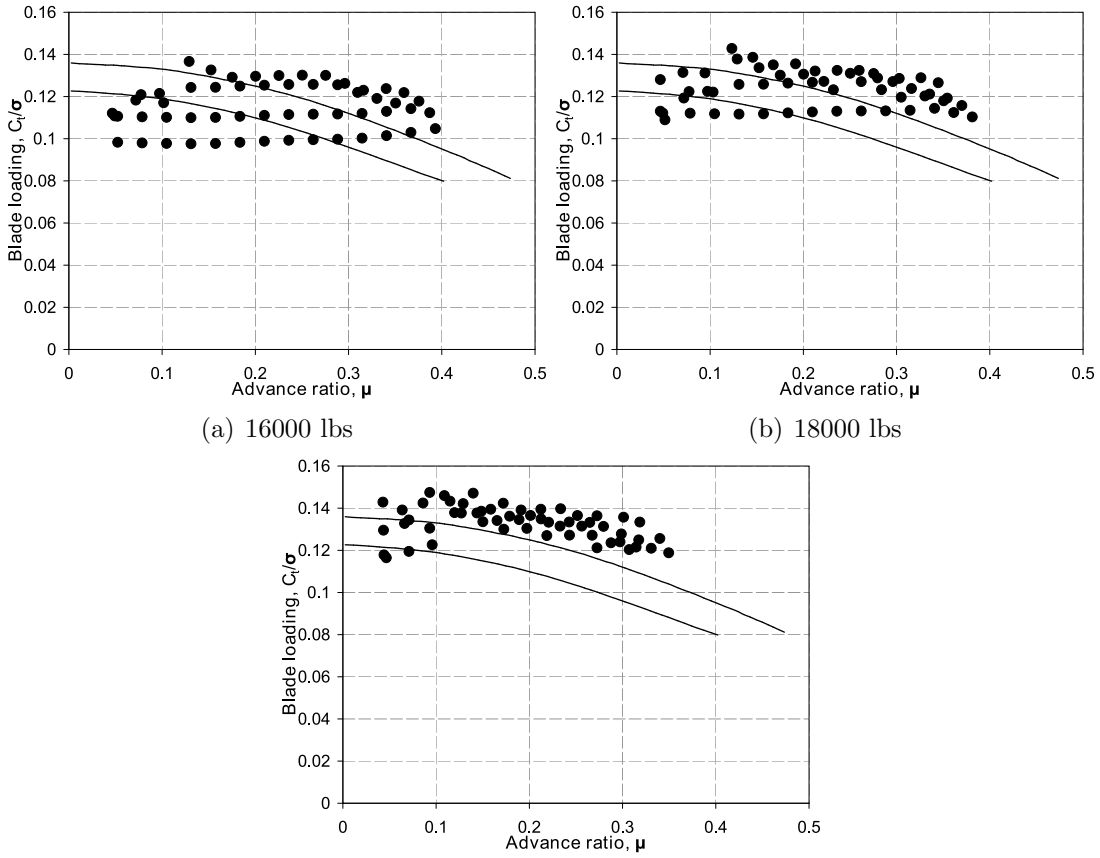

(a) 16000 lbs

(b) 18000 lbs

(c) 23000 lbs

Figure A.1. Comparison of minimum power due to rotor speed variation only to proposed optimal blade loading band [24]

The Optimum Speed Rotor patent owned by Abrahem Karem [24] hypothesis the existence of a band of blade loading (C_t/σ) as a function of advance ration (μ) in which the rotor is operating at its optimum. The patent presents the variation of the rotor speed as a method of controlling the blade loading to place it within this band. The following figures show the blade loading calculated for the minimum power condition using rotor speed variation only, radius variation only and combined varied as compared against this proposed band (Figs. A.1, A.2 and A.3 respectively) for the three gross weights considered.

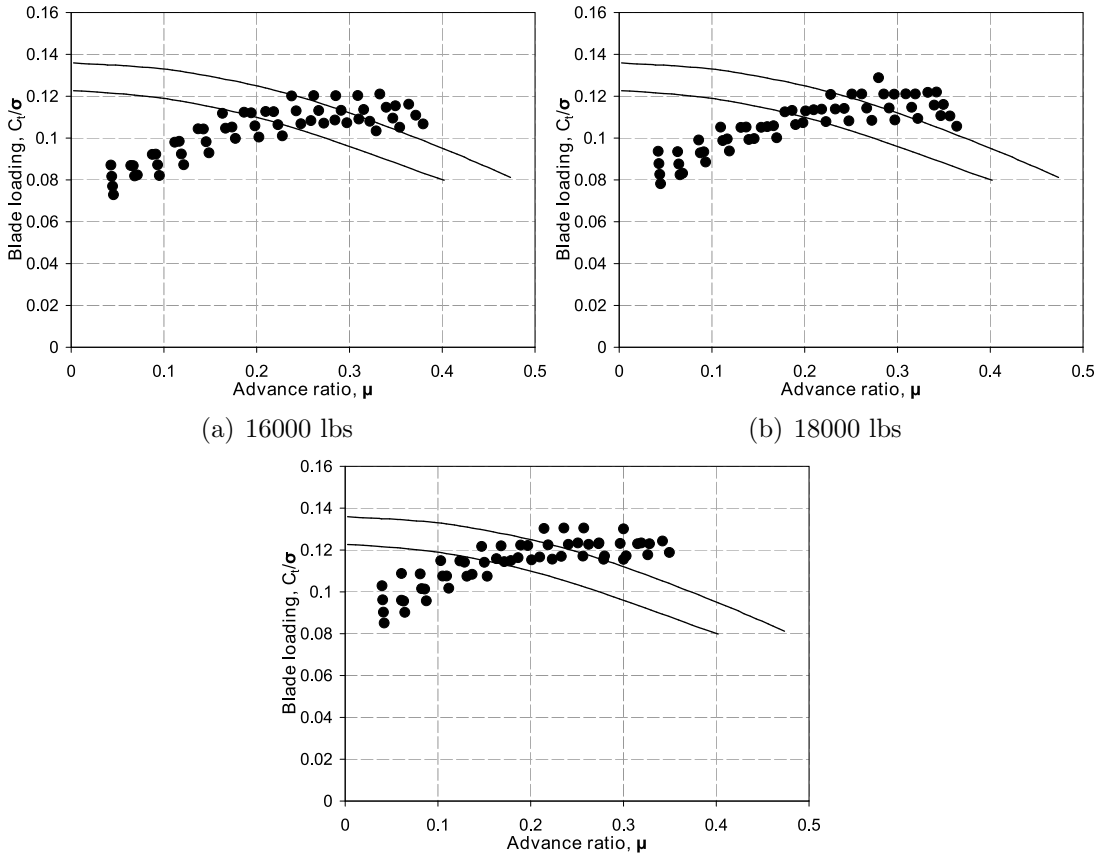

(a) 16000 lbs

(b) 18000 lbs

(c) 23000 lbs

Figure A.2. Comparison of minimum power due to radius variation only to proposed optimal blade loading band [24]

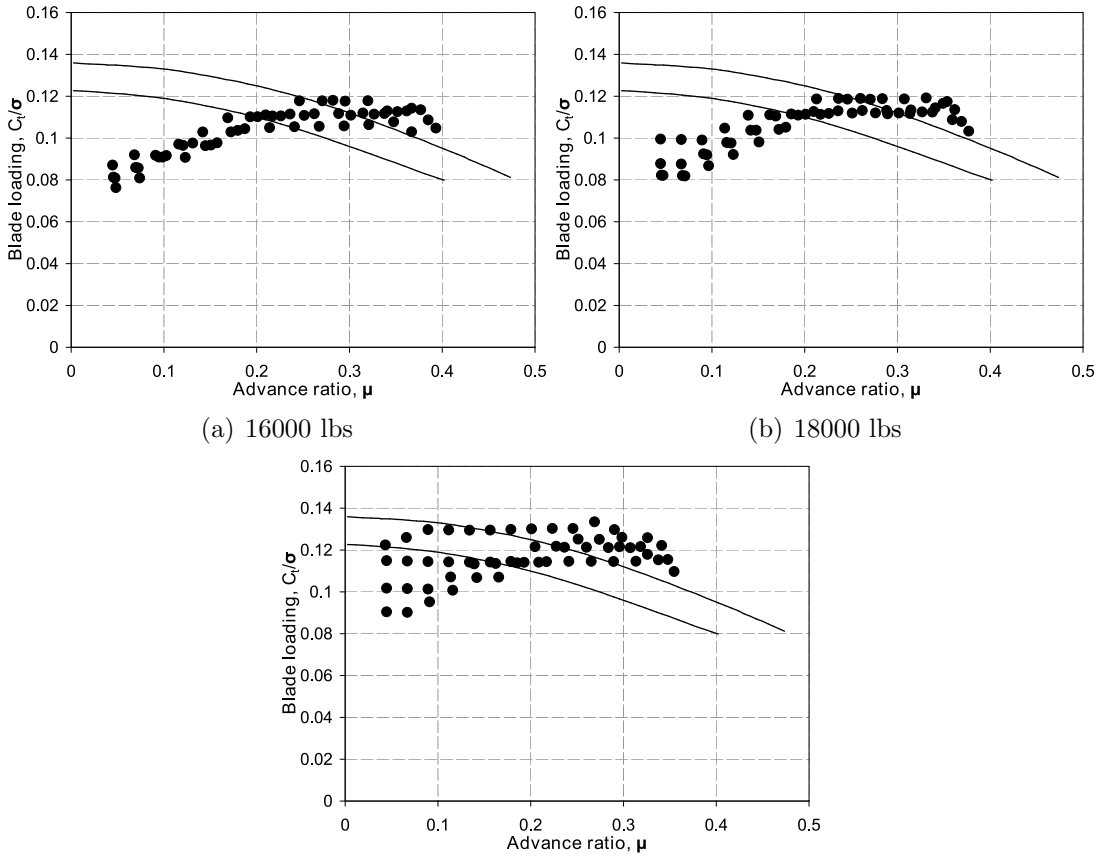

(a) 16000 lbs

(b) 18000 lbs

(c) 23000 lbs

Figure A.3. Comparison of minimum power due to combined radius and rotor speed variation to proposed optimal blade loading band [24]

A.2 Hydraulic cylinder design for case 2

Figure A.4 presents the variation of the required hydraulic pressure and piston tensile and cylinder hoop stresses as a function of cylinder bore and piston rod diameters for design case 2.

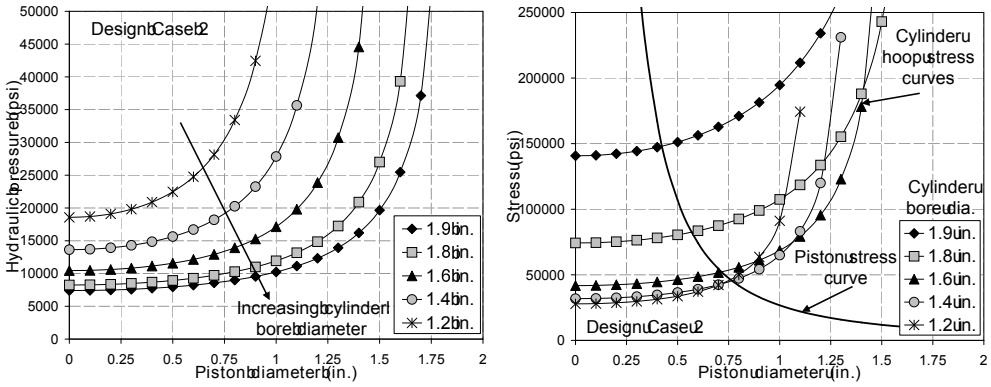

(a) Req. hydraulic pressure variation (b) Stress variation

Figure A.4. Variation of required hydraulic pressure and piston tensile and cylinder hoop stresses as a function of cylinder bore and piston rod diameters for design case 2

A.3 Supporting material for non-linear stiffness cell analysis

Figure A.5 presents the solution process flow chart used for the pareto front optimization methodology used to analyze the non-linear stiffness cell configuration.

Figure A.6 presents the pareto front solution for case 2.

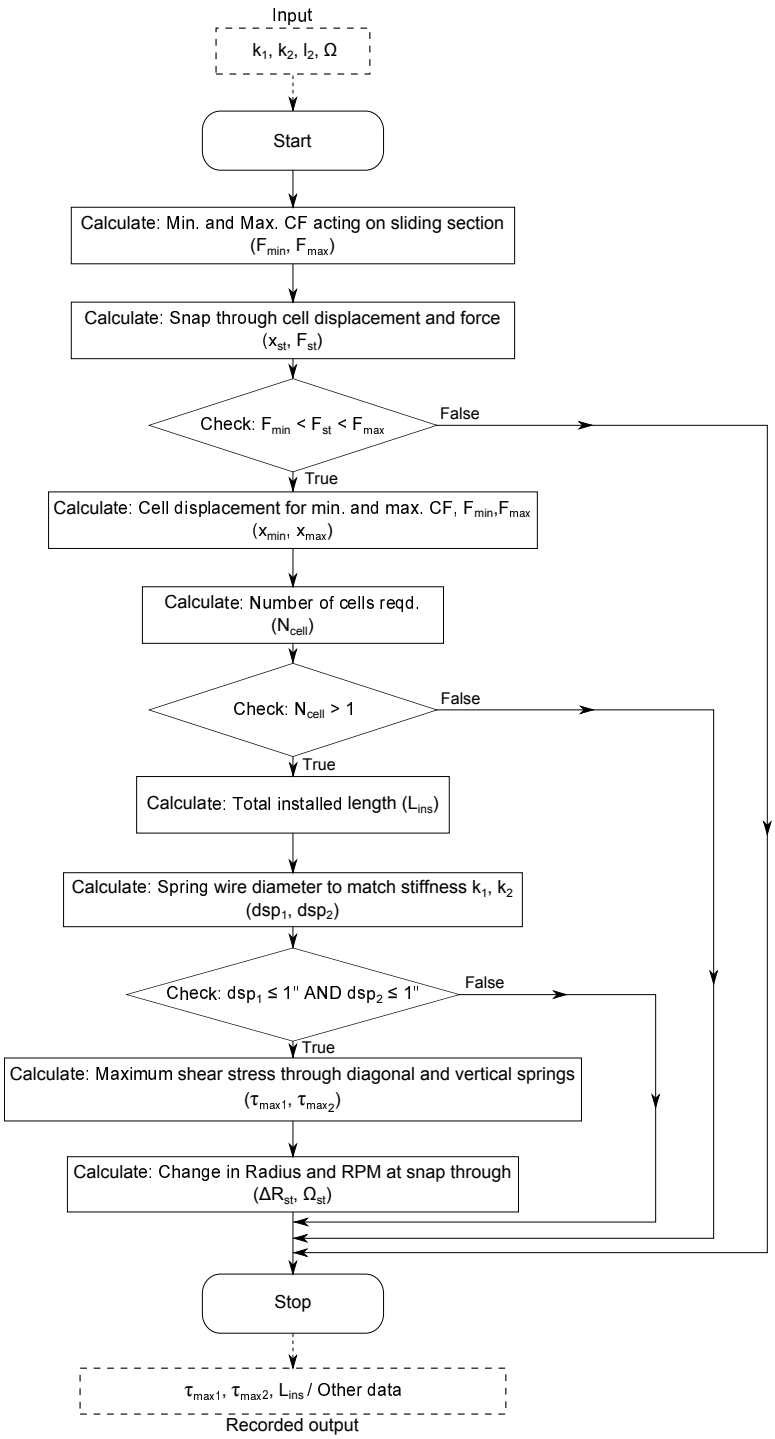

Figure A.5. Non-linear stiffness cell analysis process flowchart

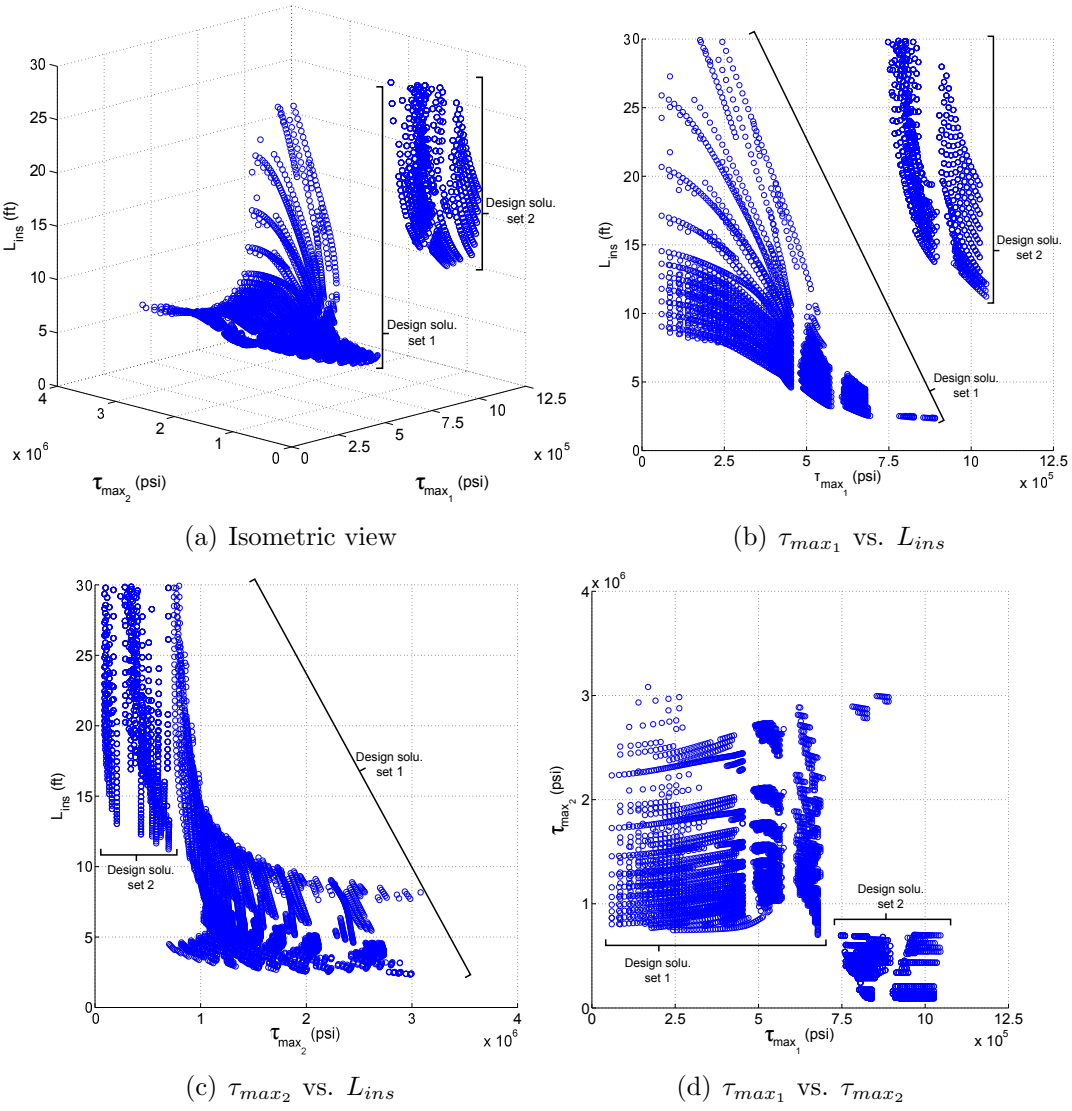

(a) Isometric view

(b) τ_{max_1} vs. L_{ins}

(c) τ_{max_2} vs. L_{ins}

(d) τ_{max_1} vs. τ_{max_2}

Figure A.6. Multiple views of the design case 2 cellular array solution pareto surface

APPENDIX B

Rotor wake model description

In order to properly understand the effects of variable camber on aircraft performance the use of a high fidelity aerodynamic model was necessary. Along with the aerodynamic coefficients of the blade airfoils it is necessary to incorporate the effects of the rotor inflow which is a direct result of the rotor wake. The following sections provide a brief background of wake modeling following by a detailed description of the wake model developed specifically for the analysis of variable camber on the hover performance of rotorcraft.

B.1 Introduction

The ability to accurately predict the complex flow field around a rotor, dominated by strong vortices, is of immense importance to rotorcraft performance analysis and design. To support this requirement, significant efforts have been devoted by researchers to the development of various types of flow field analysis. In general the more advanced methodologies can be grouped into two categories: Vortex wake models and Computational Fluid Dynamics (CFD) models. Recent efforts have

focused on using CFD to predict the rotor wake (with special attention given to the rotor blade tips); however, these models are computationally expensive [203] and suffer from numerical dissipation problems. Alternatively, vortex wake models provide a significant sophistication with marginal computational expense.

Vortex models themselves can be further categorized into: Prescribed and free wake models. Several widely used models fall into the first category, including but not limited to Langrebe [204] and Kocurek and Tangler [205] models. These models are developed with empirical corrections for the wake deformation observed during experiments. The latter group include several models as well which include time marching wake schemes [206] and other implicit and relaxation based models [207],[208],[209],[210],[211]. These models solve for the self-induced wake deformation and as such provide a more precise description of the rotor wake (which is the primary benefit over prescribed wake models).

In general, time-marching free wake models have been shown to be susceptible to instabilities. In particular these instabilities are amplified in hover due to the relative close proximity of the vortex filaments to each other. Using relaxation based models removes some of these instabilities (especially ones caused due to transients). However, most of these relaxation based models were developed to predict the wake structure for the entire aircraft operating environment and as such are not efficient for the hover case.

From the various relaxation based wake models available in literature, the Bagai and Leishman [211] Pseudo-Implicit Predictor-Corrector (PIPC) wake model was shown to be particularly robust. This property is derived from the enforcement of the wake periodicity and the inclusion of a five point solution stencil (making the solution second order accurate). However, the major contribution of this model was the added use of the predictor-corrector scheme which solved the governing differential equations of the wake using a partial implicit method (further adding to the stability).

The model developed for the current research uses the PIPC model governing differential equations for the deformable portion of the wake as the starting point, with modifications applied specifically for the hover condition. The result is a fast and robust deformable hover wake model which is ideal for parametric or optimization studies requiring a large number of run cases.

B.2 Wake structure

In to order capture the intricacies of the complex wake structure of a hover rotor, the current model is comprised of three distinct regions as shown in figure B.1 (shown for one blade). Each region is comprised of vortex filaments punctuated with collocation points and are modeled to either be prescribed (rigid) or allowed to deform due to external and self-induced velocities. The following sub-sections discuss in detail the various regions.

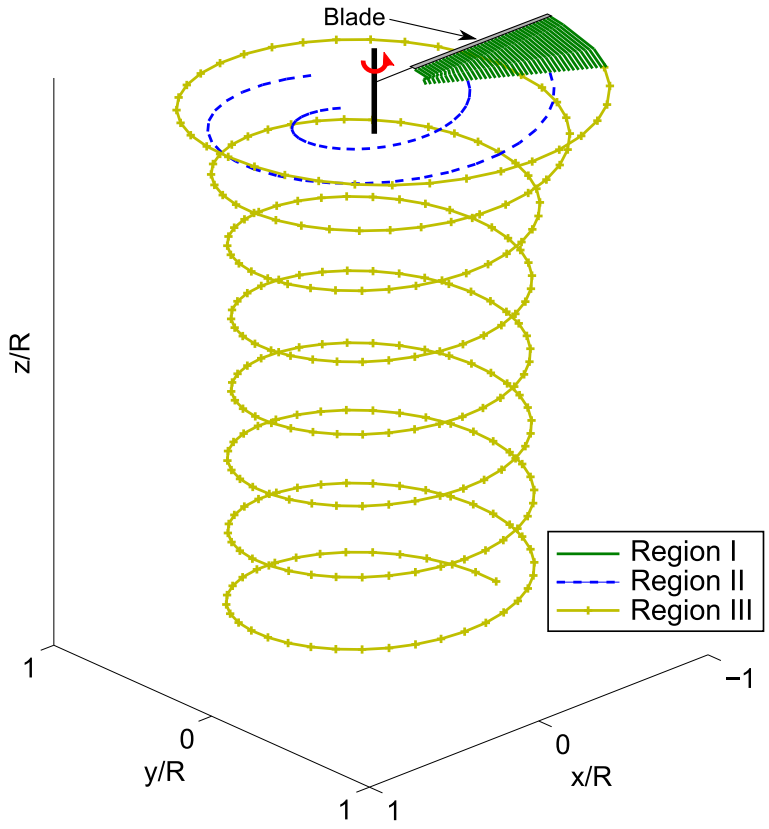

Figure B.1. Schematic representation of the regions of the wake structure

B.2.1 Region I

The region of the wake closest to the blade is comprised of a bound vortex passing through the quarter chord of the blade with trailed vortices extended 30 degrees

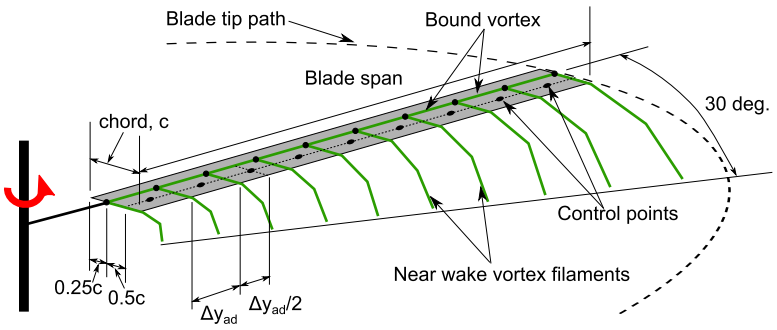

Figure B.2. Region I wake structure

into the flow (Fig. B.2). The angle of extension is based on previous well validated research bodies of work [197, 32]. The bound vortices lie within an aerodynamic element and have trailed vortices starting at either end extending into the wake. The trailed vortices themselves are divided into two sections. The first element in each trailed vortex arc is exactly parallel to the blade chord (i.e. perpendicular to the corresponding bound vortex). This vortex element lies in the plane of the blade and therefore its orientation is affected by pitch angle of the specific edge of the corresponding aerodynamic element (which itself is a function of collective input, blade twist and elastic twist variation). The succeeding elements follow the arc defined by the prescribed wake helix equation (Eq. B.1) where ζ is defined as the wake age in radians (details of this parameter will be discussed in detail in the proceeding sections), r is the radial location of the start of the helix and v_i is the induced velocity acting on the helix. Note that the downward convection of the vortex helix as described by the equation is controlled by the applied induced velocity. In this model since the induced velocity varies with spanwise location, an average of the induced velocity was used to calculate the downward convection angle of the region I trailed vortices. In the proceeding sections the trailed vortices are hereby referred to as the near wake.

$$\begin{aligned} x(\zeta) &= rcos(\zeta) \\ y(\zeta) &= rsin(\zeta) \\ z(\zeta) &= v_i \frac{\zeta}{\Omega} \end{aligned} \tag{B.1}$$

Classic lifting line theory models a lifting device as line by assuming a high

enough aspect ratio, in this configuration the control points lie directly on the bound vortex itself. Lifting surface theory alternatively models the width of the lifting device to include the effect of the variation of induced velocity along the surface. A combination of both these methods is to calculate induced velocity acting on the blade at the 75% chord mark aft of the leading edge in the middle of each aerodynamic element (along the spanwise direction). These points similiar to the first element of the trailed vortices lie in the plane of the blade, and hence their location is effected by the same factors. Note that it is due to the proxmity of the control points to the trailed vortices, that the first element is set to be parallel to the blade chord. If this was not ensured, infeasible artificial peaks in the calculated induced velocity would occur due to the close proximity of a trailed vortex filament to the control point.

B.2.2 Region II

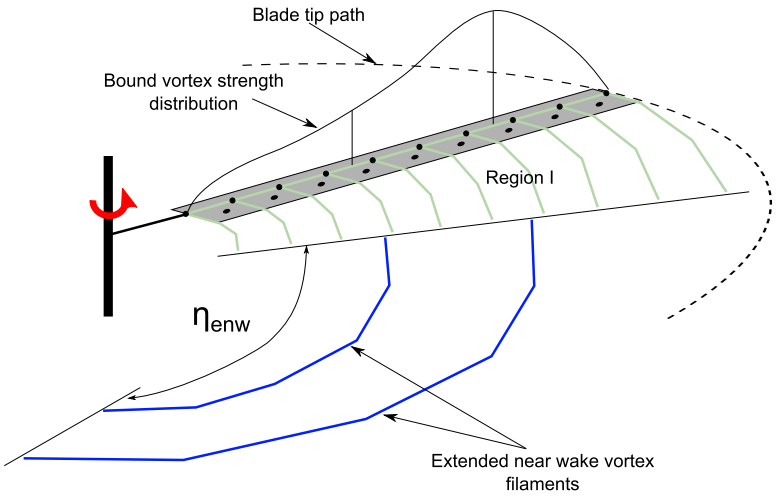

Figure B.3. Region II wake structure

Region II is added as extension to the trailed near wake vortex filaments (Fig B.3). While not traditionally found in various vortex wake models, this component of the structure was specifically added for blades with low to no twist. In particular this region is designed to compensate the difference in distribution of the wake structure aft of the blade for a blade with no or low pre-twist as compared to a blade with moderate to high pre-twist. The number of these of vortices (N_{enw})

is defined by the user and is based on the effect of the vortex on the induced velocity distribution. For example, if a concentrated vortex was placed aft of the near wake vortices, artificial peaks in the induced velocity calculated at the control points would occur. However, distributing this strength among a few extended near wake helices allows for a smoother distribution. Similarly the angle of extension (η_{enw}) of these vortices is a user defined parameter to control the magnitude of the effect of these vortices on the induced velocity. Both of these parameters can be used as empirical corrections to fine tune the model against experimental results. The arcs of these vortices are governed directly by the prescribed vortex helix equations B.1 and is not allowed to deform (similiar to that of the trailed near wake vortices). Furthermore the angle of vertical convection of the extended near wake matches that of the near wake votices (i.e. the induced velocity V_i used is the same). An explanation of the effects of these extended wake vortices will be discussed in detail in the proceeding sections. The radial location of the starting point of these vortices is always inboard of the bound vortex with highest strength, the particular location is governed by the distribution of the bound vortices and will be discussed in section B.3.

B.2.3 Region III

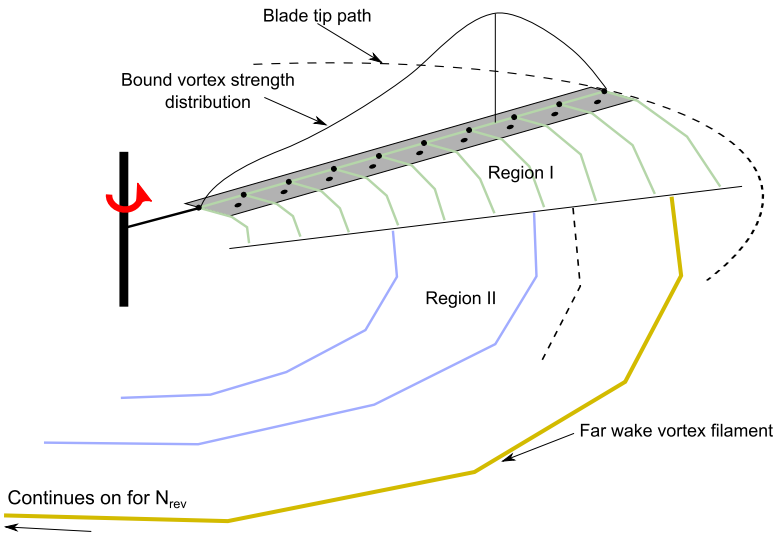

Figure B.4. Region III wake structure

The far wake region of the wake structure is comprised of one vortex filament (Fig. B.4) whose strength is equal to the maximum bound vortex strength. This part of the structure is defined to represent the strong tip vortex which emanate from rotors. This vortex filament, in a manner similar to that of the extended near wake, starts at the end of the trailed near wake vortices. However, unlike region I and II, this vortex filament (and hence this region) is the only component of the wake structure which can be set to deform due to external and self-induced velocities. Furthermore, the length of this helix generally is significantly longer than that of region I or II. Its location is always defined to be outboard of the bound vortex with highest strength, however he specific radial location is calculated using the vortex strength centroid method discussed in section B.3. When the rotor wake is analyzed as a prescribed wake this component of the wake structure is not allowed to deform and therefore the location follows the prescribed wake equations (Eq. B.1), however when allowed to deform a specific set of governing differential equations are used to calculate the deformation. The specifics of this process will be discussed in the proceeding sections.

B.3 Vortex strength and location

The strength of each vortex extended in the flow (near, extended near and far) are determined by the strength of the bound vortices. The following subsection defines the method of calculating the strength of each vortex.

B.3.1 Bound vortices

The bound vortex strength is directly governed by the lift produced by the corresponding aerodynamic section. Furthermore, the lift produced by each section is a function of a the induced velocity calculated at each control point. This induced velocity is a function of the contributions of trailed near wake, extended near wake and far wake vortices. In traditional lifting line blade theory the bound vortex effects the induced velocity calculated at the control point (along with the other components of the wake structure). Using this method the strength of the bound vortex is governed by the magnitude of the induced velocity which satisfy the no

flow through condition at the control point (i.e., the net flow perpendicular to the plane of the blade at the control point is zero). The strength of this bound vortex is then used to calculate the differential lift produced at that aerodynamic element. However, in the current case since a table look up scheme is used, once the differential lift produced by an aerodynamic element is calculated (given an applied induced velocity), equation B.2 is used to then calculate the strength of the bound vortex (where r is the location of the control point, c is the chord of the corresponding aerodynamic element and C_l is the corresponding lift coefficient at the aerodynamic element). This process is based on the process prescribed by Sitaraman [212]. As the lift produced is a function of the induced velocity which in turn is a function of the strengths of the various vortex filaments (which in turn is governed by the bound vortex strength) the process to solve the bound vortex strength has to be iterative. The bound vortices are affixed to the ends of a given aerodynamic element and therefore their position is only a function of blade geometry

$$\Gamma_b = \frac{C_l \Omega r c}{2} \tag{B.2}$$

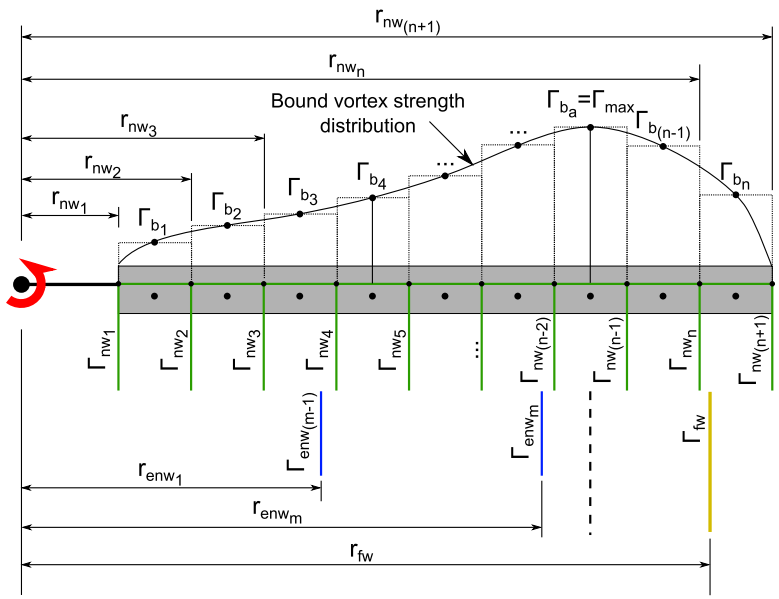

Figure B.5. Near, extended near and far wake vortex strength and location schematic

B.3.2 Trailed near wake vortices

As seen in figure B.5, trailed near wake vortices (marked in green) start at the ends of each aerodynamic element. The strengths of these vortices are governed by equation B.3. Note that it is possible for these vortices to have positive or negative strengths depending on the slope of the bound circulation variation function. While the start location of the near wake is a function of the blade geometry the shape is governed by onset induced velocity, therefore requiring an iterative procedure to obtain a solution. As seen in the equation for the trailed vortices and tip and root of the blade, the equation refers to Γ_{b_0} and $\Gamma_{b_{n+1}}$ respectively which do not exist in the model. Therefore, for these two cases the bound vortex strength is set to be zero signifying the production of no lift inboard of the blade root and outboard of the blade tip.

$$\begin{aligned} \Gamma_{nw_j} &= \Gamma_{b_j} - \Gamma_{b_{j-1}} \\ 1 &\leq j \leq n+1 \end{aligned} \tag{B.3}$$

B.3.3 Extended near wake vortices

As stated earlier the purpose of extended near wake vortex is to capture the effects of the wake structure closer to the root of blades with little to no pre-twist. As such the sum of the strengths of these vortices is equal to the sum of the strength of the near wake vortices inboard of the bound vortex with the highest circulation (this value is equivalent to the strength of the higher circulation bound vortex). The first step in determining the initial radial location and strengths of the extended near wake vortices, is to prescribe the number of vortices needed (m). The set of vortices inboard of the bound vortex of highest circulation is then divided equally into the user specified number of subsets. Post this for each subset a centroid approach is used to calculate the starting point of the extended near wake vortex using equation B.4 within each subset (note the initial and final steps of the summation in the equation). Finally, the strength of each vortex is equal to the sum of the near wake vortices within each corresponding subset (Eq. B.5). In this manner, no increase or decrease in the total vorticity of the system is realized, rather only a re-distribution is achieved.

$$r_{enw_i} = \sum_{j=j_{st_i}}^{j_{en_i}} \Gamma_{nw_j} r_{nw_j} \qquad 1 \leq i \leq m \tag{B.4}$$

$$\Gamma_{enw_i} = \sum_{j=j_{st_i}}^{j_{en_i}} \Gamma_{nw_j} \tag{B.5}$$

As an example consider the figure B.5 where maximum bound vortex is at position a. In this example, the number of extended near wake vortices is set to two. Therefore vortices inboard of the bound vortex Γ_{b_4} are grouped in one set, whereas vortices outboard of Γ_{b_4} and inboard of Γ_{b_a} are included in the second set. The resulting radial locations of the starting point of the extended near wake vortices are at r_{en_1} and r_{en_m} respectively (where m is the number of extended near wake vortices prescribed).

B.3.4 Far wake vortex

The strength of the far wake vortex is always equal to strength of the maximum strength of the bound vortex (this is equivalent to the sum of the set of near wake vortex strengths outboard of the bound vortex of highest strength as calculated by equation B.6). The start radial location is calculated in a similar fashion as the extended near wake using a centroid approach (Eq. B.7). Note that the magnitude of the vortex strength is equal to the sum of the strengths of the extended near wake vortices but the direction is opposite. Again this mathematically ensures vorticity continuity.

$$\Gamma_{fw} = \sum_{j=a+1}^{n+1} \Gamma_{nw_j} \tag{B.6}$$

$$r_{fw} = \sum_{j=a+1}^{n+1} \Gamma_{nw_j} r_{nw_j} \tag{B.7}$$

This approach is suggested by Bagai [197] and is therefore used in this model. However, for low thrust cases, using this method was found to cause model conver-

gence instabilities. In order to do abate this issue, beyond a certain high number of iterations over the starting point of the far wake was fixed to 97% of the radius (which is the method employed by Leon [32]). In the following sections the results of a parametric study on the effect of the far wake release location will be presented.

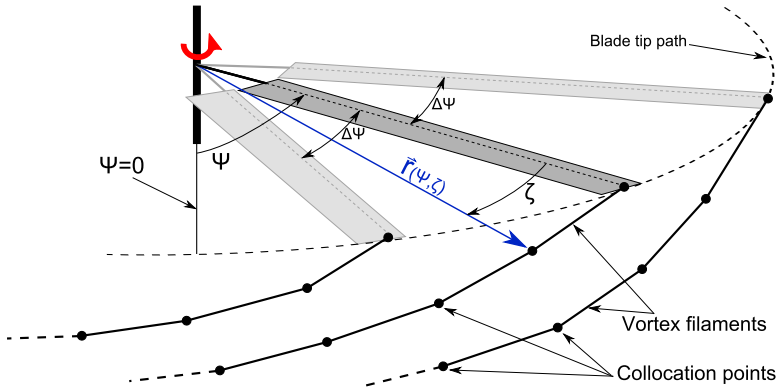

Figure B.6. Schematic of the discretization of vortices into filaments

B.4 Velocity induced by vortices

Figure B.6 presents a detail view of the vortex structure used in the current model. Each vortex is broken up into separate vortex filaments punctuated by collocation points. Each vortex filament is a straight line and is therefore a piecewise representation of the smooth arc of a vortex helix. Each collocation point can be defined as a function of two angles: Ψ: Azimuth and ζ: Wake age. The azimuthal position is defined from a fixed reference point of $\Psi = 0$. The wake age is defined as the angle between the quarter chord line of the blade and the respective collocation point of the shed vortex.

$$\begin{bmatrix} V_x \\ V_y \\ V_z \end{bmatrix} = \frac{\Gamma}{4\pi} \frac{h}{\left(r_c^{2n} + h^{2n}\right)^{1/n}} (cos\theta_1 - cos\theta_2) \begin{bmatrix} e_x \\ e_y \\ e_z \end{bmatrix} \tag{B.8}$$

The induced velocity contributions of each of these filaments is calculated using a modified formulation of the Bio-Savart law. Figure B.7 shows the details of a

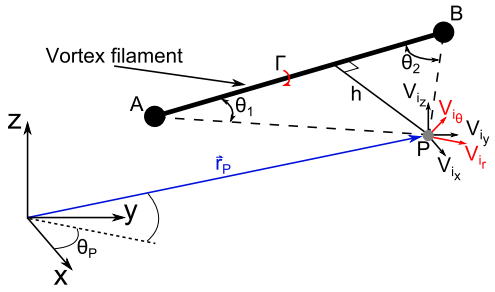

Figure B.7. Details of a vortex filament

given vortex filament with pertinent points defined. Based on this diagram the velocity induced by a vortex filament defined by points A and B can be calculated by equation B.8 where $\vec{r_1}$, $\vec{r_2}$, $\vec{l_{12}}$, $\vec{e}$, θ_1, θ_2 and h are calculated using equation set B.9 [28]. For the current model n was set to two. Furthermore, the induced velocity components in cylindrical coordinated are calculated using equation B.10 where θ_P is defined by equation B.11.

$$\begin{aligned} \vec{r_1} &= \vec{r_p} - \vec{r_A} \\ \vec{r_2} &= \vec{r_p} - \vec{r_B} \\ \vec{l_{12}} &= \vec{r_B} - \vec{r_A} \\ \theta_1 &= \frac{\vec{l_{12}}.\vec{r_1}}{|\vec{l_{12}}||\vec{r_1}|} \\ \theta_2 &= \frac{\vec{l_{12}}.\vec{r_2}}{|\vec{l_{12}}||\vec{r_2}|} \\ h &= |\vec{r_1}|sin\theta_1 = |\vec{r_2}|sin\theta_2 \end{aligned} \tag{B.9}$$

$$\begin{bmatrix} V_r \\ V_\theta \\ V_z \end{bmatrix} = \begin{bmatrix} cos\theta_P & sin\theta_P & 0 \\ -sin\theta_P & cos\theta_P & 0 \\ 0 & 0 & 1 \end{bmatrix} \begin{bmatrix} V_x \\ V_y \\ V_z \end{bmatrix} \tag{B.10}$$

$$tan^{-1}\theta_P = \frac{P_y}{P_x} \tag{B.11}$$

In equation B.8 r_c is defined as the core of the vortex filament. Classic Biot-Savart law dictates a singularity at the center of the vortex, to abate this mathematical issue the vortex is given a finite core size. Due to the viscosity of the

operating fluid vortex filaments tend to have a growth in core size until they burst. In order to realize this phenomenon into the current model, a vortex core size growth model prescribed by equation B.12 was used. This model is based on the work presented by Bhagwat and Leishman [213]. For the current study the Oseen parameter (α) was set to 1.25643, the Eddy viscosity coefficient (δ) was set to 1000 and the kinematic viscosity (ν) was set to that of air. These values were set based on the description provided by Bhagwat and Leishman [213]. The initial core size (r_0) was set to 8% of the average chord of the blade (a value picked based on model fine tuning with experimental results). Note that the core size grows with wake age.

$$r_c = \sqrt{r_0^2 + \frac{4\alpha\delta\nu\zeta}{\Omega}} \tag{B.12}$$

B.5 Free(deformable) wake model

$$\frac{\partial\vec{r}(\Psi,\zeta)}{\partial\Psi} + \frac{\partial\vec{r}(\Psi,\zeta)}{\partial\zeta} = \frac{1}{\Omega}\vec{V_{ind_{tot}}}(\vec{r}(\Psi,\zeta)) \tag{B.13}$$

As stated earlier the far wake (region III) component of the wake structure can be allowed to deform due to the application of external and self-induced velocities. Equation B.13 represents the governing differential equation of the motion of a vortex. This equation is derived based on the parametrization of wake based on blade azimuthal position and wake age. Furthermore the rate of change in the azimuth and the wake age is constant with respect to time (and equal to Ω). $\vec{V_{ind_{tot}}}(\vec{r}(\Psi,\zeta))$ here is defined as the total induced velocity acting at the point $\vec{r}(\Psi,\zeta)$; this includes the free-stream velocity and the induced velocity due to the various other vortex filaments present (for the current model the effects of near wake, extended near wake and far wake filaments were included). If this equation was further discretized using a second order accurate central difference scheme, and further assuming that the differential length along the azimuth and wake age is equal ($\Delta\Psi = \Delta\zeta$), the result is equation B.14 [197] which is the starting point for the Bagai and Leishman Pseudo-Implicit Predictor-Corrector (PIPC) free wake model (l is the index for the azimuthal steps, k is the index for the wake age steps).

In equation B.14, the total induced velocity is separated into two components, the first is $\vec{V}_\infty$ which represents the ambient velocity (in the case of our hover this is zero) and the second is $\vec{V}_{ind}$ which represents the induced velocity due to the various other vortex filaments present in the flow field. For details of this derivation please refer to [197].

$$\vec{r}_{l,k} = \vec{r}_{l-1,k-1} + \frac{\Delta\zeta}{\Omega}\left[\vec{V}_\infty + \frac{1}{4}\left[\vec{V}_{ind}(\vec{r}_{l,k}) + \vec{V}_{ind}(\vec{r}_{l-1,k-1}) + \vec{V}_{ind}(\vec{r}_{l-1,k}) + \vec{V}_{ind}(\vec{r}_{l,k-1})\right]\right] \tag{B.14}$$

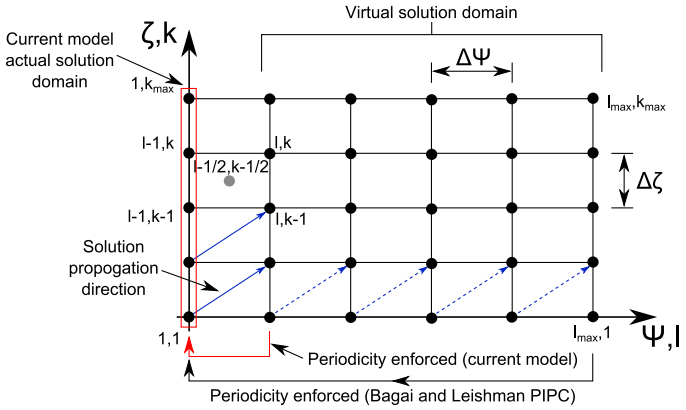

Figure B.8. Computational domain map of the proposed model as compared to the PIPC model

The solution propagation stencil for this scheme is presented in figure B.8. In order to ensure stability Bagai proposed the enforcement of periodicity of the last and first azimuthal steps (this ensures the wake structure of the last step is followed by that of the first step). Therefore, in this scheme in order to produce a complete solution the iteration sequence would have to run through all the azimuth steps, which is necessary for the case of a rotor in an arbitrary flight condition. However, for the case of hover, the wake structure for each azimuthal position is exactly the same (assuming the axis-symmetric flow condition). This allows for the periodicity to be constrained to consecutive azimuthal steps thereby reducing the computational domain significantly and therefore improving the solution speed.

Figure B.9 presents a zoomed in planar view of the collocation points of the vortex filaments shed of the blade at adjacent azimuthal steps. For simplicity,

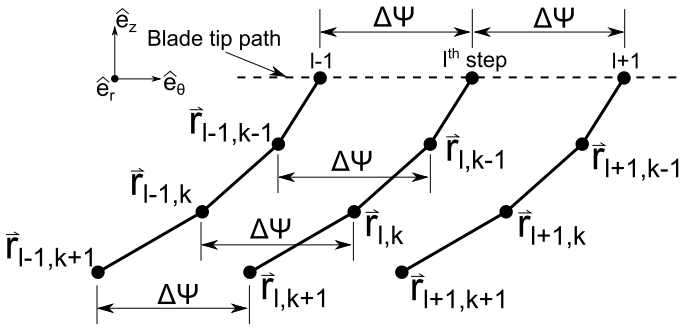

Figure B.9. Zoomed in view of collocation points of vortex filaments shed at adjacent azimuthal steps

due to the axisymmetric flow assumption, for the proceeding section the wake structure is defined in cylindrical coordinated. In hover, assuming axis-symmetric flow condition, the collocation points of a given vortex filament of a particular azimuthal step differ only by a constant value of $\Delta\Psi$ along with $\hat{e}_\theta$ direction from collocation points of vortex filaments at adjacent azimuthal steps and the same wake age (as seen in figure B.9). Using this information the position vector of a collocation point of previous azimuthal step can defined using equation B.15.

$$\vec{r}_{l-1,k-1} = \vec{r}_{l,k-1} - \Delta\Psi\hat{e}_\theta \tag{B.15}$$

Due to the axis-symmetric flow assumption, the induced velocity $\vec{V}_{ind}$ at each collocation point is the same in terms of the magnitude and the resultant direction for adjacent azimuthal steps at a particular wake age. If the induced velocity were at these collocation points were represented as a Cartesian vector, the respective component values would differ along the azimuth. However, in cylindrical coordinated, the induced velocity components are exactly the same for collocation points of a given wake age at any given azimuthal step. Taking advantage of this observation, relationships prescribed by equation B.16 can be defined.

$$\begin{aligned} \vec{V}_{ind}(\vec{r}_{l,k}) &= \vec{V}_{ind}(\vec{r}_{l-1,k}) \\ \vec{V}_{ind}(\vec{r}_{l,k-1}) &= \vec{V}_{ind}(\vec{r}_{l-1,k-1}) \end{aligned} \tag{B.16}$$

Substituting equations B.15 and B.16 into equation B.14 each component of the vector equation can be simplified to equation B.17, B.18 and B.19 for the $\hat{e}_r$, $\hat{e}_\theta$ and

$\hat{e}_z$ directions respectively (assuming no free-stream velocity). As shown in equation B.18 the induced velocity contributions in the $\hat{e}_\theta$ direction are ignored. This has been done as this component is very small compared to $\Delta\Psi$ term, this negation is similar to the method followed by Rosen and Graber [207]. Furthermore, inclusion of this term, although small, was found to de-stabilize the convergence of the wake solution.

$$r_{r_{l,k}} = r_{r_{l,k-1}} + \frac{\Delta\zeta}{\Omega}\frac{1}{2}\left[V_{r_{ind}}(\vec{r}_{l,k}) + Vr_{ind}(\vec{r}_{l,k-1})\right] \tag{B.17}$$

$$r_{\theta_{l,k}} = r_{\theta_{l,k-1}} - \Delta\Psi + \frac{\Delta\zeta}{\Omega}\frac{1}{2}\left[V_{\theta_{ind}}(\vec{r}_{l,k}) + V\theta_{ind}(\vec{r}_{l,k-1})\right] \tag{B.18}$$

ignore

$$r_{z_{l,k}} = r_{z_{l,k-1}} + \frac{\Delta\zeta}{\Omega}\frac{1}{2}\left[V_{z_{ind}}(\vec{r}_{l,k}) + Vz_{ind}(\vec{r}_{l,k-1})\right] \tag{B.19}$$

Using these simplified discretized governing differential equation components, the deformed wake structure was calculated using the Pseudo-Implicit Predictor-Corrector (PIPC) algorithm set forth by Bagai and Leishman [211]. As can be clearly seen in the equations the use of the axis-symmetric flow assumption has allowed for a significant simplification of the equation set as well as a reduction of the computational domain. This improvement corresponds to faster convergence of the solution and hence allowing for the ability to run a larger volume of high fidelity solutions in a shorter amount of time.

B.6 Multi-blade configuration

While the equations developed in the preceding sections relate to the wake structure of a given blade, they can be used to analyze the effect of multiple blades. In particular since the wake structure is axis-symmetric, including the effect of multiple blades is the same as 'virtually' repeating the wake structure in the flow field. Figure B.10 is a graphical representation of this concept. Although the figure shows the configuration for a 4 bladed rotor, the concept applies to a rotor system with any number of blades. It should be noted however, since the wake structure is repeated for every additional blade the effect to the solution is similar to that of

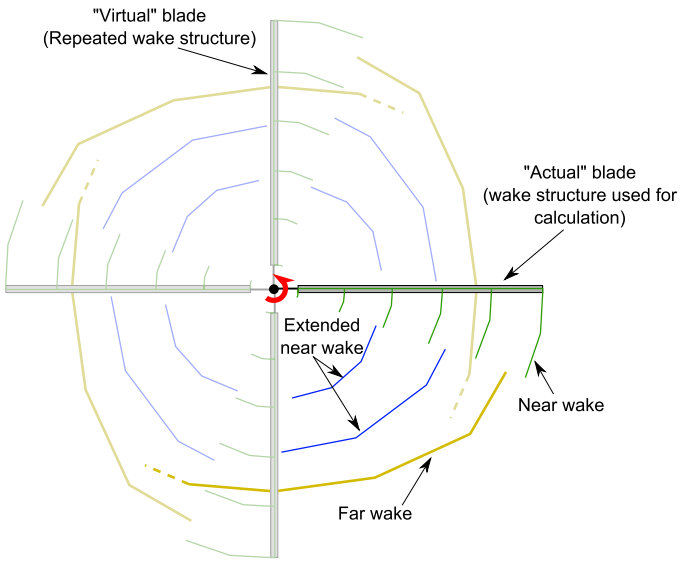

Figure B.10. Schematic representation of the use of 'virtual' blades to determine the effect of multi-blade rotor systems

having additional azimuthal steps in the computational domain and therefore will lead to some loss in computational speed.

B.7 Solution process

The overall trim solution process flow chart is presented in figure B.11. The goal here was to use the results of lower fidelity models as the input (initial estimates) of successively more sophisticated models. Once altitude, thrust level and camber variation parameters are provided, the process is run through and in the end provides the power required (and the corresponding components) along with the required control input and other important information. Since this process can be repeated for various altitudes and camber parameters for the current analysis it is unnecessary for the full process to be repeated for each successive calculation. Therefore, to speed up the solution, successive calculations (e.g. increment in altitude) are calculated only using the free (deformable, i.e. process C) wake solution only (the uniform and prescribed wake solutions are not undertaken).

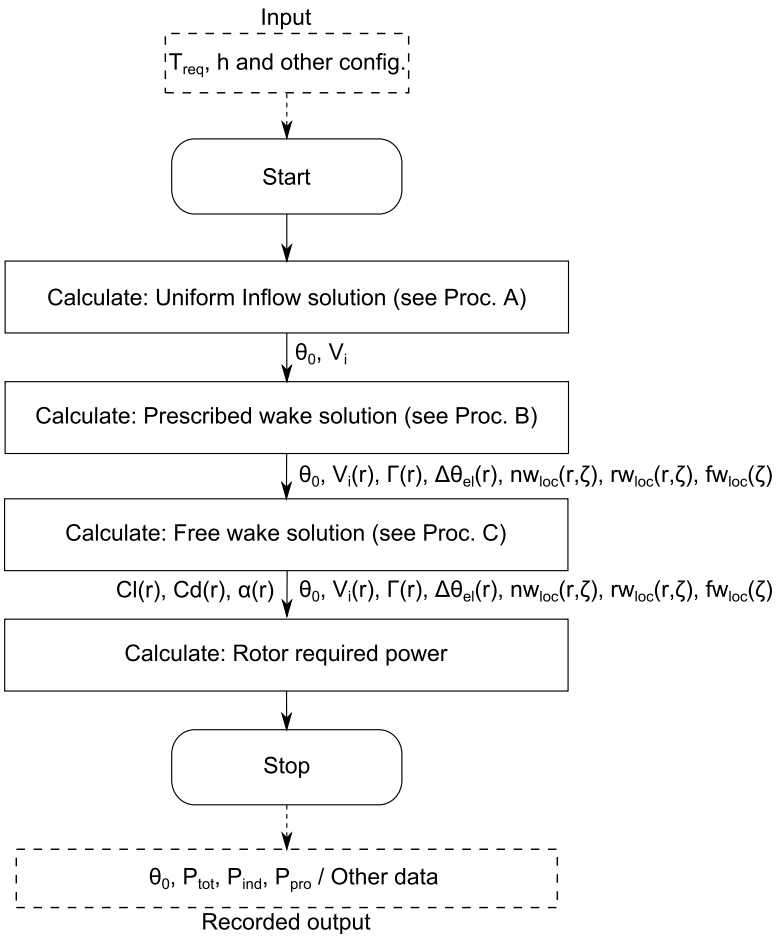

Figure B.11. Main trim solution process flow chart

B.7.1 Process A: Uniform inflow solution

A relatively simple procedure following classic methods as presented by Leishman [28] is used to calculate the rotor performance. In this process (as seen in the flow chart) while the non-linear variation in aerodynamic variation is used in the analysis, the elastic twist response is not calculated in this process (i.e. the blade is treated to be rigid in torsion). The output of this process is the inflow velocity and the initial estimate of the control input required. These values are passes on to Process B.

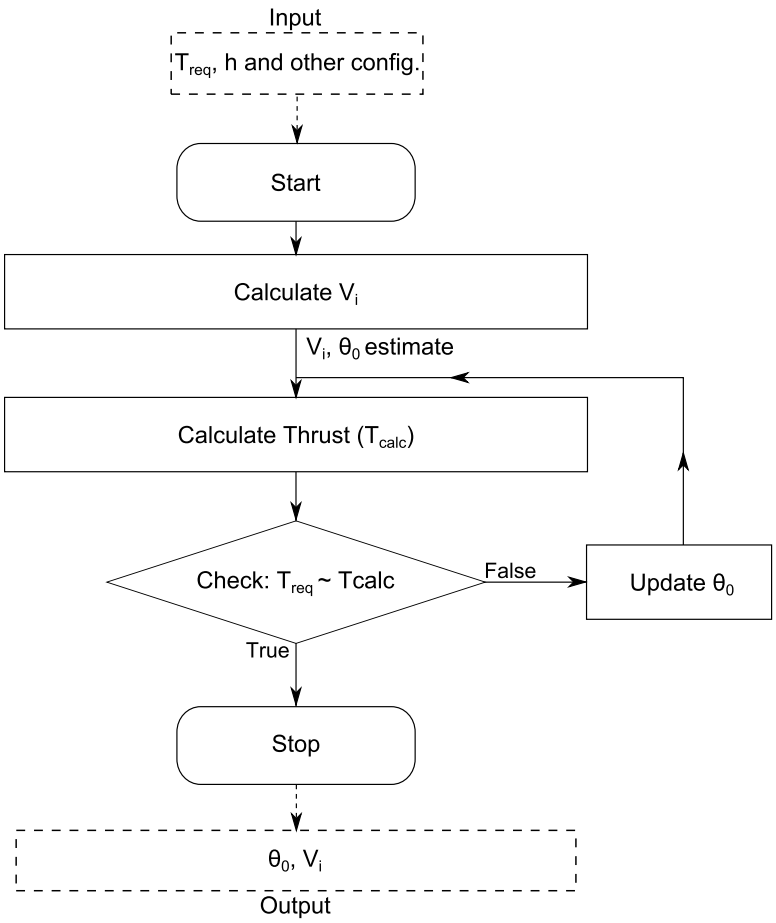

Figure B.12. Process A flow chart

B.7.2 Process B: Prescribed wake solution

Process B (Fig. B.13) is an intermediate step put in place to first provide corrections to the initial inflow velocity and control input calculation and also to provide the initial wake structure (Regions I, II and III) as an input to the Process C (deformable wake geometry). In this process, the far wake (Region III) is not allowed to deform and therefore is a simple helical vortex structure prescribed by equation B.1. Furthermore, as seen in the flow chart this process also incorporates a loop to calculate the elastic twist produced within the blade as a result of aerodynamic loading. As seen the elastic twist calculation conditional loop is positioned after a closed control loop calculation. This process required that there be two loops which check to make sure the thrust requirement is met. This method allows for

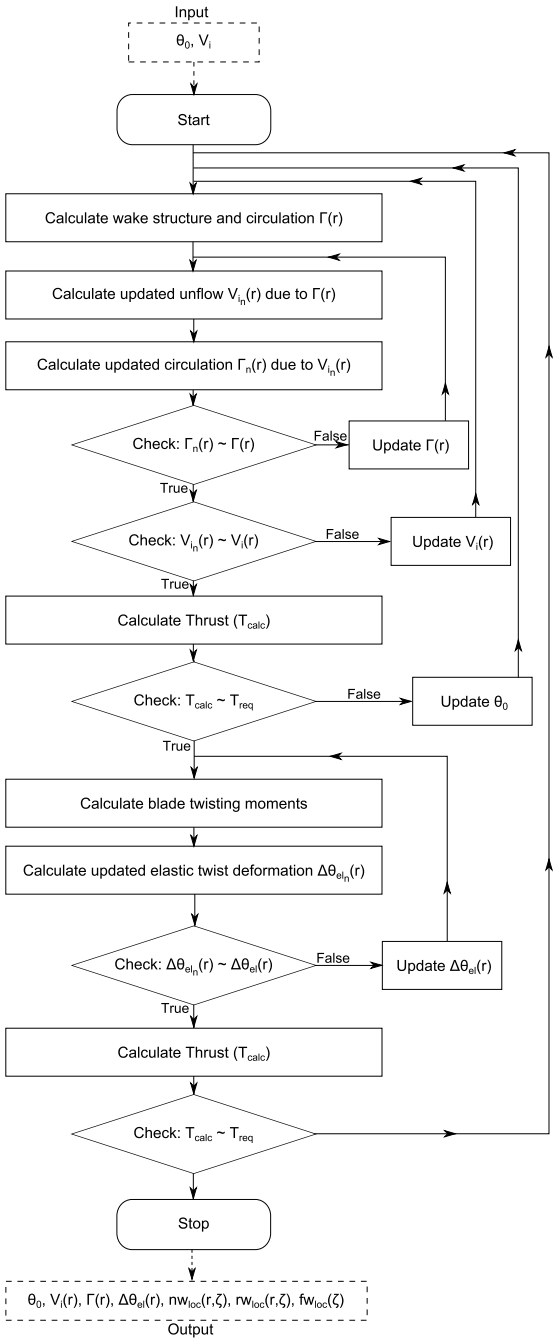

Figure B.13. Process B flow chart

the simple separation of the elastic twist and control loop and provides for solution stability as the elastic twist is effectively added as a correction to the pre-twist after an initial control solution has already been reached. Reducing the number of times the elastic twist variation is changed reduced the number of changes in the system properties for a given iteration and this is what provides the system stability. To further add to the stability of the solution, the updated elastic twist variation for each iteration was updated using a weighted function prescribed by equation B.20 ($wt_{el} = 0.7$).

$$\Delta\theta_{el_{inp}}(r) = \Delta\theta_{el_{old}}(r)(1 - wt_{el}) + \Delta\theta_{el_{new}}(r)wt_{el} \tag{B.20}$$

For the Vortex strength (Γ), consequently the induced velocity, loop a similar method was used to stabilize the solution (Eq. B.21). However in this equation a weight factor (wt_{Γ}) of 0.01 was used. This really low value was required as without it the changes in bound vortex strength distribution between each successive iteration was found to be too large and would quickly diverge the solution. This method is similar to that used by Anderson, Corda and Van Wie [214] albeit for the analysis of fixed wing aircraft. Furthermore, the weighting factor used in this analysis is also comparable to the one used by the researchers (they used 0.05).

$$\Gamma_{el_{inp}}(r) = \Gamma_{el_{old}}(r)(1 - wt_{\Gamma}) + \Gamma_{el_{new}}(r)wt_{\Gamma} \tag{B.21}$$

B.7.3 Process C: Free(deformable) wake solution

Process C (Fig. B.14) is designed to work exactly in the same was a Process B with the addition of another loop which iterates over the deformable far wake geometry. As seen in this figure the input received by Process C includes an initial estimate of the wake structure (based on prescribed solution). However, as mentioned earlier for successive solutions Processes A and B were skipped to improve speed. In this case the initial geometry estimate is wake structure solution of the previous solution. This method was helpful in improving the speed of convergence but it required that successive solutions were for cases with relative close spacing (for example trying to solve the trim solution for 10000 ft would lead to convergence issues).

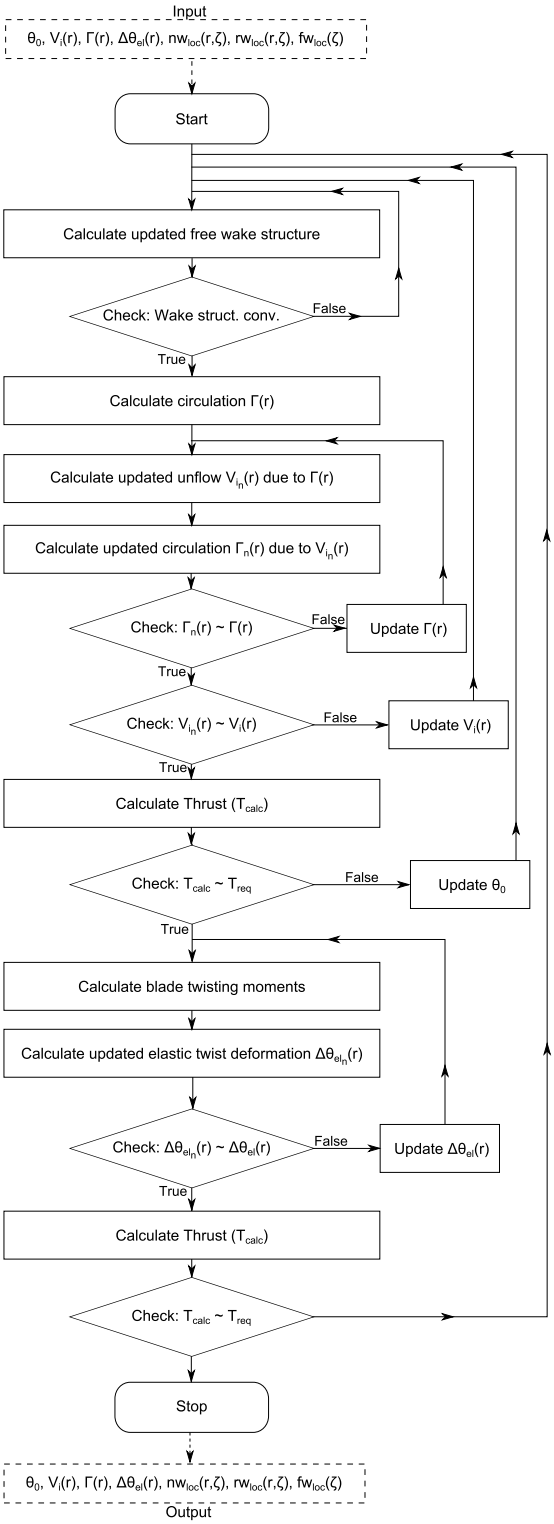

Figure B.14. Process C flow chart

As part of this study an interesting behavior was observed. In the even that an extended near wake component was used for the analysis (for blades with low or no pre-twist) beyond a critical number of extended near wake vortices the stability of the solution deteriorated. This is thought to be due to the relative close proximity of the rigid extended near wake vortices to the far wake vortex. While the magnitude of η_{nw} (the extension angle of the extended near wake) would effect the final solution the stability of the wake deformation solution was not found to be sensitive to this parameter.

B.7.4 Supporting notes

For both process B and C, the induced velocity calculated at the blade is a function of the contributions of the near wake trailed vortices, far wake and in applicable cases the extended near wake. The bound vortex effect was not included in the calculation of the induced velocity at the blade control points. This is the result of the hybrid lifting line and surface approach to the wake modeling. Adding the effect of the bound vortices was found to produce infeasible results and in some cases even prevent solution convergence.

For the current analysis the far wake structure was considered to be converged when the L^2 norm of the difference of the wake structures of successive iterations was lower than $1e-3$. This method is based on the work presented by Bagai [197]. Furthermore, the convergence criteria for both the induced velocity and bound vortex strength loops was set for the respective L^2 norms of the difference of the solutions of successive iterations to be below $1e-2$. Lastly, the elastic twist distribution calculation loop was set to have a convergence criteria for the L^2 norm (of the difference of the solutions of successive iterations) to be below $1e-4$.

Unless otherwise stated the far wake structure was extended by 8 revolutions into the free stream and $\Delta\Psi = \Delta\zeta = 10deg.$. The $\Delta\Psi$ value was set based on a parametric study presented by Bagai [197]. In order to provide a smooth wake structure of the far wake at truncation, the far-field extrapolation boundary condition technique described by Leishman [203] was used for the current analysis. In particular the bottom 30% of collocation points had the same applied induced velocity as the corresponding collocation points above (the effect of this method is

clearly seen in figure B.1 where the last few revolutions of the far wake are smooth).

B.8 Benefits of the current model

As stated earlier, the primary goal was to develop a high fidelity wake model solution algorithm which did not compromise speed or stability. The proceeding sections present the findings of the efficiency studies carried out to understand the improvements that are achieved with the current model. In order to calculate the possible improvement in speed it is important to consider the hardware and the code structure itself (aside from the trim algorithm itself). The analysis was run on a desktop PC with specifications as listed in table B.1.

Table B.1. Pertinent properties of the computer used for analysis

Prop. Name.	Specification
Processor	AMD Athlon^{TM}64 X2 Dual Core
Maximum clock speed	2.31 Ghz
RAM	1.93 GB
Operating system	Windows XP SP3

The software (which incorporates the presented wake model) was programmed using a combination of MATLAB®ver. 2011a and C++ (with pointers). The use of two separate programming language served the purpose of being able to incorporate the ease of importing external data structures and plotting information provided of MATLAB®(which is a scripting language) and the speed and efficiency of C++ into the software. To clarify, the code used MATLAB®as the base for introducing and collecting program data (i.e. the front-end) while using a C++ program to do the heavy number crunching (calculation of induced velocity, completing wake structure iterations etc.). Since any C++ programs need to be compiled before they can be run, they run at the machine level, thereby providing the speed needed.

As a comparison, a software which incorporated the Bagai and Leishman [197] Pseudo-Implicit Predictor-Corrector (classic PIPC) model was used. This second software is based on a legacy code developed by Eui Sung Bae [185]. Similar to the current model this code also used the MATLAB®platform as the front-end. Furthermore, this code also utilized a machine level compiled program for

the computational portions of the code (it was developed using the FORTRAN programming language). Due to the similarities of the code structure any benefits due to the use of machine level programs is largely abated and therefore these two softwares were used to understand the primary efficiency improvements that are possible using the proposed deformable wake model as compared to the classic PIPC algorithm. The results presented in the proceeding section compare the efficiency of only the wake structure iteration loop (see figure B.14), as this provides a better understanding of the efficiencies of the two algorithms. To clarify only the far wake structure (Region III) is used for the calculation and is assumed to have a constant vortex strength and a constant core radius. Furthermore, the far-field extrapolation boundary condition method was not used for this portion of the analysis.

B.8.1 Wake structure comparison

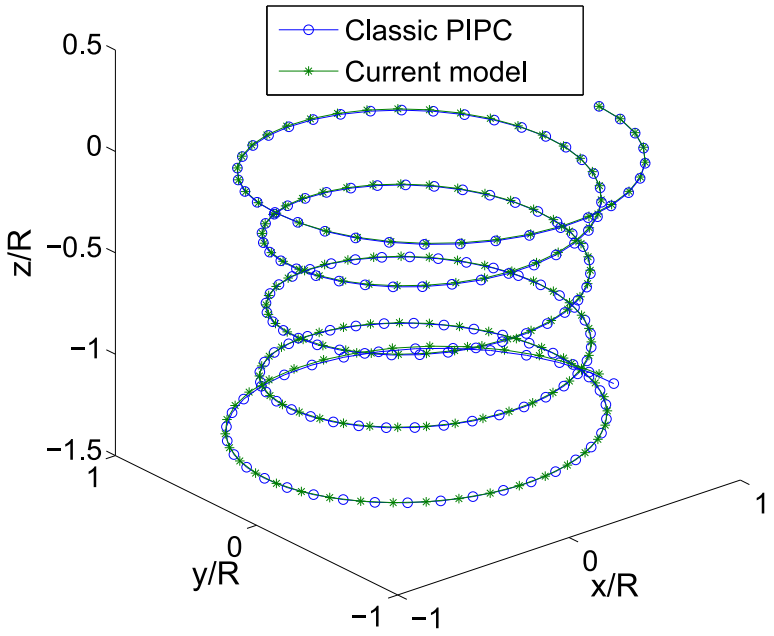

Figure B.15. Wake structure solution comparison

Figure B.15 presents the converged wake structure solution of both the methods for a qualitative comparison of both the solutions. The solution was found for two

helices (extended 5 revolutions) in the free stream, emanating 180 degrees from each other at a distance of 32.2 ft about the center of rotation (similar to a 2 bladed 16.1 ft radius rotor). As can be seen the solutions are in good agreement and provide confidence in the ability of the proposed model to provide solutions comparable to the classic PIPC algorithm. The minor deviation observed between the two solutions is attributed to the removal of the induced velocity term in the $\hat{e}_\theta$ direction as presented in section B.5.

B.8.2 Effect of number of vortex helices

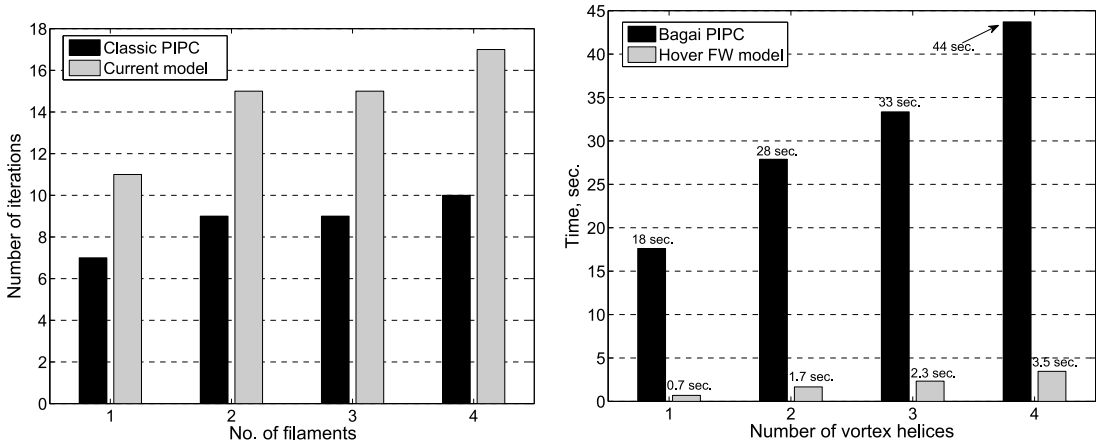

(a) Number of iterations (b) Solution time

Figure B.16. Number of iterations and time to solution convergence comparison between classic PIPC and the current model solutions for varied number of vortex helices in free stream

The analysis of multi-bladed rotors requires the incorporation of more than one wake structure in the free stream. This can have a big impact on the computational speed of the model. To quantify the extend of the impact, the wake convergence routine was executed for a set of cases with varying number of vortex helices emanating from a radius of 16.1 ft from the center of rotation (with a constant core radius and circulation strength). Each increase in the number of vortices in the free-stream is similar to an increase in the number of blades of rotor system. All the vortices are adjacent to the next one by an equal angle. Figure B.16(a) presents number of iterations required for the convergence of the wake structure

using the classic Pseudo-Implicit Predictor-Corrector algorithm along with number of iterations needed for solution convergence of the current model. Whereas, figure B.16(b) presents the variation in the time take to calculate a converged solution using each of the two models. Increasing the number of vortices in the free stream relates to marginal increases in the number iterations taken to produce a converged solution for both algorithms. Overall, the number of iterations required to calculate a converged solution with the proposed model is higher. However, when considering the time needed to calculate a solution, the present model is shown to requires significantly less time. In particular, the time taken to calculate a solution using the proposed algorithm in the case of one vortex in the free-stream is over 25 times faster than the classic PIPC routine.

B.8.3 Effect of azimuthal/wake age step size

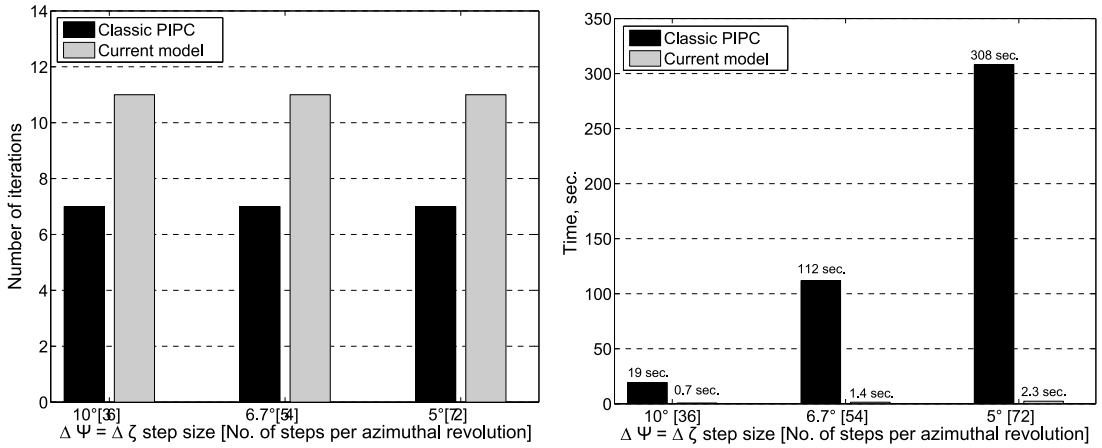

(a) Number of iterations (b) Solution time

Figure B.17. Number of iterations and time to solution convergence comparison between classic PIPC and the current model solutions for varied number of azimuthal (wake age) step sizes

The solution error of any difference scheme is proportional to the step size used in the analysis. However, while reducing the step size reduces error, it also leads to a more computational expensive solution. The current model and the classic PIPC algorithms were analyzed for a one vortex configuration for three step sizes: $\Delta\Psi = \Delta\zeta = 10$, 6.7 and 5 degrees (36, 54 and 72 azimuthal steps

per revolution respectively). Figure B.17(a) presents the number of iterations required whereas figure B.17(b) presents the time required for a converged solution using both algorithms. Similar to effect of the variation of the number of vortex helices, while the number of iterations required for the current model to calculate a converged solution is higher than that of the classic PIPC routine the time take for a converged solution is significantly reduced. As expected, while overall the time taken for a converged solution increases with the number of steps per revolution, the time required for the classic PIPC increases significantly. In particular for the smallest step size of 5 degrees, the current model is over 133 times as fast compared to the classic PIPC algorithm.

B.8.4 Effect of maximum wake age length

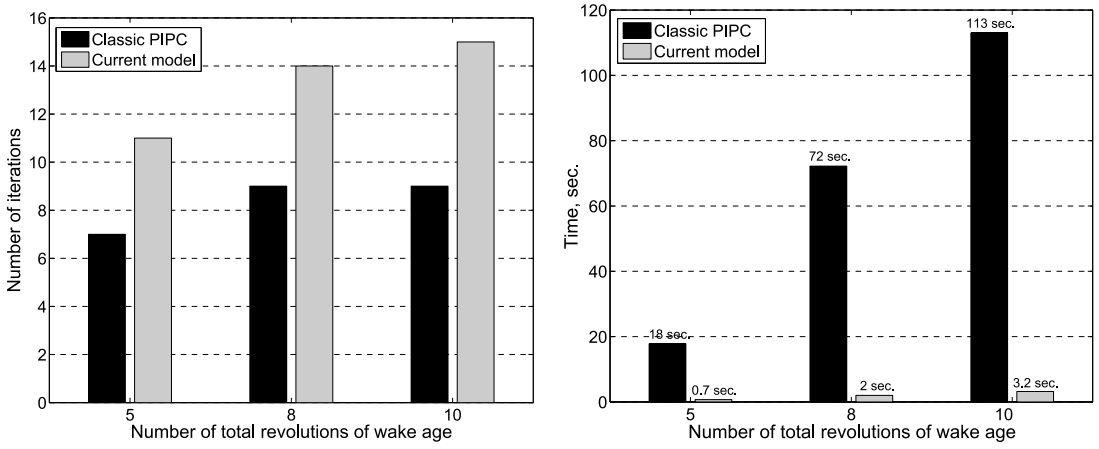

(a) Number of iterations (b) Solution time

Figure B.18. Number of iterations and time to solution convergence comparison between classic PIPC and the current model solutions for varied number of total wake length (represented as number of revolutions)

Lastly, the length of the far wake vortex helix (in number of revolutions) is also an important parameter in controlling the fidelity of the solution. In particular increasing the number of total revolutions of the deformable vortex can lead to higher fidelity. Figure B.18 presents a comparison of the number of iterations required to solve (Fig. B.18(a)) and the time taken for a converged solution (Fig. B.18(b)) for both algorithms. As can be seen in the figures increasing the total

number of revolutions of the far wake overall has a negligible effect on the number of iterations with the current model requiring more iterations to produce a converged solution. Conversely, similar to previously stated trends, the time taken to produce a solution using the current model is significantly lower for all vortex lengths. In this case, the current model can calculate a converged solution up to 35 times faster than the classic PIPC algorithm.

B.8.5 Comparison notes

As seen in the previous sections, overall while the current model requires a larger number of iterations to converge, the total time required to produce a converged solution is significantly lower than the classic PIPC algorithm. The primary reason for these observations is reduction of the actual calculation domain for the current model (see figure B.8). While the current analysis shown is for just the wake convergence solution, the benefit of the time saved can be clearly seen when applied to the full trim procedure, especially for cases where a table look-up scheme (similar to the current analysis) is used. Alternatively, the speed of the solution can be used to improve the fidelity of the solution by increasing the number of steps or the total number of revolutions of the far wake structure. Furthermore, the current model can also be adapted an applied to all the components of the wake structure mode (Regions I, II and III), thereby leading to a higher fidelity solution as all the components of the wake can deform due to external and self-induced velocities.

B.9 Model validation

Using three different sets of experimental rotor hover test data the model results were thoroughly validated. The first two sets data are from experiments conducted using two different scaled rotors by Caradonna and Tung [25] and by Ballard, Orlof and Luebs [26]. The last set of data used for the model validation is the test of the full scale BO-105 rotor system by Warmbrodt and Peterson [199]. All the experimental data used in the current analysis was digitized from the images provided in the corresponding papers and technical reports of the tests.

B.9.1 Scaled rotor experiment set I

The specifications of the rotor system and test parameters of the test conducted by Caradonna and Tung [25] is presented in table B.2. As can be seen this test is for blades with no twist and therefore was used to understand the effects and uses of the extended near wake (Region II) of the model. Considering the blade size was relatively small (and the lack of the blade stiffness data) the rotor was modeled as rigid in the analysis (i.e. the torsionally elasticity convergence routine was bypassed). The experiments were conducted for three separate collective inputs: 5 (low thrust), 8 (mid thrust) and 12 (high thrust) degrees ($C_t = 0.0021, 0.0046$ & 0.0079 respectively). The blade was instrumented with pressure ports along the chord at five separate spanwise locations. The local coefficient of lift (C_l) was calculated by integrating the pressures measured by these ports.

Table B.2. Pertinent specifications of the rotor system and test parameters of the test conducted by Caradonna and Tung [25]

Prop. Name.	Value
Radius	3.75 ft
Number of blades	2
Chord	0.63 ft
Airfoil	NACA 0012
Pre-twist	None
Rotor speed	1250 RPM

B.9.1.1 Thrust variation

Figures B.19(a), B.19(b) and B.19(c) show the spanwise variation of the local coefficient of lift as measured on the rotor as compared to the results calculated by the current model for the three thrust levels measured. As can be seen, the correlation of the numerical and experimental results for the mid and high thrust levels is very good. For the low thrust condition on the other hand, the correlation is fair as see in figure B.19(c). The figures show the capability of the current model to capture the peaks in the load distribution caused due to the proximity of the tip vortex shed by the successive blade (perpendicular blade vortex interaction). In particular the effect of the shed tip vortex is amplified as rotor thrust level is reduced (compare figure B.19(a) to B.19(c)). This phenomenon is due to the

reduction of the downward convection angle of the vortex helix as the thrust level is reduced (due to the overall reduction of the corresponding inflow velocity) which decreases the distance of the shed tip vortex to the blade. The trim solution was capable of producing a very good estimate of the control input required to produce the specified thrust (within 10% of the stated values).

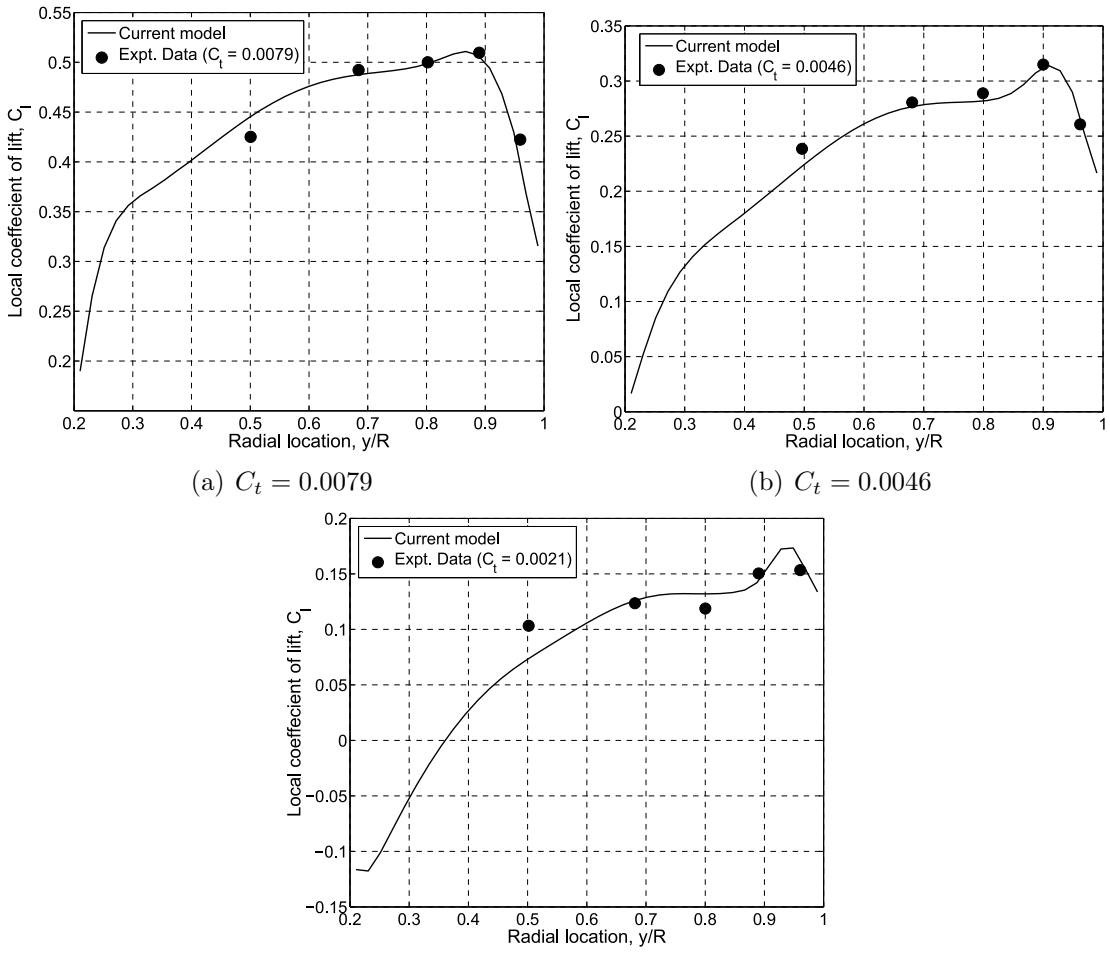

(a) $C_t = 0.0079$ (b) $C_t = 0.0046$

(c) $C_t = 0.0021$

Figure B.19. Comparison of the local coefficient of lift distribution calculated by the current model and measured experimentally by Caradonna and Tung[25]

For these results, the current model incorporated the use of the extended near wake structure which included two vortex filaments with a corresponding η_{enw} value of 290 degrees. This was based on tuning the model for the mid level thrust condition ($C_t = 0.0046$). The results of this tuning provide an insight into the

effects of the extended near wake on the results calculated and were used as a guide for other analyses and therefore presented in the proceeding sections.

B.9.1.2 Tip vortex helix structure

Figure B.20 presents the comparison of the tip vortex helix structure measured experimentally with the results of the presented model. As can be see in the figure, the results compare well and showcase capability of the proposed model to predict the wake structure of a hovering rotor. The current model was run with a far wake length of 8 revolutions which is far larger than what is shown (i.e. approximately 1.4 revolutions), as the data presented in the paper was limited to this range [25]. As can be seen this wake data corresponds to a length up to 0.5R downstream from the rotor.

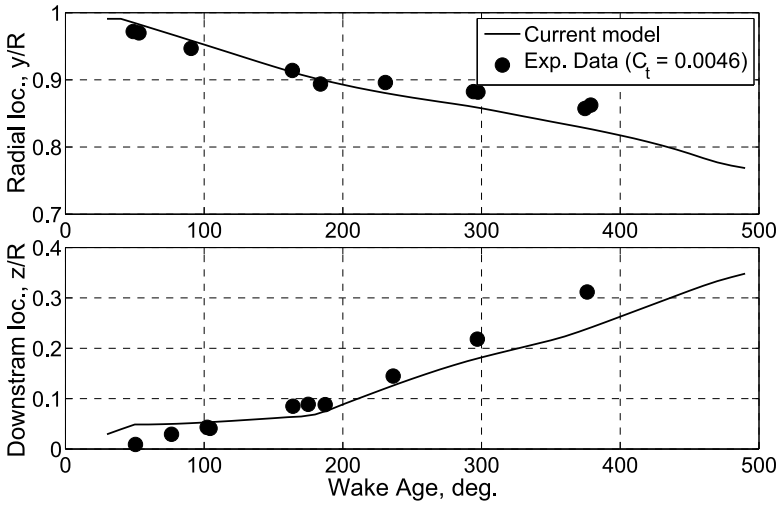

Figure B.20. Comparison of the tip vortex structure calculated by the current model and measured experimentally by Caradonna and Tung [25] ($C_t = 0.0046$)

B.9.1.3 Number of extended near wake helices

As explained earlier, the model was tuned for the mid level thrust condition by varying the parameters of the extended near wake. Figure B.21 shows the effect of the variation of the number of vortex filaments which are a part of the extended near wake component. To isolate the effects the results presented in this figure

for a constant η_{enw} value of 290 degrees. As can be seen the inclusion of the extended near wake has the effect of leveling out the distribution of lift across the blade span. In this particular case, this results in the reduction in the negative lift production area near the root of the blade. Furthermore, increasing the number of extended near wake helices has the effect of smoothing out the distribution of lift (and correspondingly the inflow). The results shown are for up to two extended near wake vortices (best correlation with experimental data) as when additional vortices were added convergence issues in the far wake structure calculation loop were encountered. Based on this observation for future analysis, the number of extended wake vortices was set to be the largest number which for which such convergence issues were not encountered. The issue of convergence was traced to the proximity of the extended near wake vortex helix to the far wake vortex helix, therefore the maximum number of vortices allowed is directly a function of the span length of the blade.

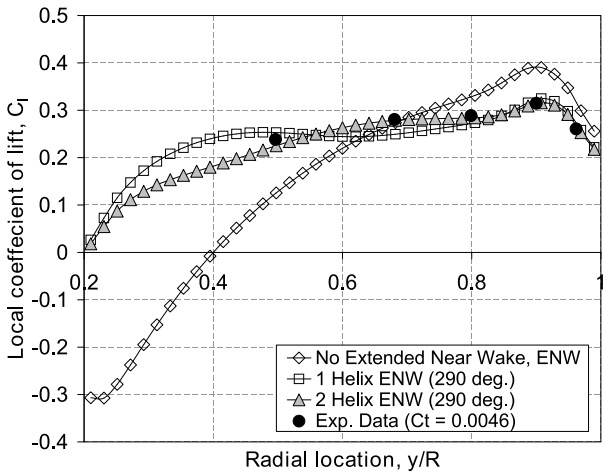

Figure B.21. Comparison of local lift coefficient calculated by the current model for varying number of extended near wake helices as compared to experimental data measured by Caradonna and Tung [25] [25] ($C_t = 0.0046$)

B.9.1.4 Length of extended near wake helices

The second parameter which was used to tune the model was the length of the extended near wake helices (eta_{enw}). Figure B.22 shows the variation of the local lift coefficient for varied eta_{enw} values. For this analysis, the number of vortex

helices was set to two. As can be seen, increasing the length of the extended near wake corresponds to the smoothing of the lift distribution and correspondingly reducing the negative lift portion of the blade near the root. During the course of this analysis no convergence issues were observed to arise due to the increase of eta_{enw}. As seen, the best correlation with the available experimental data was observed for an eta_{enw} value of 290 degrees. While the the parameters of the extended near wake were based on tuning the model for the mid level thrust, the same values were used for the remainder of the cases. The good correlation of the model results with the experimental results of the other thrust levels provide some indication that the tuned values of the extended near wake parameters are relatively insensitive to the operating thrust condition.

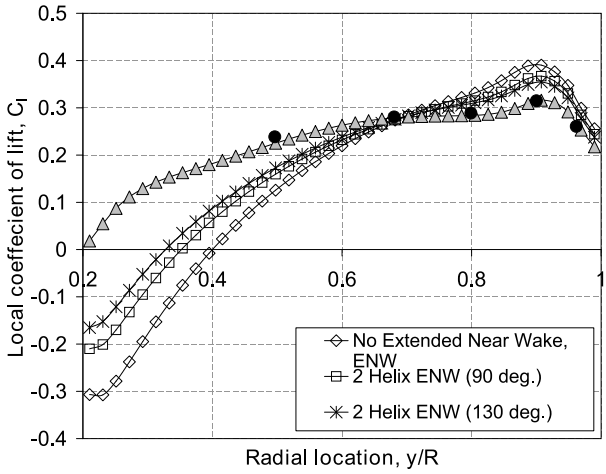

Figure B.22. Comparison of local lift coefficient calculated by the current model for varying lengths of the extended near wake as compared to experimental data measured by Caradonna and Tung [25] [25] ($C_t = 0.0046$)

Figure B.23 presents a schematic showing the contributions of the various regions of the wake structure to the total induced velocity calculated at the blade. For the case of blades with little to no twist the ratio of tip to root vortex strength will be closer to one. As a result of this the wake structure at the root may remain in the free stream before grouping. The effect of this is the production of an upwash at root resulting in a lower total induced velocity and hence increasing the angle of attack near the root region. In effect the extended near wake structure is attempting to capture the effects of the two separate roll up regions of the wake

structure behind a rotating blade in hover.

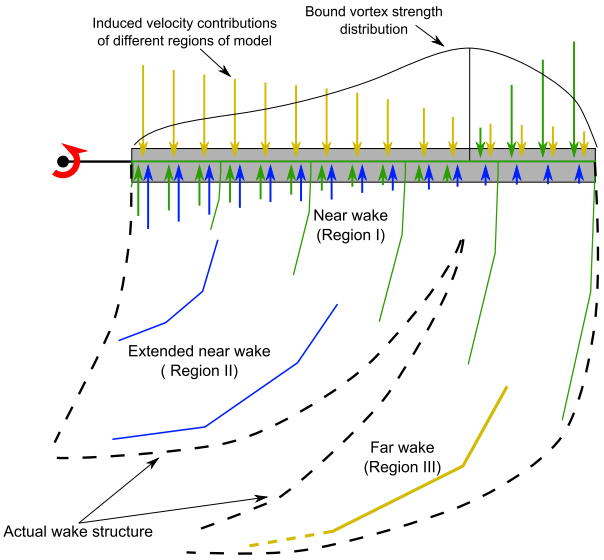

Figure B.23. Schematic explaining the effects of the extended near wake

B.9.2 Scaled rotor experiment set II

Table B.3. Pertinent specifications of the rotor system and test parameters of the test conducted by Ballard, Orloff and Luebs [26]

Prop. Name.	Value
Radius	3.44 ft
Number of blades	2
Chord	0.25 ft
Airfoil	NACA 0012
Pre-twist	Linear (-8 deg. at tip)
Rotor speed	700 RPM

Table B.3 presents the pertinent rotor system and test specification of the second experimental data set which was used for the validation of the current model [26]. This test was undertaken to understand the effect of tip shape on the rotor performance and as such the blade included an off-line replaceable tip section. The test was run only at one input pitch and therefore for a constant C_t of 0.0046. For the current analysis only the data of the rectangular planform tip

was used (i.e. the blade had not taper). The inflow was measure using a laser velocimetry system. This data was later used to calculate the distribution of the local lift coefficient (C_l).

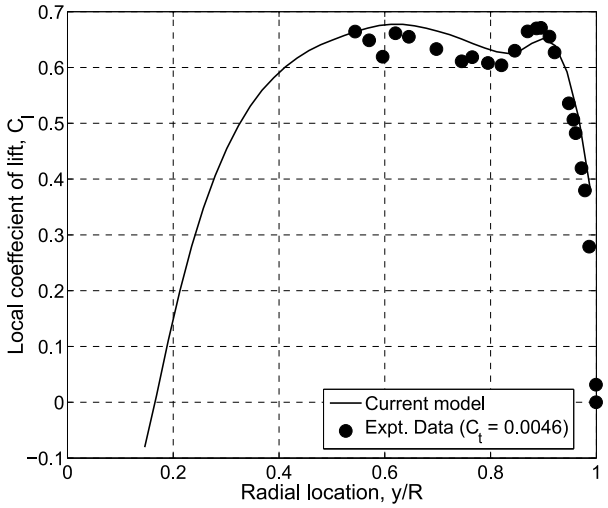

Figure B.24. Comparison of the local coefficient of lift distribution calculated by the current model and measured experimentally by Ballard, Orloff and Luebs [26] (C_t = 0.0046)

Figure B.24 presents the experimentally measured local coefficient of lift along with the solution tabulated using the presented model. As can be seen in the figure the results correlate very well. For this analysis, no extended near wake was used and therefore indicates that the extended near wake is only required for blades with little to low twist. Therefore for all proceeding analysis the extended near wake was only used for blades with lower than -8 deg tip pre-twist (with the extended near wake filament length (η_{enw}) varied linearly from 290 degrees to zero within this range). This variation of the extended near wake parameters is an initial estimate and requires significant detailed analysis to fine tune.

As seen in figure B.24 the peak loading effect at the tip of the blade caused due to the shed tip vortex is seen in greater resolution here. Furthermore, the presented model is shown to capture, in good detail, the shape and location of the peak. This comparison showcases the modeling fidelity capable with the current model.

B.9.3 Full scale experiment: BO-105 rotor system

As stated earlier, prior to proceeding with the analysis the rotor model used in this analysis was thoroughly validated using experimental data presented by Warmbrodt and Peterson [199]. The experiment was for the full scale BO-105 rotor system which was tested in hover at the 40- by 80-feet wind tunnel at NASA Ames Research Center. The experiment was conducted for various thrust levels at different operating rotor speeds (350, 375, 400 and 425 RPM). The following section presents the detailed comparison of the experimental results along with the predictions of the current model.

B.9.3.1 Overall comparison

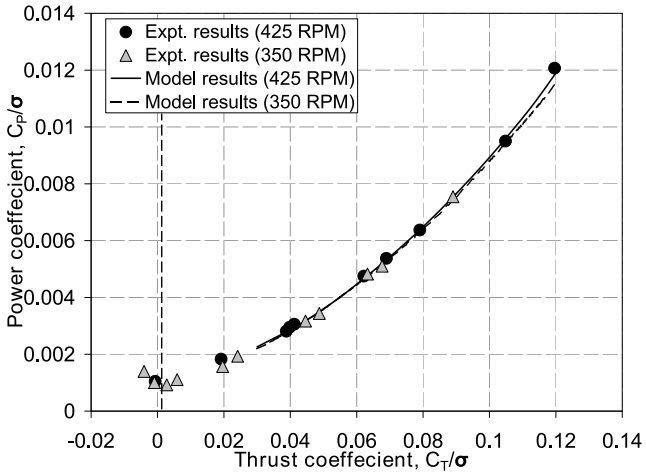

Figure B.25. Comparison of experimental and numerical results for the BO-105 full scale rotor in hover

Figure B.25 show the variation of the coefficient of power as a function of the coefficient of thrust measured experimentally as compared to the predicted results for two rotor speeds (corresponding to the lowest and highest speeds measured experimentally). The presented results include the effects of torsional elasticity and use the centroid approach for the far wake release point discussed earlier. In particular, the elastic axis was set to be $0.25c$. This value was picked on a parametric study whose results are presented in section B.9.3.2.

For the low end of the C_t/σ (below 0.04), as seen in the figure, the model

was not able to produce a converged solution when the centroid approach was used to calculate the far wake release point. This behavior is due to the large changes in bound vortex strength with small changes in far wake release point for low thrust cases. For low thrust conditions, the downward convection angle of the wake structure is lower and therefore has a more concentrated effect on the induced velocity calculated at the blade. A possible solution to predict the performance in these low ranges is to fix the far wake release point. The effect of the position of the release location is discussed in section B.9.3.3.

B.9.3.2 Elastic axis location

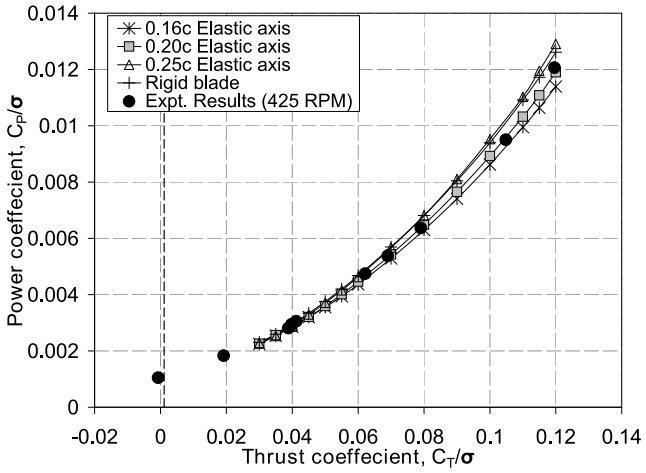

Figure B.26. Comparison of experimental (425 RPM) and numerical results for a variety elastic axis locations

Figure B.26 presents the variation of the power curves as a function of thrust for varying elastic axis location on the blade as compared to the experimental data corresponding to the 425 RPM tests (this rotor speed data was picked as it is closest to the baseline operating RPM of the BO-105). As can be seen varying the elastic twist location forward of the quarter chord axis results in lower power requirements. In particular, an elastic axis location of 0.20c (from the leading edge) was found to correlate best with the experimental results. The reduction in power with movement of the elastic axis forward of the quarter chord line is due to the increased moment applied to the blade (as the lift component produces an additive

moment) and therefore produces an elastic twist distribution that complements the existing blade pre-twist and therefore move the lift further inboard. Based on this analysis, the elastic axis for all BO-105 type rotor configurations analyzed in the presented study was set to 0.20c.

B.9.3.3 Far wake release location

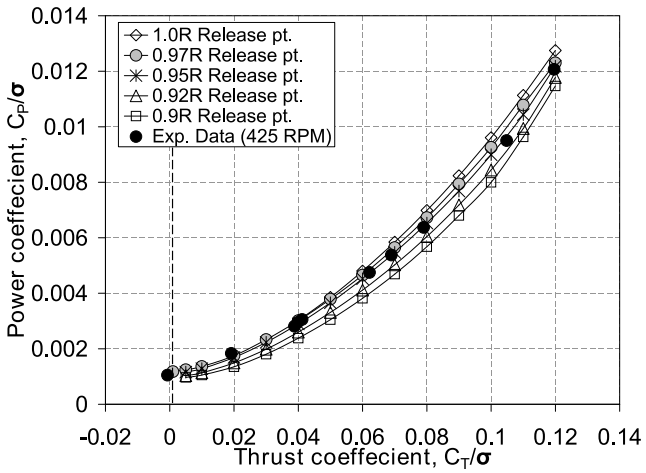

Figure B.27. Comparison of experimental (425 RPM) and numerical results for a variety far wake release locations

As stated earlier, convergence issue with the wake structure were encountered when the centroid method of calculating the far wake release point was used for low thrust configurations. In an effort to stabilize the trim solution, beyond a certain number of iterations of the bound vortex strength distribution calculation loop the faw wake vortex starting location was fixed. Figure B.27 presents the results of the analysis undertaken to determine which would be the best release location. As seen in the figure, the power curves predicted by the model for various far wake release locations are compared to the experimental data set (corresponding to the 425 RPM case). As is apparent in the figure, 0.97R shows the best correlation for the low thrust conditions (conditions corresponding to the convergence issues) whereas 0.95R works best for mid to high thrust conditions. However, since the issue lies with convergence of the low thrust conditions, the release point of the far wake was fixed to 0.97R in the event the bound vortex strength calculation loop

would not achieve convergence within a specifies number of iterations. The use of a fixed release point was shown to improve the speed of convergence and therefore is an option when the fidelity of the solution can be compromised for the solution speed.

APPENDIX C

Variable camber concept supplementary materials

C.1 Airfoil drag polars

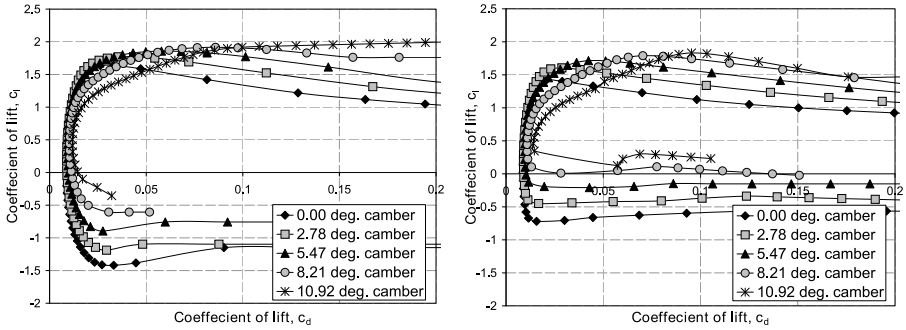

(a) Mach 0.0 (b) Mach 0.4

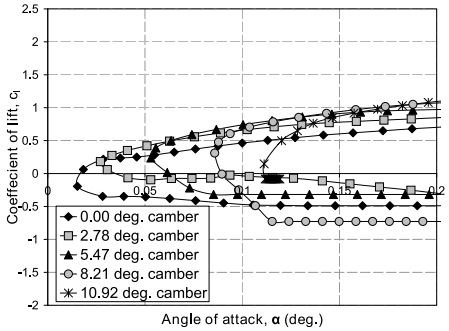

(c) Mach 0.8

Figure C.1. Airfoil drag polars for various mach numbers

C.2 Effect of rotor speed

As highlighted by Guo [132], Steiner et. al. [133], Mistry and Gandhi [134] and Bowen-Davies and Chopra [135], rotor speed has a significant impact on the power required especially at relatively low thrust levels and altitudes due to the reduction in profile power. Figure C.2 presents the effect of the rotor speed variation as it applies to the current rotor system (BO-105) independently and in combination with the quasi-static camber variation for case 1 (Sea level). The figure presents the contour levels of the change in power (in percentage as compared to the baseline) as a function rotor speed and camber. To clarify a positive change represents an increase in power and vice versa. As seen, rotor speed only variation leads to a comparable power reduction to that of the camber only for the lowest thrust

level considered (Fig. C.2(a)). However, as the gross weight is increased the improvements diminish for the rotor speed only variation whereas for the camber only case the power reduction actually improve (echoed by Fig. 4.23).

Furthermore, for the lower thrust levels, reducing the rotor speed in combination with camber variation results in twice the power reduction as compared to the camber only case (4.8% - Camber only, 10.7% - Camber and rotor speed). However, as the thrust level is increased the amplification of the improvement due to the combined rotor speed variation diminishes, leading to the best case condition for at 6400 lbs to be for the baseline rotor speed with a input camber of 10 degrees (compare Fig. C.2(a) to Fig. C.2(c)). The observed amplification of the power reduction due to rotor speed reduction for the low thrust condition is largely attributed to the reduction of the profile power resulting from lower dynamic pressures. Increases in thrust levels would require higher rotor operating speeds to prevent stall which results in the diminished effect of rotor speed on the power reductions.

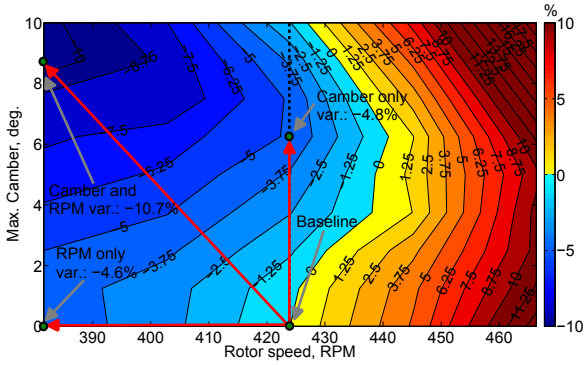

(a) 4800 lbs

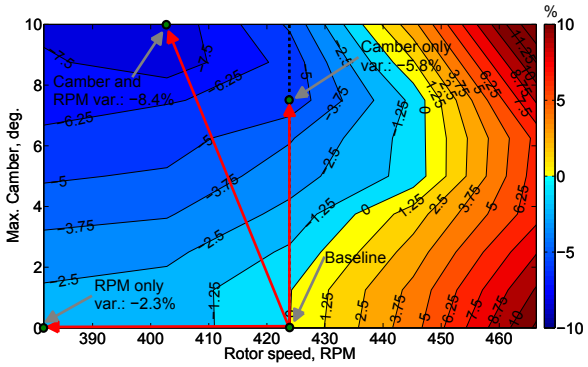

(b) 5500 lbs

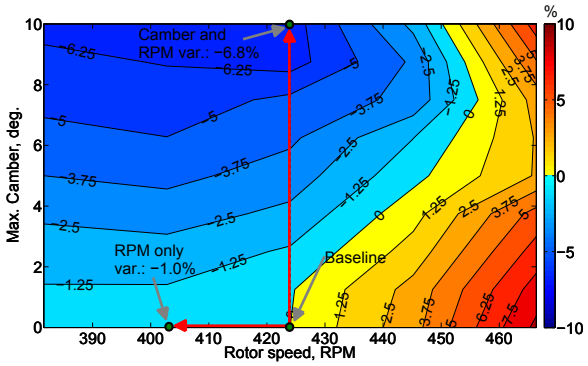

(c) 6400 lbs

Figure C.2. Percentage change in power (as compared to baseline) as a function of rotor speed and camber (Case 1, Sea level, 4800 lbs)

C.3 Sensor calibration curves

Presented in this section are the calibration curves of the three sensors used in the experiments performed on the variable camber prototype. Note that the calibration curves for the linear potentiometer and the load cell are based on that presented by Hayden [166]. The calibration curves for all the sensors are nearly linear, therefore the equations of the least square fit of a linear function (presented in the figures themselves) are used to convert the output (Bits) of the data acquisition system to physical units.

C.3.1 Linear potentiometer calibration curve

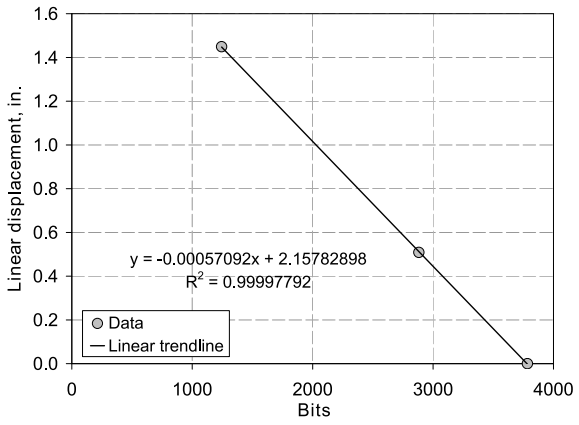

Figure C.3. Calibration curve of the linear potentiometer

C.3.2 Load cell calibration curve

C.3.3 Rotary potentiometer calibration curve

As can be see in figure C.5, due to noisy output of the rotary potentiometer the data gathered from this sensor was considered to be unreliable.

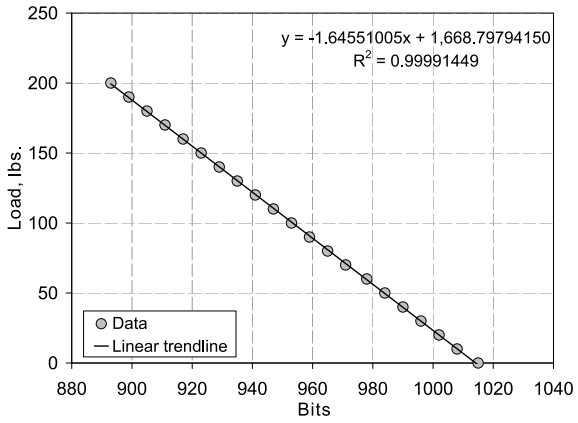

Figure C.4. Calibration curve of the load cell

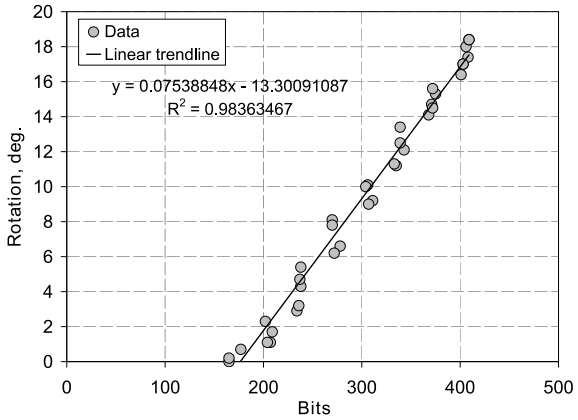

Figure C.5. Calibration curve of the rotary potentiometer

C.4 Actuation frame test

Figure C.6 presents the undeformed and deformed states of the actuation structure only. As can be clearly seen in figure C.6(b) the system produces an output chordwise motion for a given input warping. It is precisely this motion which allows for the distributed blade camber to be realized.

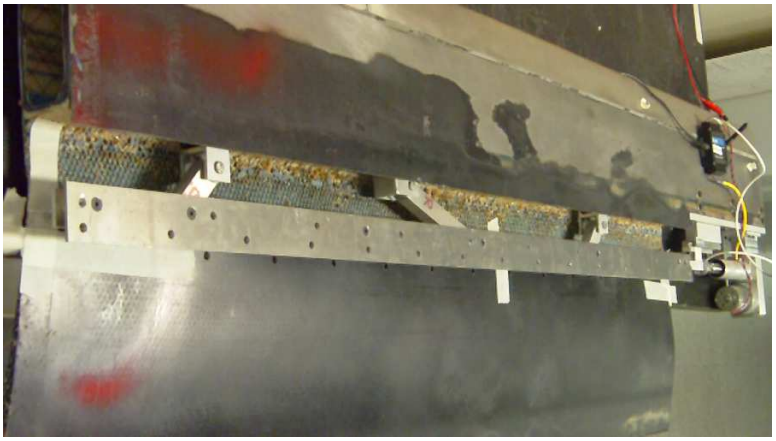

(a) Undeformed

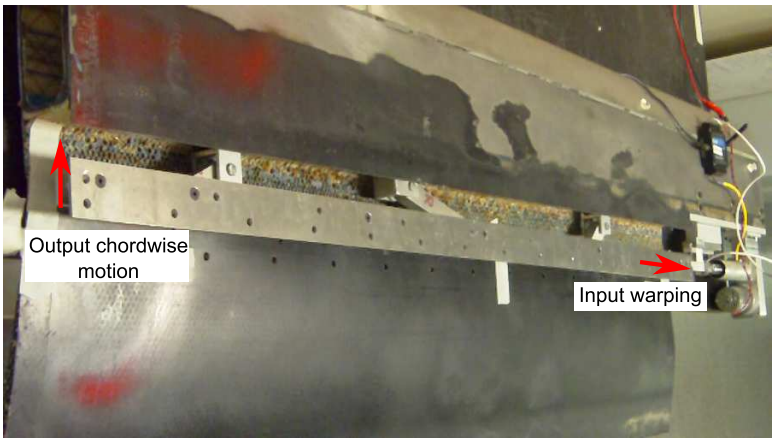

(b) Deformed config

Figure C.6. Undeformed and deformed configurations of the actuation structure only

Bibliography

[1] Samak, D. and I. Chopra (1993) "A Feasibility Study to Build a Smart Rotor: Trailing Edge Flap Actuation," in *SPIE Symposium on Smart Structures and Intelligent Systems, Vol 1917*.

[2] Walz, C. and I. Chopra (April 1994) "Design and Testing of a Helicopter Rotor Model with Smart Trailing Edge Flaps," in *35th Structures, Structural Dynamics and Materials Conference, Adaptive Structures Forum, Hilton Head, SC*.

[3] Fulton, M. and R. Ormiston (April 29-May 1, 1997) "Hover testing of a small-scale rotor with on-blade elevons," in *53rd American Helicopter Society Forum, Virginia Beach, VA*.

[4] Koratkar, N. and I. Chopra (2001) "Wind tunnel testing of a Mach-Scaled rotor model with trailing-edge flaps," *Smart Materials and Structures*, **10**, pp. 1–14.

[5] Spencer, B. and I. Chopra (Feb. 1996) "Design and Testing of a Helicopter Trailing Edge Flap with Piezoelectric Stack Actuators," in *SPIE symposium on Smart Structures and Materials, Vol. 2717*.

[6] Chandra, R. and I. Chopra (April 7-10, 1997) "Actuation of Trailing Edge Flap in Wing Model using Piezostack Device," in *38th Structures, Structural Dynamics, and Materials Conference and Adaptive Structures Forum, Kissimmee, FL*.

[7] Lee, T. and I. Chopra (2001) "Design of a piezostack-driven trailing-edge flap actuator for helicopter rotors," *Smart Materials and Structures*, **10**, pp. 15–24.

[8] ——— (05 March 2001) "Design of Bidirectional Piezoelectric Actuator for Blade Trailing-Edge Flap," in *SPIE symposium on Smart Structures and Materials, Newport Beach, CA, Vol. 4327*.

[9] Hall, S. and E. Prechtl (1999) "Preliminary testing of a Mach-Scaled Active Rotor Blade with a Trailing Edge Servo-Flap," in *SPIE Symposium on Smart Structures and Materials*.

[10] Straub, F. and D. Merkley (May 11-13, 1994) "Design of a servo-flap rotor for reduced control loads," in *50th American Helicopter Society Forum, Washington, D.C.*

[11] Hasegawa, Y., N. Katayama, N. Kobiki, E. Nakasato, E. Yamakawa, and H. Okawa (May 9-11, 2001) "Experimental and Analytical Results of Whirl Tower Test of ATIC Full Scale Rotor System," in *57th American Helicopter Society Forum, Washington D.C.*

[12] Barrett, R. (1990) *Intelligent rotor blade and structures development using directionally attached piezoelectric crystals*, Master's thesis, University of Maryland.

[13] Chen, P. and I. Chopra (1996) "Induced strain actuation of composite beams and rotor blades with embedded piezoceramic elements." *Smart Materials and Structures*, **5**, pp. 35–48.

[14] Rodgers, J. (February 1999) *Development of an Integral Twist-Actuated Rotor Blade for Individual Blade Control*, Ph.D. thesis, Massachusetts Institute of Technology.

[15] Wilbur, M. L., W. T. Y. Jr., W. K. Wilkie, C. E. S. Cesnik, and S. Shin (May 2-4, 2000.) "Hover Testing of the NASA/ARMY/MIT Active Twist Rotor Prototype Blade," in *56th Annual Forum of the American Helicopter Society, Virginia Beach, VA*.

[16] Derham, R., D. Weems, M. B. Mathew, and R. Bussom (May 9-11, 2001) "The Design Evolution of an Active Materials Rotor," in *57th American Helicopter Society Forum, Washington, DC*.

[17] Bernhard, A. and I. Chopra (July-August 2002) "Hover Test of Mach-Scale Active Twist Rotor Using Piezo-BendingTorsion Actuators," *Journal of Aircraft*, **39, No. 4**, pp. 678–688.

[18] Mercier des Rochettes, H., D. Joly, L. Buchaniek, and P. Leconte (20-24 April 2009) "A New concept of Active Twist rotor blade applied to Main rotor of helicopter," in *RTO Applied Vehicle Technology Panel (AVT) Symposium, Evora, Portugal*.

[19] Ruggeri, R., D. Arbogast, and R. Bussom (7 - 10 April 2008) "Wind Tunnel Testing of a Lightweight -Scale Actuator Utilizing Shape Memory Alloy," in *49th AIAA/ASME/ASCE/AHS/ASC Structures, Structural Dynamics, and Materials Conference, Schaumburg, IL*.

[20] Mistry, M. (2008) *Induced warp systems to obtain active twist of rotor blades*, Master's thesis, The Pennsylvania State University.

[21] Fenny, C. (June 13, 2005) "Mechanism for varying the diameter of rotors using compound differential rotary transmissions," in *61st American Helicopter Society Forum, Grapevine, TX*.

[22] Mirick, P. (1983) *A comparison of theory and flight of the BO 105/BMR in hover and forward flight*, *Tech. rep.*, U.S. Army Aerostructures Directorate, Hampton, VA.

[23] (2012), "The Bug - Precision Linear Actuator from Ultra Motion. Ultra Motion Linear Actuators," Web.
URL `http://www.ultramotion.com/products/bug.php`

[24] Karem, A. (December 28, 1999), "Optimum Speed Rotor," .

[25] Caradonna, F. X. and C. Tung (September 1981) *Experimental and Analytical Studies of a Model Helicopter Rotor in Hover*, *Tech. rep.*, National Aeronautics and Space Administration (NASA), Technical Memorandum No. 81232, USAAVRADCOM TR-81-A-23.

[26] Ballard, J., K. Orloff, and A. Luebs (May 1979) "Effect of Tip Shape on Blade Loading Characteristics and Wake Geometry for a Two-Bladed Rotor in Hover," in *35th Annual National Forum of the American Helicopter Society, Washington, D.C.*

[27] Boeing (October 1983) *Helicopter Flying Qualities Characteristics CH-46E Volume 1*, *Tech. rep.*, Naval Air Development Center (Code 6053), Report no. NADC-81118-60.

[28] Leishman, G. (2006) *Principles of Helicopter Aerodynamics*, Cambridge University Press.

[29] Straub, F., V. Anand, T. Birchette, and B. Lau (Sept. 22-25, 2009) "SMART Rotor Development and Wind Tunnel Test," in *35th European Rotorcraft Forum, Hamburg, Germany*.

[30] Dietrich, O., B. Enenkl, and D. Roth (May 9-11, 2006) "Trailing Edge Flap for Active Rotor Control Aeroelastic Characteristics of the ADASYS Rotor System," in *62nd American Helicopter Society Forum, Phoenix, AZ.*

[31] Roth, D., B. Enenkl, and O. Dietrich (September 2006) "Active Rotor Control by Flaps for Vibration Reduction - Full scale demonstrator and first flight results -," in *32nd European Rotorcraft Forum, Maastricht, The Netherlands.*

[32] Leon, O. (2009) *Reducing Helicopter Main Rotor Power Requirements Using Multiple Trailing Edge Flaps And Extendable Chord Sections*, Master's thesis, The Pennsylvania State University.

[33] Chopra, I. (November 2002) "Review of State of Art of Smart Structures and Integrated Systems," *AIAA Journal*, **40, No. 11**, pp. 2145–2187.

[34] Spangler, R. (Feb 1989) *Piezoelectric Actuators for Helicopter Rotor Control*, Master's thesis, Massachusetts Institute of Technology.

[35] Prechtl, E. (May 1994) *Development of a Piezoelectric Servo-Flap Actuator for Helicopter Rotor Control*, Master's thesis, Massachusetts Institute of Technology.

[36] Hall, S. and E. Prechtl (1996) "Development of a piezoelectric servoflap for helicopter rotor control," *Smart Materials and Structures*, **5**, pp. 26–34.

[37] Ben-Zeev, O. and I. Chopra (1996) "Advances in the development of an intelligent helicopter rotor employing smart trailing-edge flaps," *Smart Materials and Structures*, **5**, pp. 11–25.

[38] Fulton, M. and R. Ormiston (May 20-22, 1998) "Small-scale rotor experiments with on-blade elevons to reduce blade vibratory loads in forward flight," in *54th American Helicopter Society Forum, Washington, D.C.*

[39] Koratkar, N. and I. Chopra (Apr. 12-15, 1999) "Analysis and testing of Mach scaled rotor model with piezoelectric bender actuated trailing-edge flaps for helicopter vibration control," in *40th AIAA/ASME/ASCE/AHS/ASC Structures, Structural Dynamics, and Materials Conference and Exhibit, St. Louis, MO.*

[40] ——— (July 2000) "Analysis and Testing of Mach-Scaled Rotor with Trailing-Edge Flaps," *AIAA Journal*, **38, No. 7**, pp. 1113–1124.

[41] Koratkar, N. (2000) *Smart Helicopter Rotor with Piezoelectric Bender Actuated Trailing-Edge Flaps*, Ph.D. thesis, University of Maryland.

[42] Lee, T. and I. Chopra (March 1999) "Design and Static Testing of a Trailing-Edge Flap Actuator with Piezostaccks for a Rotor Blade," in *SPIE Symposium on Smart Structures and Integrated Systems, San Diego, CA, Vol. 3329*.

[43] ——— (May 2000) "Design Issues of a High-Stroke, On-Blade Piezostack Actuator for a Helicopter Rotor with Trailing-Edge Flaps," *Journal of Intelligent Material Systems and Structures*, **11**, pp. 328–342.

[44] Lee, T. (1999) *High displacement piezoelectric trailing-edge flap mechanism for helicopter rotors*, Ph.D. thesis, University of Maryland.

[45] Prechtl, E. (Feb 2000) *Design and Implementation of a Piezoelectric Servo-Flap Actuation System for Helicopter Rotor Individual Blade Control*, Ph.D. thesis, Massachusetts Institute of Technology.

[46] Hall, S., T. Tzianetopoulou, F. Straub, and H. Ngo (2000) "Design and testing of a double X-frame piezoelectric actuator," in *SPIE Symposium on Smart Strucutres and Materials*.

[47] Straub, F. and D. Merkley (Feb 26-March 3, 1995) "Design of a smart material actuator for rotor control," in *SPIE North American Conference on Smart Structures and Materials, San Diego*.

[48] Straub, F., M. Ealey, and L. Schetky (March 3-6, 1997) "Application of smart materials to helicopter rotor active control," in *SPIE Symposium on Smart Structures and Materials, San Diego*.

[49] Straub, F., H. Ngo, V. Anand, and D. Domzalski (Newport Beach, 1999) "Development of a piezoelectric actuator for trailing edge flap control of full scale rotor blades," in *SPIE Symposium on Smart Structures and Materials, 3668-104*.

[50] Straub, F., D. Kennedy, D. Domzalski, A. Hassan, H. Ngo, V. Anand, and T. Birchette (April 2004) "Smart Material-actuated Rotor Technology - SMART," *Journal of Intelligent Material Systems and Structures*, **15**, pp. 249–260.

[51] Straub, F., D. Kennedy, A. Stemple, V. Anand, and T. Birchette (March 14-18, 2004) "Development and whirl tower test of the SMART active flap rotor," in *SPIE International Symposium on Smart Structures and Materials, San Diego, CA*.

[52] Bernhard, A. and I. Chopra (May 1996) "Trailing Edge Flap Activated by a Piezo-Induced Bending-Torsion Coupled Beam," in *52nd American Helicopter Society Forum, Washington DC*.

[53] Bernhard, A. (2000) *Smart Helicopter Rotor with Active Blade Tips*, Ph.D. thesis, University of Maryland.

[54] Clement, J., D. Brei, A. Moskalik, and R. Barrett (Apr. 20-23, 1998) "Bench-top characterization of an active rotor blade flap system incorporating C-block actuators," in *39th AIAA/ASME/ASCE/AHS/ASC Structures, Structural Dynamics, and Materials Conference, Long Beach, CA.*

[55] Clement, J., D. Brei, and R. Barrett (Apr. 12-15, 1999) "Wind tunnel testing of a high authority airspeed insensitive rotor blade flap," in *40th AIAA/ASME/ASCE/AHS/ASC Structures, Structural Dynamics, and Materials Conference, St. Louis, MO.*

[56] Centolanza, L., E. Smith, and B. Munsky (2002) "Induced-shear piezoelectric actuators for rotor blade trailing edge flaps," *Smart Materials and Structures*, **11**, pp. 24–35.

[57] Centolanza, L. (2001) *Induced Shear Piezoelectric Actuators for Smart Rotor Blades*, Ph.D. thesis, The Pennsylvania State University.

[58] Szefi, J., E. Mockensturm, E. Smith, W. K., P. Rehrig, and L. Centolanza (May 9-11, 2006) "Development of a Novel High Authority Piezoelectric Actuator for Rotor Blades with Trailing Edge Flaps," in *62nd American Helicopter Society Forum, Pheonix, AZ.*

[59] Hongu, T., M. Sato, and E. Yamakawa (Sept. 14-16, 1999) "Elementary studies of Active Flap Control with Smart Material Actuators," in *12th European Rotorcraft Forum.*

[60] Mainz, H., B. van der Wall, and P. Leconte (2005) "ABC Rotor Blades : Design, Manufacturing and Testing," in *31st European Rotorcraft Forum, Florence, Italy.*

[61] Leconte, P. and H. Mercier des Rochettes (June 11-13, 2002) "Experimental assessment of an active flap device," in *58th American Helicopter Society Forum, Montral, Canada.*

[62] Delrieux, Y., A. Le Pape, P. Leconte, P. Crozier, B. Gimonet, and H. Mercier des Rochettes (May 1-3, 2007) "Wind-Tunnel Assessment of the Concept of Active Flaps on a Helicopter Rotor Model," in *63rd American Helicopter Society Forum, Virginia Beach, VA.*

[63] Enenkl, B., V. Kloppel, D. Preissler, and P. Janker (17-19 Semptember, 2002) "Full scale rotor with piezoelectric actuated blade flaps," in *28th European Rotorcraft Forum, Bristol, UK.*

[64] Lee, J., J. Kwak, K. Son, and S. Shin (May 11-13, 2010) "Development of an SNU Intelligent Rotor Blade with an Active Trailing-edge Flap," in *66th American Helicopter Society Forum, Pheonix, AZ.*

[65] Noboru, S., K. and. Saito, T. Fukami, and K. T. (May 1-3 2007) "Design and Performance Evaluation of Full Scale On-board Active Flap System," in *63rd American Helicopter Society Forum, Virginia Beach, VA.*

[66] Noboru, K. and S. Saito (April 29-May , 2008) "Performance Evaluation of Full Scale On-board Active Flap System in Transonic Wind Tunnel," in *64th American Helicopter Society Forum, Montreal, Canada.*

[67] Saito, S., N. Kobiki, Y. Tanabe, W. Johnson, G. Yamauchi, and L. Young (November 13, 2010) "Overview of the Novel Intelligent JAXA Active Rotor Program," in *Heli Japan 2010, AHS International Meeting on Advanced Rotorcraft Technology and Safety Operations, Ohmiya, Japan.*

[68] Dawson, S. and F. Straub (May 11-13, 1994) "Design, Validation and Test of A Model Rotor with Tip Mounted Active Flaps," in *50th American Helicopter Society Forum, Washington, D.C.*

[69] Milgram, J., I. Chopra, and F. Straub (October 1998) "Rotors With Trailing Edge Flaps: Analysis and Comparision With Experimental Data," *Journal of the American Helicopter Society*, **43. No. 4**, pp. 319–332.

[70] Bothwell, C., R. Chandra, and I. Chopra (April 1995) "Torsional Actuation with Extension-Torsion Composite Coupling and a Magnetostrictive Actuator," *AIAA Journal*, **33, No. 4**, pp. 723–729.

[71] Fenn, R., J. Downer, D. Bushko, V. Gondhalekar, and N. Ham (1996) "Terfenol-D driven flap for helicopter vibration reduction," *Smart Materials and Structures*, **5**, pp. 49–57.

[72] Fink, D., T. Hawkey, and M. Gaudreau (May 2-4, 2000) "An electromagnetic actuator for individual blade control," in *56th American Helicopter Society Forum, Virginia Beach, VA.*

[73] Duvernier, M., L. Reithler, J. Guerrero, and R. Rossi (2000) "Active control system for a rotor blade trailing-edge flap," in *Proceedings of SPIE Vol. 3985.*

[74] Bernhard, A., J. O'Neil, F. Kohlhepp, W. Welsh, and P. Lorber (May 9-11, 2001) "Active Rotor Control (ARC) of a Mach-Scale Trailing Edge Flap Rotor," in *57th American Helicopter Society Forum, Washington DC.*

[75] Sirohi, J. and I. Chopra (March 2003) "Design and Development of a High Pumping Frequency Piezoelectric-Hydraulic Hybrid Actuator," *Journal of Intelligent Material Systems and Structures*, **14**, pp. 135–147.

[76] Herdic, S. (Dec. 2005) *Development of piezo-hydraulic actuation systems technology for use on a helicopter trailing edge flap*, Master's thesis, Georgia Institute of Technology.

[77] Chaudhry, Z., B. Wake, A. Bagai, P. Lorber, and A. Collins (May 27-29, 2009) "Active rotor development for primary and secondary flight control," in *65th American Helicopter Society Forum, Grapevine, TX*.

[78] Lorber, P., J. O'Neil, B. Isabella, B. Wake, U. Jonsson, and F. Sun (May 11-13, 2010) "Whirl Test of a Large Scale High Authority Active Flap Rotor," in *66th American Helicopter Society Forum, Phoenix AZ*.

[79] Lorber, P., J. O'Neil, B. Hein, B. Isabella, K. Andrews, M. Brigley, J. Wong, P. LeMasurier, and B. Wake (May 3-5, 2011) "Whirl and Wind Tunnel Testing of the Sikorsky Active Flap Demonstration Rotor," in *67th American Helicopter Society Forum, Virginia Beach, VA*.

[80] Woods, B., E. Bubert, C. Kothera, J. Sirohi, and N. Wereley (23 - 26 April 2007) "Experimental Testing of Pneumatic Artifical Muscles for Trailing Edge Flap Actuation," in *48th AIAA/ASME/ASCE/AHS/ASC Structures, Structural Dynamics, and Materials Conference, Honolulu, Hawaii*.

[81] Woods, B., E. Bubert, C. Kothera, and N. Wereley (7-10 April, 2008) "Design and Testing of a Biologically Inspired Pneunatic Trailing Edge Flap System," in *49th AIAA/ASME/ASCE/AHS/ASC Structures, Structural Dynamics, and Materials Conference, Schaumburg, IL*.

[82] Woods, B., N. Wereley, and C. Kothera (Sept. 28 - Oct. 1, 2010) "Wind Tunnel Testing of a Helicopter Rotor Trailing Edge Flap Actuated via Pneumatic Artifical Muscles," in *ASME 2010 Conference on Smart Materials, Adaptive Structures and Intelligent Systems, Philadelphia, PA*.

[83] Woods, B., C. Kothera, and N. Wereley (11-13 May 2010) "Whirl Testing of a Pneumatic Artifical Muscle Driven Helicopter Trailing Edge Flap," in *66th American Helicopter Society Forum, Pheonix, AZ*.

[84] Saxena, A. and I. Chopra (3-5 May, 2011) "Development and Testing of a Swashplateless Rotor with Compact Brushless Motor Actuated Flaps for Primary Control," in *67th American Helicopter Society Forum, Virginia Beach, VA*.

[85] Liebeck, R. H. (1978) "Design of Subsonic Airfoils for High Lift," *Journal of Aircraft*, **15**, pp. 547–561.

[86] Bae, E., F. Gandhi, and M. Maughmer (May 27-29, 2009) "Optimally Scheduled Deployments of Miniature Trailing-Edge Effectors for Rotorcraft Power Reduction," in *65th American Helicopter Society Forum, Grapevine, TX*.

[87] Thepvongs, S. (2002) *Design and testing of an active Gurney flap actuator for helicopter rotor blade control, Bachelors Thesis, Tech. rep.*, The Pennsylvania State University.

[88] Thiel, M. (2006) *Actuation of an active gurney flap for rotorcraft applications*, Master's thesis, The Pennsylvania State University.

[89] Palacios, J., A. Overmeyer, E. Smith, M. Maughmer, M. Kinzel, and J. Szefi (May 3-5, 2011) "Experimental Measurement of Unsteady Lift and Pitching Moments for MiTEs on a S903 Airfoil," in *67th American Helicopter Society Forum, Virginia Beach, VA*.

[90] Wilbur, M. L., P. H. Mirick, W. T. Y. Jr., C. W. Langston, C. E. S. Cesnik, and S. Shin (May 9-11, 2001) "Vibratory Loads Reduction Testing of the NASA/ARMY/MIT Active Twist Rotor," in *57th Annual Forum of the American Helicopter Society, Washington, D.C.*

[91] Wilbur, M. L., W. T. Y. Jr., and M. K. Sekula (June 11-13, 2002) "Further Examination of the Vibratory Loads Reduction Results from the NASA/Army/MIT Active Twist Rotor Test," in *58th Annual Forum of the American Helicopter Society, Montreal, Canada*.

[92] Sekula, M., M. Wilbur, and W. Yeager (June 1-3, 2005) "A Parametric Study of the Structural Design for an Advanced Active Twist Rotor," in *61st American Helicopter Society Forum, Grapevine, TX*.

[93] Floros, M., W. Johnson, and M. Scully (January 23-25, 2002) "Advanced Rotor Aerodynamics Concepts with Application to Large Rotorcraft," in *American Helicopter Society Aerodynamics, Acoustics, and Test and Evaluation Technical Specialists Meeting, San Francisco, CA*.

[94] Keys, C., F. Tarzanin, and F. McHugh (8-11 September 1987) "Effect of twist on helicopter performance and vibratory loads," in *13th European Rotorcraft Forum, Arles, France*.

[95] Bousman, W. (June 11-13, 2002) "Airfoil Design and Rotorcraft Performance," in *58th American Helicopter Society Forum, Montral, Canada*.

[96] Jang, J. and I. Chopra (July 1988) "Ground and Air Resonance of an Advanced Bearingless Rotor in Hover," *Journal of the American Helicopter Society*, **33, No. 3**.

[97] Chen, P. (1996) *Development of a smart rotor with induced-strain actuation of blade twist*, Ph.D. thesis, University of Maryland.

[98] Chen, P. and I. Chopra (1997) "Wind Tunnel Test of a Smart Rotor Model with Individual Blade Twist Control," *Journal of Intelligent Material Systems and Structures*, **8**, pp. 414–425.

[99] ——— (January 1997) "Hover Testing of Smart Rotor with Induced-Strain Actuation of Blade Twist," *AIAA Journal*, **35 (1)**, pp. 6–16.

[100] Bent, A. and N. Hagood (1997) "Piezoelectric Fiber Composites with Interdigitated Electrodes," *Journal of Intelligent Material Systems and Structures*, **8**, pp. 903–919.

[101] Derham, R. and N. Hagood (1996) "Rotor Design Using Smart Materials to Actively Twist Blades," in *52nd Annual Forum American Helicopter Society, Washington, D.C.*

[102] Shin, S. (2001) *Integral Twist Actuation of Helicopter Rotor Blades for Vibration Reduction*, Ph.D. thesis, Massachusetts Institute of Technology.

[103] Shin, S., C. Cesnik, and S. Hall (May 6-8, 2003) "Closed-loop control test of the NASA/Army/MIT active twist rotor for vibration reduction," in *59th American Helicopter Society Forum, Phoenix, AZ.*

[104] Weems, D., D. Anderson, M. B. Mathew, and R. Bussom (June 7-10, 2004) "A Large-Scale Active-Twist Rotor," in *60th American Helicopter Society Forum, Baltimore, MD.*

[105] Wilkie, W. K., R. G. Bryant, J. W. High, R. L. Fox, and R. F. Hellbaum (2000) "Low-Cost Piezocomposite Actuator for Structural Control Applications," in *Smart Structures and Materials 2000: Industrial and Commercial Applications of Smart Structures Technologies, Proceedings of SPIE Vol. 3991.*

[106] "Smart Materials Corporation, http://www.smart-material.com/," Last Accessed: May 22, 2012.
URL `http://www.smart-material.com/`

[107] Buter, A. and E. Breitbach (2000) "Adaptive Blade Twist - calculations and experimental results," *Aerospace Science and Technology*, **4**, pp. 309–319.

[108] Wierach, P., J. Riemenschneider, S. Opitz, and F. Hoffmann (2007) "Experimental Investigation of an Active Twist Model Rotor Blade Under Centrifugal Loads," in *33rd European Rotorcraft Forum, Kazan, Russia.*

[109] Monner, H. P., S. Opitz, J. Riemenschneider, and P. Wierach (7-10 April, 2008) "Evolution of Active Twist Rotor Designs at DLR," in *49th AIAA/ASME/ASCE/AHS/ASC Structures, Structural Dynamics, and Materials Conference, Schaumburg, IL.*

[110] Hoffmann, F., S. Opitz, and J. Riemenschneider (May 27-29, 2009) "Validation of Active Twist Modeling Based on Whirl Tower Tests," in *65th Annual American Helicopter Society Forum, Grapevine, TX.*

[111] Riemenschneider, J., S. Opitz, P. Wierach, H. Mercier des Rochettes, L. Buchaniek, and D. Joly (22-25 September, 2009) "Structural design and testing of active twist blades A comparison," in *35th European Rotorcraft Forum, Hamburg, Germany.*

[112] Opitz, S., J. Riemenschneider, F. Hoffmann, and O. Schneider (2010) "Measurement of the dynamic tip twist angle of an active twist model scale rotor blade," in *36th European Rotorcraft Forum, Paris, France.*

[113] Opitz, S., J. Riemenschneider, and M. Schulz (3-5 May, 2011) "Prerequisites for the closed loop control of an active twist rotor blade," in *67th American Helicopter Society Forum.*

[114] Opitz, S. (June 2011) in *Personal Correspondence, DLR Braunschweig.*

[115] Monner, H. P., J. Riemenschneider, S. Opitz, and M. Schulz (4 - 7 April 2011) "Development of active twist rotors at the German Aerospace Center (DLR)," in *52nd AIAA/ASME/ASCE/AHS/ASC Structures, Structural Dynamics and Materials Conference, Denver, Colorado.*

[116] Sekula, M. K., M. Wilbur, and W. Yeager (January 21-23, 2004) "Aerodynamic Design Study of an Advanced Active Twist Rotor," in *American Helicopter Society 4th Decennial Specialists Conference on Aeromechanics, San Francisco, CA.*

[117] Wilbur, M. and M. Sekula (June 1-3, 2005) "The effect of tip geometry on Active-twist rotor response," in *61st American Helicopter Society Forum, Grapevine, TX.*

[118] Thornburgh, R., A. Kreshock, and M. Wilbur (May 3-5, 2011) "Structural Optimization of Active-Twist Rotor Blades," in *67th American Helicopter Society Forum, Virginia Beach, VA*, this is the Apache ATR paper.

[119] Cesnik, C., J. Mok, J. Morillo, and A. Parikh (September 2004) "Design Optimization of Active Twist Rotor Blades," in *30th European Rotorcraft Forum, Marseille, France*.

[120] Kreshock, A., R. Thornburgh, M. Wilbur, and C. W. Langston (23-26 April 2012, Honolulu, HI) "Experimental Bench Testing of an Active-Twist Rotor Blade," in *53rd AIAA/ASME/ASCE/AHS/ASC Structures, Structural Dynamics and Materials Conference*.

[121] Thakkar, D. and R. Ganguli (2007) "Induced shear actuation of helicopter rotor blade for active twist control," *Jounral of Thin-Walled Structures*, **45**, pp. 111–121.

[122] Bernhard, A. and I. Chopra (2001) "Analysis of a bending-torsion coupled actuator for a smart rotor with active blade tips," *Smart Materials and Structures*, **10**, pp. 35–52.

[123] Riemenschneider, J., S. Keye, P. Wierach, and H. des Rochetter (14-16 September 2004) "Review of the common DLR/ONERA project "Active Twist Blade" (ATB)," in *30th European Rotorcraft Forum, Marseille, France*, pp. 22.1–9.

[124] Centolanza, L. and E. Smith (22 - 25th April 2002) "Induced-Shear Piezoelectric Actuators for Active Twist Rotor Blades." in *43rd AIAA/ASME/ASCE/AHS/ASC Structures, Structural Dynamic and Materials Conference, Denver, CO*.

[125] Nixon, M. (April 1988) *Improvements to Tilt Rotor Performance Through Passive Blade Twist Control, Tech. rep.*, NASA TM 100583, USAAVSCOM TM 88-B-010.

[126] ——— (Apr 6-8, 1987) "Extension-twist coupling of composite circular tubes with application to tilt rotor blade design," in *28th Structures, Structural Dynamics and Materials Conference, Monterey, CA*.

[127] Lake, R., M. Nixon, M. Wilbur, and J. Singleton (Apr 13-15, 1992) "A demonstration of passive blade twist control using extension-twist coupling," in *33rd AIAA/ASME/ASCE/AHS/ASC Structures, Structural Dynamics and Materials Conference, Dallas, TX*.

[128] Lake, R., M. Nixon, M. Wilbur, J. Singleton, and P. Mirick (April 13-15, 1992) "Demonstration of an Elastically Coupled Twist Control Concept for Tilt Rotor Blade Application," in *33rd AIAA/ASME/ASCE/AHS/ASC Structures, Structural Dynamics, and Materials Conference, Dallas, TX*.

[129] Kosmatka, J. and R. Lake (Apr. 15-17, 1996) "Extension-twist behavior of initially twisted composite spars for tilt-rotor applications," in *37th AIAA/ASME/ASCE/AHS/ASC Structures, Structural Dynamics and Materials Conference and Exhibit, Salt Lake City, UT.*

[130] Nampy, S. (August 2005) *Structural behavior and design of flexible matrix composite box beams with extension twist coupling*, Master's thesis, The Pennsylvania State University.

[131] DiOttavio, J. and D. Friedmann (May 11-13, 2010) "Operational Benefits of an Optimal, Widely Variable Speed Rotor," in *66th American Helicopter Society Forum, Phoenix, AZ.*

[132] Guo, W. (December 2009) *Flight control design for rotorcraft with variable rotor speed*, Ph.D. thesis, The Pennsylvania State University.

[133] Steiner, J., F. Gandhi, and Y. Yoshizaki (April 29 May 1, 2008) "An Investigation of Variable Rotor RPM on Performance and Trim," in *American Helicopter Society 64th Annual Forum, Montreal, Canada.*

[134] Mistry, M. and F. Gandhi (May 11-13, 2010) "Performance Improvement with Variable Rotor Span and RPM," in *66th Annual AHS Forum, Phoenix, AZ.*

[135] Bowen-Davies, G. and I. Chopra (May 3-5, 2011) "Aeromechanics of a Variable-Speed Rotor," in *67th American Helicopter Society Forum, Virginia Beach, VA.*

[136] Berry, B. and I. Chopra (May 3-5, 2011) "Wind Tunnel Testing for Performance and Vibratory Loads of a Variable-Speed Mach-Scale Rotor," in *67th American Helicopter Society Forum, Virginia Beach, VA.*

[137] Datta, A., H. Yeo, and T. Norman (May 3-5, 2011) "Experimental Investigation and Fundamental Understanding of a Slowed UH-60A Rotor at High Advance Ratios," in *67th American Helicopter Society Forum, Virginia Beach, VA.*

[138] Berry, B. and I. Chopra (May 1-3, 2012) "Performance and Vibratory Load Measurements of a Slowed-Rotor at High Advance Ratios," in *68th Annual American Helicopter Society Forum, Fort Worth, TX.*

[139] Clingman, D. J. and D. Jacot (07 March 2000) "Shape Memory Alloy Consortium and Demonstration," in *Smart Structures and Materials Conference (SPIE), Newport Beach, CA.*

[140] Ruggeri, R., D. Jacot, and D. Clingman (18 March 2002) "Shape memory actuator systems and the use of thermoelectric modules." in *Smart Structures and Materials Conference (SPIE), San Diego, CA.*

[141] Caldwell, N. and E. Gutmark (8 - 11 Jan 2007) "Performance Predictions of a Blade Twist Actuator System." in *45th AIAA Aerospace Sciences Meeting and Exhibit (2007), Reno, NV.*

[142] Arbogast, D., R. Ruggeri, and R. Bussom (2008) "Development of a -Scale NiTinol Actuator for Reconfigurable Structures," in *SPIE, Industrial and Commercial Applications of Smart Structures Technologies, Vol 6930.*

[143] Prahlad, H. and I. Chopra (05 March 2001) "Design of a Variable Twist Tiltrotor Blade Using Shape Memory Alloys (SMA) Actuators," in *Smart Structures and Materials Conference (SPIE), Newport Beach, CA.*

[144] ——— (22 - 25th April 2002) "Characterization of SMA Torsional Actuators for Active Twist of Tilt Rotor Blades," in *43rd AIAA/ASME/ASCE/AHS/ASC Structures, Structural Dynamics and Materials Conference, Denver, CO.*

[145] Prahlad, H. (2002) *Development of Shape Memory Alloy (SMA) Torsional Actuators for Variable Twist Tilt Rotor (VTTR) blades*, Ph.D. thesis, University of Maryland.

[146] Park, J., S. Kim, and S. N. Jung (May 11-13, 2010) "Application of Shape Memory Alloy Hybrid Composites for Variable-Twist Proprotors," in *66th American Helicopter Society Forum, Phoenix, AZ.*

[147] Mistry, M. and F. Gandhi (7 - 10 April 2008,) "Twist Control of an I-beam through Vlasov Bimoment Actuation," in *49th AIAA/ASME/ASCE/AHS/ASC Structures, Structural Dynamics, and Materials Conference, Schaumburg, IL.*

[148] Van Weddingen, Y., O. Bauchau, S. Kottapalli, S. Ozbay, and M. Y. (January 20-22, 2010) "Application of out-of-plane warping to control rotor blade twist," in *American Helicopter Society Aeromechanics Specialists Conference, San Francisco, CA.*

[149] Linden, A., B. W., D. Beck, M. D'Onofrio, R. Flemming, E. Hibyan, R. Johnston, R. J. Murrill, and D. Unsworth (January 1972) *Variable Diameter Rotor Study, Tech. rep.*, Air Force Flight Dynamics Laboratory, Airf Force Systems Command, Wright-Patterson Air Force Base, Ohio, Report No. AFFDL-TR-71-170.

[150] Fradenburgh, E. A., L. Hager, and N. Kefford (Feb. 1976) *Evaluation of the TRAC Variable-Diameter Rotor: Preliminary Design of a Full-Scale Rotor and Parametric Mission Analysis Comparision*, *Tech. rep.*, Sikorsky Aircraft, USAAMRDL-TR-75-54, Eustis Directorate, U.S. Army Air Mobility R&D Laboratory, Fort Eustis, VA.

[151] Fradenburgh, E. A. and D. G. Matuska (June 3-5, 1992) "Advancing Tiltrotor State-of-the-art with Variable Diameter Rotors," in *48th American Helicopter Society Forum, Washington D.C.*

[152] Segel, R. M. and E. A. Fradenburgh (Feb 17-19 1969) "Development of the TRAC Variable Diameter Rotor Concept," in *AIAA/AHS VTOL Research, Design, and Operations Meeting.*

[153] Fradenburgh, E. A., R. J. Murrill, and E. Kiely (July 1973) *Dynamic Model Wind Tunnel Tests of a Variable Diameter, Telescoping-Blade Rotor System (TRAC Rotor)*, *Tech. rep.*, Sikorsky Aircraft, USAAMRDL-TR-73-32, Eustis Directorate, U.S. Army Air Mobility R&D Laboratory, Fort Eustis, VA.

[154] Fradenburgh, E. A. (May 13-15, 1975) "Application of a Variable Diameter Rotor System to Advanced VTOL Aircraft," in *31st American Helicopter Society Forum, Washington, D.C.*

[155] Frint, H. (Jan. 1977) *Design Selection Tests for TRAC Retraction Mechanism*, *Tech. rep.*, Sikorsky Aircraft, USAAMRDL-TR-76-43, Eustis Directorate, U.S. Army Air Mobility R&D Laboratory, Fort Eustis, VA.

[156] Studebaker, K. and D. G. Matuska (May 19-21, 1993) "Variable Diameter Tiltrotor Wind Tunnel Test Results," in *49th American Helicopter Society Forum, St. Louis, MO.*

[157] Turmanidze, R. S., S. N. Khutsishvili, and L. Dadone (Nov. 11-16, 2001) "Design and Experimental Investigation of Variable-Geometry Rotor Concepts," in *Adaptive Structures and Materials Symposium, International Mechanical Engineering Congress and Exposition, New York, NY.*

[158] Turmanidze, R. S. and L. Dadone (May 11-13, 2010) "New Design of a Variable Geometry Prop-Rotor with Cable and Hydraulic-System Actuation," in *66th American Helicopter Society Forum, Phoenix, AZ.*

[159] Prabhakar, T., F. Gandhi, J. Steiner, and D. McLaughlin (May 1-3, 2007) "A Centrifugal Force Actuated Variable Span Morphing Helicopter Rotor," in *American Helicopter Society 63rd Annual Forum, Virginia Beach, VA.*

[160] Prabhakar, T. (2007) *A centrifugal force actuated morphing rotor*, Master's thesis, The Pennsylvania State University.

[161] Leon, O., E. Hayden, and F. Gandhi (May 27-29, 2009) "Rotorcraft Operating Envelope Expansion Using Extendable Chord Sections," in *American Helicopter Society 65th Annual Forum, Grapevine, Texas*.

[162] Khoshlajeh, M. and F. Gandhi (May 3-5 2011) "Extendable Chord Rotors for Helicopter Envelope Expansion and Performance Improvement," in *67th American Helicopter Society Forum, Virginia Beach, VA*.

[163] Noboru, K., N. Kondo, S. Saito, T. Akasaka, and Y. Tanabe (14-16 Sept. 2004) "An Experimental Study of On-blade Active Tab for Helicopter Noise Reduction," in *30th European Rotorcraft Forum, Marseilles, France*.

[164] ——— (16-18 Sept. 2003) "Active Tab, a New Active Technique for Helicopter Noise Reduction," in *29 European Rotorcraft Forum, Firedrichshafen, Germany*.

[165] Barbarino, S., F. Gandhi, and S. Webster (Sept . 28 - Oct. 1, 2010) "Design of extendable chord sections for morphing helicopter rotor blades," in *ASME 2010 conference on Smart Materials, Adaptive Structures and Intelligent Systems, Philadelphia, PA*.

[166] Hayden, E. (August 2012) *Design and testing of a helicopter rotor blade chord extension system*, Master's thesis, The Pennsylvania State University.

[167] Moser, P., S. Barbarino, and F. Gandhi (September 19-21, 2012) "Helicopter rotor blade chord extension morphing using a centrifugally actuated von-mises truss," in *ASME 2012 conference on Smart Materials, Adaptive Structures and Intelligent Systems (SMASIS), Stone Mountain, Georgia*.

[168] Buter, A., C. Ehlert, U, D. Sachau, and E. Breitbach (8-11 May 2000) "Adaptive Rotor Blade Concepts - Direct Twist and Camber Variation -," in *RTO AVT Symposium on Active Control Technology for Enhanced Performance Operational Capabilities of Military Aircraft, Land Vehicles and Sea Vehicles, Braunschweig, Germany*.

[169] Anusonti-Inthra, P., R. Sarjeant, M. Frecker, and F. Gandhi (August 2005) "Design of a Conformable Rotor Airfoil Using Distributed Piezoelectric Actuators," *AIAA Journal*, **43, No. 8**, pp. 1684–1695.

[170] Nissly, A., P. Anusonti-Inthra, F. Gandhi, and M. Frecker (June 1-3 2005) "Design optimization of a controllable camber rotor airfoil," in *61st American Helicopter Society Forum, Grapevine, TX*.

[171] Gandhi, F. and P. Anusonti-Inthra (2008) "Skin design studies for variable camber morphing airfoils," *Smart Materials and Structures*, **17**, p. 8.

[172] Daynes, S., S. Nall, P. Weaver, K. Potter, P. Margaris, and P. Mellor (4-7 May 2009) "On a Bistable Flap for an Airfoil," in *50th AIAA/ASME/ASCE/AHS/ASC Structures, Structural Dynamics, and Materials Conference, Palm Springs, CA*.

[173] Quackenbush, T., D. Wachspress, R. McKilllip, and C. Solomon (May 11-13, 2010) "Tiltrotor/tiltwing performance enhancement via active on-blade flaps," in *66th Annual American Helicopter Society Forum, Phoenix, AZ*.

[174] Maucher, C., B. Grohmann, P. Janker, A. Altmikus, F. Jensen, and H. Baier (September 2007) "Actuator design for the active trailing edge of a helicopter rotor blade," in *33rd European Rotorcraft Forum, Kazan, Russia*.

[175] Grohmann, B., C. Maucher, P. Janker, and P. Wierach (7 - 10 April 2008) "Embedded Piezoceramic Actuators for Smart Helicopter Rotor Blades," in *49th AIAA/ASME/ASCE/AHS/ASC Structures, Structural Dynamics, and Materials Conference, Schaumburg, IL*.

[176] Grohmann, B., F. Muller, E. Ahci, R. Pfaller, M. Bauer, C. Maucher, O. Dietrich, S. Storm, and P. Janker (May 3-5, 2011) "Design, Evaluation and Test of Active Trailing Edge," in *67th American Helicopter Society Forum, Virginia Beach, VA*.

[177] McKilllip, R. and T. Quackenbush (January 18-20, 2012) "The Flight Adaptive Blade For Optimum Rotor Response (FABFORR) Concept," in *American Helicopter Society Future Vertical Lift Aircraft Design Conference*.

[178] Martin, P., K. McAlister, M. Chandrasekhara, and W. Geissler (May 6 8, 2003) "Dynamic Stall Measurements and Computations for a VR-12 Airfoil with a Variable Droop Leading Edge," in *59th American Helicopter Society Forum, Phoenix, AZ*.

[179] Shaner, M. and I. Chopra (March 1999) "Design and Testing of a Piezostack Actuated Leading-Edge Flap," in *SPIE symposium on Smart Structures and Materials, Vol. 3668*.

[180] Fink, D., N. Reinhardt, R. Severance, R. Phillips, M. Gaudreau, and R. Ormiston (May 1-3, 2007) "Deformable leading edge electromagnetic airfoil," in *63rd American Helicopter Society Forum, Virginia Beach, VA*.

[181] Kota, S., G. Ervin, R. Osborn, and R. Ormiston (April 29-May 1, 2008) "Design and Fabrication of an Adaptive Leading Edge Rotor Blade," in *64th American Helicopter Society Forum, Montreal, Canada*.

[182] Guo, W. and J. Horn (May 27-29, 2009) "Helicopter Flight Control with Variable Rotor Speed and Torque Limiting," in *65th Annual American Helicopter Society Forum, Grapevine, Texas*.

[183] Steiner, J. (2008) *An investigation of performance benefits and trim requirements of a variable speed helicopter rotor*, Master's thesis, The Pennsylavania State University.

[184] Liu, L., P. Freidmann, I. Kim, and D. Bernstein (April 2008) "Rotor performance enhancement and vibration reduction in presence of dynamic stall using actively controlled flaps," *Journal of the Americal Helicopter Society*, **53(2)**, pp. 152–163.

[185] Bae, E. S. (December 2012) *The Reduction of Rotorcraft Power and Vibration Using Optimally Controlled Active Gurney Flap*, Ph.D. thesis, The Pennsylvania State University.

[186] McVeigh, M. A., H. J. Rosenstein, and F. J. McHugh (May 1983) "Aerodynamic design of the XV-15 advanced composite tiltrotor blade," in *39th Annual Forum of the American Helicopter Society, St. Louis, MO*, pp. 72–80.

[187] Khoshlahjeh, M. (August 2012) *Extendable chord rotors for helicopter performance improvement and envelope expansion*, Ph.D. thesis, The Pennsylvania State University.

[188] Howlett, J. (December 1981) *UH-60 Black Hawk Engineering Simulation Program*, *Tech. rep.*, NASA Contractor Report 166309.

[189] Ormiston, R. (June 1-3, 2005) "Further Investigations of Helicopter Rotor Induced Power," in *61st American Helicopter Society Forum, Grapevine, TX*.

[190] Hamrock, B., B. Jacobson, and S. Schmid (1999) *Fundamentals of Machine Elements*, WCB/McGraw-Hill.

[191] (2012), Web.
URL `http://www.matweb.com`

[192] Cao, Y., Web.
URL `http://www.mathworks.com/matlabcentral/fileexchange/17251-pareto-front`

[193] Prouty, R. W. (2002) *Helicopter Performance, Stability, and Control*, Krieger Pub Co.

[194] Staley, J. (January 1976) *Validation of rotorcraft flight simulation program through correlation with flight data for soft-in-plane hingeless rotors*, *Tech. rep.*, U.S. Army Air Mobility Research and Development Laboratory, Eustis Directorate, Fort Eustis, VA (ADA 21176, AMRDL-TR-75-50).

[195] Vlasov, V. (1961) *Thin-Walled Elastic Beams.*, Israel Program for scientific translations.

[196] Bagai, A. and G. Leishman (20-23 June 1994) "Rotor Free-Wake Modeling Using a Pseudoimplicit Relaxation Algorithm," in *12th AIAA Applied Aerodynamics Conference, Colorado Springs, CO*.

[197] Bagai, A. (1995) *Contributions to the mathematical modeling of rotor flowfields using a pseudo-implicit free-wake analysis*, Ph.D. thesis, University of Maryland.

[198] Anderson, J. D. (2005) *Introduction to Flight*, McGraw-Hill.

[199] Warmbrodt, W. and R. Peterson (August 1984) *Hover Test of a Full-Scale Hingeless Rotor*, *Tech. rep.*, National Aeronautics and Space Administration (NASA), Ames Research Center.

[200] Wachspress, D., T. Quackenbush, and C. Solomon (June 2005) "On minimum induced power of the helicopter rotor," in *61st Annual American Helicopter Society Forum, Grapevine, TX*.

[201] Kroninger, C. (May 2008) *Characteristics of a rotor optimized for hover and forward flight*, Master's thesis, The Pennsylvania State University.

[202] Mistry, M., M. Nagelsmith, F. Gandhi, and Z. Gurdal (June 2011) "Actuation Requirements of a Warp Induced Variable Twist Rotor Blade," *Journal of Intelligent Material Systems and Structures*, **Vol. 22, No. 9**, pp. 919–933.

[203] Leishman, G., M. J. Bhagwat, and A. Bagai (Sept-Oct 2002) "Free-Vortex Filament Methods for the Analysis of Helicopter Rotor Wakes," *Journal of Aircraft*, **39 (5)**.

[204] Landgrebe, A. J. (May 1972) "The Wake Geometry of a Hovering Helicopter Rotor and Its Influence on Rotor Performance," in *28th Annual National Forum of the American Helcopter Society*.

[205] Kocurek, J. and J. L. Tangler (May 1976) "A Prescribed Wake Lifting Surface Hover Performance Analysis," in *32nd Annual National Forum of the American Helicopter Society*.

[206] Clark, D. R. and A. C. Leiper (May 1969) "The Free Wake Analysis: A Method for the Prediction of Helicopter Rotor Hovering Performance," in *25th Annual National Forum of the American Helicopter Society*.

[207] A., R. and A. Graber (February 19-21, 1985) "Free Wake Model of Hovering Rotors Having Straight or Curved Blades," in *The International Conference on Rotorcraft Basic Research, Research Triangle Park, North Carolina*.

[208] Scully, M. P. (June 1967) *A method of computing helicopter vortex wake distortion*, *Tech. rep.*, Massachusetts Institute of Technology Aeroelastic and Structures Research Laboratory, Technical Report No. ASRL TW 138-1.

[209] Quackenbush, T., D. B. Bliss, D. Wachspress, and C. Ong (July 1990) *Free Wake Analysis of Hover Performance Using a New Influence Coefficient Method*, *Tech. rep.*, National Aeronautics and Space Administration, Technical Report no. 4309.

[210] Crouse Jr., G. L. and G. Leishman (January 11-14, 1993) "A New Method for Improved Rotor Free-Wake Convergence," in *31st Aerospace Sciences Meeting and Exhibit, Reno, NV*.

[211] Bagai, A. and G. Leishman (November-December 1995) "Rotor Free-Wake Modeling Using a Pseudoimplicit Relaxation Algorithm," *Journal of Airc*, **32 (6)**.

[212] Sitaraman, J. (2003) *CFD Based Unsteady Aerodynamic Modeling for Rotor Aeroelastic Analysis*, Ph.D. thesis, University of Maryland.

[213] Bagwat, M. and G. Leishman (June 11-13, 2002) "Generalized viscous vortex model for application to Free-vortex wake and aeroacoustic calculations," in *58th Annual Forum and Technology Display of the American Helicopter Society International, Montreal, Canada*.

[214] Anderson, J. D., S. Corda, and D. M. Van Wie (December 1980) "Numerical Lifting Line Theory Applied to Drooped Leading-Edge Wings Below and Above Stall," *Journal of Aircrat*, **17 (12)**, pp. 898–904.

Vita

Mihir Mistry

Mihir Mistry was born in Sharjah, United Arab Emirates on the 20th of July, 1985. He moved to the United States in 2000 and graduated from Passaic High School (Passaic, New Jersey) in 2003. Following this he completed his Bachelors of Science and Masters of Science in Aerospace Engineering at the Pennsylvania State University (University Park, Pennsylvania) in August of 2008. The topic of his thesis research was 'Induced warp systems to obtain active twist of rotor blades'. After graduating he was enrolled in the doctoral program with the Aerospace engineering department at the same institution. During the course of his studies Mihir Mistry has completed two internships, the first at the Boeing Company in Seattle, Washington (2006) and the second at the German Aerospace Center (DLR) in Braunschweig, Germany (2008).